SEISMIC BEHAVIOR OF SLENDER COUPLING BEAMS CONSTRUCTED WITH HIGH-PERFORMANCE FIBER-REINFORCED CONCRETE

by

Monthian Setkit

A dissertation submitted in partial fulfillment
of the requirements for the degree of
Doctor of Philosophy
(Civil Engineering)
in The University of Michigan
2012

Doctoral Committee:

Professor James K. Wight, Co-Chair
Professor Gustavo J. Parra-Montesinos, Co-Chair
Assistant Professor Jason P. McCormick
Professor Anthony M. Waas

To My Family

for their relentless love and support

ACKNOWLEDGEMENTS

The writer would like to acknowledge Professor James K. Wight and Professor Gustavo J. Parra-Montesinos, Co-Chairmen of his doctoral thesis committee, for their invaluable guidance and support throughout this study. It is a great honor to work with professors, educators, and researchers like them, particularly in the field of reinforced concrete design. The writer would also like to thank the other members of his doctoral committee, Assistant Professor Jason P. McCormick and Professor Anthony M. Waas, for reviewing this report and offering helpful comments and suggestions.

The writer would like to thank the Fulbright Program and the Office of Higher Education, Thailand, for awarding him a fellowship to pursue graduate studies in the U.S. The partial support for this research study provided by the National Science Foundation under grant No. F013628 is greatly appreciated. Bekaert Corporation is acknowledged for their donation of material and partial support for the construction and testing of specimens.

The writer wishes to thank the technicians in the Structures Laboratory, Robert Fisher, Jan Pantolin, and especially Robert Spence, whose expertise enabled him to complete the experimental work in a timely manner. Sincere thanks are due to several friends who helped construct and test specimens: Alex DaCosta, Dr. Wen-Cheng Liao, Dr. Min-Yuan Cheng, Dr. Mantia Athanasopoulou, Beverly Smith, and Chirag Kapadia. The writer especially wants to thank Dr. Remy Lequesne, who helped and taught him to work in the laboratory during the initial phase of this research project. Conversations with him about coupling beams were always enjoyable. Thanks are also due to Dr. Seong-Cheol Lee from the University of Toronto for many helpful suggestions and materials related to the VecTor2 program.

The writer would also like to thank fellow graduate students, especially Matt Fadden, Xiaohu Fan, Antonio Conforti, and Thai Dam for their friendship along the way. Special thanks are extended to Thai friends and the Thai Student Association for their

friendship and warm community. Appreciation is due to Dr. Kittinun Sirijaroonchai, Dr. Thaweesak Jirathanathaworn, Dr. Chachrist Srisuwanrat, and Dr. Supat Suwannakarn for their friendship and good times spent together both inside and outside the Department of Civil and Environmental Engineering during my first two years of study. The writer also owes great thanks to Pawinee Mahasittiwat for her continuous love, support, and encouragement.

Finally, the writer would like to thank his family for their love and support throughout the course of his studies. The writer would not have come this far without them.

TABLE OF CONTENTS

DEDICATION…… ii
ACKNOWLEDGEMENTS……..……. iii
LIST OF FIGURES…….....x
LIST OF TABLES…… .xvii
LIST OF APPENDICES……...xix
ABSTRACT …….....xx
CHAPTER 1 INTRODUCTION..... 1
1.1 Background and Motivation..... 1
1.2 Objective 5
1.3 Organization of Thesis 5
CHAPTER 2 LITERATURE REVIEW..... 7
2.1 Review of Research on Coupling Beams..... 7
2.1.1 Background..... 7
2.1.2 Reinforced Concrete Coupling Beams..... 9
2.1.3 Slender Coupling Beams..... 15
2.1.4 Composite Coupling Beams 17
2.2 High-Performance Fiber Reinforced Concrete 17
2.2.1 Background..... 17
2.2.2 Strain-hardening and Deflection-hardening..... 21
2.2.3 Mechanical Properties of Fiber Reinforced Concrete..... 22
2.2.4 Seismic Applications of HPFRC 25
2.2.5 HPFRC Coupling Beams..... 26
2.3 ACI Building Code Seismic Provisions for RC Coupling Beams 27

CHAPTER 3 EXPERIMENTAL PROGRAM 29
3.1 Description of Test Specimens 29
3.2 Test Setup 32
3.3 Design of Test Specimens 33
3.4 Reinforcement Details of Test Specimens 37
3.4.1 Specimen CB-1 (HPFRC with $\ell_n/h = 2.75$) 37
3.4.2 Specimen CB-2 (HPFRC with $\ell_n/h = 2.75$) 38
3.4.3 Specimen CB-3 (HPFRC with $\ell_n/h = 3.3$) 39
3.4.4 Specimen CB-4 (RC with $\ell_n/h = 2.75$) 40
3.4.5 Specimen CB-5 (HPFRC with $\ell_n/h = 3.3$) 40
3.4.6 Specimen CB-6 (HPFRC with $\ell_n/h = 2.75$) 41
3.5 Construction of Specimens 43
3.6 HPFRC and Concrete proportions and mixing 47
3.7 Instrumentation and Testing Procedure 50
3.8 Material Properties 56
3.8.1 Reinforcing Bars 56
3.8.2 Compressive Strength 57
3.8.3 HPFRC Flexural Strength 58
3.8.4 Compressive and Tensile Stress-Strain Responses of HPFRC Material 60
3.8.5 Constitutive Model of Reinforcing Steels under Cyclic Loading 62
CHAPTER 4 EXPERIMENTAL RESULTS AND ANALYSIS 64
4.1 Processing of Optotrak Data and Calculation of Drift, Stress, and Strain 64
4.1.1 Coordinate Transformation 64
4.1.2 Average Shear Stress 66
4.1.3 Drift 67
4.1.4 Strains 69
4.2 Load versus Drift Responses and Damage Progression 70

4.2.1 Specimen CB-1 (HPFRC with $\ell_n/h = 2.75$ and diagonal reinforcement, and $f_c' = 7.2$ ksi) 71

4.2.2 Specimen CB-2 (HPFRC with $\ell_n/h = 2.75$ and diagonal reinforcement, and $f_c' = 8.6$ ksi) 75

4.2.3 Specimen CB-3 (HPFRC with $\ell_n/h = 3.3$ and diagonal reinforcement, and $f_c' = 8.9$ ksi) 79

4.2.4 Specimen CB-4 (RC with $\ell_n/h = 2.75$ and diagonal reinforcement, and $f_c' = 9.0$ ksi) 82

4.2.5 Specimen CB-5 (HPFRC with $\ell_n/h = 3.3$ and no diagonal reinforcement, and $f_c' = 9.9$ ksi)..... 86

4.2.6 Specimen CB-6 (HPFRC with $\ell_n/h = 2.75$ and no diagonal reinforcement, and $f_c' = 9.8$ ksi)..... 89

4.2.7 Summary of Test Observations..... 93

4.3 Beam Elongation and Axial Force 95

4.4 Flexural Behavior..... 101

4.4.1 Flexural Strength..... 101

4.4.2 Inflection Points..... 103

4.4.3 Longitudinal Strain Distribution..... 105

4.4.4 Curvature Distribution 108

4.4.5 Moment-Curvature Response 112

4.4.6 Plastic Hinge Length..... 118

4.5 Shear Behavior 119

4.5.1 Analysis of Shear Strength 119

4.5.2 Shear Contribution of Shear Resistance Mechanisms 119

4.5.3 Sliding Shear Response..... 125

4.5.4 Average Shear Strains..... 133

4.5.5 Shear Friction 138
4.6 Reinforcement Steel Strains 144
4.7 Energy Dissipation Capacity 150
4.8 Drift Components 155
4.9 Stiffness Retention Capacity 161
4.10 Flexural Stiffness 165
4.11 Shear Stiffness 167
CHAPTER 5 NONLINEAR FINITE ELEMENT MODELING OF COUPLING BEAMS 169
5.1 VecTor2 169
5.2 Guidelines for Modeling HPFRC Coupling Beams in VecTor2 170
5.2.1 Geometry Modeling and Element Types 170
5.2.2 Material Models 175
5.2.3 HPFRC Models in VecTor2 184
5.2.4 Boundary Conditions and Imposed Displacements 186
5.3 Analysis results 187
5.3.1 Load-Drift Responses 187
5.3.2 Failure Modes and Crack Patterns 197
5.4 A Summary of Recommendations for Finite Element Modeling of HPFRC Coupling Beams 202
CHAPTER 6 SUMMARY AND CONCLUSIONS 203
6.1 Summary 203
6.2 Conclusions 204
6.3 Recommendations for Future Research 207
Appendix A 208
Appendix B 214
Appendix C 221
Appendix D 227

References 234

LIST OF FIGURES

Figure 1.1 Coupled walls and coupling beams (Taranath 2010) 1
Figure 1.2 Flexural resistance of coupled walls (Canbolat 2004) 2
Figure 1.3 Standard reinforcement detailing in earthquake-resistant coupling beams (courtesy of Rémy Lequesne) 3
Figure 2.1 Deflection patterns of coupling beams in a coupled wall structure..... 9
Figure 2.2 Sliding shear failure in coupling beams (Park and Paulay 1975)..... 10
Figure 2.3 Diagonally reinforced coupling beam (Paulay and Santhakumar 1976)..... 11
Figure 2.4 Reinforcement configurations investigated by Tassios et al. (1996) 14
Figure 2.5 Stress-strain behavior of HPFRC (Naaman 1998) 19
Figure 2.6 Tensile stress-strain response of HPFRCCs and FRCCs (Naaman 2008) 20
Figure 2.7 Implicit classification of FRC and HPFRC based on bending response of structural elements (Naaman 2008) 22
Figure 2.8 Stress-strain behavior of FRC in compression with various fiber contents (Fanella and Naaman 1985) 23
Figure 2.9 Coupling beam design with diagonally oriented reinforcement (ACI 318-11). 27
Figure 2.10 Alternate confinement reinforcement detailing for coupling beams in ACI 318-11 (ACI 318-11) 28
Figure 3.1 Dimensions of the test specimens..... 31
Figure 3.2 Test setup..... 32
Figure 3.3 Top and base blocks 37
Figure 3.4 Reinforcement detailing for test coupling beams..... 43
Figure 3.5 Three stages of strain gauging: (a) attachment of strain gauge to bar by glue (b) coating of strain gauge with coating agents, and (c) covering of strain gauge with mastic tape 44
Figure 3.6 Coupling beam cage assembled in a wood formwork and ready for casting .. 45

Figure 3.7 Precast coupling beam after demolding 45
Figure 3.8 Reinforcement cages for top and base blocks 45
Figure 3.9 Precast coupling beam connected to base and top blocks representing walls prior to casting of blocks..... 46
Figure 3.10 Complete specimen ready for testing 47
Figure 3.11 Dramix RC80/30 BP hooked steel fibers used in this study 49
Figure 3.12 HPFRC mixture ready for casting 50
Figure 3.13 Optotrak system..... 52
Figure 3.14 Optotrak markers attached on the back of the coupling beam 52
Figure 3.15 Optotrak marker layout for coupling beams with aspect ratio of 2.75 53
Figure 3.16 Optotrak marker layout for coupling beams with aspect ratio of 3.3 53
Figure 3.17 Optotrak marker labels for coupling beams with aspect ratio of 2.75..... 54
Figure 3.18 Optotrak marker labels for coupling beams with aspect ratio of 3.3..... 54
Figure 3.19 Pre-defined cyclic displacement history..... 55
Figure 3.20 Direct tension test of a reinforcing bar using Optotrak markers to measure axial elongation..... 56
Figure 3.21 Casting HPFRC beams for flexural tests..... 59
Figure 3.22 Test of HPFRC beam according to ASTM 1609-05 59
Figure 3.23 Typical stress and deflection response for ASTM 1609 beam specimens 60
Figure 3.24 Compressive constitutive responses of HPFRC (Liao et al. 2006) 61
Figure 3.25 Tensile constitutive responses of HPFRC (Liao et al. 2006) 62
Figure 3.26 Shear imposed on coupling beam versus recorded strain for strain gauge D1 of Specimen CB-2..... 63
Figure 3.27 Calculated reinforcing bar stress versus recorded strain for strain gauge D1 of Specimen CB-2 63
Figure 4.1 Transformation of coordinates of markers 66
Figure 4.2 Drift calculation accounting for rotations of top and base blocks..... 68
Figure 4.3 Comparison of lateral displacements measured from LVDT and Optotrak.... 68
Figure 4.4 Deformation of a quadrilateral element used to calculate average strains 70
Figure 4.5 Average shear stress versus drift response of Specimen CB-1 73

Figure 4.6 Shear force versus drift response and selected limit states for Specimen CB-1 74
Figure 4.7 Damage progress in Specimen CB-1 at (a) 3.2% and (b) 5.2% drift 74
Figure 4.8 Damage on the back side of Specimen CB-1 at 5.2% drift at (a) the bottom end and (b) the top end of the beam 75
Figure 4.9 Average shear stress versus drift response of Specimen CB-2 77
Figure 4.10 Shear force versus drift response and selected limit states for Specimen CB-2 77
Figure 4.11 Damage in the positive loading direction in Specimen CB-2 at (a) 2.8% drift and (b) 5.3% drift 78
Figure 4.12 Damage at 5.3% drift in the positive loading direction in Specimen CB-2 at (a) the bottom and (b) the top end of the beam 78
Figure 4.13 Average shear stress versus drift response of Specimen CB-3 80
Figure 4.14 Shear force versus drift response and selected limit stages for Specimen CB-3 81
Figure 4.15 Damage in Speciemen CB-3 at (a) 3.4% drift in the positive loading direction and (b) at 5% drift in the negative loading direction 81
Figure 4.16 Damage in Specimen CB-3 at the end of the test in (a) bottom plastic hinge and (b) top plastic hinge 82
Figure 4.17 Average shear stress versus drift response of Specimen CB-4 84
Figure 4.18 Shear force versus drift response and selected limit states for Specimen CB-4 84
Figure 4.19 State of damage in Specimen CB-4 in the positive loading direction at (a) 2.6% and (b) 3.7% drift 85
Figure 4.20 Damage in Specimen CB-4 at the bottom end of the beam at 3.7 % drift 85
Figure 4.21 Average shear stress versus drift response of Specimen CB-5 87
Figure 4.22 Shear force versus drift response and selected limit states for Specimen CB-5 88
Figure 4.23 Damage at 4% drift (left) and 6.7% drift (right) in Specimen CB-5 88
Figure 4.24 Damage in (a) bottom and (b) top plastic hinge of Specimen CB-5 89
Figure 4.25 Average shear stress versus drift response of Specimen CB-6 91

Figure 4.26 Shear force versus drift response and selected limit states for Specimen CB-6 91
Figure 4.27 Damage states in the positive loading direction at (a) 3.2% drift (b) 6.5% drift for Specimen CB-6 92
Figure 4.28 Damage at the bottom beam at the end of the test in Specimen CB-6 92
Figure 4.29 Beam "Strips" defined by adjacent rows of markers..... 95
Figure 4.30 Average axial strain based on markers at beam ends 97
Figure 4.31 Average axial strain based on markers at top and base blocks..... 97
Figure 4.32 Relationship between the maximum imposed drift and average axial strain 98
Figure 4.33 Relationship between the maximum imposed drift due to flexural rotation and average axial strain..... 98
Figure 4.34 Axial force normalized by the axial force capacity..... 100
Figure 4.35 Axial force normalized by the applied shear..... 100
Figure 4.36 Location of inflection points 104
Figure 4.37 Longitudinal strains at selected drifts..... 107
Figure 4.38 Corner markers and notation used to calculate average curvature for a given strip 108
Figure 4.39 Average curvature distribution of all coupling beam specimens 111
Figure 4.40 Tensile stress-strain model for HPFRC matrix 113
Figure 4.41 Tensile stress-strain model for reinforcing steel 114
Figure 4.42 Moment versus curvature response for Specimens CB-1..... 115
Figure 4.43 Moment versus curvature response for Specimens CB-4..... 116
Figure 4.44 Moment versus curvature response for Strip 12 of Specimens CB-2 116
Figure 4.45 Moment versus curvature response for Strip 11 of Specimens CB-2 117
Figure 4.46 Moment versus curvature at the end strip for Specimen CB-1 118
Figure 4.47 Shear contribution from HPFRC and concrete at each cycle peak drift..... 121
Figure 4.48 Estimated shear contribution from HPFRC, diagonal bars, and stirrups for Specimens CB-1, CB-2, and CB-3 123
Figure 4.49 Estimated shear contribution from concrete, diagonal bars, and stirrups for Specimen CB-4 123

Figure 4.50 Estimated shear contribution from HPFRC and stirrups for Specimens CB-5 and CB-6 124
Figure 4.51 Load versus relative horizontal displacement response for Strip 2 of Specimen CB-2 125
Figure 4.52 Secant shear stiffness (for marker strip involving sliding plane) versus drift response and identification of drift at which sliding displacements were assumed to begin 126
Figure 4.53 Sliding shear displacement at selected cycle peak drifts 130
Figure 4.54 Drift at which sliding was assumed to begin 132
Figure 4.55 Shear stress versus shear strain for Specimen CB-2 135
Figure 4.56 Average shear strains for all specimens 137
Figure 4.57 Shear force resisted by shear friction normalized by shear friction strength versus slip 142
Figure 4.58 Shear force resisted by shear friction normalized by shear friction strength versus slip at cold joints for Specimens CB-5 and CB-6 143
Figure 4.59 Yielding progress of reinforcement 147
Figure 4.60 Definition of energy dissipation per cycle 151
Figure 4.61 Energy dissipate per cycle versus drift 152
Figure 4.62 Energy dissipated in repeated cycles is similar to that in the first cycles, indicating no degradation of energy dissipation mechanisms 152
Figure 4.63 An equivalent elasto-plastic system used to normalize the energy dissipated per cycle 153
Figure 4.64 The normalized energy dissipation of approximately 0.4 was generally exhibited beyond 1% drift. 154
Figure 4.65 Relative contributions of deformation components to specimen drift 160
Figure 4.66 Peak-to-peak stiffness versus peak cycle drift in the first and second cycle ..... .164
Figure 4.67 Normalized peak-to-peak stiffness versus peak cycle drift 165
Figure 4.68 Experimental secant flexural stiffness 166
Figure 4.69 Experimental shear stiffness normalized by G 168
Figure 4.70 Experimental shear stiffness normalized by E_c 168

Figure 5.1 Concrete materials for modeling coupling beams 171
Figure 5.2 Concrete Type 4 and truss elements used to model steel links 172
Figure 5.3 Softened stress-strain concrete compression model (Wong and Vecchio 2002) 177
Figure 5.4 Incorporation of HPFRC tensile stress-strain properties in VecTor2 185
Figure 5.5 Tensile stress-strain model for HPFRC matrix 185
Figure 5.6 Experimental and simulated VecTor2 shear force versus drift responses..... 190
Figure 5.7 Comparison of shear-drift response from VecTor2 and experimental shear versus drift response (excluding shear sliding along beam-wall interfaces) 193
Figure 5.8 Experimental hysteresis response and envelopes of analytical shear force versus drift responses with stiff and flexible steel links 196
Figure 5.9 Crack patterns for the HPFRC coupling beam numerical models at approximately 4.8% drift 199
Figure 5.10 Crack patterns of the RC coupling beams numerical model at approximately 2% drift 200
Figure 5.11 Crack patterns of the RC coupling beams numerical model at approximately 3% drift 200
Figure A.1 Specimen CB-1 strain gauge layout 208
Figure A.2 Specimen CB-2 strain gauge layout 209
Figure A.3 Specimen CB-3 strain gauge layout 210
Figure A.4 Specimen CB-4 strain gauge layout 211
Figure A.5 Specimen CB-5 strain gauge layout 212
Figure A.6 Specimen CB-6 strain gauge layout 213
Figure C.1 Longitudinal strains at various drifts in negative loading direction for Specimen CB-1 221
Figure C.2 Longitudinal strains at various drifts in negative loading direction for Specimen CB-2 222
Figure C.3 Longitudinal strains at various drifts in negative loading direction for Specimen CB-3 223
Figure C.4 Longitudinal strains at various drifts in the negative direction of Specimen CB-4 224

Figure C.5 Longitudinal strains at various drifts in negative loading direction for Specimen CB-5 225
Figure C.6 Longitudinal strains at various drifts in negative loading direction for Specimen CB-6 226

LIST OF TABLES

Table 3.1 Description of the test specimens 30
Table 3.2 Mixture proportions by weight for the coupling beams 47
Table 3.3 Properties of hooked steel fibers..... 49
Table 3.4 Yield and ultimate stresses of steel reinforcement 57
Table 3.5 Compressive strength of HPFRC and concrete mixed in the laboratory..... 58
Table 3.6 Compressive strength of ready-mixed concrete used in top and base blocks.. 58
Table 3.7 ASTM 1609-05 beam test results 60
Table 4.1 Summary of test results..... 71
Table 4.2 Damage description at various test states 94
Table 4.3 Specimen CB-1 capacity predicted by the moment-curvature analysis 101
Table 4.4 Specimen CB-2 capacity predicted by the moment-curvature analysis 101
Table 4.5 Specimen CB-3 capacity predicted by the moment-curvature analysis 102
Table 4.6 Specimen CB-4 capacity predicted by the moment-curvature analysis 102
Table 4.7 Specimen CB-5 capacity predicted by the moment-curvature analysis 102
Table 4.8 Specimen CB-6 capacity predicted by the moment-curvature analysis 102
Table 4.9 Theoretical yield curvature based on section modeling..... 109
Table 4.10 Stress-strain values for modeling of regular concrete and HPFRC 113
Table 4.11 Estimated contribution to shear resistance from V_{HPFRC}, V_c, V_d, and V_s at peak shear force of all specimens..... 121
Table 4.12 Drift at which sliding was assumed to begin 127
Table 4.13 Initial secant stiffness values at approximately 0.25% drift 161
Table 5.1 Concrete element types used for modeling Specimen CB-1 173
Table 5.2 Concrete element types used for modeling Specimen CB-2 173
Table 5.3 Concrete element types used for modeling Specimen CB-3 174
Table 5.4 Concrete element types used for modeling Specimen CB-4 174
Table 5.5 Concrete element types used for modeling Specimen CB-5 175

Table 5.6 Concrete element types used for modeling Specimen CB-6 175
Table 5.7 Material and analysis models used for modeling the test coupling beams 176
Table 5.8 Tensile stress-strain values for modeling HPFRC 186
Table B.1 Load-displacement history for Specimen CB-1 214
Table B.2 Load-displacement history for Specimen CB-2 216
Table B.3 Load-displacement history for Specimen CB-3 217
Table B.4 Load-displacement history for Specimen CB-4 218
Table B.5 Load-displacement history for Specimen CB-5 219
Table B.6 Load-displacement history for Specimen CB-6 220
Table D.1 Lateral displacement pattern for the model of Specimen CB-1 227
Table D.2 Lateral displacement pattern for the model of Specimen CB-2 229
Table D.3 Lateral displacement pattern for the model of Specimen CB-3 230
Table D.4 Lateral displacement pattern for the model of Specimen CB-4 231
Table D.5 Lateral displacement pattern for the model of Specimen CB-5 232
Table D.6 Lateral displacement pattern for the model of Specimen CB-6 233

LIST OF APPENDICES

Appendix A: Strain Gauge Location ……..209
Appendix B: Load-Displacement History …….. 215
Appendix C: Longitudinal Strain Distribution …….. 222
Appendix D: Idealized Displacement Patterns Imposed on the VecTor2 Models ..…. 228

ABSTRACT

Coupling beams greatly influence the behavior of coupled wall systems. In order to ensure adequate coupling beam behavior under earthquake-induced deformations and stresses, intricate reinforcement detailing is required for reinforced concrete coupling beams, typically in the form of diagonal bars and extensive confinement reinforcement. Such reinforcement detailing, however, creates major construction difficulties. Furthermore, in slender coupling beams, where beam span-to-depth ratios are on the order of 3.0, the effectiveness of diagonal reinforcement is questionable because of its shallow angle (less than 20 degrees) with respect to the beam longitudinal axis.

In this study, a design alternative for slender coupling beams that puts less reliance on diagonal reinforcement was experimentally investigated. The use of tensile strain-hardening, high-performance fiber reinforced concrete (HPFRC) as a means to reduce or totally eliminate the need for diagonal bars and substantially reduce confinement reinforcement was evaluated. To validate this design alternative, six precast coupling beams were tested under large displacement reversals. The parameters considered were the coupling beam span-to-depth ratio (2.75 and 3.3), presence of diagonal reinforcement, and material type (HPFRC and regular concrete). Results from large-scale tests indicated excellent damage tolerance, and strength and stiffness retention capacity for slender HPFRC coupling beams. Moreover, tests results showed that diagonal reinforcement can be completely eliminated without a detrimental effect on seismic behavior. The contribution of the HPFRC material to shear strength of the coupling beam was estimated to be on the order of $5\sqrt{f_c'}$ (psi) times the cross section area.

To simulate the behavior of the tested precast coupling beams under displacement reversals, analytical modeling was conducted using VecTor2, a nonlinear finite element program in which an HPFRC material model can be incorporated. It was found that the

behavior of the tested coupling beams could be reasonably predicted in VecTor2. Simulated shear resultant was in good agreement with that of the test specimens. Excluding drift contributed by sliding, which could not be properly captured in VecTor2, drift capacity obtained from the numerical models agreed well with that of the test specimens. Modeling guidelines critical to simulating the seismic behavior of the HPFRC coupling beams were also provided.

CHAPTER 1
INTRODUCTION

1.1 BACKGROUND AND MOTIVATION

Reinforced concrete walls coupled by beams above openings, as shown in Figure 1.1, are very efficient lateral load resisting systems for seismic resistance and are widely used in tall buildings. However, in current practice, reinforced concrete coupling beams are very difficult to construct, especially in the case of slender coupling beams whose aspect ratio is on the order of 3.0. This is due to a large amount of reinforcement required in diagonal directions. Therefore, an alternative coupling beam design that has simpler details and exhibits as good behavior, if not better, as diagonally reinforced concrete coupling beams, is needed.

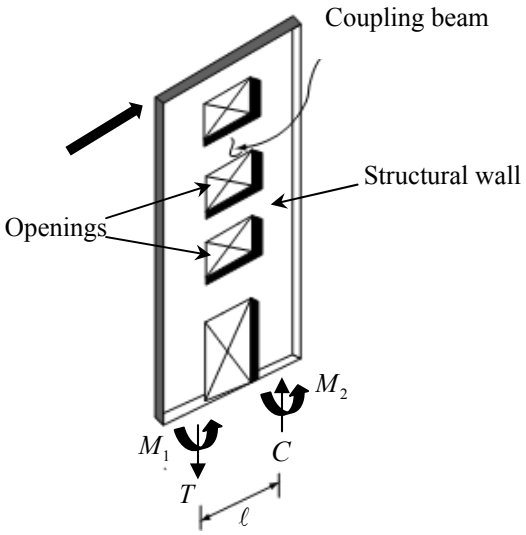

Figure 1.1 Coupled walls and coupling beams (Taranath 2010)

The structural behavior of reinforced concrete coupled walls is significantly influenced by the behavior of their coupling beams. Thus, the coupling beams must be strong and stiff, behave in a ductile manner, and possess significant energy dissipation

capacity. Studies have shown that coupling beams are the key energy dissipating elements in coupled wall systems. Well-proportioned coupling beams generally develop plastic hinges over the height of the building, resulting in good energy dissipation (Aktan and Bertero 1981; Shui et al. 1981; Aristizabal-Ochoa 1982). Coupled wall systems are more efficient than isolated walls because the walls are coupled to produce larger lateral stiffness and strength. Under lateral load, shear is resisted by the wall units while overturning moment is resisted jointly by flexure in the wall units, M_1 and M_2, and the couple lT from axial forces T and C developed in the wall units, which result from the accumulation of shear forces in the coupling beams, as shown in Figure 1.2.

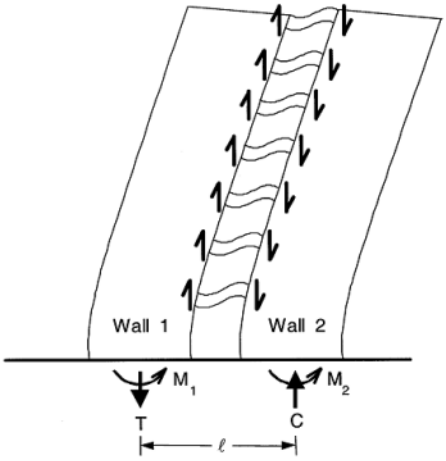

Figure 1.2 Flexural resistance of coupled walls (Canbolat 2004)

Previous studies have shown that the behavior of short coupling beams is different than that of ordinary beams (Paulay 1969) and a diagonal reinforcement configuration in coupling beams is crucial. Experiments showed that coupling beams with conventional reinforcement consisting of longitudinal bars and stirrups are vulnerable when subjected to large load reversal (Paulay 1971). In the 1970s, extensive research on the seismic behavior of coupling beams was conducted to develop a new design for improved seismic performance. Paulay and Biney (1974) proposed the use of a group of diagonal reinforcing bars confined by closely spaced transverse reinforcement. This improved reinforcement detailing enables most of the beam shear to be resisted by the heavily reinforced diagonal cages. Experimental studies (Paulay and Binney 1974; Barney et al. 1978; Tassios et al. 1996; Galano and Vignoli 2000) have shown that diagonal

reinforcement significantly improves ductility, stiffness retention, and energy dissipation in coupling beams, which has led to its wide acceptance in seismic design worldwide.

The diagonal reinforcement detailing, however, creates major construction difficulties. To resist the entire shear demand in coupling beams, large diameter diagonal bars with long development lengths must be employed, which causes interference with boundary wall reinforcement. In order to maintain concrete integrity and prevent premature buckling of diagonal bars, column-type transverse reinforcement to confine either each diagonal cage or the entire beam is needed. This requirement makes the construction of coupling beams even more complicated, as shown in Figure 1.3.

Figure 1.3 Standard reinforcement detailing in earthquake-resistant coupling beams (courtesy of Rémy Lequesne)

Typical coupling beams are short with a span-to-depth ratio (ℓ_n/h) less than 4. In recent years, the use of relatively slender coupling beams, where beam aspect ratios (span-to-overall depth ratios) are between 2.0 and 3.5, has become popular due to limitations in story heights. For such beams, the effectiveness of diagonal reinforcement is questionable because of its shallow angle, less than 20 degrees, with respect to the beam longitudinal axis. In addition, shear is not as critical in these slender coupling beams. This makes the use of diagonal reinforcement to resist the entire shear even more doubtful. However, recent tests (Naish et al. 2009) have shown that diagonal reinforcement, combined with column-type confinement, led to a stable behavior under seismic loading. Because for a given area the shear strength provided by diagonal

reinforcement decreases as its angle with the beam axis decreases, the use of a large amount of diagonal reinforcement is inevitable to sustain the high shear stress demand imposed on slender coupling beams. This scenario becomes more complicated when the placing of the confinement reinforcement is considered, especially at the intersection between diagonal bar cages.

Other reinforcement detailing alternatives, such as various rhombic configurations, have been proposed and investigated (Tegos and Penelis 1988; Tassios et al. 1996; Galano and Vignoli 2000). However, test results showed that coupling beams with those reinforcement alternatives exhibited inadequate seismic behavior or posed significant construction difficulties. Another potential alternative, consisting of steel or concrete encased steel coupling beams (Gong et al. 1998), showed a favorable seismic behavior. However, the need for embedding the steel section into the walls creates severe interference problems with the wall boundary reinforcement (Canbolat et al. 2004).

For several years, structural applications of strain-hardening or high-performance fiber-reinforced concretes (HPFRCs) have been experimentally investigated. These materials exhibit multiple cracking under uniaxial tension and a compression behavior that resembles that of well-confined concrete. Test results (Parra-Montesinos 2005) have shown that HPFRC is a viable alternative to regular concrete in shear critical members.

Recently, design alternatives for HPFRC coupling beams with span-to-depth ratios equal to 1.0 and 1.75 were proposed (Canbolat 2004; Lequesne et al. 2009; Lequesne et al. 2010). In these designs, coupling beams were precast with HPFRC and reinforcement detailing was simplified by significantly reducing both diagonal and confinement reinforcement. Test results have shown that the use of HPFRC in coupling beams can successfully eliminate the problem of reinforcement congestion without compromising seismic performance. Results from large-scale tests also showed the superior damage tolerance and stiffness retention capacity of HPFRC coupling beams of short and intermediate aspect ratios.

1.2 OBJECTIVE

The main objective of this research was to develop a new design for slender earthquake-resistant coupling beams with simplified reinforcement detailing and enhanced seismic behavior. For this purpose, the use of HPFRC as a means to reduce the need for diagonal bars accompanied by a substantial reduction in confinement reinforcement was evaluated. To further simplify reinforcement detailing, the possibility of eliminating diagonal reinforcement in slender HPFRC coupling beams was also investigated. To accomplish the research objective, six large-scale coupling beams with span-to-depth ratios of 2.75 and 3.3 were tested under displacement reversals to evaluate the seismic behavior of slender coupling beams that combine the use of an HPFRC material with simplified reinforcement detailing relative to that of code-compliant reinforced concrete coupling beams.

The following parameters were considered important in this study.

- Coupling beam aspect ratio (2.75 and 3.3)
- Reinforcement detailing (with and without diagonal reinforcement)
- Material type (HPFRC and regular concrete)

Apart from the experimental study, finite element analyses of the coupling beams were performed to obtain models suitable to simulate the behavior of precast coupling beams tested in this research study. These finite element models are very useful for investigating the influence of various parameters on seismic behavior of the coupling beams. To fulfill this goal, the finite element program "VecTor2" was used. VecTor2, developed at the University of Toronto, is well-suited for analyzing reinforced concrete members under monotonic and reversed cyclic loads. The ability to include fiber reinforced concrete in finite element models made VecTor2 an appealing tool for modeling the HPFRC coupling beams tested in this study.

1.3 ORGANIZATION OF THESIS

This thesis report is organized in six chapters. In the first chapter, an introduction and the objectives of the study are given. The second chapter presents a literature review of previous work related to the proposed study. The third chapter focuses on the experimental program, where the test protocol, specimens, and other test-related aspects

are discussed. Results and analytical work from the tests of six coupling beam specimens are reported in Chapter 4. Finite element modeling of the test specimens is presented in Chapter 5. Finally, a summary of the work conducted and major conclusions drawn from this study are presented in Chapter 6. Future research recommendations are also given in this final chapter.

CHAPTER 2
LITERATURE REVIEW

This chapter presents an overview of topics related to this research study. A review of previous research on coupling beams is presented in Section 2.1. Of particular interest is the behavior of conventionally and diagonally reinforced concrete coupling beams. Section 2.2 provides background information on fiber reinforced concrete and selected applications. At the end of this chapter is a summary of the 2011 ACI Building Code seismic provisions for coupling beams.

2.1 REVIEW OF RESEARCH ON COUPLING BEAMS

2.1.1 Background

Because coupling beams are expected to sustain large inelastic displacement reversals during strong earthquakes, they must be designed to undergo several load reversals without significant loss in strength and stiffness. Previous studies have shown that coupling beams are quite different from the conventional beams in ductile moment-resisting frames. First, coupling beams are generally deep with span-to-depth ratios less than three. Second, shear stress demands in coupling beams are considerably larger than those in beams of moment frames. A shear stress demand of $6\sqrt{f_c'}$ (psi) or greater is frequently encountered. Third, coupling beams are generally subjected to significant inelastic end rotation demands and a large number of yield excursions (Aktan and Bertero 1981). To achieve a high level of toughness and ductility, the following parameters must be taken into consideration in the design of coupling beams (Aktan and Bertero 1981; Aristizabal-Ochoa 1987).

1. **Span-to-depth ratio (ℓ_n/h)**: The span-to-depth ratio, or simply called the aspect ratio, of coupling beams is a major parameter that affects beam behavior and failure mechanism. The required stiffness of coupling beams usually results in aspect ratios of

less than 4. Indeed, aspect ratios of 2 or less are common. Deep coupling beams behave quite differently from shallow coupling beams, particularly when subjected to large inelastic reversing displacements. The aspect ratio defines the relative contributions of beam and arch actions to the shear resistance of reinforced concrete beams. As the ℓ_n/h ratio decreases, arching (strut) action contributes more significantly to shear strength than flexural behavior.

2. **Shear stress**: The maximum shear stress is a function of the span-to-length ratio, the ratio of flexural reinforcement, and the yield strength and strain hardening of flexural reinforcement. As the span length decreases, the shear stress increases. As the flexural reinforcement ratio and yield strength increase, the shear stress increases because shear that can be developed in a flexural member is directly related to the flexural capacity of the members (assuming member can develop its flexural capacity). Shear stress in coupling beams fall into three levels. For shear stresses of $3\sqrt{f_c'}$ (psi) or less, conventionally reinforced coupling beams, which consist of longitudinal and transverse reinforcement, perform satisfactorily and fail in a flexural mode (Aktan and Bertero 1981). Shear stresses between $3\sqrt{f_c'}$ to $6\sqrt{f_c'}$ (psi) will often cause a flexural-shear failure. For shear stresses exceeding $6\sqrt{f_c'}$ (psi), sliding shear becomes the dominant failure mode and diagonal reinforcement arrangements, which will be discussed in the following section, are recommended to prevent such failures.

3. **Reinforcement details**: Arrangement of flexural and shear reinforcement plays an important role in the behavior of coupling beams under load reversals. Conventional, diagonal, and rhombic reinforcement arrangements have been investigated under load reversals. These reinforcement configurations are discussed in the next section.

4. **Anchorage of beam flexural reinforcement**: Anchorage of coupling beam reinforcement in the walls is important as it can affect overall behavior of coupled wall systems. Due to the large inelastic deformations expected at the ends of coupling beams, slip of reinforcing bars anchored in the walls could be significant, which is highly detrimental to the overall response of coupled wall systems (Aristizabal-Ochoa 1982; Aristizabal-Ochoa 1983).

2.1.2 Reinforced Concrete Coupling Beams

Prior to the 1964 Alaska earthquake, coupling beams were normally designed with conventional reinforcement consisting of longitudinal flexural bars, vertical stirrups, and distributed horizontal bars. In this design, shear strength was assumed to be provided by the so called "concrete" mechanism (i.e., shear carried in the compression zone, aggregate interlock and dowel action), and by vertical stirrups through truss action with the concrete.

The structural action on coupling beams results from lateral displacements of the wall causing a differential movement between the supported ends (Figure 2.1). As a result, the beams undergo flexural and shear deformations. Flexural deformation causes the coupling beams to bend in a double-curvature pattern with, theoretically, tension along one half of the beams changing into compression along the other half on top and bottom surfaces. This behavior contrasts with shear deformation, which causes the beams to be in tension on both top and bottom surfaces along the length. Whether either flexure or shear will govern is greatly dependent on the aspect ratio of the coupling beams.

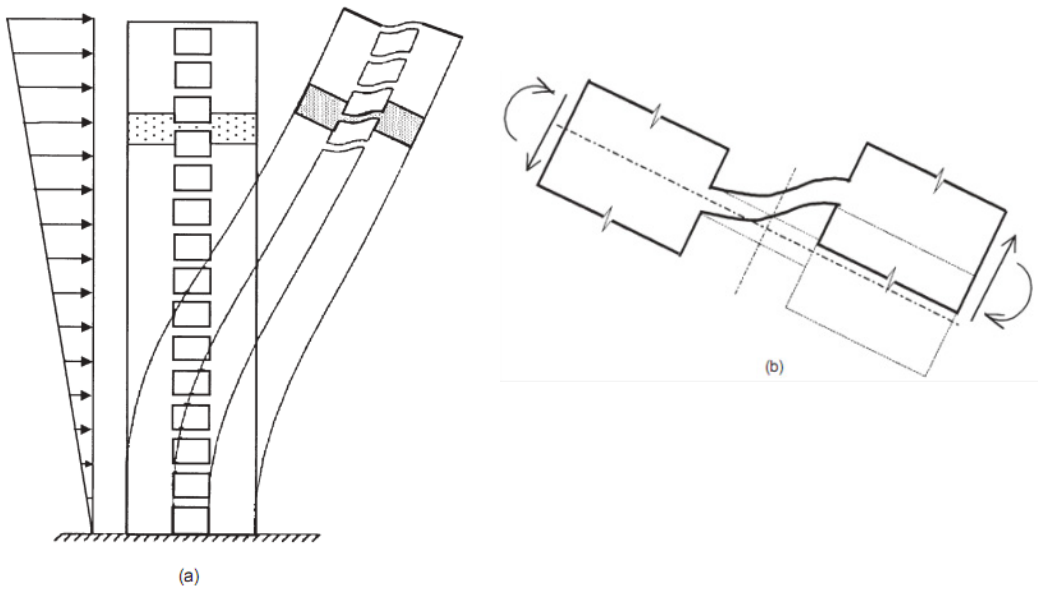

Figure 2.1 Deflection patterns of coupling beams in a coupled wall structure (a) deflection of walls under lateral load (b) deflection of coupling beam due to differential movement between the beam ends (Kwan and Xhao 2002)

After the 1964 Alaska earthquake, it was found that conventional RC coupling beams were severely damaged due to inadequate shear capacity. Thereafter, extensive research was conducted to understand the seismic behavior of conventionally reinforced concrete coupling beams.

The prevention of a shear failure is a major difficulty in the design of deep RC coupling beams (Barney et al. 1978; Paulay 1971). In general, a deep coupling beam tends to fail in a diagonal tension mode, in which the coupling beam is split into two triangular halves tied together by the transverse reinforcement. This failure mode can be avoided by increasing the amount of transverse reinforcement. However, under cyclic loading, a deep coupling beam might also fail in a shear-sliding mode, as shown in Figure 2.2 (Paulay and Binney 1974). In this failure mode, intersecting flexural-shear cracks propagate across the entire depth of the beam at its ends. Because sliding is developed along a plane parallel to the transverse reinforcement, even closely spaced stirrups become ineffective in transmitting shear. This observation by Paulay and Binney (Paulay 1971; Paulay and Binney 1974) was confirmed by later investigations (Barney et al. 1978; Tassios et al. 1996; Xiao et al. 1999; Galano and Vignoli 2000).

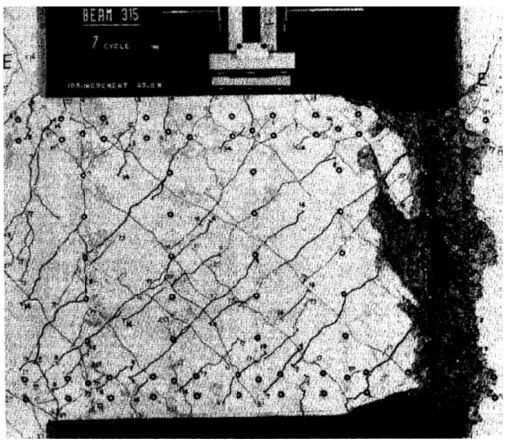

Figure 2.2 Sliding shear failure in coupling beams (Park and Paulay 1975)

The concern about inadequate ductility of conventional RC coupling beams led to the study of other reinforcement arrangements. Therefore, the idea of using diagonal reinforcement to improve beam behavior was introduced in the early 1970's (Luison et al. 1970; Binney 1972; Paulay and Binney 1974). This reinforcement configuration, which generally consists of diagonal reinforcement cages, enables the whole shear force to be

transferred by diagonal steel (Figure 2.3). Shear and moment capacities provided by the diagonal reinforcement can be determined as,

$$T_u = C_u = A_s f_y \tag{2-1}$$

$$V_u = 2T_u \sin\alpha = 2A_s f_y \sin\alpha \tag{2-2}$$

$$M_u = \left(A_s f_y \cos\alpha\right)\left(h - 2d'\right) \tag{2-3}$$

where T_u and C_u are the tension and compression force in diagonal reinforcement, respectively, A_s is the reinforcement area in a diagonal reinforcement cage, f_y is the yield strength of diagonal reinforcement, α is the angle of diagonal reinforcement with respect to the beam longitudinal axis, h is the beam depth, and V_u and M_u are the shear and moment, respectively, associated with yielding of the diagonal reinforcement.

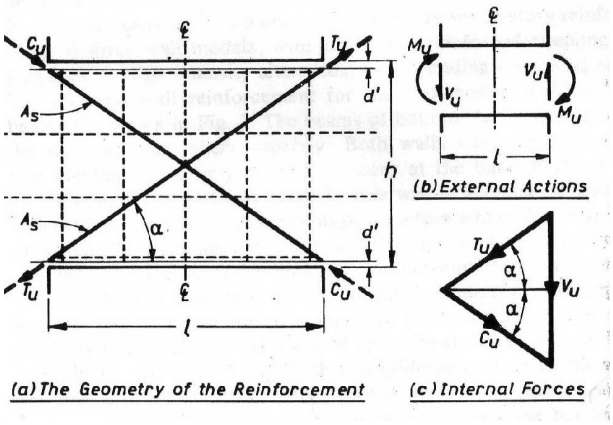

Figure 2.3 Diagonally reinforced coupling beam (Paulay and Santhakumar 1976)

The intended function of the diagonal reinforcement is to prevent a sliding shear failure and provide a stable shear resisting mechanism along the beam span. To verify this reinforcement scheme, Paulay and Binney (1974) tested three diagonally reinforced coupling beams with span-to-depth ratios of 1.0 and 1.3. Test results showed that full length diagonal reinforcement significantly improved ductility and energy dissipation compared to conventionally reinforced concrete coupling beams. Failure of diagonally reinforced concrete coupling beams resulted from the buckling of diagonal bars. Therefore, it was recommended that closely spaced transverse reinforcement be provided along the length of diagonal bars to delay bar buckling at large displacement reversals.

Shortly after the coupling beam tests by Paulay and Binney, Paulay and Santhakumar (1976) reported on the test of an approximately one-quarter scale model of a coupled wall with short diagonally reinforced coupling beams (span-to-depth of 1.25). In this experiment it was confirmed that the reinforcement arrangement proposed by Paulay and Binney (1974) yielded the desirable ductile behavior for a coupling beam. The failure mechanism of the coupling beams of this experiment was buckling of the compression reinforcement.

Another testing program to study the behavior of coupling beams under reversed cyclic loading was conducted at the Portland Cement Association by Barney et al. (1978). Eight reinforced concrete coupling beams with three different reinforcement schemes were tested. The first set consisted of three beams with conventional reinforcement configuration. Stirrups were designed to resist the whole shear as recommended by Paulay (1971). The second set included three beams with diagonal bars near the beam-wall interface. Diagonal reinforcement in the hinging region was designed to carry the entire shear force. The third set was comprised of two beams with full-length diagonal reinforcement, using one bar in one direction and two bars in the other direction. For each type of detailing, span-to-depth ratios of 2.5 and 5.0 were tested.

The inelastic response of the conventionally reinforced concrete coupling beams was limited by sliding shear failure near the ends of the beams. Transverse reinforcement could not prevent this type of failure because vertical cracks propagated across the entire depth of the beam between stirrups.

The diagonal reinforcement in the hinge region, so-called rhombic reinforcement, could eliminate sliding shear failure but did not significantly improve the performance of the coupling beams as anticipated. Because concrete within the region of diagonal reinforcement deteriorated by spalling and crushing as loading progressed into the inelastic range, the bent points of the diagonal bars loosened, which led to the loss of efficient truss action. Because of the little improvement in energy dissipation and stiffness retention, there was no reason to add complexity and cost of construction for this reinforcement configuration.

The specimens with full-length diagonal reinforcement showed the best performance among all tested specimens. Full-length diagonal reinforcement

significantly improved ductility and toughness of the coupling beams with a small aspect ratio. However, improvement in hysteretic response of the slender coupling beams (an aspect ratio of 5.0) with full-length diagonal reinforcement was relatively small.

Although diagonally reinforced coupling beams exhibit good seismic behavior, it is evident that there are some disadvantages. First, closely spaced transverse reinforcement is required around diagonal bars, which causes difficulty in construction. Second, the diagonal cages are in different planes to avoid interference between diagonal bars at the mid-span of the beam. This often leads to an increase in beam width, which may result in larger walls.

Tegos and Penelis (1988) proposed a simple technique to prevent short coupling beams from failing in shear by arranging main reinforcements with an inclination such as to form a rhombic truss. They tested twenty four columns and coupling beams with aspect ratios ranging from 2.0 to 5.0. Eighteen specimens were tested with inclined rhombic reinforcement, three specimens with diagonal reinforcements, and three specimens with only longitudinal and transverse reinforcement. The tests were conducted under either monotonic or cyclic loadings. Unlike other previous research studies in which no axial force was considered, axial load was applied to the specimens through an oil jack at one end of the specimen. The test results showed that the beams with rhombic layout of reinforcement performed satisfactorily in a manner similar to diagonally reinforced concrete beams. In their results, however, ultimate strength, stiffness decay, and energy dissipation were not compared directly.

To evaluate the possibility of alternative detailing, Tassios et al. (1996) conducted an experimental program consisting of the tests of ten coupling beams under cyclic loading. These specimens, at approximately 50% of full scale, included five different reinforcement layouts and two different span-to-depth ratios (1.0 and 1.66). The five reinforcement layouts are shown in Figure 2.4. Three reinforcement configurations (Figure 2.4(c), 2.4(d), and 2.4(e)) were investigated and their behaviors were compared with that of conventionally and diagonally reinforced coupling beams (Figure 2.4(a) and 2.4(b)).

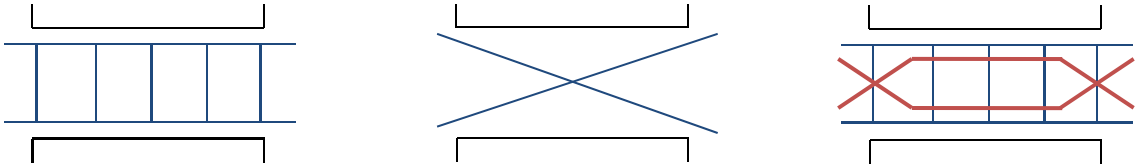

(a) Conventional reinforcement (b) Diagonal reinforcement (c) Rhombic reinforcement

(d) Full-length dowels (e) Cut-off dowels

Figure 2.4 Reinforcement configurations investigated by Tassios et al. (1996)

The first detailing, called a rhombic layout, used additional bent-up bars intersecting at the mid-height of the beam (Figure 2.4(c)). These bent-up bars contributed to the sliding resistance without considerably increasing the flexural capacity at the beam ends. The second and third detailing contained long and short dowels across the ends of the beams (Figure 2.4(d) and 2.4(e)). The dowel bars were intended to prevent a sliding shear failure at the wall-beam boundaries. Test results showed that the rhombic layout led to an improved overall behavior with respect to that of the conventionally reinforced specimen. This reinforcement scheme also requires less complicated detailing than diagonally reinforced coupling beams. However, severe pinching of the hysteresis loops, which indicates reduced energy dissipation, was observed. For specimens with dowel bars, it was found that dowel bars in the end regions of the beam may help prevent a sliding shear failure. However, stiffness degradation and severe pinching in the hysteresis loops were still observed. A comparison of hysteresis loops indicated that the diagonally reinforced coupling beams exhibited the best performance in term of shear resistance and energy dissipation. In sum, for coupling beams with span-to-depth ratio less than 2.0, diagonal reinforcement was still found to be the best solution.

Galano and Vignoli (2000) reported on the testing of fifteen short coupling beams. Four different reinforcement arrangements were tested. They consisted of: (a) conventional layout; (b) diagonal layout without confining ties; (c) diagonal layout with confining ties; and (d) inclined bars in a rhombic layout. All specimens had a span-to-

depth ratio of 1.5. Test results showed that the beams with diagonal or rhombic reinforcement detailing behaved better than beams with conventional reinforcement layout. The differences in energy dissipation between diagonal and rhombic layouts were negligible. However, the rhombic layout was more advantageous in terms of rotational ductility capacity and strength retention compared with diagonal layouts. This claim contradicts the finding by Tassios et al. (1996).

Using high strength concrete in coupled shear wall systems could be useful to increase shear strength of the systems. Most of previous studies on coupling beams focused on behavior of normal strength concrete coupling beams. In order to study the seismic behavior of coupling beams made of high strength concrete, Xiao et al. (1999) tested six coupling beams with an average concrete strength of 10.1 ksi. Experimental parameters included beam aspect ratio (3.0 to 4.0), flexural reinforcement ratio (from 2.1 to 4.1%), and reinforcement configuration. Reinforcement configurations included conventional reinforcement layout and longitudinal reinforcement distributed over the beam height. Test results revealed that flexural yielding can be developed in all tested specimens prior to sliding shear failure of the beams. Compared with the coupling beams with conventional reinforcement, the coupling beams with distributed flexural reinforcement exhibited considerably improved hysteretic response and ductility. This significant improvement resulted from the better cracking control provided by the distributed flexural reinforcement, thus maintaining concrete interlocking and as a result, delaying sliding shear failure.

2.1.3 Slender Coupling Beams

The effectiveness of diagonal reinforcement in slender reinforced concrete coupling beams has been questioned due to the shallow angle of inclined diagonal bars. Most coupling beams tested between 1970 and 2000 were short and deep, with span-to-depth ratios less than 2 (Paulay and Binney 1974; Tassios et al. 1996; Galano and Vignoli 2000). To the writer's knowledge, the first tests done on slender diagonally reinforced concrete coupling beams were carried out at the Portland Cement Association (Barney et al. 1978). The coupling beam span-to-depth ratios were 2.5 and 5.0. All beams were subjected to shear stresses ranging from $7\sqrt{f_c'}$ to $11\sqrt{f_c'}$ (psi). These tests indicated that

diagonal reinforcement was not justified for slender members with span-to-depth ratio of 5.0. For shorter coupling beams (span-to-depth of 2.5), it was found that full-length diagonal reinforcement significantly improved the ductility and toughness of the beams. It should be noted that these tests were conducted on very small scale model whose beam sections were only 4 in. x 6.6 in. The researchers also suggested that further studies were needed on coupling beams with span-to-depth ratios between 2.5 and 5.0.

Not until 2000 were relatively slender coupling beams tested again. Adebar et al. (2001) tested one full-scale diagonally reinforced coupling beam with span-to-depth ratio of 2.74 and diagonal reinforcement confined according to the Canadian Concrete Code (CSA Standard A23.3-94). The specimen was axially restrained using high strength Dywidag bars to simulate the concrete slab on the top of the beam in a high-rise building. Test results showed good ductility and stable hysteresis behavior. The specimen failed by crushing of the concrete core and buckling of the diagonal reinforcement.

Tests on slender coupling beams were also recently conducted at the University of California at Los Angeles (Naish et al. 2009). Eight approximately half-scale coupling beams were tested under reversed cyclic loading. Five of them had a span-to-depth ratio of 2.4 and the rest had a ratio of 3.3. For the beams with aspect ratio of 2.4, four specimens had full section confinement and hoops along diagonal bars were eliminated. This was a new detailing option that was included in ACI 318-08 for design of coupling beams. One control specimen with a 2.4 ratio contained hoops along diagonal bars according to the detailing requirements in ACI 318-05. For more slender beams (span-to-depth ratio of 3.3), three specimens featuring either diagonal bars with full section confinement, or diagonal bars with inclined hoop confinement, or longitudinal bars without diagonal reinforcement were tested. Test results indicated that "the new detailing approach provides equal, if not improved behavior as compared to the alternative detailing approach, that simple modeling approaches reasonably capture measured force versus deformation behavior, and that including a slab had only a modest impact on strength, stiffness, ductility, and observed damage" (Naish et al. 2009).

2.1.4 Composite Coupling Beams

To overcome the construction problems of diagonally reinforced coupling beams, researchers resorted to hybrid steel-concrete alternatives (Paparoni 1972; Shahrooz et al. 1992; Shahrooz et al. 1993; Harries et al. 1993; Gong et al. 1998). The hybrid steel-concrete alternatives refer to either steel or concrete-encased steel coupling beams in which the steel section is embedded in the reinforced concrete walls for moment and shear transfer. When properly detailed and fully anchored into the adjoining structural walls, these alternatives have shown favorable response to cyclic shear with wide hysteresis loops. Unfortunately, the steel elements require a long embedment into the adjoining structural walls to ensure full development of their flexural and shear capacity and prevent excessive bearing-related damage with the associated increase in connection flexibility. This embedment inevitably interferes with critical transverse and longitudinal reinforcement in the wall boundary regions.

2.2 HIGH-PERFORMANCE FIBER REINFORCED CONCRETE

2.2.1 Background

The use of fibers in construction is not a new concept. It can be dated back to the Egyptian and Babylonian epochs in which straw was used to reinforce adobe bricks (ACI 544.1R-96 2009). The idea of using steel fibers in concrete can be traced back as early as 1874 when adding metallic waste in concrete was patented (Minelli 2005). However, this practice was not often used after that. Not until early 1960s did the modern era of research and development on fiber reinforced cement composites (FRCCs) began. Research on fiber reinforced cement composites (FRCCs) by Romualdi, Batson and Mandel (Romualdi and Batson 1963; Romualdi and Mandel 1964) attracted the attention of researchers around the world (Zollo 1997). Since then, the use of fibers as reinforcement in concrete has been growing.

FRCCs are generally defined as composites with two main components, namely the matrix and the fibers. The matrix consists of cement paste, water, and aggregates. Additives and pozzolanic cement replacements such as fly ash and silica fume are sometimes added in the matrix. Fibers interact with the concrete matrix through bond, but contrary to reinforcing bars in concrete, fibers are expected to pullout rather than yield or

fracture (except for local yielding at fiber deformations in the case of deformed steel fibers). FRCCs are usually referred to as fiber reinforced concrete (FRC) when coarse aggregates (gravel) are used in the matrix. If only fine aggregates such as sand are used in the matrix, the composites are simply called fiber reinforced cement composites (FRCCs).

The concept of FRCCs is simple. Concrete is strong in compression but weak in tension. Reinforcement steel is continuous and incorporated at the specified location in the concrete member to strengthen the concrete in tension. On the other hand, fibers are discontinuous and generally randomly distributed throughout the matrix. They serve as a complementary reinforcement to increase post-cracking resistance and shear and flexural capacity. Once a crack forms in the matrix fibers bridge the crack and control its opening. In some cases, this resistance enables additional cracks to develop in the matrix. Cracking continues and maximum load is typically reached when pull-out of the fibers occurs.

Having an obvious advantage over conventional concrete in that they can resist significant amount of tensile stress after cracking, FRCCs have been used for traditional applications such as slabs on ground, tunnel liners, and architectural elements. However, applications of FRCCs in building structures have been rather limited. This has been mainly due to limited experimental research and design recommendations (Wight and MacGregor 2009). Several fiber materials with various shapes and geometries that have been used with different degree of success include steel fibers (flat, hooked, twisted, crimped), synthetic fibers (acrylic, aramid, carbon, nylon, polyester and polypropylene), glass fibers, and natural fibers. Currently, steel fibers are the most commonly used fibers in both research and industry.

High-performance fiber reinforced cement composites (HPFRCCs) are a special class of fiber reinforced cement composites (FRCCs). HPFRCCs are defined as FRCCs that develop a quasi strain-hardening behavior in tension with a post-cracking strength higher than the first cracking strength (Naaman and Reinhardt 1996). Multiple cracking and high energy absorption capacity is typically observed with this quasi strain-hardening behavior. The behavior is illustrated in Figure 2.5. HPFRCC members exhibit multiple cracking under tension with smaller crack spacing. These multiple cracks are much narrower in HPFRCC members compared to those in reinforced concrete or FRCC

members. Generally, HPFRCC members begin to fail when the fibers that bridge a particular crack start pulling out from the matrix, which results in localized deformation (crack opening).

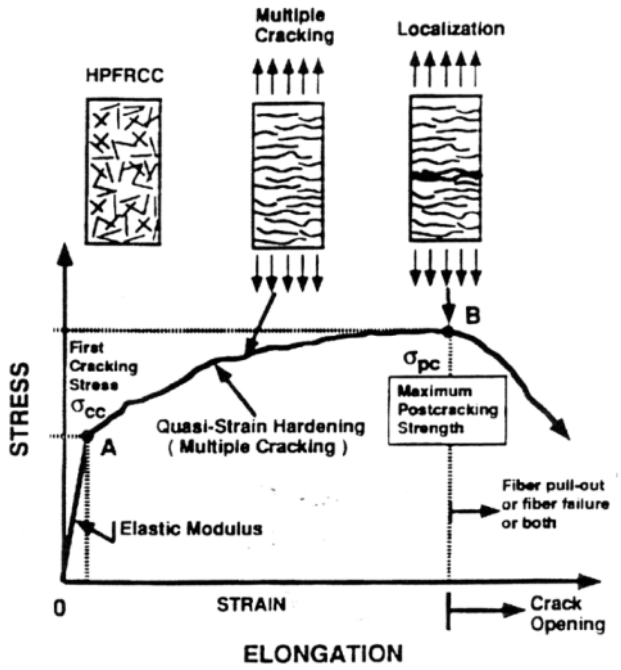

Figure 2.5 Stress-strain behavior of HPFRC (Naaman 1998)

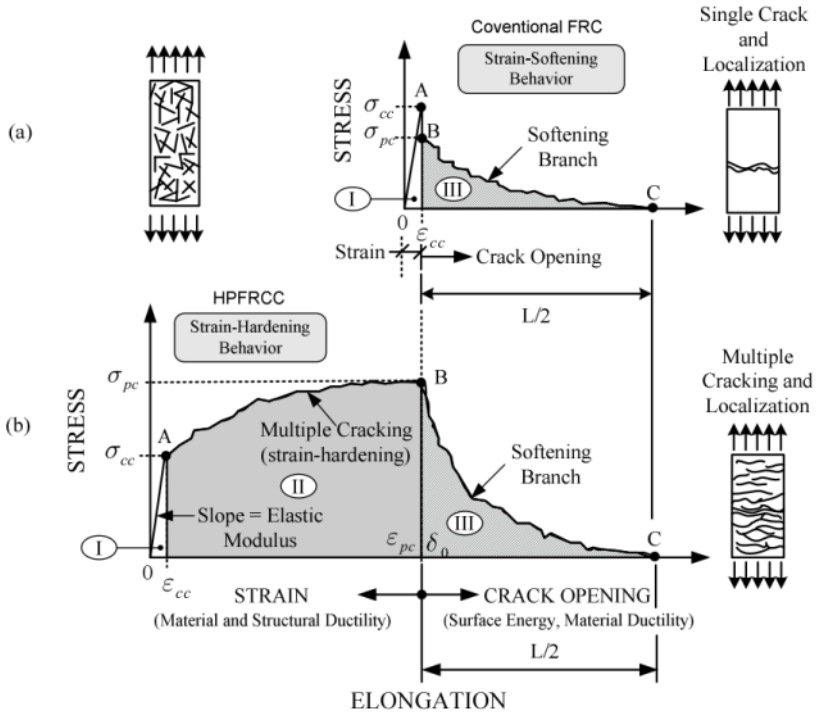

Figure 2.6 Tensile stress-strain response of HPFRCCs and FRCCs (Naaman 2008)

It should be noted that the behavior of HPFRCCs is different from that of traditional FRCCs. FRCCs are characterized by a softened response after first cracking. The stress-strain curve in tension of FRCCs before the first crack (Stage I in Figure 2.6) is the same as that of HPFRCCs. However, localization will occur immediately after the first crack without strain- hardening and multiple cracks. Stage II (Figure 2.6) does not exist in the response of FRCCs in tension. From Figure 2.6, it is obvious that HPFRCCs exhibit substantially larger toughness compared with FRCCs. Therefore, HPFRCCs are ideal for applications in members subjected to large inelastic deformation due to earthquake motions (Parra-Montesinos 2005).

HPFRCCs are simply referred to as high-performance fiber reinforced concrete (HPFRC) when coarse aggregates are added in the matrix. In this report, the terms HPFRC and FRC will be used to describe both HPFRCCs and FRCCs for simplicity. A distinction will be made where no coarse aggregates are used in the matrix.

Achieving strain-hardening behavior unique to HPFRCs depends on fiber type and amount, mixture properties, and the matrix-fiber interaction. Not all fibers can be used to produce HPFRC. Hooked and twisted steel fibers and ultra-high molecular-

weight polyethylene (Spectra) have been successfully used to form HPFRCs with a relatively low volume of fraction of fibers, typically less than 2%. Examples of mixtures and procedures for HPFRC can be found in Liao et al. (2006).

2.2.2 Strain-hardening and Deflection-hardening

As discussed in the previous section, HPFRCs can be distinguished from regular FRCs by their behavior under direct tension. Numerous test methods to determine the stress-strain response of HPFRC in tension have been proposed. The so-called dog-bone tests are complicated and the results dependent on the test setup. Despite differences in test methods, the idealized HPFRC response, shown in Figure 2.5, is generally obtained.

Tensile behavior of FRC and HPFRC can be implicitly related to the bending response of structural members. The flexural test methods according to ASTM C1609/C1609M-05 or RILEM TC 162-TDF are more reliable and easier to perform than tension tests. The bending response from flexural tests can be classified as either deflection-hardening or deflection-softening response (Naaman 2003). This classification is depicted in Figure 2.7. All strain-hardening composites exhibit deflection-hardening response. On the other hand, tension strain-softening composites can lead to structural elements with either deflection-hardening or deflection-softening behavior. This indicates that the flexural test alone cannot be used to distinguish strain-hardening composites from strain-softening ones. However, the flexural test is still useful, particularly for structural applications where it is desirable that fiber reinforced concrete exhibits at least deflection-hardening behavior.

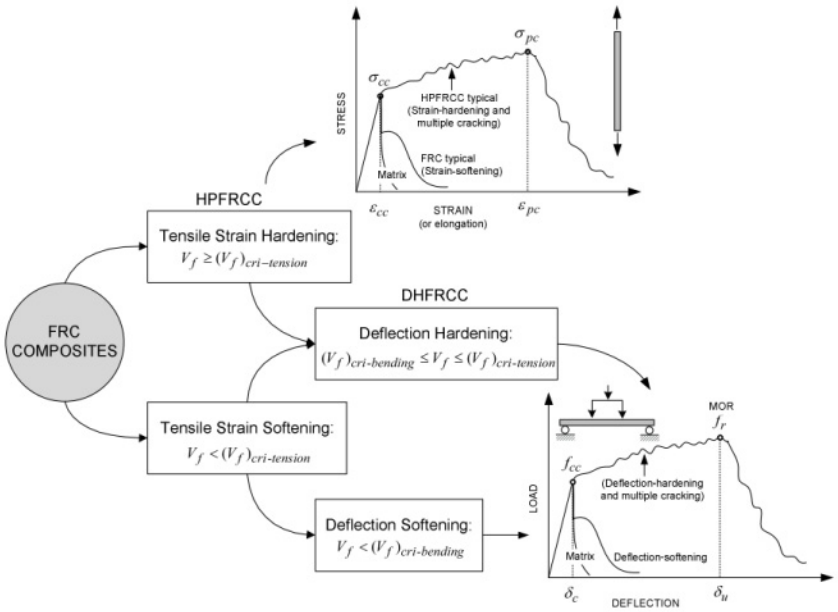

Figure 2.7 Implicit classification of FRC and HPFRC based on bending response of structural elements (Naaman 2008)

2.2.3 Mechanical Properties of Fiber Reinforced Concrete

The behavior of FRC before cracking is not significantly improved by the addition of fibers. Fibers in low amounts have a negligible impact on modulus of elasticity, Poisson's ratio, and compressive strength. The main advantage of fibers is to increase ductility, which comes from the fibers controlling the opening of cracks. Factors influencing the mechanical properties of FRC include fiber material and shape, fiber aspect ratio, fiber volume fraction, and matrix composition.

2.2.3.1 Compressive Strength of FRC

Fibers have little influence on compressive strength of concrete with increases in strength rarely exceeding 25% for a volume fraction less than 2% (Shah and Rangan 1971; Fanella and Naaman 1985; Wafa and Ashour 1992). Even in steel fiber reinforced concrete members where conventional reinforcement is used, fibers do little to increase compressive strength (Adepegba and Regan 1981; Mangat and Motamedi Azari 1985). On the other hand, fibers substantially enhance ductility and toughness. The addition of fibers leads to a shallower descending branch, as shown in Figure 2.8. This enhancement

is even more obvious in the case of HPFRC, which can sustain large compression strain without spalling.

Factors affecting ductility of FRC include fiber volume fraction, fiber geometry, and matrix composition. As shown in Figure 2.8, an increase in fiber content improves energy absorption capacity. Increasing the aspect ratio of fibers also increases toughness. Contribution of the matrix composition to ductility can be attributed to bonding characteristics and concrete strength. For example, a matrix containing silica fume generally has very good bond with the fibers and exhibits increased ductility. Also, the fact that normal concrete is less brittle than high strength concrete makes the addition of fibers with the same volume fraction more effective in normal strength concrete. Therefore, to produce ductile behavior of high-strength concrete, a higher volume fraction of fibers is necessary.

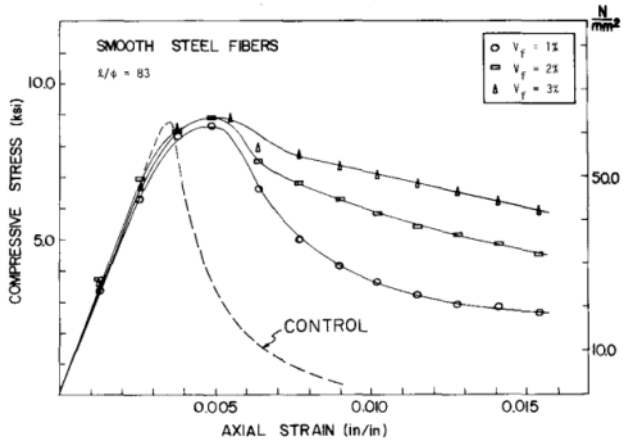

Figure 2.8 Stress-strain behavior of FRC in compression with various fiber contents (Fanella and Naaman 1985)

2.2.3.2 Flexural Strength and Toughness of FRC

For typical fiber volume contents used in structural applications (generally less than 1.5%), the presence of fibers does not affect appreciably first flexural cracking strength. Flexural post-cracking strength, however, could be greatly enhanced by the use of fibers. Deformed fibers are more effective than straight fibers in increasing post-cracking flexural strength due to the mechanical bond provided by the fiber deformations. Ramakrisnan et al. (1980) found that the addition of hooked steel fibers to concrete in a

dosage as low as approximately 0.6% by volume led to a post-cracking strength almost equal to or greater than the first cracking strength (i.e., deflection-hardening behavior).

As in the case of compressive strength, toughness is a more noticeable result of fiber addition. Actually, the primary purpose of adding fibers in concrete is to increase flexural toughness or energy absorption capacity. Increases in strength are normally of secondary importance. Toughness can be determined from the area under the load-deflection curve obtained from a four-point bending test, as shown in Figure 2.7.

2.2.3.3 Shear Strength of FRC

The use of fiber-reinforced concrete to increase shear strength is one of its most promising applications. Unlike steel reinforcement, fibers are often randomly distributed in concrete. Therefore, they can bridge cracks in all directions, which is particularly useful in members that experience diagonal cracking due to shear. .

Batson, Jenkins, and Spatney (1972) first investigated the possibility of using steel fibers in lieu of stirrups in beams. Test parameters included shear span-to-depth ratio (a/d), fiber type and geometry, and fiber volume fraction. Test results indicated the effectiveness of steel fibers in increasing shear strength. Later tests by Narayanan and Darwish (1987) also confirmed the ability of steel fibers to increase shear resistance. In these tests, fibers were intended to replace, either partially or totally, conventional stirrups. Swamy and Bahia (1985) found that steel fibers reduced shear deformations and acted as shear reinforcement, which resulted in higher shear strength. Steel fibers also controlled cracking, which enhanced contribution of dowel action to shear resistance. Numerous reports on shear behavior of FRC beams confirmed the effectiveness of steel fibers as shear reinforcement (for example, Lim and Paramasivam 1987; Mansur et al. 1986; Adebar et al. 1997). When used with stirrups, fibers help bridge cracks, making it possible to increase spacing of stirrups; thus reducing reinforcement congestion in areas where shear demand is high.

Several models based on test data and theoretical analyses have been proposed to predict shear capacity of steel fiber reinforced concrete beams (SFRC) (for example, Mansur et al. 1986; Sharma 1986; Narayanan and darwish 1987; Khuntia et al. 1999; Kwak et al. 2002). These strength models are generally empirical and thus limited to the

parameters covered by the data they are based on. Dinh et al. (2011) proposed a semi-empirical model for estimating the shear strength of SFRC beams. This model is based on the material performance obtained through a standard ASTM 1609 four-point bending test; thus avoiding the difficulty in determining the post-cracking tensile strength of FRC through a direct tension test.

A database consisting of almost 150 FRC beams with and without steel fibers was published by Parra-Montesinos (2006). The relevant parameters included shear span-to-depth ratio (*a/d*), beam depth, concrete strength, fiber volume fraction, steel fiber type and aspect ratio (*L/d*), and longitudinal reinforcement ratio. It was not until 2008 that a provision was adopted in ACI 318-08 to allow the use of steel fiber reinforcement as shear reinforcement.

2.2.4 Seismic Applications of HPFRC

The major benefit of using HPFRCs in structural members is given by the improved tensile behavior. The compressive strength of the mortar or concrete is not appreciably improved by the addition of fibers, unless a high volume of fibers is used. However, the fibers provide confinement and could lead to a large compressive strain capacity. The bond between the reinforcement and the matrix can also be improved with the use of fibers (Chao et al. 2009; Hota and Naaman 1997).

A comprehensive review of applications of FRCC and HPFRCC materials in earthquake-resistant elements was given by Parra-Montesinos (2005). Applications investigated include beam-column connections (Parra-Montesinos 2000; Parra-Montesinos and Wight 2000; Parra-Montesinos et al. 2005), plastic hinges in flexural members (Chompreda 2005), structural walls (Kim and Parra-Montesinos 2003; Parra-Montesinos et al. 2006), and coupling beams (Canbolat et al. 2005; Lequesne et al. 2009). In general, structural elements constructed with HPFRCC exhibit higher strength and stiffness retention compared to those of reinforced concrete elements. From all the tests to date, it is evident that HPFRCC materials can offer a superior structural performance for earthquake-resistant structural components.

2.2.5 HPFRC Coupling Beams

Using the advantages of HPFRCCs, Canbolat et al. (2005) proposed a design alternative for short coupling beams (span-to-depth ratio on the order of 1.0). In this design, (HPFRCCs were used and diagonal reinforcement detailing was simplified by eliminating closely spaced transverse reinforcement around the diagonal bars. Four coupling beams with a span-to-depth ratio of 1.0 were tested under displacement reversal. The first specimen was made of conventional concrete with diagonal reinforcement and cast monotonically with the structural walls. Specimen 2 was constructed with HPFRCC and without diagonal bars. Specimen 3 was made of HPFRCC reinforced with diagonal bars, but the confining reinforcement around the diagonal bars was eliminated. To further investigate the possibility of simplifying construction, the HPFRC specimens were precast. Specimen 4 was similar to Specimen 3 except that the diagonal bars were bent at beam ends to ease placement of the precast beam into the walls. Test results showed that HPFRCCs can successfully eliminate the problem of reinforcement congestion while leading to good seismic performance. Results from large-scale tests also showed the superior damage tolerance and stiffness retention capacity of HPFRCC coupling beams.

Shortly after these tests, an investigation on the potential of using high-performance fiber-reinforced concrete (HPFRC) for coupling beams with aspect ratio of 1.75 began. Lequesne et al. (2010) conducted three tests on HPFRC coupling beams and two tests on coupled walls at the University of Michigan. The three precast HPFRC coupling beams were reinforced with diagonal bars. No confining reinforcement around the diagonal bars was used in either of the three beams. To move possible flexural damage away from the cold joint between the precast beam and cast-in-place walls, each beam contained either U-shaped or straight dowel bars at its ends. Test results confirmed that HPFRC can reliably confine diagonal reinforcement and ensure stable hysteresis behavior. HPFRC also significantly increased shear strength, thereby forcing a flexural dominated failure mode with modest stiffness degradation and good energy dissipation.

2.3 ACI BUILDING CODE SEISMIC PROVISIONS FOR RC COUPLING BEAMS

Requirements for the design of coupling beams are provided in Chapter 21 (21.9.7) of ACI 318-11 (2011). For clear span (ℓ_n) to depth (h) ratios greater than 4 ($\ell_n / h > 4$), coupling beams are designed as flexural members. If the ratio is between 2 and 4, it is permitted to use either diagonal or conventional reinforcement. When $\ell_n / h < 2$ and $V_n > 4\sqrt{f_c'} A_{cw}$, sliding shear failure may occur. Thus, the use of two intersecting groups of diagonally placed bars, symmetrical about the mid-span, is required. The detailing requirements of diagonal reinforcement are described in ACI Code Section 21.9.7.4. Detailing of diagonal reinforcement in ACI 318-11 is shown in Figure 2.9.

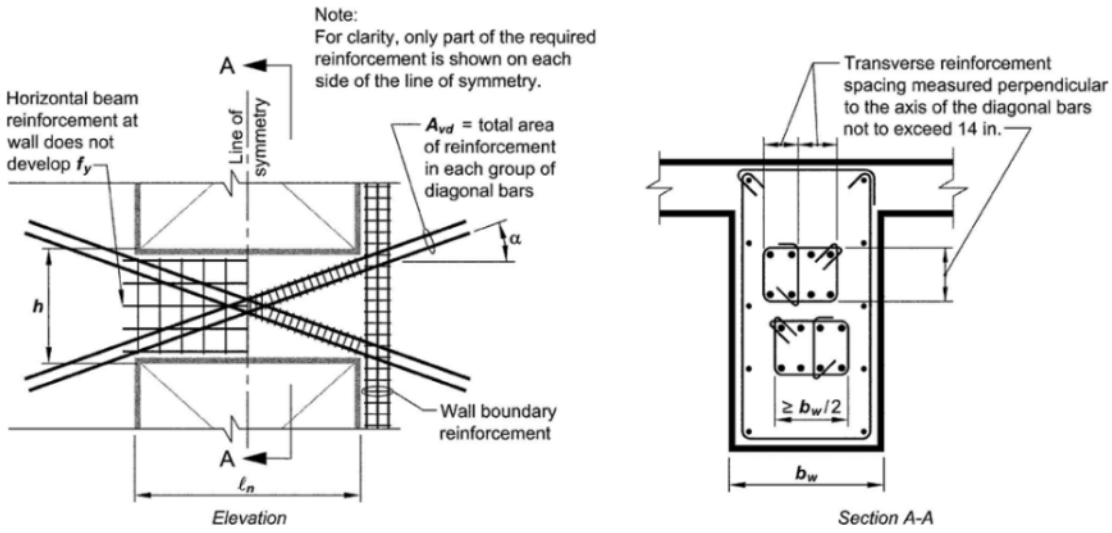

Figure 2.9 Coupling beam design with diagonally oriented reinforcement (ACI 318-11)

An alternate detailing, shown in Figure 2.10, has been adopted in the ACI Code since 2008. In this detailing, nearly the entire beam cross section is confined by transverse reinforcement. This scheme provides full confinement of the diagonally reinforced concrete beam section.

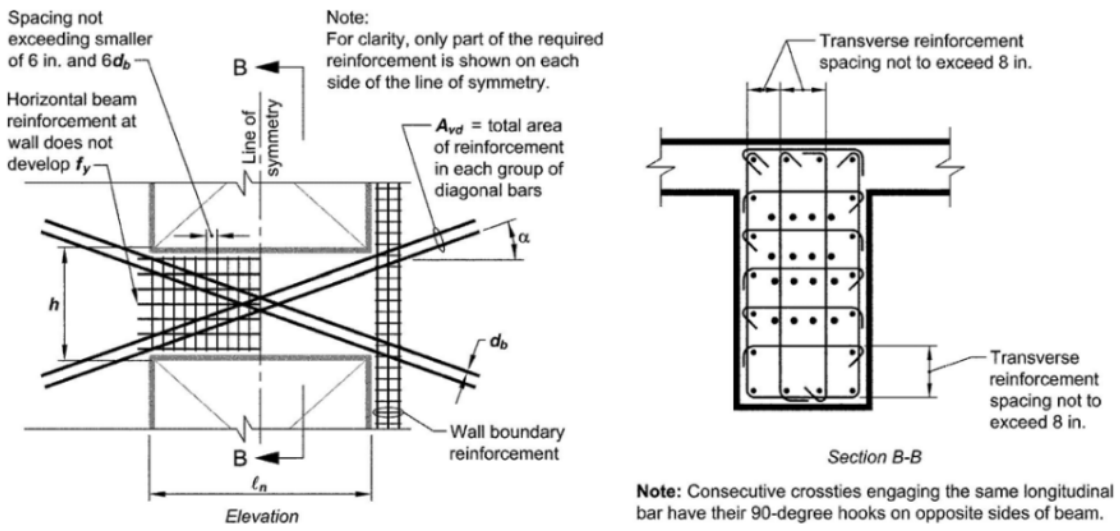

Figure 2.10 Alternate confinement reinforcement detailing for coupling beams in ACI 318-11 (ACI 318-11)

CHAPTER 3
EXPERIMENTAL PROGRAM

As mentioned in Chapters 1 and 2, most experimental programs on coupling beams have been conducted on short coupling beams with an aspect ratio (ℓ_n/h) less than 2, where ℓ_n and h are the clear span and height of the coupling beam, respectively. This research, on the other hand, focused on relatively slender coupling beams, with aspect ratios on the order of 3. In particular, the main objective of this research was to evaluate the seismic behavior of a new coupling beam design that combines the use of an HPFRC material with simplified reinforcement detailing compared to that of code-compliant reinforced concrete coupling beams. The following parameters were considered in the experimental studies:

- Coupling beam aspect ratio (2.75 and 3.3)
- Reinforcement configurations (with and without diagonal reinforcement)
- Material type (HPFRC and concrete)

The experimental program included the design, construction and testing of six coupling beams under large displacement reversals. Five specimens were constructed with HPFRC, three of them containing diagonal bars. To further simplify reinforcement detailing of coupling beams, the remaining two HPFRC specimens were constructed without diagonal bars. In the following sections, a detailed description of the experimental program, including specimen design, construction process, test setup, instrumentation, and material properties is provided.

3.1 DESCRIPTION OF TEST SPECIMENS

Five large-scale HPFRC coupling beam specimens, three of them containing diagonal bars, were tested under large displacement reversals. To better evaluate the influence of HPFRC on coupling beam behavior, a diagonally reinforced concrete

coupling beam with the same reinforcement detailing as one of the HPRFC specimens was tested.

Each specimen consisted of a coupling beam connected to heavily reinforced concrete top and bottom blocks, with the bottom block anchored to the laboratory strong floor. The top and bottom blocks in all test specimens were constructed with regular concrete. The dimensions of the test specimens are shown in Figure 3.1.

In all test specimens, the clear span length of the coupling beams was 66 in. In order to evaluate the seismic behavior of coupling beams with various span-to-depth ratios, two different depths of 24 in. and 20 in. were selected for the coupling beams, corresponding to aspect ratios of 2.75 and 3.3, respectively. These aspect ratios, on the order of 3.0, represent span-to-depth ratios of coupling beams typically used in current tall buildings. The main features of the test specimens are provided in Table 3.1.

Table 3.1 Description of the test specimens

Specimen	Aspect ratio	Diagonal reinforcement	Target shear stress (psi)	Concrete material
CB-1	2.75	Yes	$10\sqrt{f_c'}$	HPFRC
CB-2	2.75	Yes	$8\sqrt{f_c'}$	HPFRC
CB-3	3.3	Yes	$8\sqrt{f_c'}$	HPFRC
CB-4	2.75	Yes	$8\sqrt{f_c'}$	Concrete
CB-5	3.3	No	$8\sqrt{f_c'}$	HPFRC
CB-6	2.75	No	$8\sqrt{f_c'}$	HPFRC

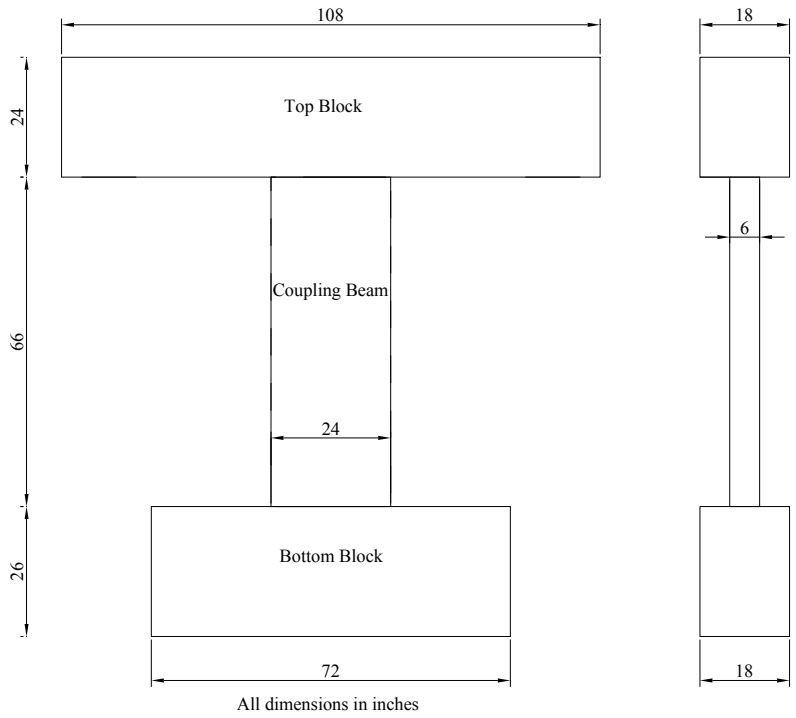

(a) Coupling beam with an aspect ratio of 2.75

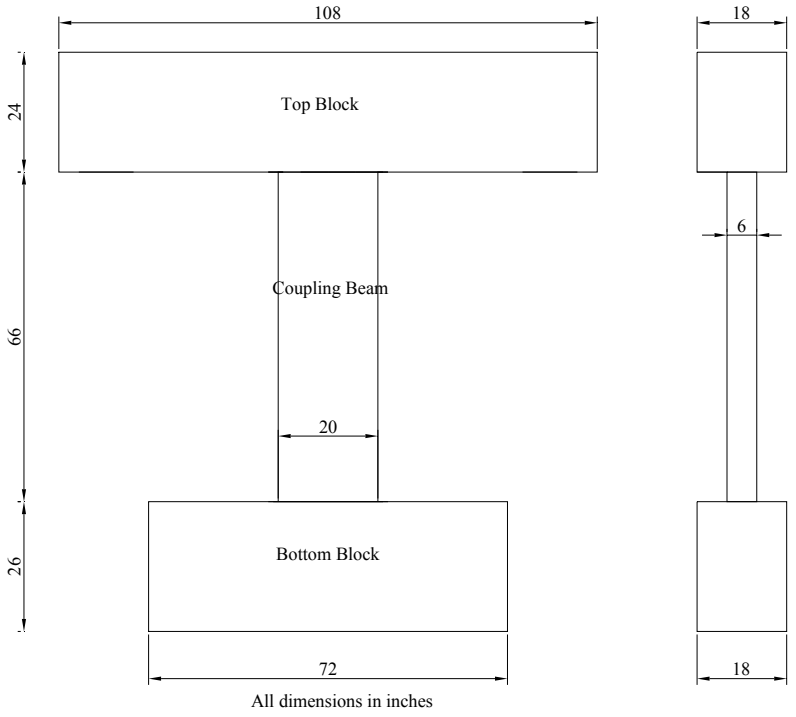

(b) Coupling beam with an aspect ratio of 3.3

Figure 3.1 Dimensions of the test specimens

3.2 TEST SETUP

All coupling beams were precast and embedded into large reinforced concrete blocks simulating the adjacent structural walls being coupled. All the coupling beams were 68 in. long and were embedded 1 in. into the concrete blocks. The coupling beams had cross sectional dimensions of 6 x 24 in. and 6 x 20 in. for aspect ratios of 2.75 and 3.3, respectively. The coupling beam dimensions were dictated by an existing test setup available in the University of Michigan Structures Laboratory. For testing convenience, the specimens were rotated 90 degrees with respect to their position in a real building. Thus, the coupling beams were oriented vertically as opposed to horizontally. A 300-kip hydraulic actuator with ±8-inch stroke was connected to the top block to apply quasi-static reversed cyclic displacements to the test specimens. Two vertical steel arms, instrumented with load cells, were used to maintain the two concrete blocks parallel during loading, as well as to provide some degree of axial restraint to the coupling beams to simulate that provided by walls in a real structure. The test setup is shown in Figure 3.2.

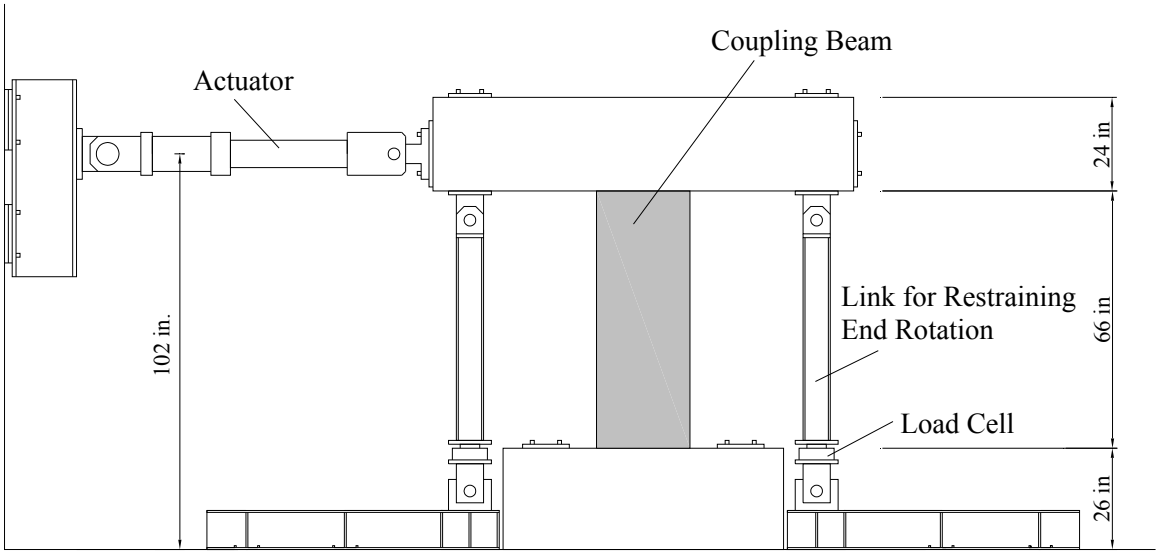

Figure 3.2 Test setup

3.3 DESIGN OF TEST SPECIMENS

ACI 318-08 provides two design options for coupling beams with span-to-depth ratio between 2 and 4. Coupling beams can be designed either as a diagonally reinforced coupling beam or as a beam in a special moment resisting frame. For diagonally reinforced coupling beams, ACI 318-08 requires the diagonal reinforcement to be designed to resist the entire shear demand. Because of the use of an HPFRC material, however, the design of the test specimens in this study did not satisfy either of these two approaches, particularly with regard to diagonal and transverse reinforcement.

For design purposes, shear resistance in the test specimens was assumed to be provided by the HPFRC material, diagonal reinforcement, if any, and transverse reinforcement (truss action). The resistance from the HPFRC material is due primarily to post-cracking diagonal tension resistance, although some strut action is expected due to the relatively low aspect ratios of the test beams. The design process started with the selection of a target shear demand. A high shear demand level, Vu , of $(8\sqrt{f_c'} - 10\sqrt{f_c'})A_{cw}$ (psi), where A_{cw} is the gross cross sectional area of the coupling beam and f_c' is the specified compressive strength of the concrete, was chosen. Given this expected high shear demand, which is close to the upper limit in the ACI Code $(10\sqrt{f_c'})A_{cw}$ (psi), the drift capacity exhibited by the test beams should represent a lower bound for that when subjected to lower shear demands. With the shear force demand selected, the moment demand, M_u, was calculated as $M_u = V_u \ell_n / 2$, where ℓ_n is the length of the coupling beam measured from face to face of the walls.

For relatively slender coupling beams with an aspect ratio greater than approximately 2.5, the angle of inclination of diagonal bars is normally less than 15 degrees. This shallow angle results in the vertical component of the force in the diagonal bars being approximately 25% of the bar force. If the whole shear is to be resisted by diagonal bars, a very large amount of diagonal reinforcement would have to be used. Therefore, a design relying only on diagonal bars for shear resistance does not seem appropriate. Previous studies on the seismic behavior of HPFRC coupling beams with an aspect ratio of 1.0 and 1.75 (Canbolat 2005; Lequesne 2009) showed the potential for HPFRC to increase shear resistance. Test results showed that HPFRC and transverse

reinforcement, along with diagonal reinforcement, could jointly resist a large shear force. For this reason, it was assumed that approximately 25% - 30% of the total shear would be carried by diagonal reinforcement. The remaining shear would then be resisted by transverse reinforcement and HPFRC. Thus, the area of diagonal reinforcement, A_d, was calculated as,

$$A_d = \frac{(0.25 \text{ to } 0.3)V_u}{2f_y \sin\alpha} \tag{3-1}$$

where α is the angle of inclination of the diagonal bars with respect to the longitudinal axis of the beam. To facilitate the beam construction, the coupling beam was precast and diagonal bars were bent within the clear span of the beam, making them parallel to other longitudinal reinforcement as they exit the precast portion of the beam. This reinforcement layout made it easier to slide the coupling beam into the walls. Bending the diagonal bars within the beam clear span also increased the angle of inclination of diagonal reinforcement, although by a small amount (on the order of 1 degree). Even though this angle increase is very small, for diagonal bar angles on the order of 20 degrees with respect to the beam axis it represents approximately a 5% increase in the theoretical contribution of the diagonal bars to shear strength.

The transverse reinforcement in the HPFRC coupling beams tested in this study did not satisfy the confinement requirements in ACI 318-08 except for the end regions. This reduction of transverse reinforcement was believed possible due to the large ductility exhibited by HPFRC materials in both tension and compression, and their ability to provide confinement to the diagonal bars outside of the plastic hinge regions. This substantial reduction in transverse reinforcement greatly simplifies coupling beam construction.

The design of the transverse reinforcement outside of the plastic hinge regions was performed assuming a contribution to total shear strength on the order of 30% - 40% of the expected shear demand. The area of transverse reinforcement, A_v, was determined as,

$$V_s = \frac{A_v f_y d \cdot \cot\theta}{s} \tag{3-2}$$

where the angle θ was taken as 45 degrees and $f_y = 60\ ksi$. The remainder of the shear was assumed to be resisted by the HPFRC material. Results from a previous investigation (Lequesne, 2009) indicate that limiting the shear force contribution to $5\sqrt{f_c'}A_{cw}$ (psi) is adequate to prevent extensive shear-related damage outside of the beam plastic hinge regions.

The plastic hinge region was assumed to extend $h/2$ from the face of the walls, where h is the overall depth of the coupling beam. In these regions, special transverse reinforcement was added such as to provide sufficient confinement to ensure adequate rotation capacity under large shear reversals. This confinement reinforcement also resisted the outward thrust at the bent of the diagonal bars near the ends of the coupling beam. The amount of special transverse reinforcement was calculated as that required for column-type confinement according to Chapter 21 of the 2008 ACI Building Code. With a combination of column-type confinement and HPFRC, it was expected that the coupling beam would behave satisfactorily and exhibit a flexural failure mode within the plastic hinge region.

As will be discussed in Section 4.5.2, the behavior exhibited by the test beams with diagonal reinforcement suggested that it was possible to completely eliminate diagonal reinforcement without a detrimental effect on seismic performance. Thus, two of the tested coupling beams (Specimen CB-5 and CB-6) were designed without diagonal reinforcement. The design of these specimens followed the same approach as that for the diagonally reinforced coupling beams except that shear was assumed to be resisted only by the HPFRC material and a truss mechanism governed by the strength of the transverse reinforcement. Transverse reinforcement, through truss action, was assumed to carry 70% - 80% of the applied shear.

The next step in the design of the coupling beams was the selection of longitudinal reinforcement. The coupling beam behavior was expected to be governed by flexural yielding at both ends. Therefore, selection of the appropriate amount of longitudinal reinforcement such that the intended shear demand would be applied while ensuring a flexural hinging mechanism was critical. For this purpose, moment-curvature analyses were performed for sections at the beam-wall interface and other locations along

the coupling beam span. The contribution of diagonal reinforcement to the expected or probable moment strength, M_{pr}, was included in the analyses by modeling the diagonal bars as equivalent longitudinal bars with a cross-sectional area adjusted based on the angle of inclination of the diagonal bars.

The precast coupling beam was embedded only 1 in. into the walls. To ensure that the intended moment capacity could be developed at the beam-wall interface, the coupling beam reinforcement must be properly anchored into the walls. In this study, longitudinal and diagonal bars of the coupling beams were extended 21 in. (greater than the corresponding development length) into the walls. To force plastic rotations to occur away from beam-wall interface, dowel bars in the form of U-shaped and straight dowel bars were provided.

The top and base blocks representing the walls were designed to resist the forces associated with a coupling beam shear of 150 kips. The expected maximum applied coupling beam shear for this study, on the other hand, was 130 kips. This ensured that the blocks did not exhibit significant distress during testing. Reinforcement details for the top and base blocks are shown in Figure 3.3.

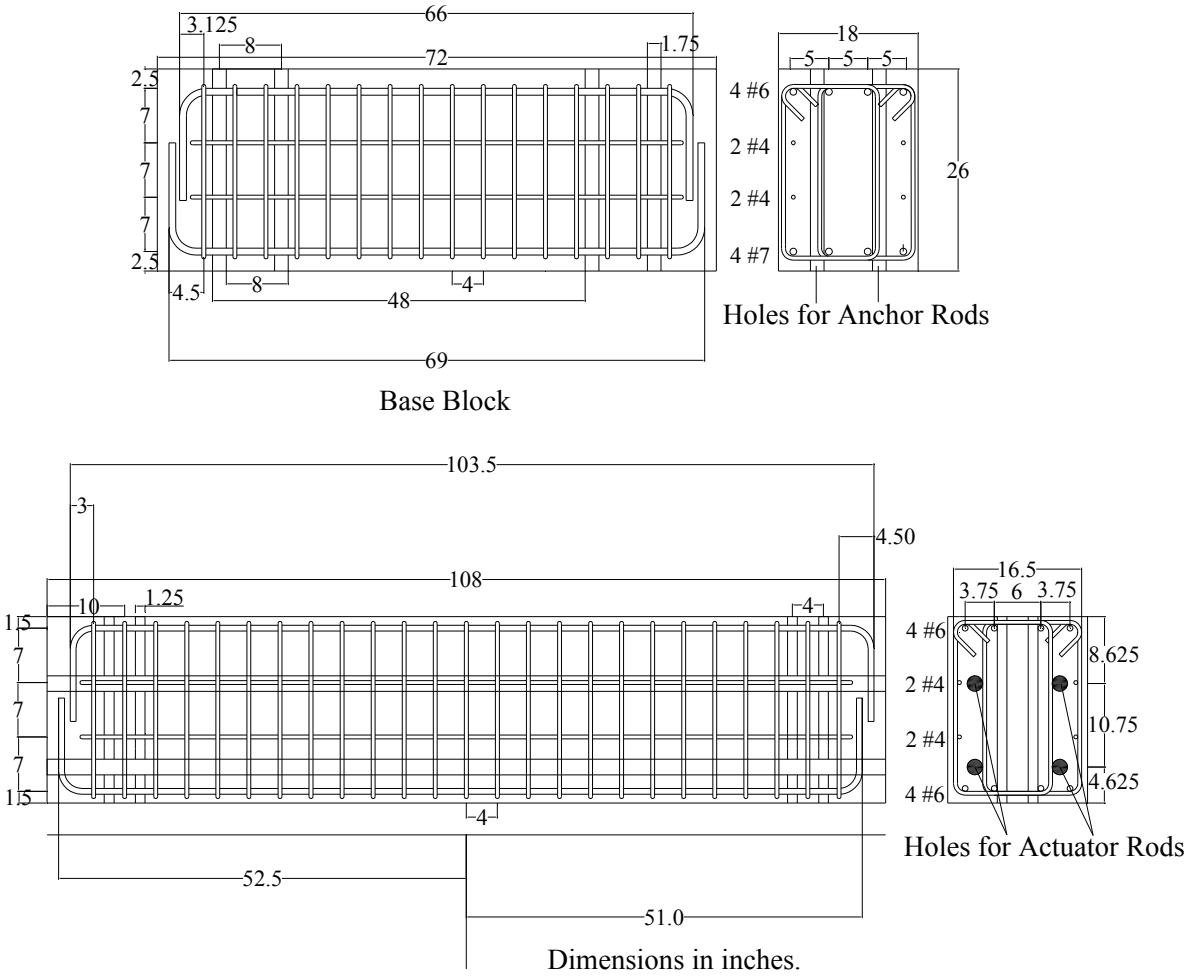

Figure 3.3 Top and base blocks

3.4 REINFORCEMENT DETAILS OF TEST SPECIMENS

Reinforcing steels used in the test specimens can be categorized into six groups: main flexural reinforcement, diagonal reinforcement (if any), intermediate longitudinal reinforcement, dowel bars, stirrups, and special column-type transverse reinforcement. In the following, a summary of the design details for all specimens is provided.

3.4.1 Specimen CB-1 (HPFRC with $\ell_n/h = 2.75$)

With success of the earlier tests of the HPFRC coupling beams with an aspect ratio of 1.75 at the University of Michigan (Lequesne 2008), the potential of using

HPFRC material in more slender coupling beams was investigated. The first specimen with an aspect ratio of 2.75 was constructed with an HPFRC material with specified compressive strength of 6,000 psi. The specimen was designed to resist a shear stress of approximately $10\sqrt{f_c'}$ (psi). Main flexural reinforcement consisted of two layers of No. 5 bars near the top and bottom surfaces of the beam. To sustain an approximately 25% of the expected peak shear demand, each group of diagonal reinforcement consisted of two No. 6 diagonal bars placed in two layers in between the main longitudinal reinforcement. The angle of diagonal bars was approximately 16 degrees with respect to the beam longitudinal axis. To force plastic hinges away from the beam-wall interfaces, intermediate No. 4 dowel bars extending 8 in. into the beam were used. To control cracks and delay shear strength decay, intermediate No. 3 longitudinal reinforcing bars were placed near mid-height over the full length of the beam.

Transverse reinforcement was designed to carry approximately 30% of the shear demand. No. 3 hoops spaced at 8 in. were selected, which resulted in a transverse reinforcement ratio of 0.46% (and a volumetric ratio of 0.67%). At the ends of the beams, special column-type confinement was provided according to the requirements of the Chapter 21 of ACI Building Code (ACI 318-08). A pair of No. 3 hoops was used at 2.75 in. spacing, resulting in a transverse reinforcement ratio of 1.33% (and a volumetric ratio of 2.9%). Figure 3.4 (a) shows the reinforcement details for Specimen CB-1.

3.4.2 Specimen CB-2 (HPFRC with $\ell_n/h = 2.75$)

With advances in concrete technology, high-strength concrete becomes common in construction of tall buildings. To evaluate the behavior of slender coupling beams made of high-strength concrete, Specimen 2 was constructed with a high-strength HPFRC material with a specified compressive strength of 10,000 psi. This specimen was designed to sustain a shear stress of approximately $8\sqrt{f_c'}$ (psi). The main longitudinal reinforcement consisted of one layer of No. 5 bars placed near the top and bottom of the specimen. It was estimated that 30% of shear demand would be resisted by diagonal reinforcement. Therefore, No. 6 bars were placed diagonally in two layers in each direction. The previous tests on shorter HPFRC coupling beams (Lequesne et al. 2010)

showed that both intermediate cut-off and U-shape dowel bars were effective to force plastic hinges away from the wall interface. Thus, two layers of No. 4 U-shaped dowels were embedded into the beams up to 6 in. from the faces of the walls. Intermediate No. 3 longitudinal bars were placed over the length of the beam to control cracks and delay strength decay, as used in Specimen CB-1.

Stirrups were expected to carry approximately 45% of the peak shear imposed on the beam. This expected shear resistance by stirrups was higher than that of Specimen CB-1 due a reduction in the stirrup spacing The spacing of No. 3 transverse reinforcement was selected to be 6.5 in., resulting in a transverse reinforcement ratio of 0.59% (and a volumetric ratio of 0.82%). Special column-type confinement consisted of a pair of No. 4 stirrups spaced at 3.25 in. to provide adequate confinement such that plastic hinges at the beam ends would have adequate ductility. This resulted in a transverse reinforcement ratio of 2.1% (and a volumetric ratio of 4.5%). The reinforcement layout for Specimen CB-2 is shown in Figure 3.4 (b).

3.4.3 Specimen CB-3 (HPFRC with $\ell_n/h = 3.3$)

An aspect ratio of 3.3 is typically used in coupling beams of current office buildings. To investigate the potential of using high-strength HPFRC material for such slender coupling beams, the third specimen was designed with an HPFRC specified compressive strength of 10,000 psi. A high shear stress demand of approximately $8\sqrt{f_c'}$ (psi) was targeted for this specimen. For a coupling beam with this large aspect ratio to develop the same level of shear as in Specimen CB-2, a larger amount of longitudinal reinforcement was required. Two No. 6 bars were chosen as longitudinal reinforcement placed near the extreme top and bottom fibers of the specimen. Diagonal bars were expected to resist approximately 25% of the peak shear demand. Thus, No. 6 bars were placed diagonally in two layers for each direction. It should be noted that less reliance was put on diagonal reinforcement for shear resistance because its angle of inclination with the beam axis was only 12.8 degrees. To compare the efficiency of intermediate bars in forcing plastic hinges away from the wall interface, No. 4 U-shaped bars at one end and No. 4 straight dowels at the other end were embedded in the beam and extended up to 8 in. from the faces of the walls. As in Specimen CB-1 and CB-2, full-length intermediate

No. 3 bars were used at mid-height of the beam to control cracks and delay shear strength decay.

As in Specimen CB-2, stirrups were expected to carry approximately 45% of the peak shear demand. Therefore, No. 3 stirrups spaced at 6 in. were chosen. In order to satisfy the special confinement requirements for columns in Chapter 21 of ACI 318-08, No. 4 double stirrups spaced at 3 in. were used within the plastic hinge regions. This resulted in a transverse reinforcement ratio of 2.5% (and a volumetric ratio of 5.2%). Figure 3.4 (c) illustrates the reinforcement details for Specimen 3.

3.4.4 Specimen CB-4 (RC with $\ell_n/h = 2.75$)

To better evaluate the influence of HPRFC on coupling beam behavior, the fourth specimen was constructed using the same reinforcement detailing as that of Specimen CB-2 but with regular concrete. The specified concrete compressive strength was 10,000 psi.

3.4.5 Specimen CB-5 (HPFRC with $\ell_n/h = 3.3$)

Test results from the first three specimens confirmed the effectiveness of HPFRC material to increase shear strength and provide excellent confinement to the coupling beams. This led to the investigation of the possibility of eliminating diagonal bars in slender coupling beams. An aspect ratio of 3.3 was first chosen because at this ratio the inclined angle of diagonal reinforcement is as shallow as 12.8 degrees. Using diagonal reinforcement with a very shallow inclined angle cannot be justified considering the complexity of construction. Therefore, the shear strength of this specimen was to be provided by the high-strength HPFRC and transverse reinforcement. This beam was intended to resist a shear demand of approximately $8\sqrt{f_c'}$ (psi) with an HPFRC specified compressive strength of 10,000 psi.

Because the shear strength of the coupling beam relied on stirrups and HPFRC material, No. 4 stirrups spaced at 5.75 in. were selected to carry approximately 70-80% of the applied shear demand through truss action, resulting in a transverse reinforcement ratio of 1.2% and a volumetric ratio of 1.8%. To satisfy the requirement of ACI 318-08, column-type confinement consisting of a pair of No. 4 hoops at 3 in. spacing was used at

the ends of the beam. This confinement represented a transverse reinforcement ratio of 2.2% and a volumetric ratio of 4.9%.

Main longitudinal reinforcement consisted of No. 6 bars placed in two layers near the top and bottom of the coupling beam. Intermediate U-shape bars were embedded 8 in. into the coupling beam from the faces of the walls to force plastic hinges to develop away from the beam-wall interface. Intermediate No. 4 longitudinal bars were used over the length of the beam to control cracks and delay shear strength decay. The reinforcement layout for Specimen 5 is illustrated in Figure 3.4(d).

3.4.6 Specimen CB-6 (HPFRC with $\ell_n/h = 2.75$)

With the successful test of Specimen CB-5, the possibility of eliminating diagonal reinforcement in shorter HPFRC coupling beams was explored. An aspect ratio of 2.75 was chosen and an HPFRC compressive strength of 10,000 psi was specified. This beam was intended to resist a shear demand of approximately $8\sqrt{f_c'}$ (psi). The same transverse reinforcement and column-type confinement as that used in Specimen CB-5 were used. Main flexural reinforcement consisted of No. 6 bars at the outmost layer and No. 5 bars in the second layer. Intermediate No. 4 U-shaped dowels were embedded in the coupling beam as in Specimen CB-5. The reinforcement details of Specimen CB-6 are depicted in Figure 3.4(e).

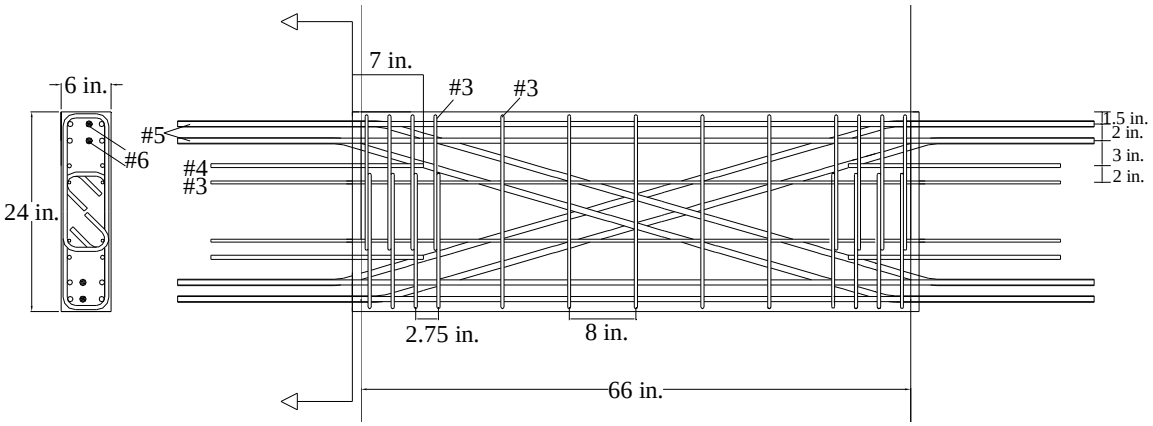

(a) Specimen CB-1

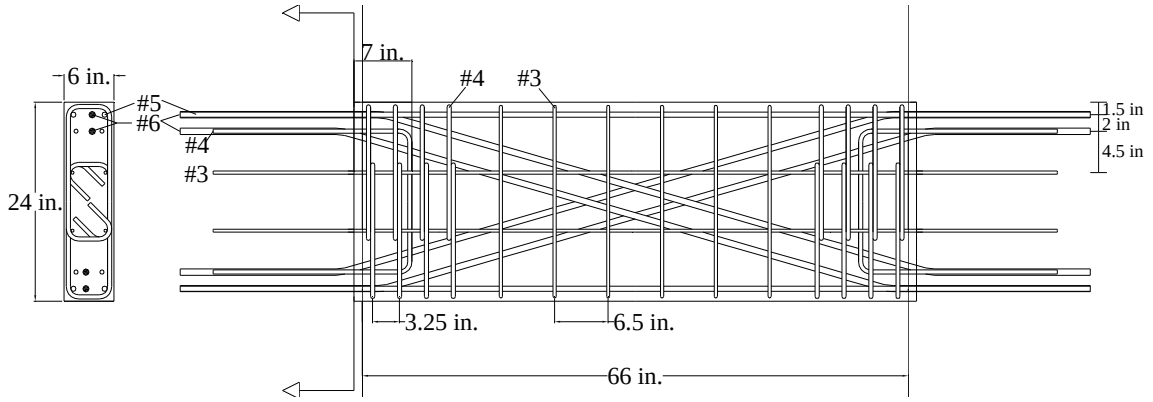

(b) Specimens CB-2 and CB-4

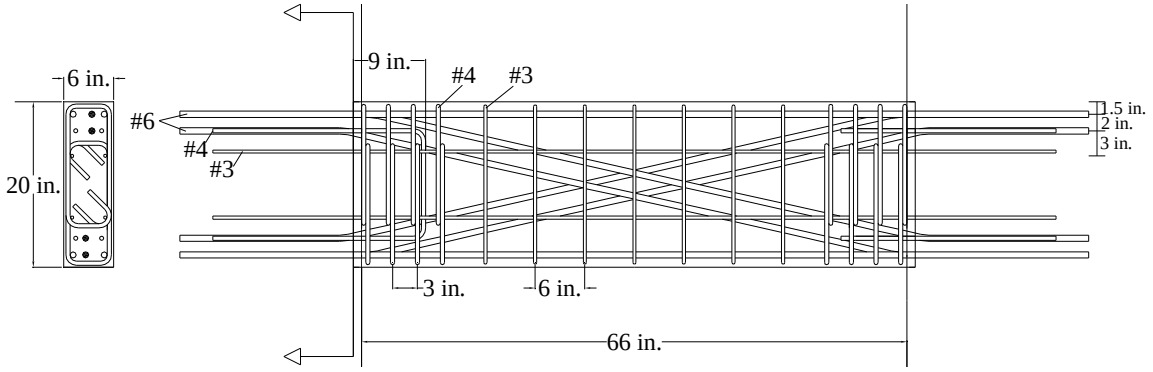

(c) Specimen CB-3

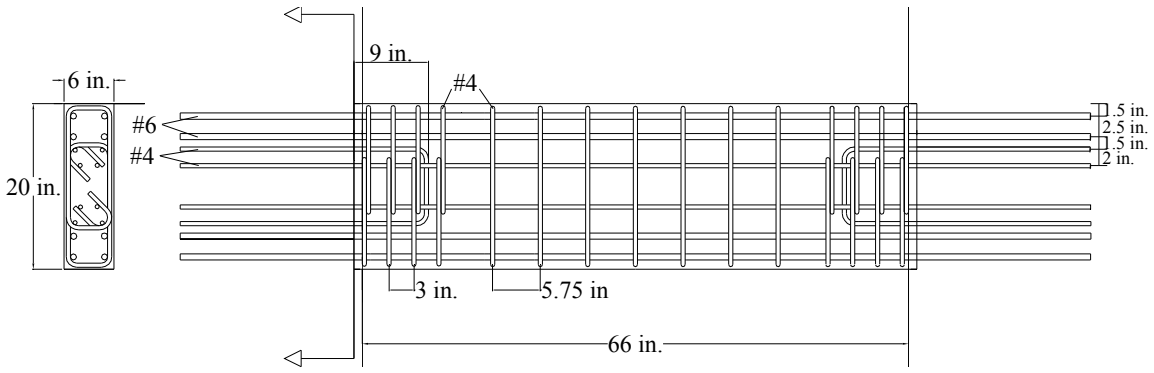

(d) Specimen CB-5

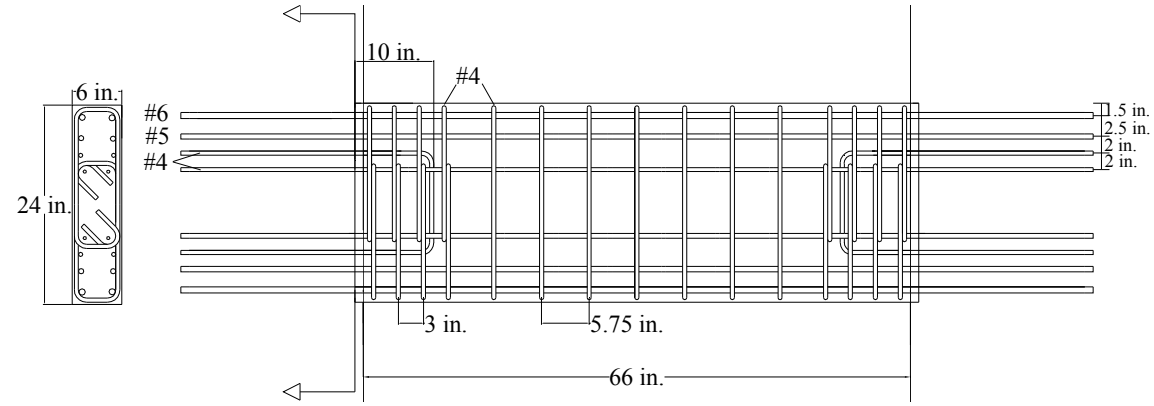

(e) Specimen CB-6

Figure 3.4 Reinforcement detailing for test coupling beams

3.5 CONSTRUCTION OF SPECIMENS

All specimens were constructed in the Structures Laboratory at the University of Michigan. Reinforcing bars and stirrups were cut and bent by a local supplier. For each specimen, approximately 30 strain gauges were attached to several reinforcing bars and stirrups to measure strains developed in the reinforcement during testing. Electrical resistance strain gauges, Type YFLA-5-5L with a length of 5 mm and manufactured by Tokyo Sokki Kenkyujo Co., were used for the whole experimental program. At the strain gauge locations, a surface of bar approximately 1 in. long was first ground and then smoothened by sanding discs. Smoothened surfaces were then cleaned by acid and neutralizer before strain gauges were attached. After being glued to the bar, the strain gauges were coated by three layers of two different coating agents, namely polyurethane and nitrile coating. The strain gauges were then covered by vinyl mastic tape to protect

them from damage during concrete casting. Various stages of strain gauge installation are shown in Figure 3.5.

(a) (b) (c)

Figure 3.5 Three stages of strain gauging: (a) attachment of strain gauge to bar by glue (b) coating of strain gauge with coating agents, and (c) covering of strain gauge with mastic tape

Once the reinforcement cage for the coupling beam was tied inside a wooden formwork (Figure 3.6), concrete was mixed in the laboratory and poured into the formwork. After concrete casting, the exposed precast coupling beam was covered with plastic sheets for 2-3 days and the formwork was removed about one week later. A precast coupling beam after demolding is shown in Figure 3.7. At the same time, two reinforcement cages for members representing the walls were constructed. Steel reinforcing bars for both top and base blocks were tied together to form steel cages, as shown in Figure 3.8, and then placed into the wooden formworks. After the reinforcement cages for the top and base blocks were completed, the coupling beam was lifted with a crane and inserted into the top block. The reinforcing cage for the base block was then slid through the other end of the coupling beam.

Figure 3.6 Coupling beam cage assembled in a wood formwork and ready for casting

Figure 3.7 Precast coupling beam after demolding

Figure 3.8 Reinforcement cages for top and base blocks

Four PVC pipes were embedded into the top block for passage of the high strength threaded rods that were used to connect that block to a hydraulic actuator. Eight PVC pipes embedded into the base block were used for passing the high strength threaded rods that anchored the base block to the strong floor. Eight small PVC pipes were placed inside the top block for the passage of threaded rods for connection with the steel links. A specimen ready for concrete casting is shown in Figure 3.9. A local concrete supplier was hired to deliver concrete for the end blocks, which were cast inside the Structures Laboratory. Concrete was placed by the use of a crane and bucket system. After casting, the top and base blocks were covered by plastic sheets for 2-3 days. Formwork was taken off about one week later and the specimen was cured in the laboratory environment. A few days before the test, the specimen was then lifted with a crane, rotated to a vertical position, and placed into the test setup as shown in Figure 3.10.

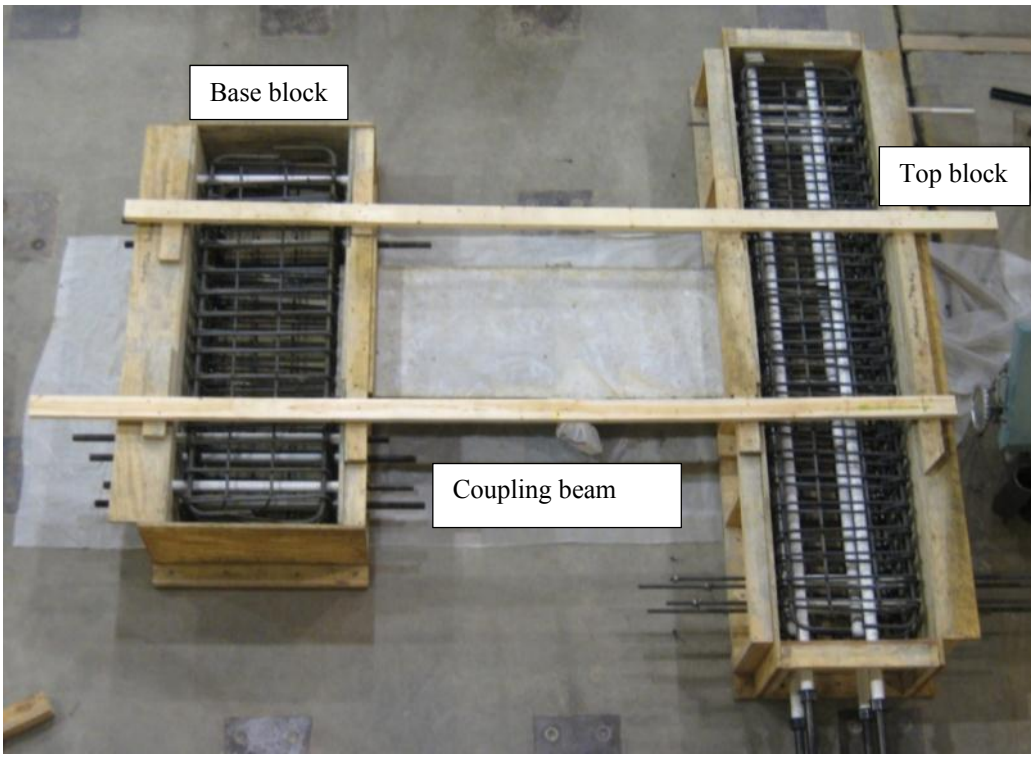

Figure 3.9 Precast coupling beam connected to base and top blocks representing walls prior to casting of blocks.

Figure 3.10 Complete specimen ready for testing

3.6 HPFRC AND CONCRETE PROPORTIONS AND MIXING

HPFRC and concrete for the coupling beams were mixed in the concrete mixing laboratory at the University of Michigan. Detailed concrete mixture proportions are summarized in Table 3.2.

Table 3.2 Mixture proportions by weight for the coupling beams

Material	HPFRC [1]	HPFRC [2]	HPFRC [3]	Concrete [4]
Cement	1	1	1.2	1.2
Fly Ash	0.875	0.5	0.3	0.3
Sand	2.2	1.7	1.7	1.4
Coarse Aggregate	1.2	1	1	1.3
Water	0.8	0.6	0.6	0.55
Viscosity Modifying Agent	0.038	0.0095	0.0095	0.0095
Super plasticizer	0.005	0.01	0.01	0.01
Steel Fibers	0.315*	0.246*	0.246*	-

[1] HPFRC for Specimen CB-1
[2] HPFRC for Specimen CB-2
[3] HPFRC for Specimens CB-3, CB-5, and CB-6
[4] Concrete for Specimen CB-4
*1.5% by volume

HPFRC mixtures used in this study were adapted from a series of self-consolidating HPFRC (SCHPFRC) mixtures developed at the University of Michigan (Liao et al. 2006), which had been successfully used in research on coupling beams (Lequesne 2010) and low-rise walls (Athanasopoulou 2010). Mixture proportions in this study used Type III cement (early high strength) and Type C fly ash. Coarse aggregates consisted of crushed limestone with $1/2$ in. maximum aggregate size. The sand used was Silica sand #16, a product referred to as "Flint Silica #16", manufactured by U.S. Silica Company, with particles sized from mesh #20 (diameter of 0.03346 in.) to mesh #140 (diameter of 0.00417 in.). The 1.5% volume fraction of steel fibers was maintained in all HPFRC mixes. A polycarboxylate-based superplasticizer was used to reduce the water requirement and impart high workability. A viscosity modifying agent (VMA) was added to enhance the viscosity and reduce fiber segregation in the presence of a high water-cement ratio. Types of superplasticizer and VMA used in this study can be found in Liao et al. (2006).

High-strength hooked steel fibers were used in all HPFRC mixtures. These fibers, manufactured by Bekaert S.A., Belgium, have been successfully used in research and are readily obtained in the market. under the name of "Dramix RC80/30 BP" (Figure 3.11). The hooks (bends) at the fiber ends create additional mechanical bond to the concrete. The fibers used in this study were made of a wire with approximately twice the tensile strength of most steel fiber wires (approximately 330 ksi versus 160 ksi). Also, these fibers had a diameter of 0.015 in., which is smaller than that of most hooked steel fibers available in the market. The properties of the fibers used in this investigation are listed in Table 3.3.

Figure 3.11 Dramix RC80/30 BP hooked steel fibers used in this study

Table 3.3 Properties of hooked steel fibers

Length (in)	Diameter (in)	Length / diameter	Tensile Strength (ksi)
1.2	0.015	80	330

Materials in the concrete mixture used in Specimen CB-4 were the same as those used in the HPFRC mixtures, except that no steel fibers were added to the concrete.

Concrete and HPFRC was mixed in a 5-cubic feet capacity mixer. Two batches of mixtures were prepared for each coupling beam. Three ASTM 1609 beams (6 x 6 x 20 in.) and six cylinders were cast along with the HPFRC coupling beam for each batch of mixing. For the reinforced concrete coupling beam (Specimen CB-4), no ASTM beams were cast. Mixing procedures for HPFRC followed the recommendations by Liao et al. (2006). To obtain good quality of HPFRC, the sequence and time for each mixing process were strictly followed. For the mixtures used in this study, cement, fly ash, and sand were dry mixed for 30 seconds. Pre-mixed liquid consisting of water, VMA, and superplastizer was then added slowly to obtain a good HPFRC matrix. Coarse aggregates were then added and two minutes later steel fibers were slowly poured into the mixture. The mixing process continued for 3 minutes after addition of the steel fibers. HPFRC in the mixer ready for casting coupling beams, ASTM beams, and cylinders is shown in Figure 3.12.

Figure 3.12 HPFRC mixture ready for casting

3.7 INSTRUMENTATION AND TESTING PROCEDURE

Strain gauges were attached to reinforcement at several locations to measure strains developed during the test. Strain gauges were intended to remain intact through large inelastic deformation. Locations and labels for strain gauges placed on longitudinal, diagonal, and transverse reinforcement are shown in Figures A.1-A.6 in Appendix A.

Shear force applied to the specimen was measured by the load cell attached to the hydraulic actuator. Applied displacement at the top block was measured by a Linear Variable Differential Transformer (LVDT) attached to the actuator. Axial forces developed in the coupling beam during the test were monitored by two load cells attached to the vertical steel arms that restrained top block rotations. Each load cell had 110-kip capacity. Data from load cells were also used to calculate the moment imposed at the ends of the coupling beam. The readings from all instruments were collected simultaneously through a data acquisition system at a sampling rate of 2 Hz.

Deformations of the specimen were tracked by an active infrared optical position tracking system called Optotrak Certus. The key components of this system are shown in Figure 3.13. The Optotrak Certus system consists of a light emitting diode (marker) that

emits infrared light at a certain frequency controlled by a strober. The infrared camera with high resolution sensors detects infrared light and calculates the position of the marker in space through triangulation. Depending on the number of markers used and their programmed frequency, the marker frequency and maximum sampling rate can be adjusted. For this experimental program, a sampling rate of 2 Hz was selected to match the sampling rate of the other data acquisition system used in this study.

In this experimental program, a grid of markers was attached to one face of the specimens using thermoplastic adhesive (hot-melt glue) as shown in Figure 3.14. Grids with 5.5-inch and 6-inch spacing between markers were selected for the coupling beams with aspect ratio of 2.75 and 3.3, respectively (Figures 3.15 and 3.16). The labels of markers on the specimens are illustrated in Figures 3.17 and 3.18. With the recorded coordinates of these markers, relative displacements, shear strains, curvatures, and several other deformations could be calculated at several locations on the specimen throughout the test.

Only one linear potentiometer was used to measure slip of the base block during the test, allowing the real-time adjustment of target displacements to be imposed on the specimen.

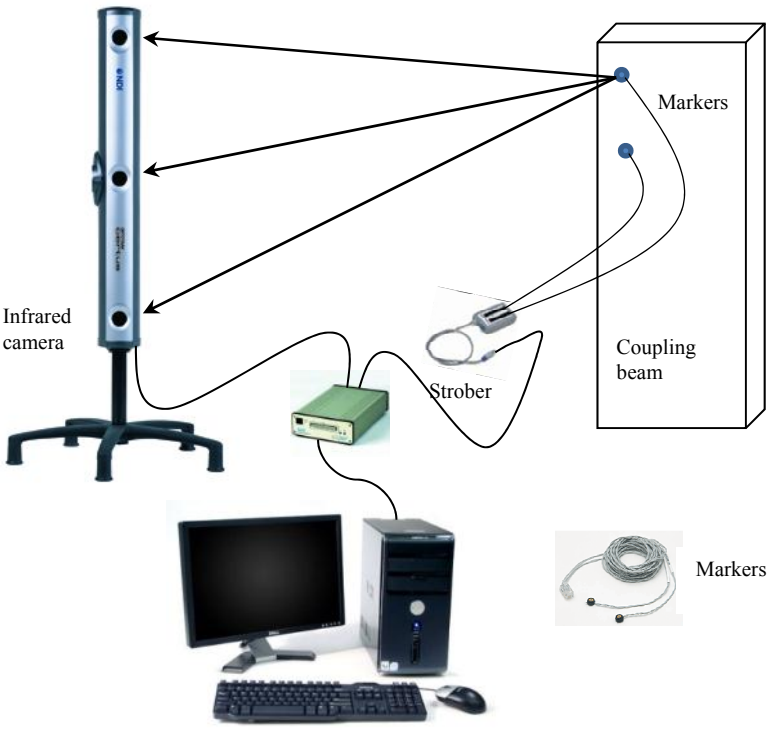

Figure 3.13 Optotrak system

Figure 3.14 Optotrak markers attached on the back of the coupling beam

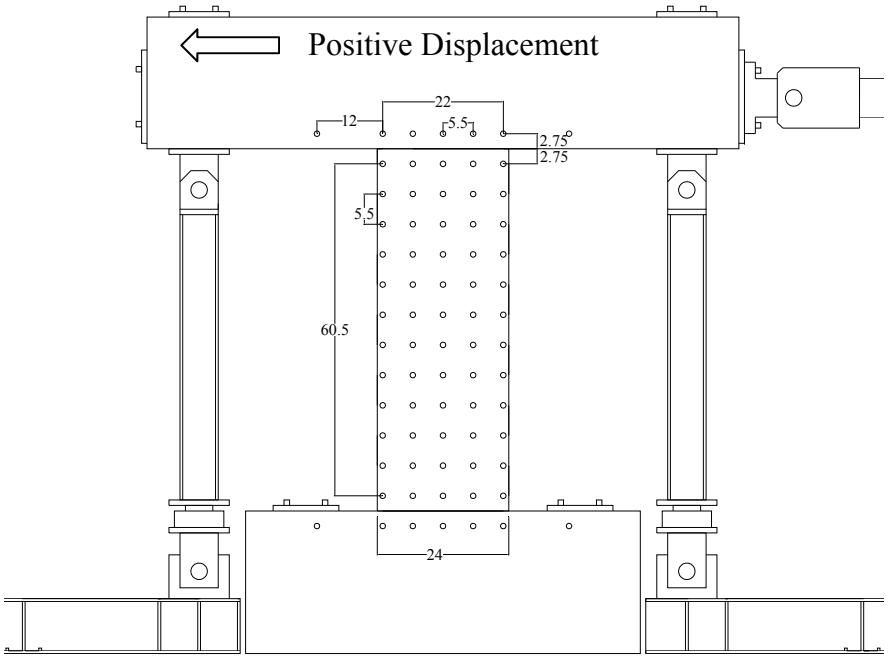

Figure 3.15 Optotrak marker layout for coupling beams with aspect ratio of 2.75

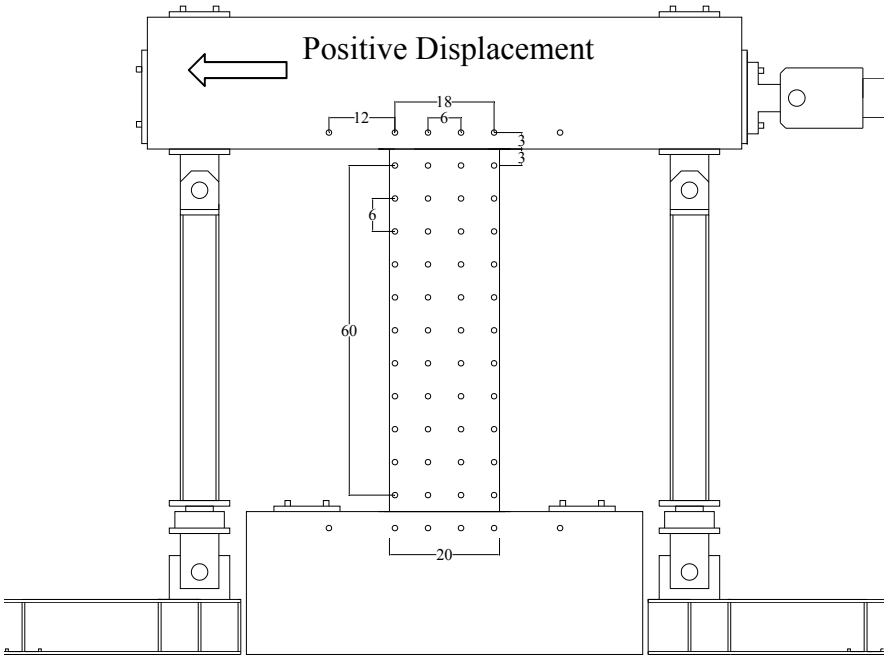

Figure 3.16 Optotrak marker layout for coupling beams with aspect ratio of 3.3

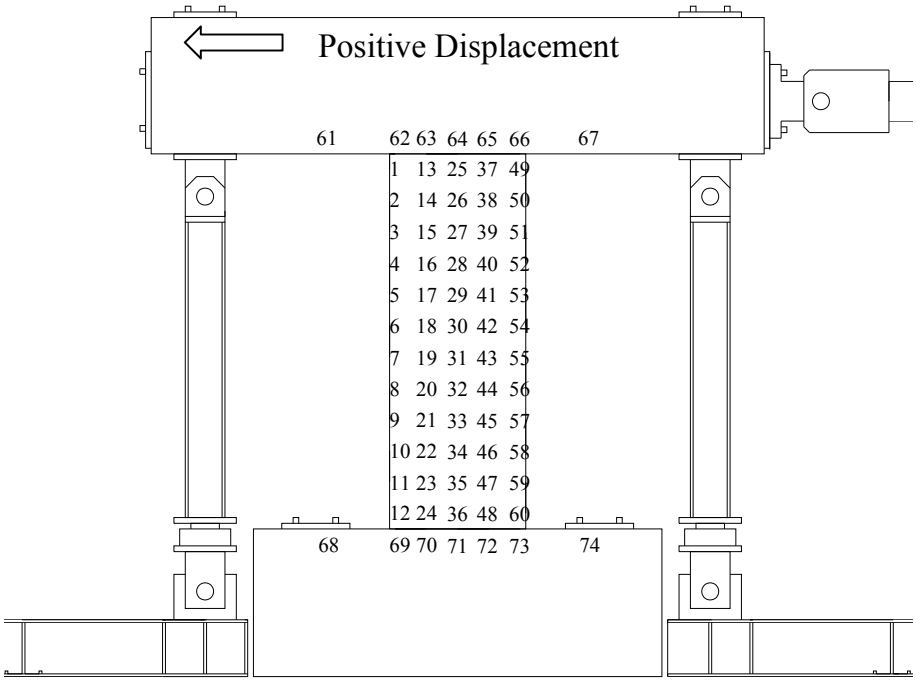

Figure 3.17 Optotrak marker labels for coupling beams with aspect ratio of 2.75

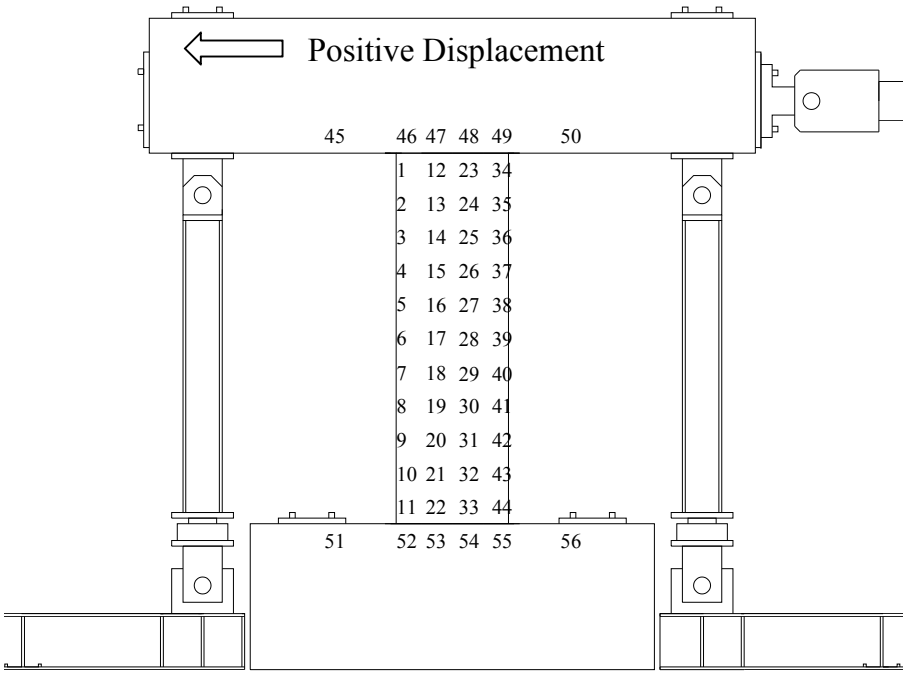

Figure 3.18 Optotrak marker labels for coupling beams with aspect ratio of 3.3

The specimens were subjected to quasi-static loading in a displacement controlled mode, following a predefined reversed cyclic displacement pattern. A displacement rate of approximately 1 in. per minute was used. The lateral displacement history for Specimen CB-1 consisted of cycles of drifts at 0.25% increments up to 2.5% drift. Then, cycles at 0.5% drift increments were applied until the end of the test. Every displacement cycle up to 4.0% was performed twice to evaluate any decrease in strength and stiffness with repeated displacement cycles. The displacement history for Specimen CB-1 is shown in Figure 3.19(a). For Specimen CB-2 through CB-6, the cyclic displacement pattern was modified and single cycles at drift increments of 0.5% for drifts larger than 2.0% were applied (Figure 3.19 (b)). This modification was made in order to reduce the number of cycles applied, which for Specimen CB-1 was believed to be excessive.

During testing, up to approximately 3% drift, the actuator was held momentarily at peak drift for the first cycle to allow students to mark cracks developed on the specimens.

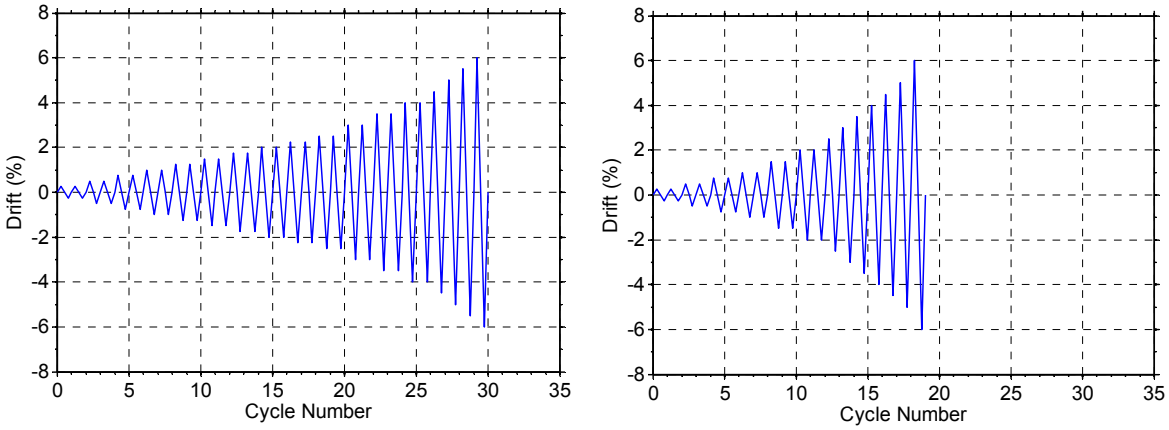

(a) Specimen CB-1 (b) Specimens CB-2 through CB-6

Figure 3.19 Pre-defined cyclic displacement history

3.8 MATERIAL PROPERTIES

Each coupling beam was constructed with Grade 60 mild-steel reinforcement obtained from local suppliers. HPFRC and concrete for the coupling beams were mixed in the laboratory as previously described in Section 3.6. Concrete for top and base blocks of the specimens was obtained from a local supplier. Details of material properties are presented in the following sections.

3.8.1 Reinforcing Bars

Tensile stress-strain relationships for reinforcing bars were obtained through direct tension tests. For each bar size in each specimen, at least three 24-in. long coupons were randomly selected and tested. In these direct tension tests, the Optotrak system was used to measure the axial elongation of the coupon. Coordinates obtained from two markers placed near the top and bottom of the coupon were then used to calculated axial strain. Figure 3.20 shows a sample of the tested coupon along with markers used to measure elongation. Reinforcement yield and ultimate stresses are given in Table 3.4.

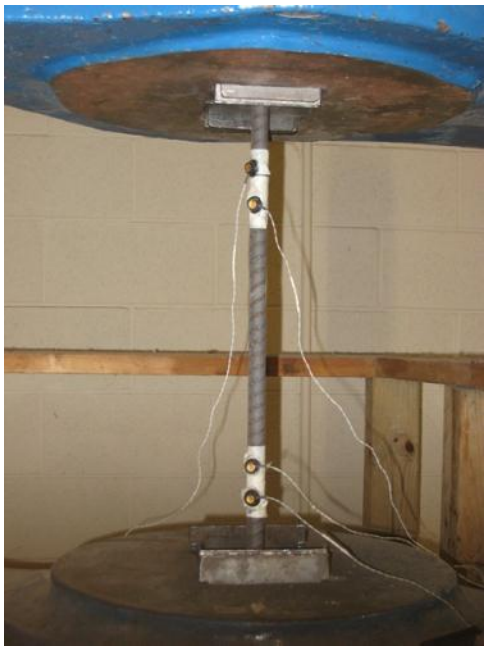

Figure 3.20 Direct tension test of a reinforcing bar using Optotrak markers to measure axial elongation

Table 3.4 Yield and ultimate stresses of steel reinforcement

Specimen	Bar Size	Average Yield Stress (ksi)	Average Ultimate Stress (ksi)
CB-1	#3	60	92
	#4	61	101
	#5	61	99
	#6	74	95
CB-2	#3	60	92
	#4	60	99
	#5	61	100
	#6	83	102
CB-3	#3	65	108
	#4	77	96
	#6	79	100
CB-4	#3	62	98
	#4	64	100
	#5	69	107
	#6	65	100
CB-5	#4	77	96
	#6	79	100
CB-6	#4	85	101
	#5	64	97
	#6	76	94

3.8.2 Compressive Strength

Average compressive strength of concrete and HPFRC was determined through compressive tests of 4 x 8 in. cylinders. Six cylinders were prepared for each batch of material mixed in the laboratory and all delivered ready-mixed concrete. Three cylinders were tested at 28 days and the other three were used to determine compressive strength on the test day. Cylinders were immersed in water from one day after casting until one day before compressive testing and capped with sulfur compound to make both ends of the cylinders flat. The cylinders were tested using an Instron hydraulic testing machine and following ASTM C39/C39M (2003). Test results are shown in Table 3.5.

Table 3.5 Compressive strength of HPFRC and concrete mixed in the laboratory

Specimen	f'_c (ksi) (28 days)	f'_c (ksi) (Test day)	Age at test day (days)
CB-1 (HPFRC)	4.9	7.2	136
CB-2 (HPFRC)	7.4	8.6	51
CB-3 (HPFRC)	7.7	8.9	50
CB-4 (Concrete)	9.0	9.0	28
CB-5 (HPFRC)	7.7	9.9	50
CB-6 (HPFRC)	8.8	9.8	48

Table 3.6 Compressive strength of ready-mixed concrete used in top and base blocks

Specimen	f'_c (ksi) (28 days)	f'_c (ksi) (Test day)	Age at test day (days)
CB-1	3.6	5.5	50
CB-2	-	4.7	23
CB-3	5.8	5.8	28
CB-4	-	6.2	16
CB-5	-	6.2	21
CB-6	5.2	5.5	33

3.8.3 HPFRC Flexural Strength

For each batch of HPFRC, three beams with dimensions of 6 x 6 x 20 in. were prepared to evaluate flexural behavior, as shown in Figure 3.21. Beams were cured in a water tank from one day after casting until the test day, which was one day after the coupling beam testing. All beams were tested under four-point loading following ASTM 1609-05. The beam had a span length L of 18 in. Midspan deflections were measured by two linear potentiometers with a 0.5-in stoke length. The four-point bending test setup is illustrated in Figure 3.22. The equivalent bending stresses at first crack, peak, and deflections of L/600 and L/150 are summarized in Table 3.7. Typical equivalent bending stress-deflection curves for HPFRC beam specimens are shown in Figure 3.23.

Figure 3.21 Casting HPFRC beams for flexural tests

Figure 3.22 Test of HPFRC beam according to ASTM 1609-05

Table 3.7 ASTM 1609-05 beam test results

Specimen	First Peak		Second Peak		L/600	L/150
	f_1 (psi)	δ_1 (in)	f_p (psi)	δ_p (in)	$f_{150,0.75}$	$f_{150,3.0}$
CB-1 (HPFRC)	830	0.005	1000	0.016	936	510
CB-2 (HPFRC)	810	0.003	1075	0.020	1050	560
CB-3 (HPFRC)	1030	0.002	1215	0.020	1210	530
CB-5 (HPFRC)	890	0.006	1140	0.015	1080	650
CB-6 (HPFRC)	1050	0.003	1620	0.039	1575	1130

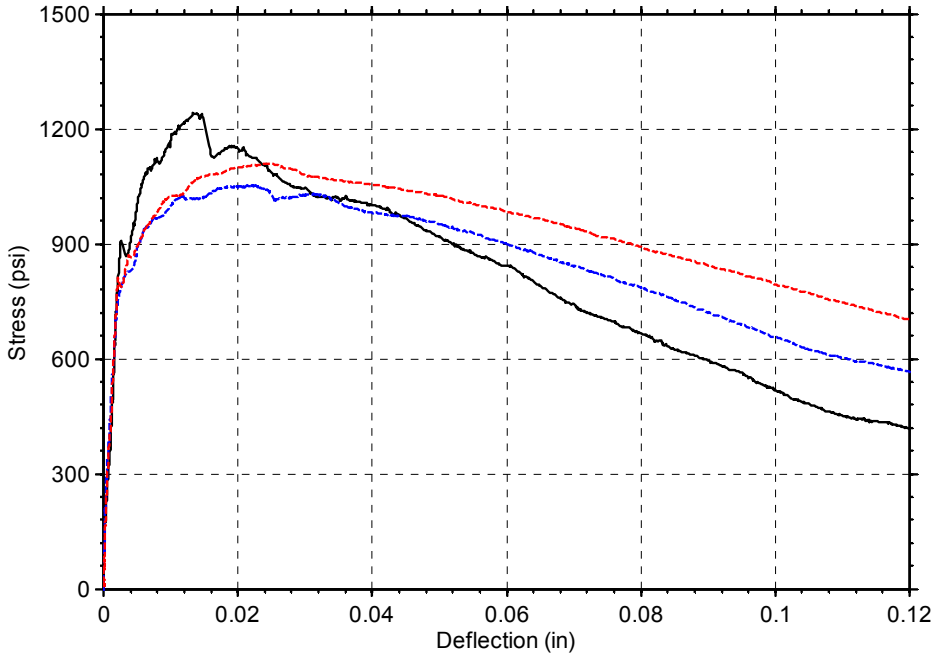

Figure 3.23 Typical stress and deflection response for ASTM 1609 beam specimens

3.8.4 Compressive and Tensile Stress-Strain Responses of HPFRC Material

The design process of the HPFRC coupling beams described in Section 3.3 involved moment-curvature analyses to determine the ultimate moment capacity, and hence associated shear strength, of the specimens. In the moment-curvature analyses, compressive and tensile constitutive models for HPFRC were required and assumed to have relationships as shown in Figure 3.24 and 3.25. These relationships were based on previous tests of cylinders and dogbone specimens by Liao et al. (2006). HPFRC mixtures described in Section 3.6 were based on "Mix 3" and "Mix 5" in Figure 3.24 and 3.25.

The ascending branch of the compressive constitutive response was assumed to be parabola defined by Eq. (3.3) (Hognestad 1952), up to the peak stresses, $f_c^{'}$, of 6 and 9 ksi and corresponding compressive strains, ε_o, of 0.2% and 0.4% for Mix 5 and Mix 3, respectively. In this equation, ε_c is the concrete strain.

$$f_c = f_c^{'}\left[\frac{2\varepsilon_c}{\varepsilon_o} - \left(\frac{\varepsilon_c}{\varepsilon_o}\right)^2\right] \tag{3-3}$$

The descending branch of the constitutive responses was linear as defined by Eq. (3.4) (Kent and Park 1971).

$$f_c = f_c^{'}\left[1 - Z(\varepsilon_c - \varepsilon_o)\right] \tag{3-4}$$

where Z is the slope of the descending tail for a concrete with unit compressive strength and assumed to be 50 to account for the ductile behavior exhibited by HPFRC.

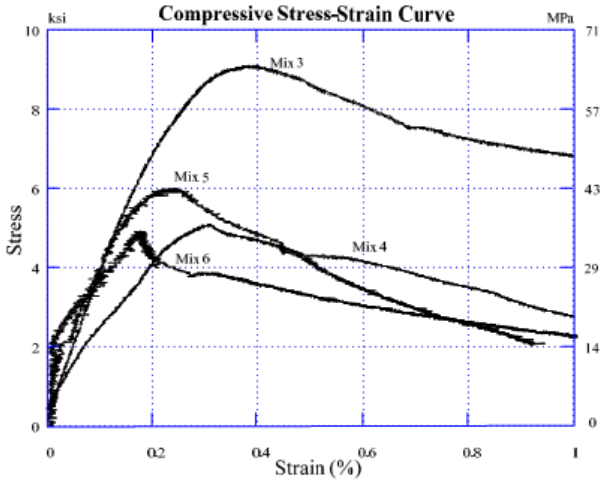

Figure 3.24 Compressive constitutive responses of HPFRC (Liao et al. 2006)

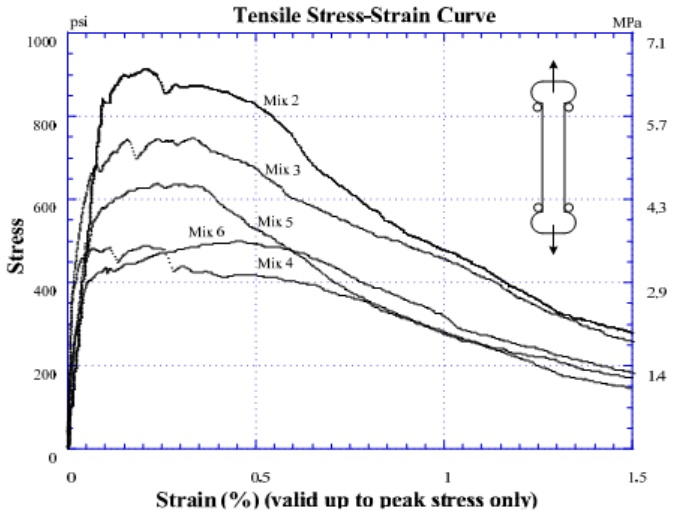

Figure 3.25 Tensile constitutive responses of HPFRC (Liao et al. 2006)

Piece-wise linear constitutive relationships were used to model the HPFRC tensile stress-strain behavior. These relations were selected to fit the tensile responses in Figure 3.25. The assumed piecewise linear relations, along with their corresponding values of stress and strain, are shown in Figure 4.40 and Table 4.10 in Section 4.4.5, where moment-curvature analyses of the test specimens are discussed.

3.8.5 Constitutive Model of Reinforcing Steels under Cyclic Loading

Reinforcement strains recorded from strain gauges provided useful information about the drifts at which first yielding of reinforcement occurred and the location of inelastic deformations in the test specimens. Moreover, these recorded strains were used to estimate the contribution of reinforcement to shear strength, as will be discussed in Section 4.5.2. To approximate shear carried by reinforcing steel, stresses developed in the reinforcing bars are required. Unfortunately, due to the cyclic displacement imposed on the specimens, this stress cannot simply be determined from the corresponding recorded strain using the stress-strain relationship obtained from the direct tension test. Constitutive models that can capture the hysteresis behavior of steel are needed to relate the recorded strain to the corresponding stress. In this study, a relatively simple model reported in Sakai and Mahin (2004) was adopted for such purpose. Examples of the recorded strains and corresponding stresses obtained from this model are shown in Figures 3.26 and 3.27.

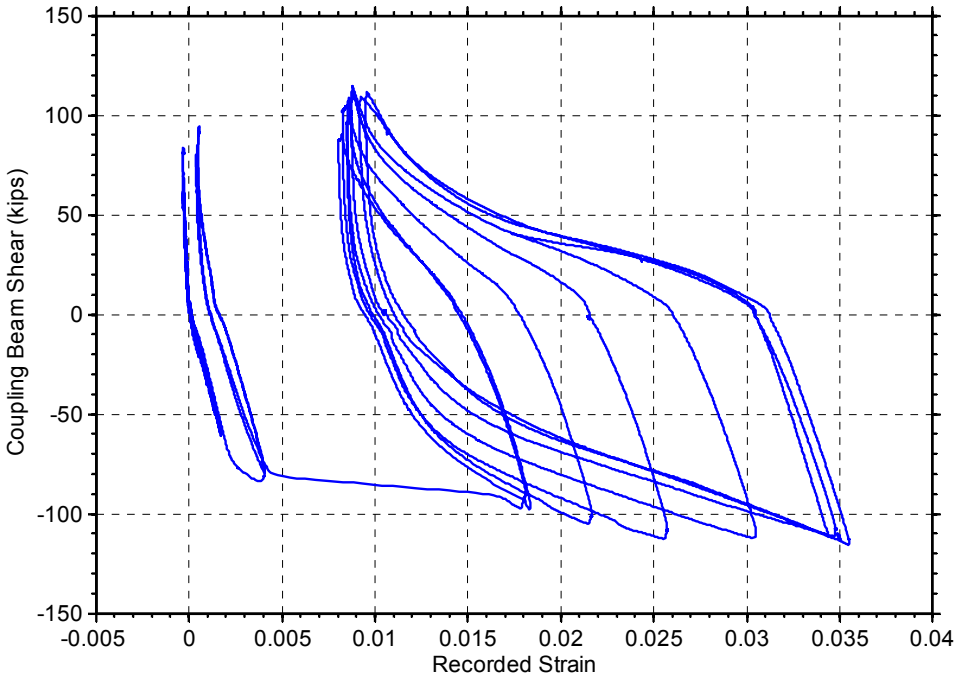

Figure 3.26 Shear imposed on coupling beam versus recorded strain for strain gauge D1 of Specimen CB-2

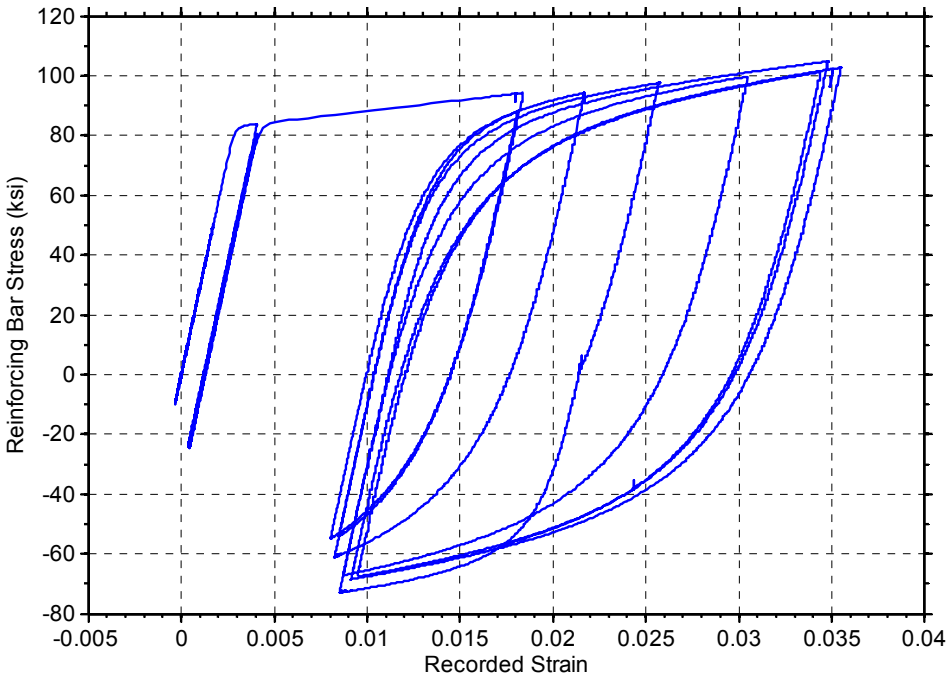

Figure 3.27 Calculated reinforcing bar stress versus recorded strain for strain gauge D1 of Specimen CB-2

CHAPTER 4
EXPERIMENTAL RESULTS AND ANALYSIS

4.1 PROCESSING OF OPTOTRAK DATA AND CALCULATION OF DRIFT, STRESS, AND STRAIN

4.1.1 Coordinate Transformation

Data obtained from the Optotrak Certus system had to be transformed to a local coordinate system with axes corresponding to those of the coupling beams. As described in Section 3.7, this system uses an infrared camera to calculate the positions of markers on the coupling beams. The coordinate systems of the infrared camera and the coupling beam are different unless the vertical plane of the infrared camera is parallel to the vertical face of the coupling beam. Generally, coordinates obtained from the infrared camera do not represent the actual coordinates of markers on the coupling beam and thus, coordinate transformation is required.

Let $\left\langle \overrightarrow{E_1}, \overrightarrow{E_2}, \overrightarrow{E_3} \right\rangle$ and $\left\langle \vec{e}_1, \vec{e}_2, \vec{e}_3 \right\rangle$ be the unit vectors of the coordinate system XYZ and xyz of the Optotrak camera and the beam, respectively, as shown in Figure 4.1. If the origin of the xyz coordinate system is located at B, the coordinates of point D in the xyz system can be calculated from

$$\begin{Bmatrix} x_D \\ y_D \\ z_D \end{Bmatrix} = \begin{bmatrix} \vec{e}_1 \cdot \overrightarrow{E_1} & \vec{e}_1 \cdot \overrightarrow{E_2} & \vec{e}_1 \cdot \overrightarrow{E_3} \\ \vec{e}_2 \cdot \overrightarrow{E_1} & \vec{e}_2 \cdot \overrightarrow{E_2} & \vec{e}_2 \cdot \overrightarrow{E_3} \\ \vec{e}_3 \cdot \overrightarrow{E_1} & \vec{e}_3 \cdot \overrightarrow{E_2} & \vec{e}_3 \cdot \overrightarrow{E_3} \end{bmatrix} \left(\begin{Bmatrix} X_D \\ Y_D \\ Z_D \end{Bmatrix} - \begin{Bmatrix} X_B \\ Y_B \\ Z_B \end{Bmatrix} \right) \tag{4-1}$$

where $\left\langle X_D, Y_D, Z_D \right\rangle$ and $\left\langle X_B, Y_B, Z_B \right\rangle$ are the coordinates at point D and B, respectively, obtained from the Optotrak camera and $\overrightarrow{E_1} = (1,0,0)$, $\overrightarrow{E_2} = (0,1,0)$, $\overrightarrow{E_3} = (0,0,1)$.

Unit vectors $\left\langle \vec{e}_1, \vec{e}_2, \vec{e}_3 \right\rangle$ can be determined from any three markers on the coupling beam surface. If markers A, B, and C are selected, with direction BC parallel to the beam longitudinal axis, $\vec{e}_1$ can be calculated as,

$$\vec{e}_1 = \frac{\overline{BC}}{\left|\overline{BC}\right|} \tag{4-2}$$

Since BA and BC may not be perfectly perpendicular, $\vec{e}_2$ cannot be determined directly from a unit vector in the direction BA. However, $\vec{e}_3$ can be calculated from any two vectors in the *xy* plane as,

$$\vec{e}_3 = \frac{\vec{e}_1 \times \overline{BA}}{\left|\overline{BA}\right|} \tag{4-3}$$

Then, $\vec{e}_2$ can be determined as

$$\vec{e}_2 = \vec{e}_3 \times \vec{e}_1 \tag{4-4}$$

Point B, which is the origin of the xyz coordinate system, must remain constant throughout the test. Thus, the coordinates $\left\langle X_B, Y_B, Z_B \right\rangle$ for the first frame (or first scan), prior to loading, are used in the calculation of coordinates at any frame or scan *i* as follows,

$$\begin{Bmatrix} x_D \\ y_D \\ z_D \end{Bmatrix}_{frame\ i} = \begin{bmatrix} \vec{e}_1 \cdot \vec{E}_1 & \vec{e}_1 \cdot \vec{E}_2 & \vec{e}_1 \cdot \vec{E}_3 \\ \vec{e}_2 \cdot \vec{E}_1 & \vec{e}_2 \cdot \vec{E}_2 & \vec{e}_2 \cdot \vec{E}_3 \\ \vec{e}_3 \cdot \vec{E}_1 & \vec{e}_3 \cdot \vec{E}_2 & \vec{e}_3 \cdot \vec{E}_3 \end{bmatrix}_{frame\ 1} \left(\begin{Bmatrix} X_D \\ Y_D \\ Z_D \end{Bmatrix}_{frame\ i} - \begin{Bmatrix} X_B \\ Y_B \\ Z_B \end{Bmatrix}_{frame\ 1} \right) \tag{4-5}$$

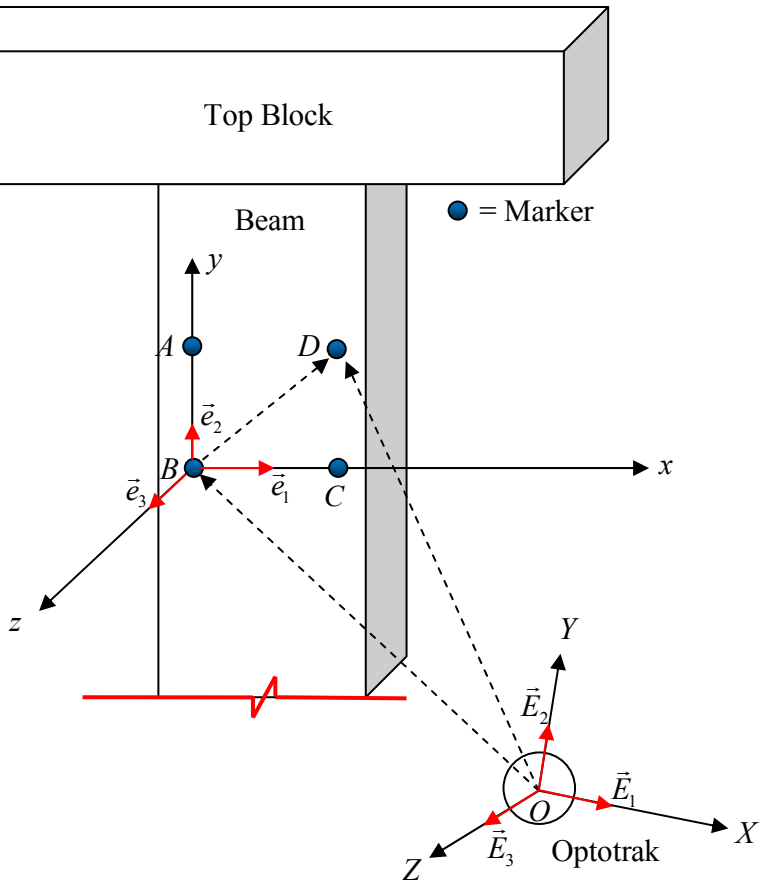

Figure 4.1 Transformation of coordinates of markers

4.1.2 Average Shear Stress

Average shear stress, v, was determined by dividing the applied lateral load, V, recorded from the load cell on the actuator, by the cross-sectional area of the coupling beam, bh, where b and h are the width (thickness) and overall depth of the coupling beam, respectively.

$$v = \frac{V}{bh} \tag{4-6}$$

To allow the comparison of shear stresses between different specimens, and to facilitate stress comparisons with the shear strength equations given in the ACI Building Code, a normalized average shear stress, v_{norm}, was calculated as,

$$v_{norm} = \frac{V}{bh\sqrt{f_c'}} \tag{4-7}$$

where f'_c is the cylinder compressive strength in psi.

4.1.3 Drift

Drift, sometimes referred to as chord rotation, is defined as the ratio of the applied lateral displacement to the length of the coupling beam. Drifts in this study were adjusted to account for the slip and rotations of end blocks, as well as the flexibility of loading fixtures. From Figure 4.2, the adjusted drift can be calculated as,

$$drift = \frac{\Delta}{L} - \left(\frac{\alpha_1 + \alpha_2}{2} \right) \tag{4-8}$$

where Δ is the relative lateral displacement of the top and base blocks, L is the length of the coupling beam, and α_1 and α_2 are the rotations of the top and base blocks, respectively.

Reading from Optotrak markers on the top row (Figure 3.15-3.16), rather than from the actual LVDT, were used to calculate the horizontal movement and rotation of the top block. Figure 4.3 shows a comparison of lateral displacements obtained from LVDT and Optotrak markers for Specimen CB-5. It can be seen that lateral displacements in the pushing direction from both measurements were very close. On the other hand, displacements in the pulling direction were slightly different, which resulted from the flexibility of the loading fixtures under pulling (primarily elongation of the rods passing through the top block).

Another source of flexibility in the test setup was sliding of the base block. The magnitude of this sliding was measured by a potentiometer and Optotrak markers. Results from both measurements were similar in all test specimens.

Rotations of both top and bottom blocks, as well as sliding of the base block and flexibility of the loading fixtures resulted in the difference between predefined and "actual" or adjusted drifts. If not mentioned otherwise, the drift values shown in this thesis are the adjusted drifts. Moreover, drifts are positive in the actuator pushing direction (Figures 3.15 - 3.16).

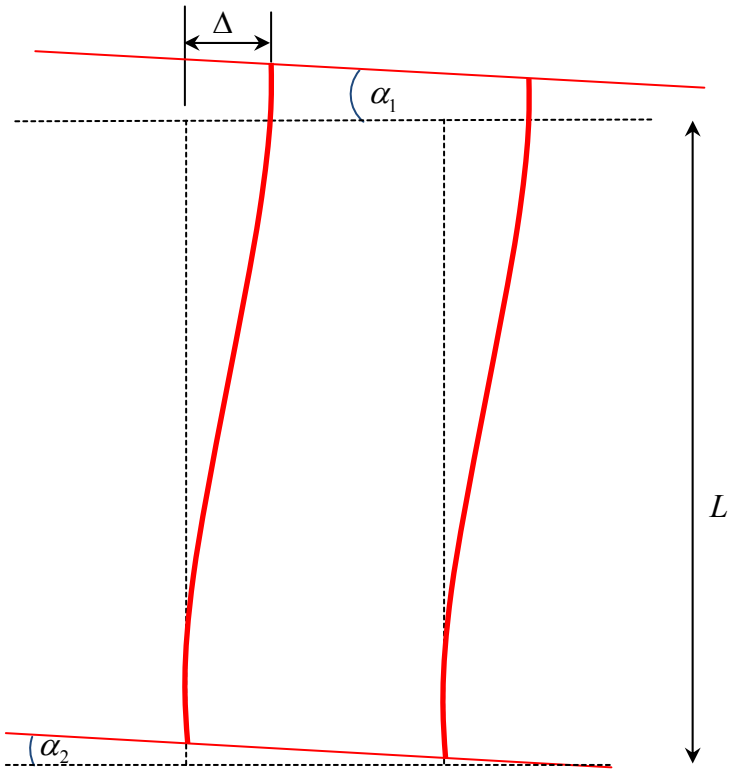

Figure 4.2 Drift calculation accounting for rotations of top and base blocks

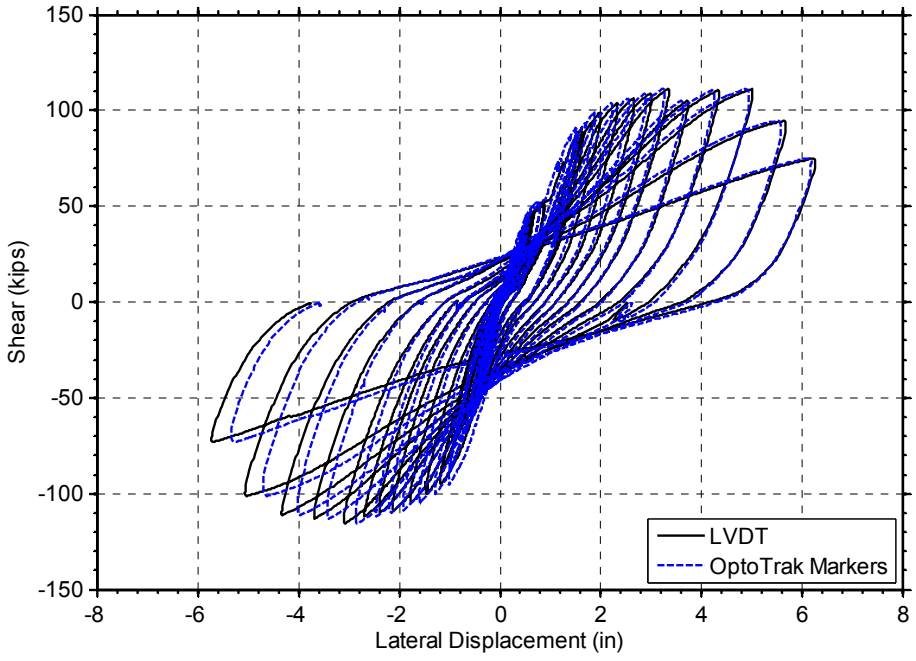

Figure 4.3 Comparison of lateral displacements measured from LVDT and Optotrak

4.1.4 Strains

Average strains in the coupling beams were calculated from the grids of markers attached on the coupling beam, as shown in Figures 3.15-3.16. Each strip of markers contained three and four quadrilateral elements for the coupling beams with an aspect ratio of 3.3 and 2.75, respectively. The coordinates defining the position of the markers based on the Optotrak coordinate system were transformed to a coordinate system defined by the coupling beam vertical plane, as described in Section 4.1.1. With the position of the markers known based on the beam local axes, longitudinal, transverse, and shear strains at various locations could be determined from the coordinates of the four points of each quadrilateral element, as shown in Figure 4.4.

When subjected to stress, each element is distorted as shown in the red lines of Figure 4.4. Points 1, 2, 3, and 4 move to the new positions defined by their horizontal and vertical movements u_1, u_2, u_3, u_4 and v_1, v_2, v_3, v_4, respectively. Transverse strain (ε_x), longitudinal strain (ε_y), and shear strain (γ_{xy}) can be calculated from

$$\varepsilon_x = \frac{1}{2}\left(\frac{u_3 - u_2}{\Delta x_{23}} + \frac{u_4 - u_1}{\Delta x_{14}}\right) \tag{4-9}$$

$$\varepsilon_y = \frac{1}{2}\left(\frac{v_1 - v_2}{\Delta y_{12}} + \frac{v_4 - v_3}{\Delta x_{43}}\right) \tag{4-10}$$

$$\begin{aligned}\gamma_{xy} &= \frac{1}{2}(\alpha_1 + \alpha_2) + \frac{1}{2}(\alpha_3 + \alpha_4) \\ &= \frac{1}{2}\left(\frac{u_1 - u_2}{\Delta y_{12}} + \frac{u_4 - u_3}{\Delta y_{43}}\right) + \frac{1}{2}\left(\frac{v_3 - v_2}{\Delta x_{23}} + \frac{v_4 - v_1}{\Delta x_{14}}\right)\end{aligned} \tag{4-11}$$

Where $(\Delta y_{12})_{frame\,1} = |y_1 - y_2|_{frame\,1}$

$(\Delta y_{43})_{frame\,1} = |y_4 - y_3|_{frame\,1}$

$(\Delta x_{14})_{frame\,1} = |x_4 - x_1|_{frame\,1}$

$(\Delta x_{23}) = |x_3 - x_2|_{frame\,1}$

Frame 1 refers to the coordinates prior to loading (the gauge length does not change).

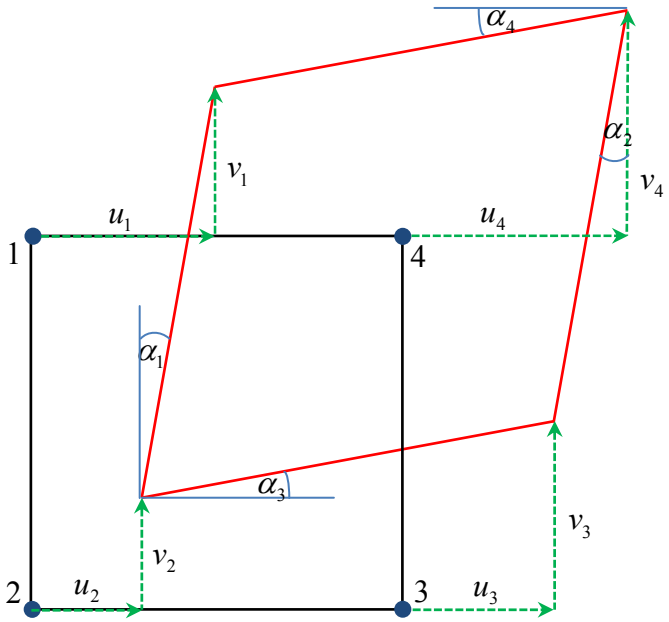

Figure 4.4 Deformation of a quadrilateral element used to calculate average strains

Once the state of strain is defined, the principal strains (ε_1 and ε_2) and the corresponding angle (θ) can be determined as,

$$\varepsilon_1 = \frac{1}{2}\left(\varepsilon_x + \varepsilon_y\right) + \frac{1}{2}\sqrt{\left(\varepsilon_x - \varepsilon_y\right)^2 + \gamma_{xy}^2} \tag{4-12}$$

$$\varepsilon_1 = \frac{1}{2}\left(\varepsilon_x + \varepsilon_y\right) - \frac{1}{2}\sqrt{\left(\varepsilon_x - \varepsilon_y\right)^2 + \gamma_{xy}^2} \tag{4-13}$$

$$\theta = \frac{1}{2}\tan^{-1}\left(\frac{\gamma_{xy}}{\varepsilon_x - \varepsilon_y}\right) \tag{4-14}$$

4.2 LOAD VERSUS DRIFT RESPONSES AND DAMAGE PROGRESSION

Overall behavior of the coupling beams was evaluated through the average shear stress versus drift hysteresis response, as well as damage progress throughout the tests. Table 4.1 summarizes the key results of the coupling beam tests, such as maximum shear force (V_u), maximum shear stress (v_u), peak normalized shear stress, and drift capacity.

The applied loads, target drifts, and adjusted drifts for all test specimens are given in Tables B.1-B.6 in Appendix B.

Table 4.1 Summary of test results

Specimen	V_u (kips)	v_u (psi)	$v_u / \sqrt{f_c'}$ (psi)	Drift capacity * (%)	
				Positive	Negative
1	129	897	10.7	5.6	5.2
2	116	803	8.7	5.3	3.9
3	115	959	10.1	5.5	4.5
4	103	714	7.6	3.0	2.6
5	116	965	9.7	6.9	6.8
6	126	877	8.9	6.5	5.7

* Largest drift level before a strength loss of 20% or more occurred ($V \geq 0.8V_u$)

4.2.1 Specimen CB-1 (HPFRC with $\ell_n/h = 2.75$ and diagonal reinforcement, and $f_c' = 7.2$ ksi)

Specimen CB-1 exhibited a stable hysteresis response under high shear and deformation demand (Figure 4.5). The hysteresis loops were relatively wide with minor pinching, showing good energy dissipation. This specimen was first loaded in the west direction, corresponding to the actuator pushing direction. The maximum force applied to the specimen was 131 kips, which corresponded to shear stress level of 910 psi. Given the cylinder concrete compressive strength for this specimen (7200 psi), the maximum applied shear stress was equivalent to $10.2\sqrt{f_c'}$ (psi). This maximum shear occurred at 3.8% drift in the negative loading direction. Specimen CB-1 remained elastic up to approximately 0.6% and 0.7% drift in the positive and negative loading direction, respectively, when yielding of reinforcing bars was first detected at the beam-wall interfaces, as shown in Figure 4.6. The specimen retained 80% of the peak shear force until 5.6% and 5.2% drift in the positive and negative loading direction, respectively. Specimen CB-1 failed during the loading cycle to 7.4% drift, when one of the main longitudinal bars ruptured. Figure 4.6 shows key limit states superimposed to the shear force versus drift response for Specimen CB-1.

Some pinching of the stress versus drift response could not be prevented through the use of steel fibers because this reinforcement does not provide any meaningful resistance against crack closing. However, the fact that diagonal cracks remained narrow because of the increased shear resistance and better cracking control provided by the HPFRC material greatly limited the degree of pinching in the shear force versus drift hysteresis behavior.

Flexural cracks were observed on the tension sides at both ends of the beam during the first few cycles of loading. The first diagonal or web-shear cracks were observed at approximately 0.45% drift in the positive loading direction. Multiple diagonal cracks formed as the test continued up to 1.4% drift in both loading directions. No additional diagonal cracks formed beyond this drift level. At approximately 2.7% drift in the positive loading direction, flexural cracks formed at sections where the dowel bars were terminated. Damage was still minimal at 3.5% drift in the positive loading direction (Figure 4.7(a)). Flexural cracks became wider in the plastic hinge regions as applied displacements increased, indicating flexure dominated the behavior of the coupling beam (Figure 4.7(b)). These wide flexural cracks significantly reduced shear transfer through aggregate interlock, which required most the shear to be transferred along these cracks by tension and compression in the diagonal bars and dowel action and shear friction provided by the longitudinal reinforcement. Ultimately, these flexural cracks created large continuous planes along which significant sliding displacements took place, leading to significant loss of specimen stiffness and strength. The critical flexural cracks at both ends of the beam at 5.2% drift in the positive loading direction are shown in Figure 4.8.

Diagonal reinforcement was provided to resist approximately 1/4 of the expected shear demand. The high shear capacity, large drift capacity, and narrow diagonal cracks indicate that HPFRC and transverse reinforcement were efficient in resisting high shear even at large drifts. Moreover, the special column-type confinement at the ends of the beam, together with HPFRC, provided sufficient confinement to ensure large rotation capacity and effectively resist the outward thrust generated by the bent diagonal reinforcement near the beam-wall interface. The results from this test therefore indicate that the increase in shear capacity and confinement provided by the HPFRC material, combined with the special column-type transverse reinforcement at the beam ends,

allowed the specimen to exhibited a flexure-dominated behavior with negligible shear distress other than the shear sliding displacements that occurred near the end of the test along the critical flexural cracks.

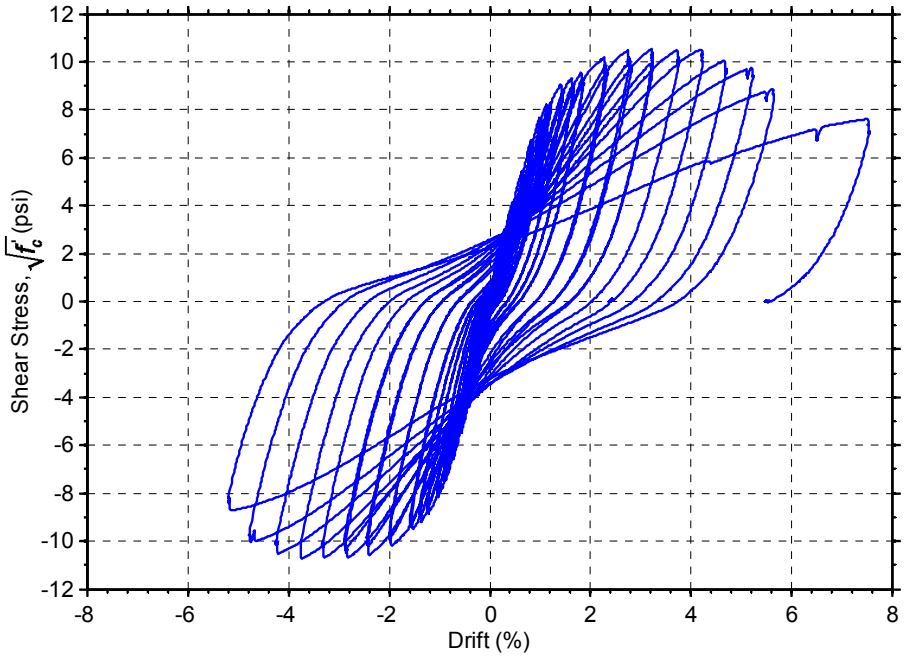

Figure 4.5 Average shear stress versus drift response of Specimen CB-1

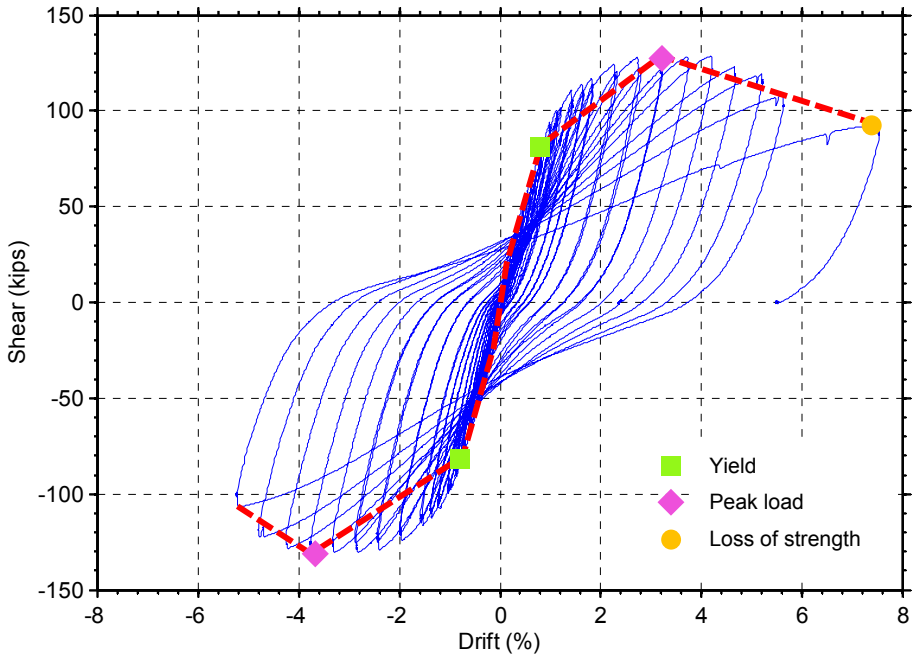

Figure 4.6 Shear force versus drift response and selected limit states for Specimen CB-1

(a) (b)

Figure 4.7 Damage progress in Specimen CB-1 at (a) 3.2% and (b) 5.2% drift

(a) (b)

Figure 4.8 Damage on the back side of Specimen CB-1 at 5.2% drift at (a) the bottom end and (b) the top end of the beam

4.2.2 Specimen CB-2 (HPFRC with $\ell_n/h = 2.75$ and diagonal reinforcement, and $f_c' = 8.6$ ksi)

The shear stress versus drift response of Specimen CB-2, shown in Figure 4.9, indicates stable behavior and good energy dissipation. Longitudinal reinforcement for this specimen was reduced by 23%, while concrete compressive strength was increased by nearly 20% compared to those of Specimen CB-1. Transverse reinforcement ratio was 0.56%, which was 24% greater than that of Specimen CB-1. This specimen was first pushed in the west direction, which was designated as the positive loading direction.

Specimen CB-2 sustained a maximum load of 116 kips at approximately 3.5% drift in the negative direction, which was equivalent to a shear stress of 803 psi or $8.7\sqrt{f_c'}$ (psi), based on the cylinder concrete compressive strength of 8600 psi. A stable hysteresis response was observed up to 5.3% drift in the positive loading direction. The beam failed during the second half cycle to 4.8% drift in the negative loading direction, which was evidenced by a significant loss of strength. It is worth mentioning that the maximum negative drift attained prior to this cycle was 3.9%. No fracture of reinforcement was observed at failure of the beam. The shear force versus drift response for Specimen CB-2, along with marks indicating various limit states, is shown in Figure 4.10.

Similar to the Specimen CB-1, multiple narrow diagonal cracks developed in this specimen throughout the test. As shown in Figure 4.10, the specimen remained elastic up to 0.7% drift in both positive and negative loading directions, where diagonal cracks and first yielding of longitudinal reinforcement were first observed. Additional diagonal cracks formed up to 2% drift, which remained relatively narrow for the remainder of the test. When pushed to approximately 1.6% drift (positive loading direction), flexural cracks started to form at the bottom of the beam, near the section where the U-shaped dowel bars were terminated. These cracks became continuous at approximately 2% drift. Similar flexural cracks were observed at the top of the beam at approximately 2.6% drift. At 2.8% drift in the positive loading direction, the damage associated with these through flexural cracks could be considered moderate (approximately 0.04 in.), as shown in Figure 4.11(a). The further opening of these flexural cracks at both ends of the beam led to the development of a sliding shear failure plane (Figure 4.11(b)) and ultimately, the termination of the test. Close-up photos of damage at both ends of the specimen at 5.3% drift in the positive loading direction are shown in Figure 4.12.

In Specimen CB-2, diagonal steel was provided such as to resist approximately 1/3 of the expected maximum shear force applied to the specimen. Thus, large shear forces had to be resisted by the HPFRC and stirrups. The stable hysteresis response, minor shear-related damage in the middle region of the beam, and good drift capacity are a clear indication of the ability of the HPFRC material to contribute to shear strength of the coupling beam. As in Specimen CB-1, the special column-type confinement, together with the HPFRC material, provided excellent confinement at the beam ends to sustain the large inelastic rotation demands and effectively resist the outward thrust at the bent of the diagonal reinforcement near the ends of the beam.

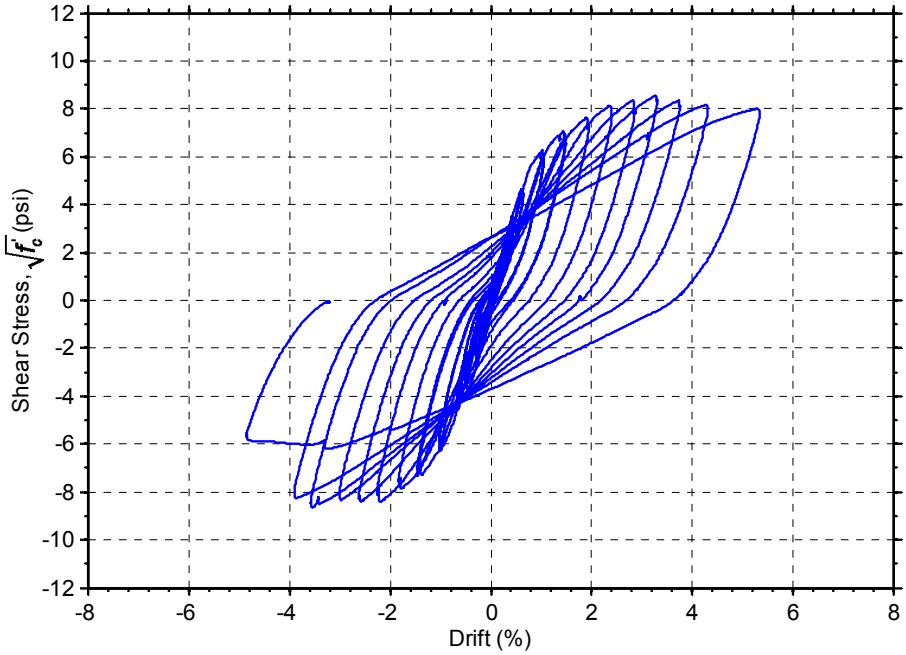

Figure 4.9 Average shear stress versus drift response of Specimen CB-2

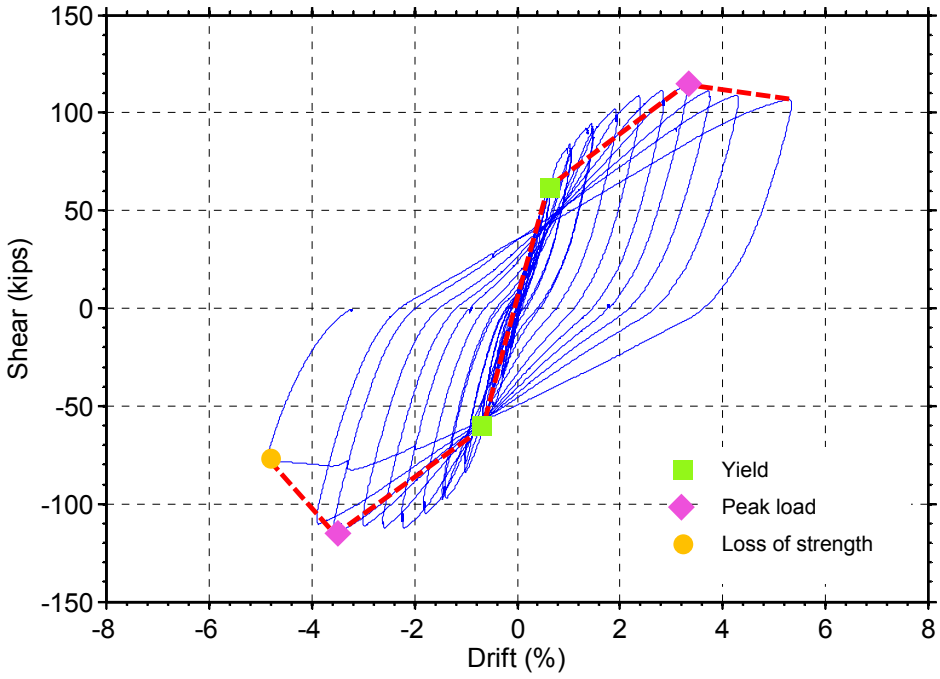

Figure 4.10 Shear force versus drift response and selected limit states for Specimen CB-2

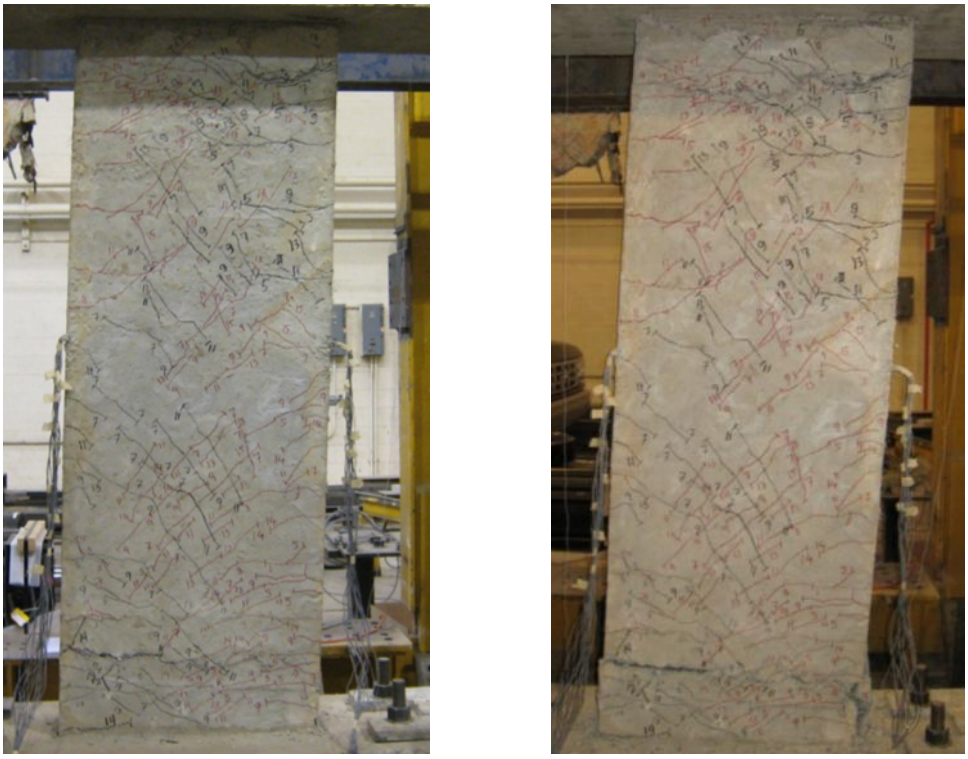

(a) (b)

Figure 4.11 Damage in the positive loading direction in Specimen CB-2 at (a) 2.8% drift and (b) 5.3% drift

(a) (b)

Figure 4.12 Damage at 5.3% drift in the positive loading direction in Specimen CB-2 at (a) the bottom and (b) the top end of the beam

4.2.3 Specimen CB-3 (HPFRC with $\ell_n/h = 3.3$ and diagonal reinforcement, and $f_c' = 8.9$ ksi)

A larger flexural reinforcement ratio compared to that in Specimens CB-1 and CB-2 was used in Specimen CB-3, which had a higher aspect ratio, in order to ensure a comparable shear stress demand. Specimen CB-3 was first loaded in the pulling direction, which was designated as the negative loading direction. The maximum load imposed on this specimen was 115 kips, which was equivalent to an average shear stress of 959 psi or $10.2\sqrt{f_c'}$ (psi), measured at 3.3% drift in the negative loading direction, as shown in Figure 4.13. The specimen remained elastic up to approximately 0.9% and 1% drift in the negative and positive loading direction, respectively (Figure 4.14). This specimen exhibited stable and wide hysteresis loops, with good strength and stiffness retention up to 5.5% drift. As the specimen was displaced beyond 3% drift, the axial force generated due to elongation of the coupling beam became close to the capacity of the load cells attached to the vertical steel arms. Thus, the bolts connecting the steel links and the top block were loosened in order to reduce the generated axial force and avoid damage to the load cells. This was the reason for the drop in load observed at 3.6% drift in the negative loading direction. Damage from diagonal cracks was minor throughout the test. Diagonal cracking began during the cycle to 0.9% drift in the negative loading direction. Multiple diagonal cracks developed during the early cycles, up to 2.4% drift in the positive direction. At 3% drift in the positive loading direction, flexural damage started localizing at the sections where either the U-shaped or the straight dowel bars were terminated. These flexural cracks became wider with each increment of displacement. Failure of the coupling beam occurred during the first half cycle to 5.7% drift due to the sliding along shear planes created by through depth flexural cracks, along with the fracture of one diagonal bar. Figure 4.15 shows the state of damage at 3.4% and 5.0% drifts. It can be seen that none of the diagonal cracks that developed over the beam span opened widely throughout the test despite the high shear stresses imposed on the specimen. Flexural cracks within the plastic hinge regions at the end of the test are shown in Figure 4.16.

The contribution of diagonal steel to shear strength was expected to be approximately 25% of the peak shear demand due to the very shallow angle between the

diagonal bars and the beam longitudinal axis, the remaining shear strength being provided primarily by the HPFRC material and the stirrups. Despite the high shear demand, the beam exhibited stable behavior without appreciable pinching in the hysteresis loops. Similar to Specimens CB-1 and CB-2, the special column-type confinement and the HPFRC material were effective in ensuring adequate plastic hinge rotation capacity.

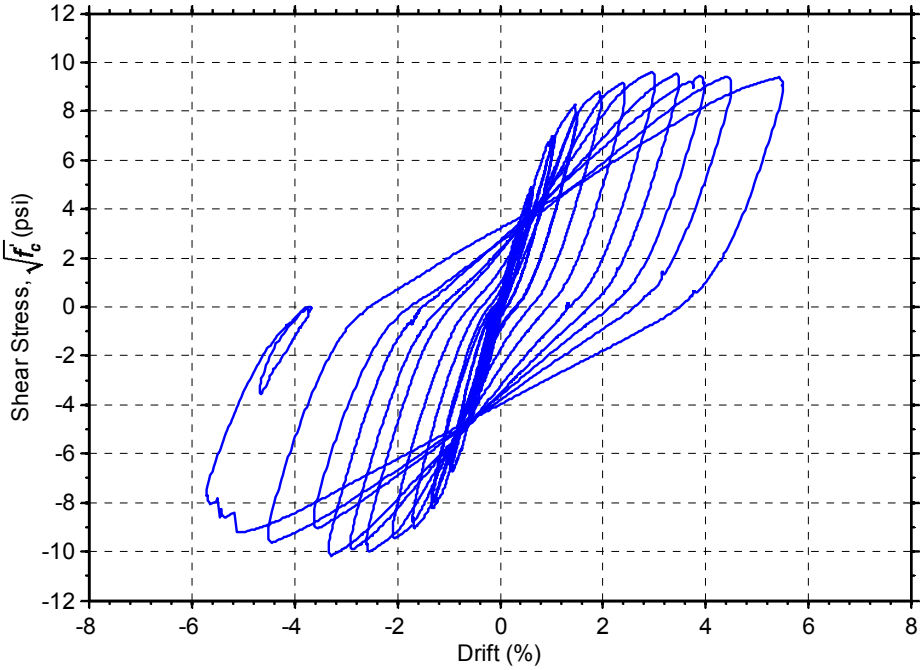

Figure 4.13 Average shear stress versus drift response of Specimen CB-3

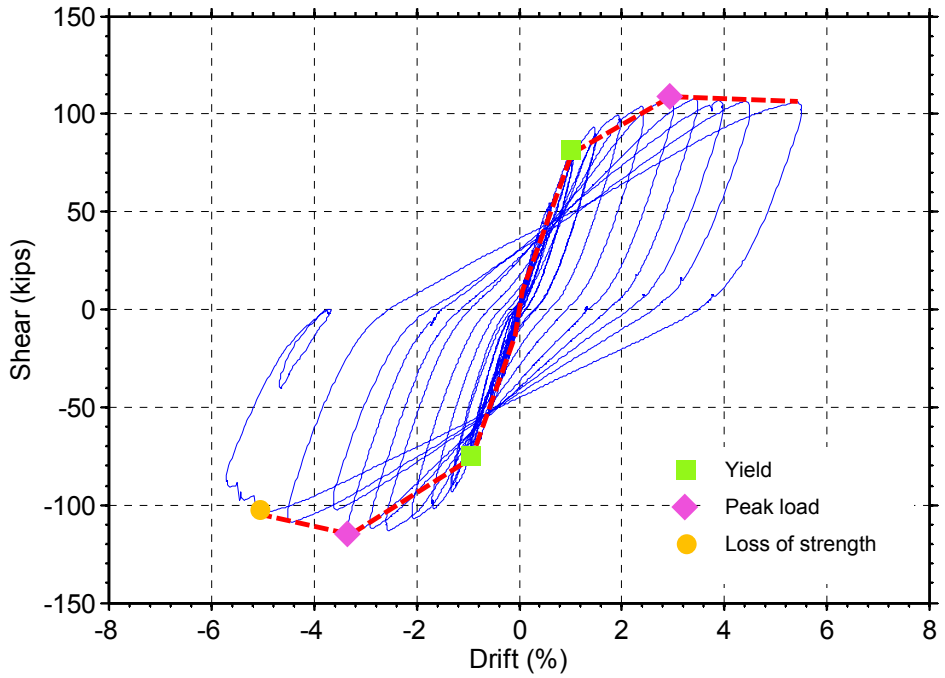

Figure 4.14 Shear force versus drift response and selected limit stages for Specimen CB-3

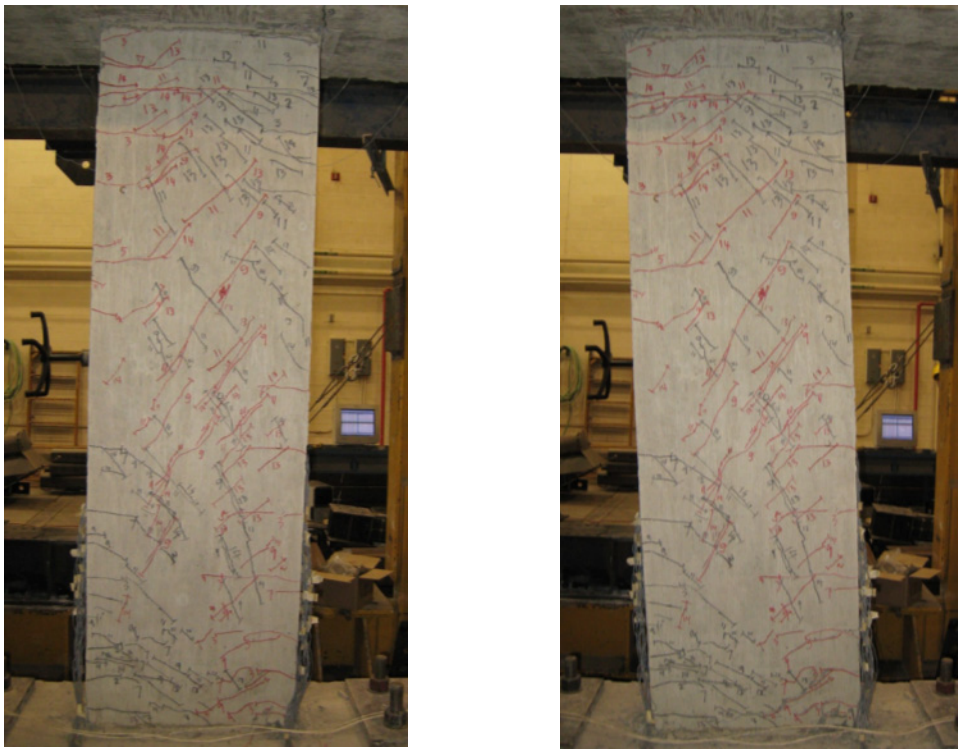

(a) (b)

Figure 4.15 Damage in Speciemen CB-3 at (a) 3.4% drift in the positive loading direction and (b) at 5% drift in the negative loading direction

(a) (b)

Figure 4.16 Damage in Specimen CB-3 at the end of the test in (a) bottom plastic hinge and (b) top plastic hinge

4.2.4 Specimen CB-4 (RC with $\ell_n/h = 2.75$ and diagonal reinforcement, and $f_c' = 9.0$ ksi)

Specimen CB-4 was constructed with high strength concrete without steel fibers. Reinforcement detailing for this specimen was identical to that of Specimen CB-2. Concrete cylinder strength was 8.9 ksi, which was close to the cylinder compressive strength of the HPFRC material used in Specimen CB-2. This specimen exhibited stable hysteresis loops during the early drift cycles, as shown in Figure 4.17. However, drift capacity of this RC specimen was only approximately 3% drift and 2.6% drift in the positive and negative loading direction, respectively, which was slightly above half that of Specimen CB-2.

Specimen CB-4 was first pushed in the positive loading direction. It remained elastic up to approximately 0.5% and 0.7% drift in the positive and negative loading direction, respectively (Figure 4.18). The maximum applied shear of 103 kips was reached at 2.6% drift in the positive loading direction, which corresponded to an average shear stress of 714 psi or $7.53\sqrt{f_c'}$ (psi). This maximum shear was 13% less than that for Specimen CB-2.

Initially, damage progress in this specimen was similar to that observed in the HPFRC specimens. Flexural cracks developed during the early cycles and diagonal

cracks first appeared at midheight of the middle third of the beam at approximately 0.2% drift. Multiple diagonal cracks developed during the cycles up to 1.3% drift. This damage pattern was similar to that of Specimen CB-2, but developed at earlier drift cycles and with wider crack spacing, which proved the effectiveness of the HPFRC material to deform more uniformly through a dense array of narrow cracks, resist higher diagonal tension, and increase coupling beam drift capacity. At approximately 2.6% drift in the positive loading direction, significant concrete crushing and spalling at the beam bottom end was observed, as well as flexural damage localization at the end of the U-shaped dowel bars. During the second half of the last cycle, severe flexural damage resulted in a significant loss of strength, which led to the termination of the test. No fracture of reinforcing bars was observed. Figure 4.19 shows the damage states at 2.6% and 3.7% drifts in the positive loading direction.

Despite a limited drift capacity compared to Specimen CB-2, no sign of shear-related damage in the middle third of the beam was observed. However, the confinement provided by the special column-type confinement was not sufficient to preserve the integrity of the concrete core, leading to significant concrete degradation, as shown in Figure 4.20. It should be emphasized that diagonal reinforcement in this specimen was only expected to resist approximately 1/3 of the peak shear force, which led to a much higher shear demand on the concrete compared to that expected in diagonally reinforced coupling beams designed according to the ACI Building Code (ACI Committee 318, 2011).

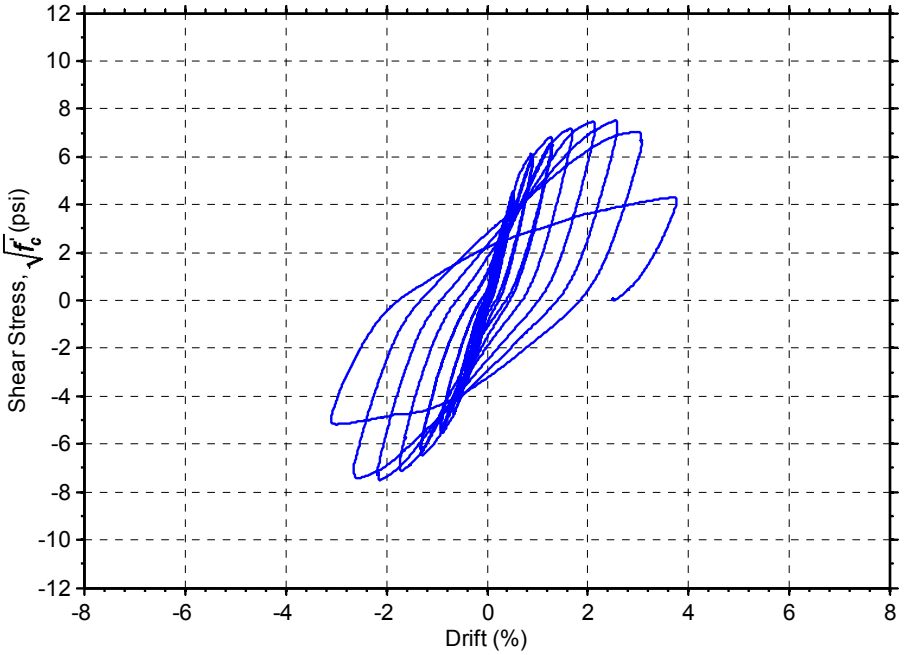

Figure 4.17 Average shear stress versus drift response of Specimen CB-4

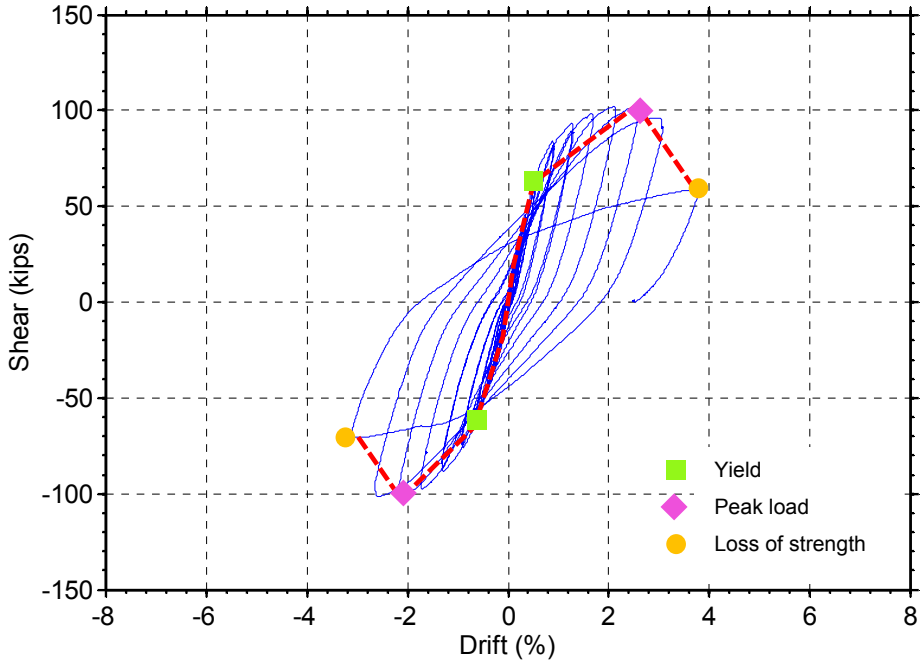

Figure 4.18 Shear force versus drift response and selected limit states for Specimen CB-4

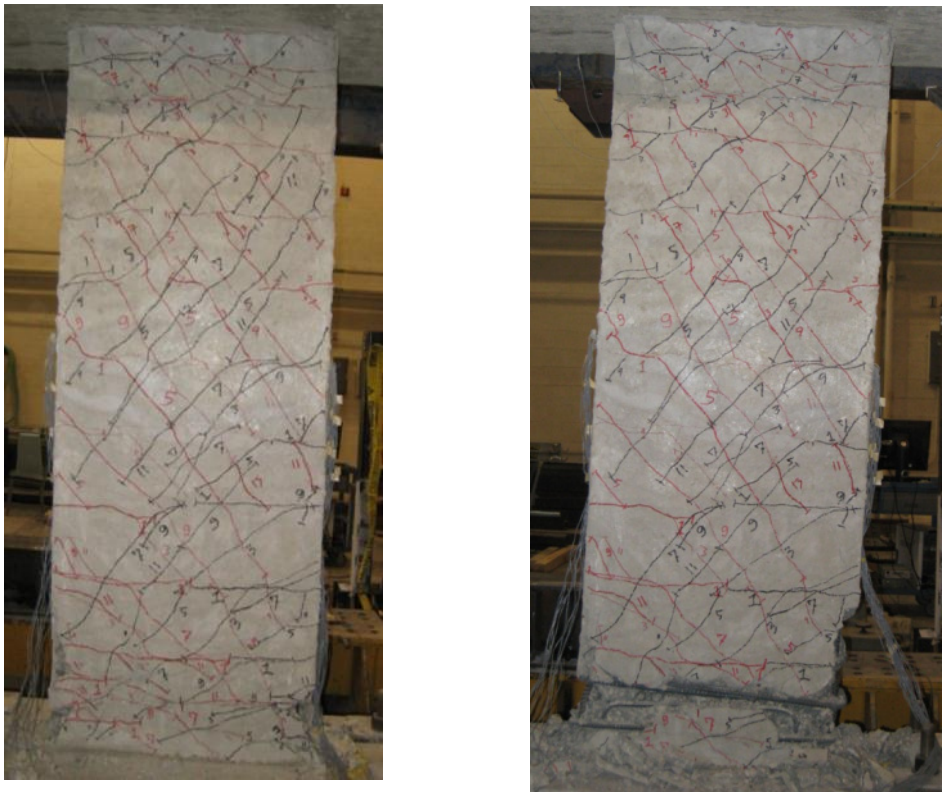

(a) (b)

Figure 4.19 State of damage in Specimen CB-4 in the positive loading direction at (a) 2.6% and (b) 3.7% drift

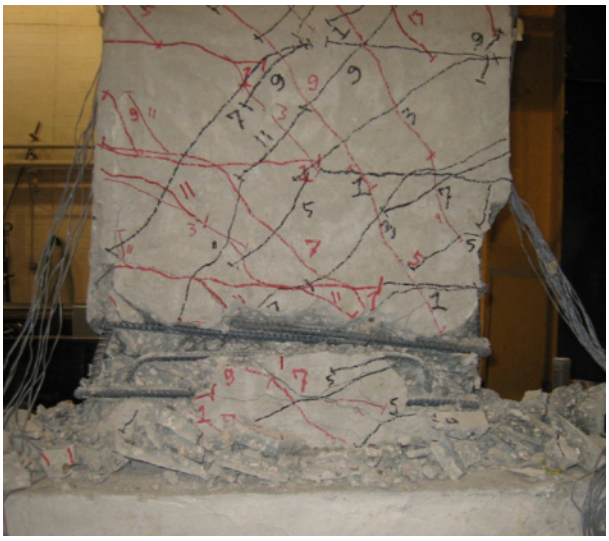

Figure 4.20 Damage in Specimen CB-4 at the bottom end of the beam at 3.7 % drift

4.2.5 Specimen CB-5 (HPFRC with $\ell_n/h = 3.3$ and no diagonal reinforcement, and $f_c' = 9.9$ ksi)

Without diagonal reinforcement, the shear stress demand for this specimen was resisted primarily by the HPFRC and stirrups, with a large portion of the applied shear expected to be carried by truss action. Therefore, the transverse reinforcement ratio in this specimen was almost twice that of the other specimens. Despite the absence of diagonal reinforcement, this coupling beam exhibited stable hysteresis response with large drift capacity, as shown in Figure 4.21. The specimen was first loaded in the positive loading direction (actuator pushing direction) and remained elastic up to approximately 0.9% drift in both loading directions (Figure 4.22), where yielding of longitudinal reinforcement in the bottom beam-wall interface was detected. Specimen CB-5 sustained a peak shear of 116 kips, which was equivalent to a shear stress of 965 psi or $9.7\sqrt{f_c'}$ (psi) at 4.2% drift in the negative loading direction. The response was stable up to 6.8% drift in both positive and negative directions. At this drift level, shear strength had decreased by 9% and 14% in the positive and negative loading directions, respectively. The coupling beam failed during the cycle to 8% drift, during which a significant loss of strength occurred. No fracture of reinforcement was observed during the test.

Diagonal cracks were first observed at 0.6% drift in the positive loading direction. As the test continued, more diagonal cracks formed, but their widths remained narrow. It should be noted that diagonal cracks in this specimen were denser along the beam span compared to the HPFRC specimens with diagonal bars. This was due to the fact that the absence of diagonal bars resulted in a higher shear carried by the stirrups and HPFRC material. However, only minor damage was observed up to approximately 4% drift (Figure 4.23). This damage confirmed the efficiency of HPFRC in controlling resisting shear.

Flexural cracks were evident in the plastic hinge regions at both ends of the beam at approximately 5% drift. The joining of several flexural cracks in the plastic hinge region led to planes along which sliding displacements occurred (Figure 4.23), which governed the beam behavior and led to the ultimate failure of the specimen. Close-up

views of flexural cracks within the plastic hinge regions at both ends of the beam are shown in Figure 4.24.

The stable hysteresis response with large drift capacity of Specimen CB-5 shows that diagonal reinforcement can be eliminated in relatively slender HPFRC coupling beams, leading to a substantially simpler coupling beam design.

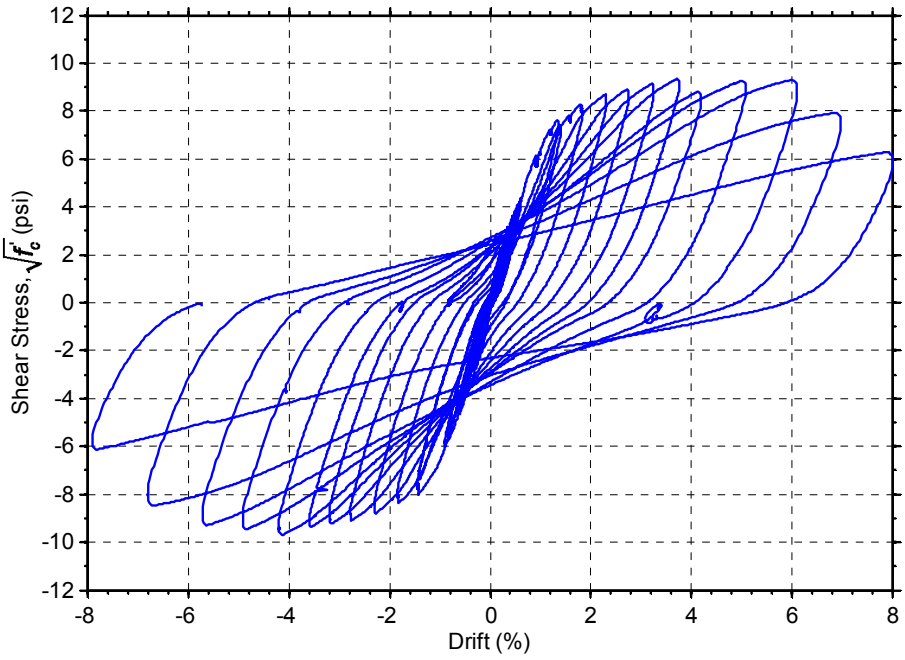

Figure 4.21 Average shear stress versus drift response of Specimen CB-5

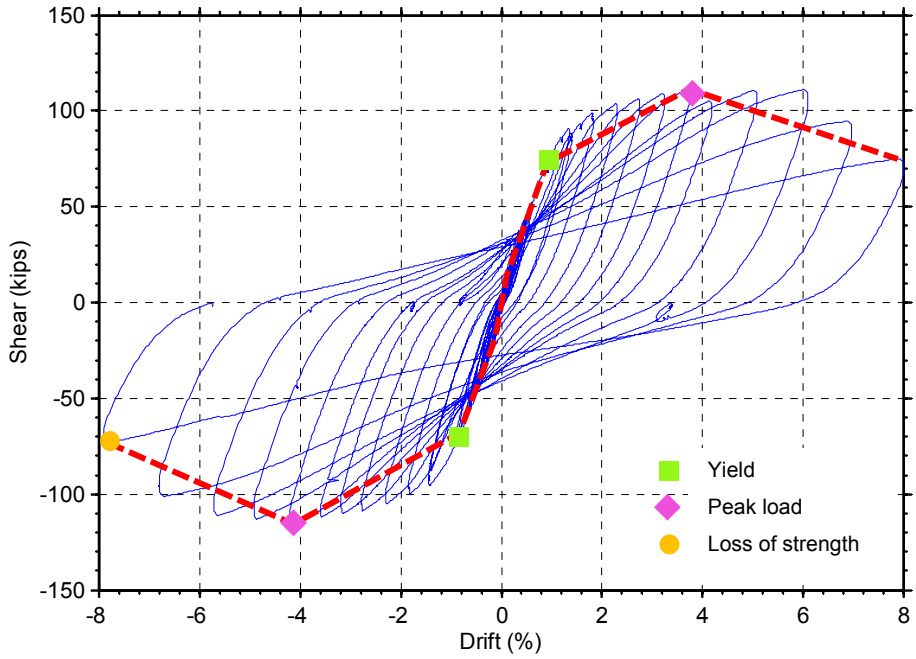

Figure 4.22 Shear force versus drift response and selected limit states for Specimen CB-5

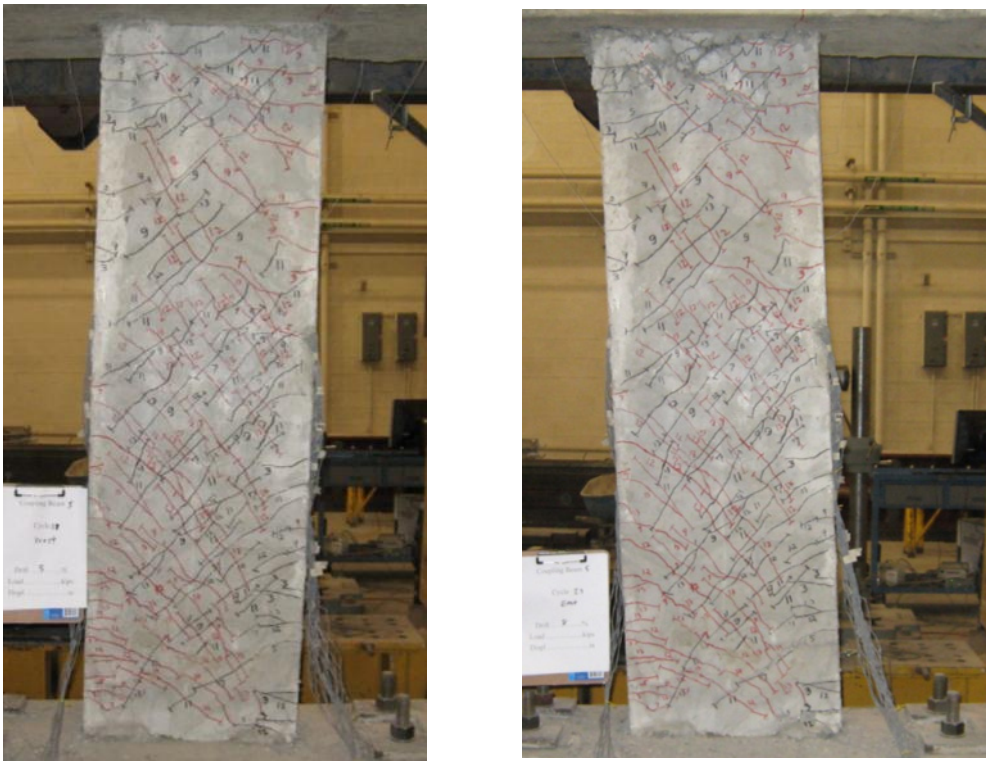

Figure 4.23 Damage at 4% drift (left) and 6.7% drift (right) in Specimen CB-5

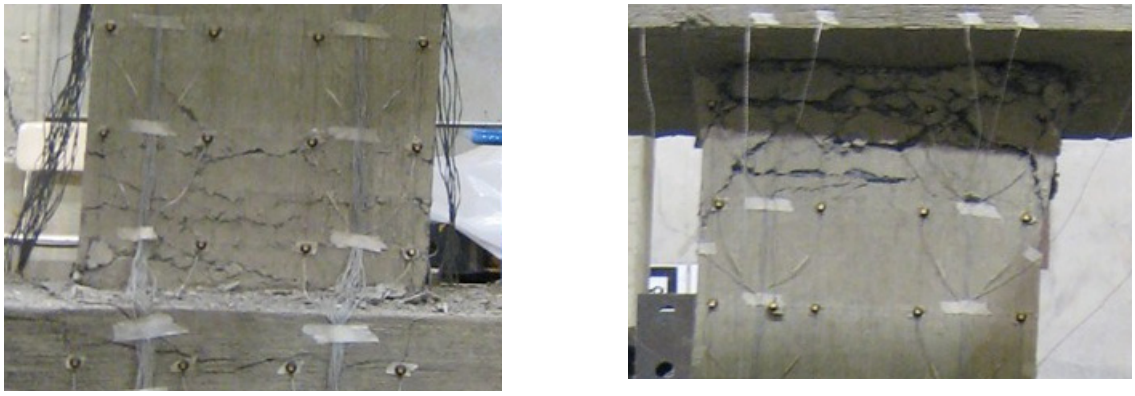

(a) (b)

Figure 4.24 Damage in (a) bottom and (b) top plastic hinge of Specimen CB-5

4.2.6 Specimen CB-6 (HPFRC with $\ell_n/h = 2.75$ and no diagonal reinforcement, and $f_c' = 9.8$ ksi)

Despite some pinching in the hysteresis behavior of Specimen CB-6 (Figure 4.25), the response of Specimen CB-6 was stable up to large drift levels. Similar to Specimen CB-5, the shear applied to this coupling beam was to be carried primarily by stirrups and the HPFRC material. Thus, the transverse reinforcement ratio was kept the same as that used in Specimen CB-5.

Specimen CB-6 behaved elastically up to 0.9% drift in both positive and negative loading directions, as shown in Figure 4.26. At this drift level, yielding of longitudinal reinforcement was first detected at the bottom beam-wall interface. The maximum shear stress of $8.9\sqrt{f_c'}$ (psi) was imposed at 4.3% drift in the positive loading direction. The hysteresis loops were slightly narrower compared to those of Specimen CB-5, which was expected due to the lesser aspect ratio, but the specimen still showed good energy dissipation. Specimen CB-6 was able to maintain its strength up to approximately 5% drift. During the following cycle at 6.5% and 5.7% drift the peak shear decreased by 12% and 8% in the positive and negative loading directions, respectively. In the last loading cycle (7.4%), the maximum applied shear dropped by almost 30% of the peak shear due to the fracture of two longitudinal bars at the bottom end of the beam, resulting in the

termination of the test. The drift capacity of this specimen was approximately 6.5%, which is similar to that of Specimen CB-5.

As in Specimen CB-5, multiple narrow diagonal cracks were observed, which indicated that stirrups and HPFRC were effective in resisting the applied shear despite the lack of diagonal reinforcement. Diagonal cracks were first observed at approximately 0.6% drift in the positive loading direction and continued to develop up to 1.8% drift. Similar to Specimen CB-5, only minor damage had occurred by 3% drift. At around 3.7% drift, concrete crushing and spalling was also observed at the bottom end of the beam. Flexural cracks at the end of the coupling beam led to a sliding shear plane at the bottom beam-wall interface at around 4.3% drift. Ultimately, failure occurred during the cycle at 7% drift due to reinforcing bar fracture at the sliding shear plane at the bottom end of the specimen. Beam damage at 3.2 and 6.5% drift can be seen in Figure 4.27, while Figure 4.28 illustrates the concrete crushing and spalling near the bottom beam-wall interface after the test (after removal of loosed concrete).

Similar to Specimen CB-5, Specimen CB-6 was able to sustain shear demand close to the upper limit in the ACI Code (ACI Committee 318, 2011) without diagonal reinforcement. Despite some pinching in the hysteresis loops, the overall behavior was stable with large drift capacity. This is further evidence of the possibility of eliminating diagonal reinforcement in relatively slender coupling beams through the use of an HPFRC material.

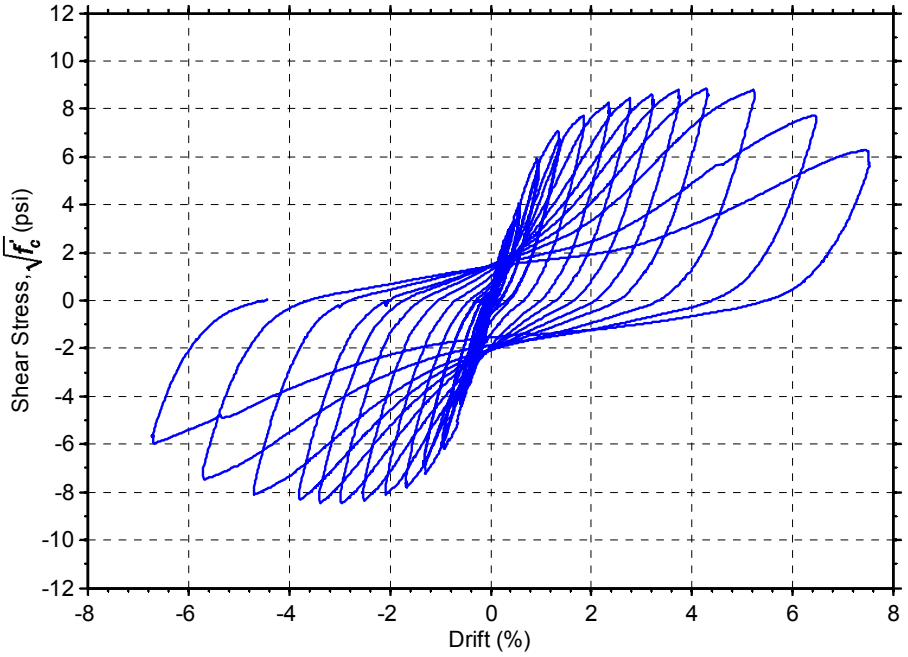

Figure 4.25 Average shear stress versus drift response of Specimen CB-6

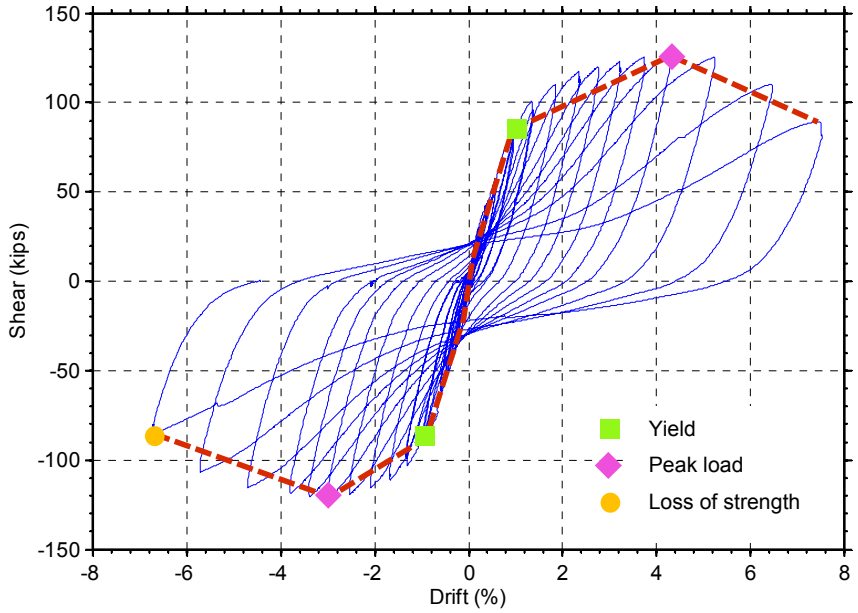

Figure 4.26 Shear force versus drift response and selected limit states for Specimen CB-6

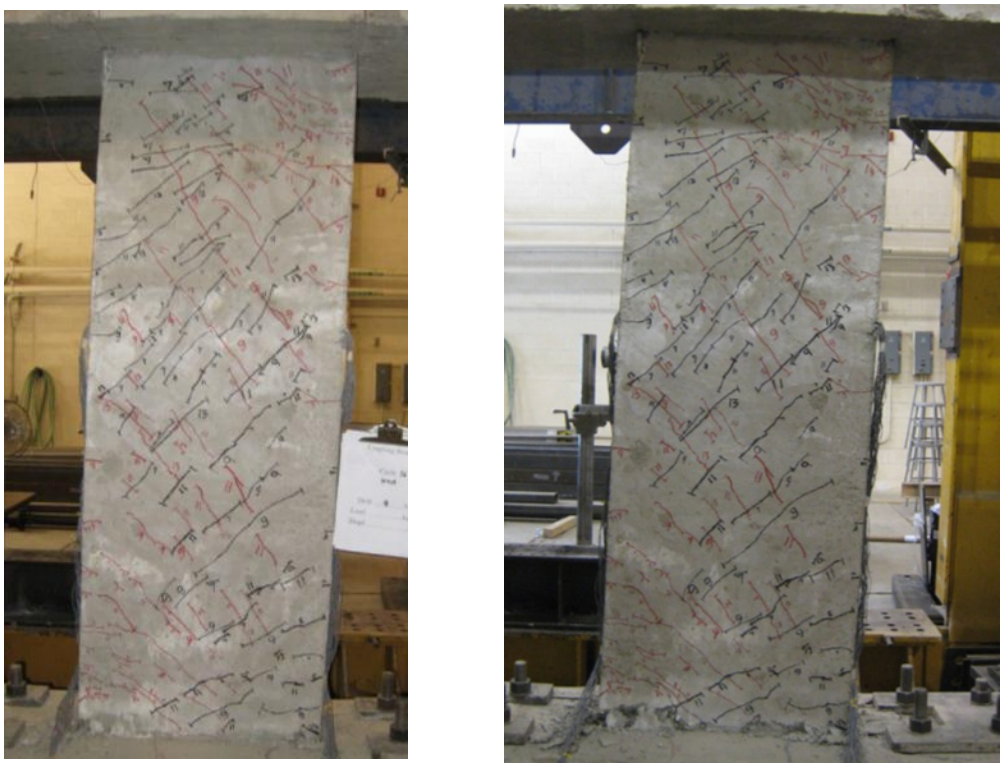

(a) (b)

Figure 4.27 Damage states in the positive loading direction at (a) 3.2% drift (b) 6.5% drift for Specimen CB-6

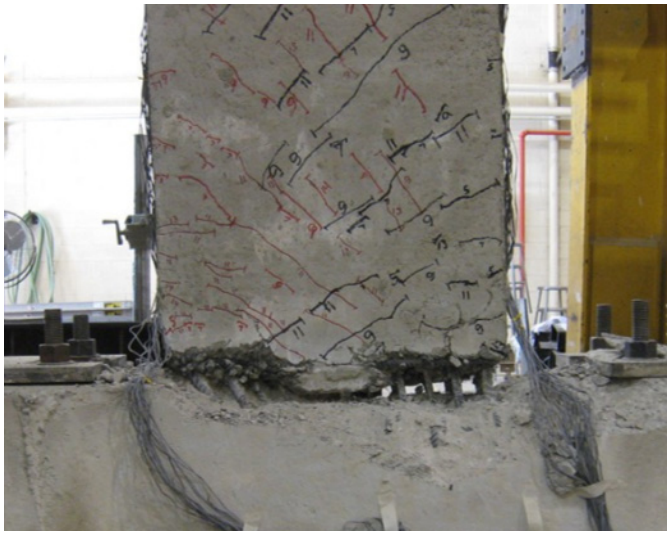

Figure 4.28 Damage at the bottom beam at the end of the test in Specimen CB-6

4.2.7 Summary of Test Observations

The experimental results support the potential of using HPFRC as a means to substantially simplify the reinforcement detailing in coupling beams with aspect ratio on the order of 3. Test results also shows that elimination of diagonal bars by using HPFRC is possible while maintaining large drift capacity. In all tests, all HPFRC coupling beams sustained large shear stresses, close to the upper limit in ACI 318-11, with good drift and energy dissipation capacity. Steel fibers limited the growth of diagonal or inclined cracks and contributed directly to transferring tensile stresses across cracks and enhancing aggregate interlock. All HPFRC specimens showed negligible shear-related damage. The special column-type bar confinement, combined with the use of an HPFRC material, allowed concrete integrity to be maintained under large inelastic rotations. This confinement was required only at the beam ends, within approximately *h/2* from the beam-wall interface, where *h* is the depth of the coupling beam.

A summary of damage observed at first flexural yielding, peak load, and final stage of the test is given in Table 4.2.

Table 4.2 Damage description at various test states

Specimen	Damage at yielding	Damage at peak load	Damage at loss of strength
CB-1	yielding at 0.7% drift; minor inclined cracks (less than 0.004 in.) at the top and bottom 1/3 of the beam; yielding of longitudinal bars at the bottom end	peak load at -3.7% drift; moderate flexural cracks (larger than 0.04 in.) near both ends of the beam; a host of minor diagonal cracks	loss strength at 7.4% drift; large flexural cracks at both ends of the beam; concrete spalling; main longitudinal rebar fracture
CB-2	yielding at 0.6% drift; minor inclined cracks (less than 0.004 in.) at beam mid-height; yielding of longitudinal bars at the bottom end	peak load at -3.6% drift; major flexural cracks (0.08 in.) within plastic hinge region; a host of minor diagonal cracks	loss strength at -4.8% drift; large flexural cracks at both ends of the beam; concrete spalling; no rebar fracture
CB-3	yielding at 0.9% drift; minor inclined cracks (less than 0.004 in.) along the beam; yielding of longitudinal bars at the bottom end	peak load at -3.3% drift; moderate flexural cracks (larger than 0.04 in.) within plastic hinge region; a host of minor diagonal cracks	loss strength at -5.1% drift; large flexural cracks at both ends of the beam; concrete spalling; diagonal rebar fracture
CB-4	yielding at 0.5% drift; minor inclined cracks (less than 0.006 in.) along the beam; yielding of longitudinal bars at the bottom end	peak load at -2.6% drift; major flexural cracks within plastic hinge region; a host of minor diagonal cracks; concrete saplling	loss strength at -3.0% drift; large flexural cracks at the bottom end of the beam; concrete spalling; no rebar fracture
CB-5	yielding at 0.9% drift; minor inclined cracks (less than 0.004 in.) along the beam; yielding of longitudinal bars at the bottom end	peak load at -4.1% drift; dense arrays of minor diagonal cracks	loss strength at -7.8% drift; large flexural cracks at both ends of the beam; concrete spalling; no rebar fracture
CB-6	yielding at 0.9% drift; minor inclined cracks (less than 0.004 in.) along the beam; yielding of longitudinal bars at the bottom end	peak load at 4.3% drift; dense arrays of minor diagonal cracks	loss strength at -6.7% drift; concrete crushing at the bottom end of the beam; main longitudinal rebar fracture

4.3 BEAM ELONGATION AND AXIAL FORCE

Coupling beams subjected to displacement reversal elongate due to concrete cracking and reinforcement yielding. In most previous experimental tests, coupling beams were allowed to elongate freely. However, this is not the case for coupling beams in a real structure, in which axial growth is partially restrained by the walls and slabs, leading to the development of axial forces in the coupling beams. Axial force in coupling beams might be large, especially at high drift levels, which are typically associated with large axial elongations. In this experimental program, the coupling beams were partially restrained by steel links, as shown in Figure 3.2. Axial force was monitored by load cells connected to both steel links, while axial elongations were measured through the Optotrak markers placed on the coupling beams, as shown in Figures 3.15-3.16.

To allow easier discussion of axial elongations measured during the tests, the coupling beams were divided into several strips based on rows of markers, as shown in Figure 4.29.

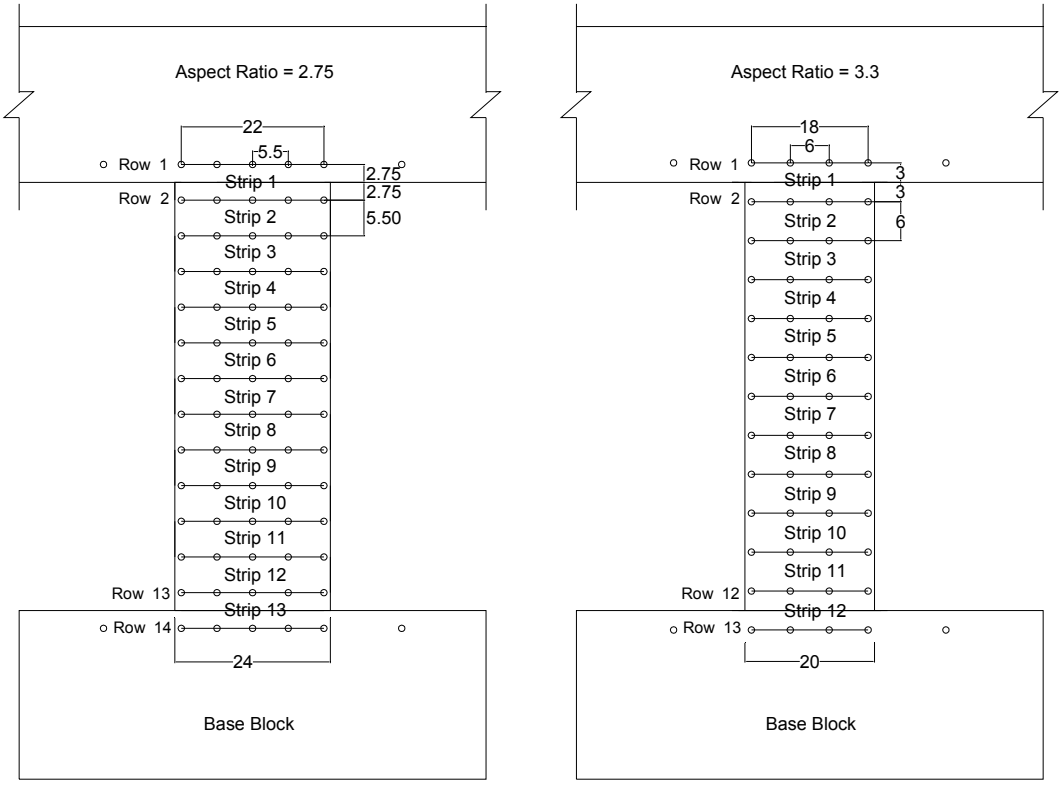

Figure 4.29 Beam "Strips" defined by adjacent rows of markers

Figure 4.30 shows average axial strain versus cycle peak drift for all specimens. The axial strains in this plot were calculated from the first and last row of markers placed on the coupling beams (row 2&13 and row 2&12 for the coupling beams with an aspect ratio of 2.75 and 3.3, respectively). Therefore, these average strains did not include the effect of concentrated deformations at the beam-wall interfaces.

Axial strains ranged from 1% to 2.8% for Specimens CB-1 through CB-4. However, axial strains for Specimens CB-5 and CB-6 were significantly lower, between 0.3% and 0.6%. This difference arises from the fact that large flexural deformations concentrated on the first and last strips for Specimen CB-5 and CB-6 (beam-wall interfaces), while major flexural cracks in Specimens CB-1 through CB-4 were located farther from the beam ends, outside the first and last strips.

Average axial strains calculated from markers on the top and base blocks revealed larger cracks developed on the first and last strips, which encompassed the beam-wall interfaces. Figure 4.31 shows the average axial strains calculated from markers on the top and base blocks. Axial strains exceeding 4% in all specimens can be observed. Axial elongation in Specimens CB-5 and CB-6 mostly resulted from flexural cracks at the beam ends and concentrated rotations at the beam-wall interfaces due to bar slip within the walls. For the other test specimens, the contribution of end beam deformations to average axial strain varied, from a relatively minor contribution (1.5% in the negative direction for Specimen CB-4) to a significant contribution (6% in Specimen CB-3).

Test data indicate a relationship between coupling beam elongation and drift exist. Figure 4.32 shows a plot of average axial strain based on markers at top and bottom blocks versus cycle peak drift. Even though the data are somewhat scattered, a nearly linear relation between coupling beam elongation and drift can be observed. Because relatively minor shear-related damage was observed in the coupling beams, coupling beam elongations must also be strongly related to flexural rotations in the coupling beams. A plot of axial strain versus drift component due to flexural deformations, including bar slip, is shown in Figure 4.33. A similar trend to that shown in Figure 4.32 can be observed, as expected.

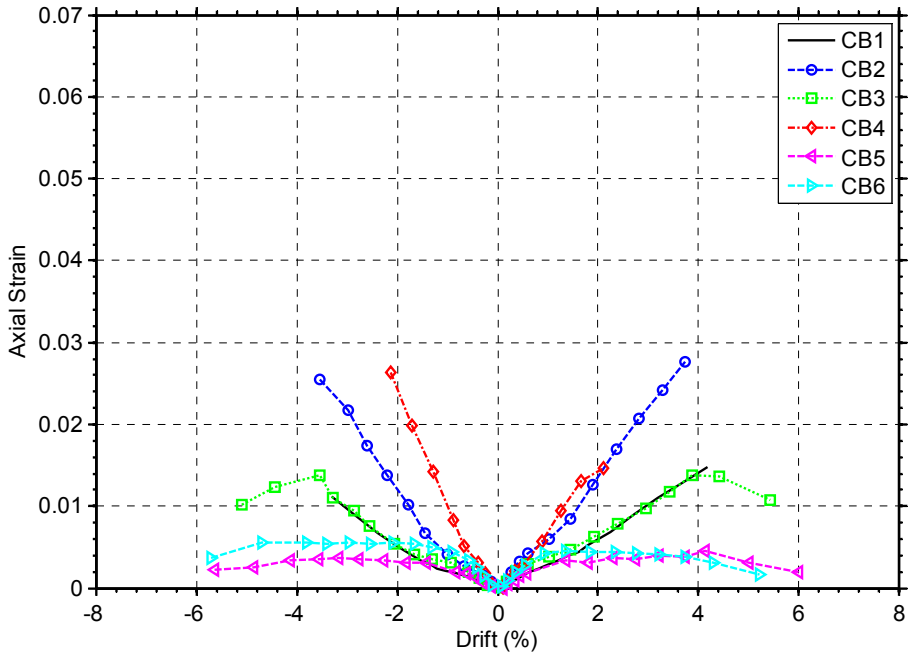

Figure 4.30 Average axial strain based on markers at beam ends

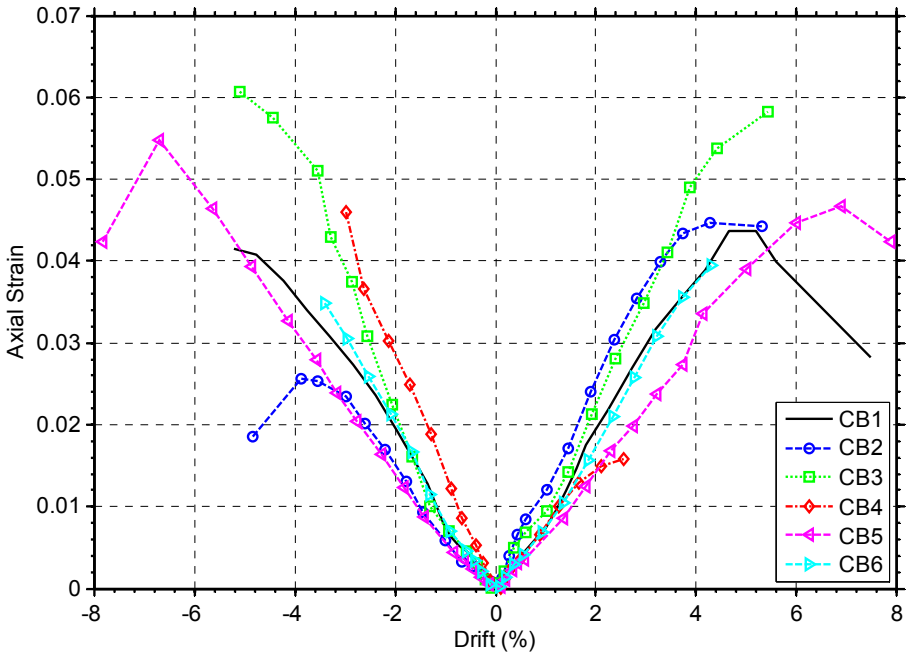

Figure 4.31 Average axial strain based on markers at top and base blocks

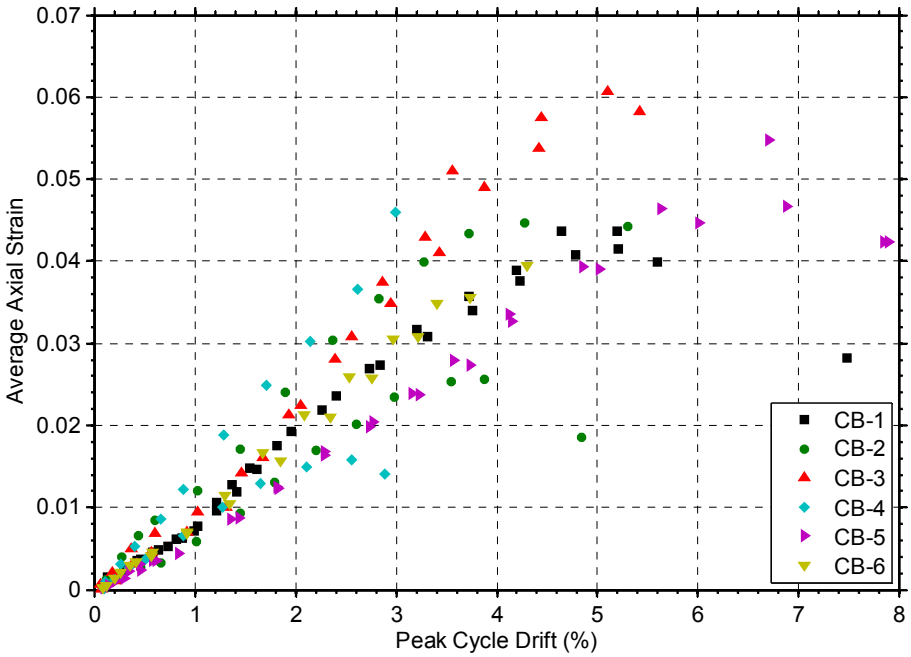

Figure 4.32 Relationship between the maximum imposed drift and average axial strain

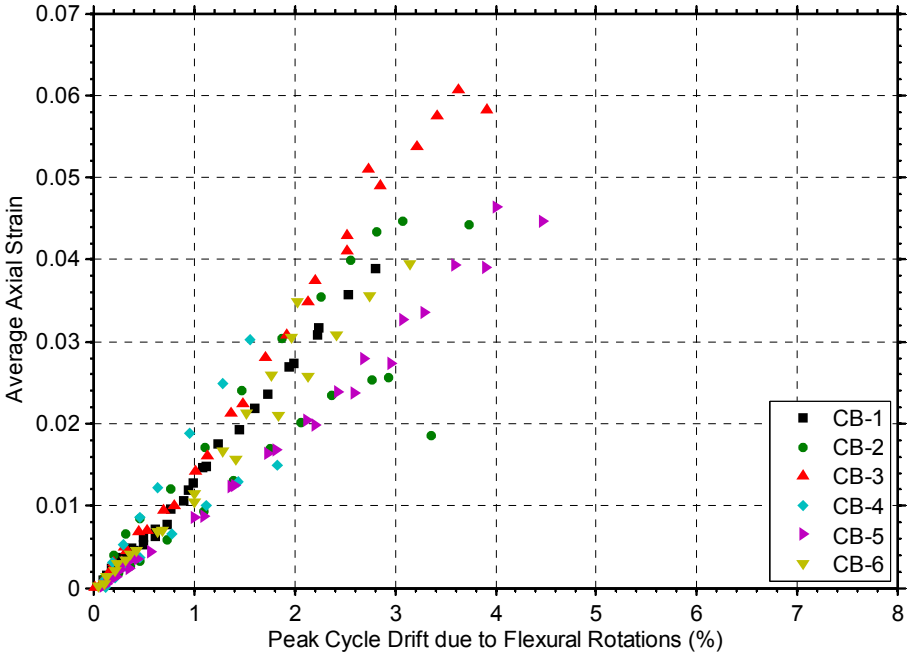

Figure 4.33 Relationship between the maximum imposed drift due to flexural rotation and average axial strain

The partial restrained to axial elongations provided by the vertical steel arms led to axial forces in the coupling beams on the order of 5% of the pure axial force capacity, calculated according to the ACI Building Code (Figure 4.34). Even though these axial forces were small compared to the axial capacity of the coupling beams, they do increase their flexural and shear capacity, as discussed in Section 4.4.1. Therefore, in the analysis and design of the coupling beams, axial forces should be taken into account.

In Figure 4.34, the axial force capacity of the coupling beams was calculated as $P_o = f_c^{'}(A_g - A_{st}) + f_y A_{st}$, where $f_c^{'}$ is the compressive strength of concrete, f_y is the measured yield stress of the steel reinforcement, A_g is the gross cross-sectional area of the beam, and A_{st} is the total area of longitudinal steel. An approximately linear relation between axial force ratio (measured axial force divided by P_o) and drift was obtained prior to the development of significant sliding displacements, which led to a decrease in the beam axial force. It should be noted that there were abrupt changes in the magnitude of axial forces, especially in Specimen CB-2 and CB-5. These sudden changes resulted from the loosening of bolts attaching the vertical steel arms to the upper block, which was necessary when the force developed approached the capacity of the load cell.

Unfortunately, a model to predict the axial force expected to develop in the coupling beams could not be developed in this experimental program due to limited test data and difficulties in estimating the degree of axial restraint imposed by structural walls and floor slabs in real coupled wall structures. However, as a rough estimate, the expected axial force can be conveniently estimated in term of the expected shear demand. As shown in Figure 4.35, the axial forces developed in the coupling beams were beyond 60% of the applied shears. Thus, the lower-bound expected axial force in the coupling beam can be estimated as $0.6V$, where V is the applied shear.

It should be noted that Figure 4.34 and Figure 4.35 did not include the response of Specimen CB-6 due to what appeared to be a malfunction of the data acquisition card to which the load cells in the vertical arms were connected. Therefore, data from the load cells were not available to calculate the axial forces developed in this coupling beam.

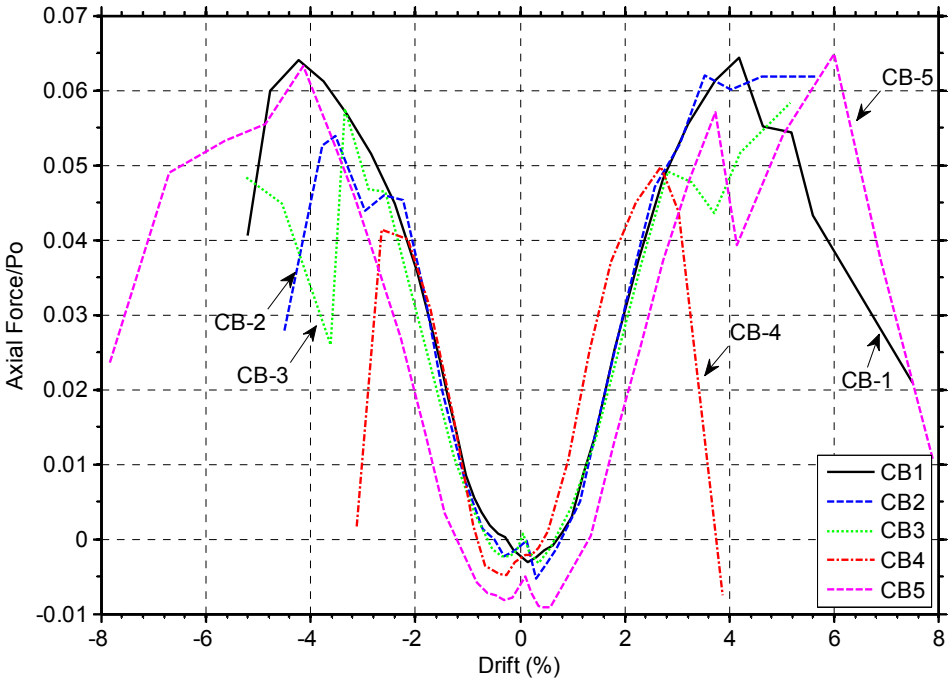

Figure 4.34 Axial force normalized by the axial force capacity

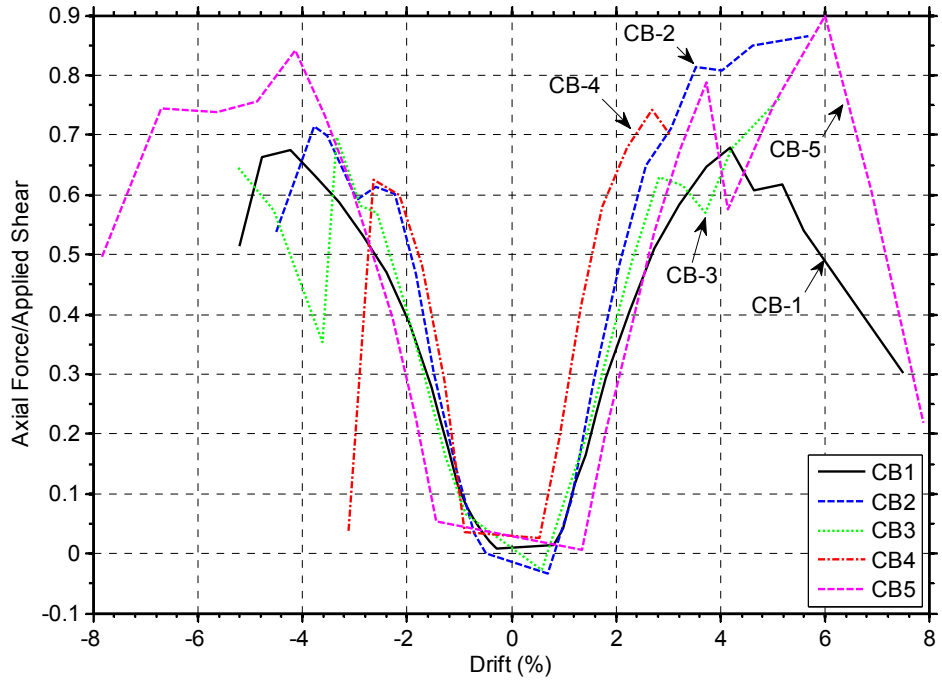

Figure 4.35 Axial force normalized by the applied shear

4.4 FLEXURAL BEHAVIOR

4.4.1 Flexural Strength

Flexure plays an important role in the behavior of slender coupling beams. Because the test beams were expected to fail in a flexural mode with flexural hinges forming at their ends, accurate prediction of flexural strength of the tested coupling beams was important. In this study, flexural strength was estimated through a moment-curvature analysis. This analysis is relatively straight-forward and will be discussed in Section 4.4.5. Rather than comparing moment capacity, it is easier to compare the shear associated with the beam reaching its flexural capacity at both ends to the peak applied shear force. The shear associated with the coupling beam flexural capacity (V) was calculated as $V = 2M / L$, where M is the beam moment capacity and L is the length of the coupling beam.

Table 4.3 Specimen CB-1 capacity predicted by the moment-curvature analysis

Axial force (kips)	V_{tested} (kips)	$M_{predicted}$ (kip-in)	$V_{predicted}$ (kips)	$V_{tested}/V_{predicted}$
0	131	4230	128	1.02
20	131	4326	131	1.00
40	131	4422	134	0.98
60	131	4518	137	0.96
80	131	4611	140	0.94
90	131	4660	141	0.93

Table 4.4 Specimen CB-2 capacity predicted by the moment-curvature analysis

Axial force (kips)	V_{tested} (kips)	$M_{predicted}$ (kip-in)	$V_{predicted}$ (kips)	$V_{tested}/V_{predicted}$
0	116	3718	113	1.03
20	116	3814	116	0.99
40	116	3963	120	0.96
60	116	4083	123	0.93
80	116	4200	127	0.91
90	116	4254	128	0.90

Table 4.5 Specimen CB-3 capacity predicted by the moment-curvature analysis

Axial force (kips)	V_{tested} (kips)	$M_{predicted}$ (kip-in)	$V_{predicted}$ (kips)	$V_{tested}/V_{predicted}$
0	115	3573	108	1.06
20	115	3672	111	1.03
40	115	3768	114	1.01
60	115	3860	117	0.98
80	115	3951	120	0.96
90	115	3996	121	0.95

Table 4.6 Specimen CB-4 capacity predicted by the moment-curvature analysis

Axial force (kips)	V_{tested} (kips)	$M_{predicted}$ (kip-in)	$V_{predicted}$ (kips)	$V_{tested}/V_{predicted}$
0	103	2944	111	0.93
20	103	3068	116	0.89
40	103	3192	120	0.85
60	103	3306	125	0.82
80	103	3417	129	0.80
90	103	3472	131	0.78

Table 4.7 Specimen CB-5 capacity predicted by the moment-curvature analysis

Axial force (kips)	V_{tested} (kips)	$M_{predicted}$ (kip-in)	$V_{predicted}$ (kips)	$V_{tested}/V_{predicted}$
0	116	3438	104	1.11
20	116	3531	107	1.08
40	116	3624	110	1.05
60	116	3715	112	1.03
80	116	3807	116	1.00
90	116	3852	117	0.99

Table 4.8 Specimen CB-6 capacity predicted by the moment-curvature analysis

Axial force (kips)	V_{tested} (kips)	$M_{predicted}$ (kip-in)	$V_{predicted}$ (kips)	$V_{tested}/V_{predicted}$
0	126	4006	121	1.04
20	126	4126	125	1.01
40	126	4244	129	0.98
60	126	4360	132	0.96
80	126	4461	135	0.93
90	126	4500	136	0.92

From Tables 4.3-4.8, it can be seen that the applied shears were lower than the predicted shear at flexural capacity. However, the difference was approximately 10% in most cases. The maximum axial forces developed in the coupling beams were approximately 90 kips in most tests. The moment capacity at this level of axial force can thus be considered as an upper-bound capacity. The moment capacity of RC Specimen CB-4, however, was significantly smaller than the predicted capacity. This was due to the beam losing concrete integrity when subjected to displacement reversal beyond 3% drift. The confinement provided by the special column-type confinement was not sufficient to preserve the integrity of the concrete core, leading to significant concrete degradation and a failure of the beam at low drift capacity.

The reason that the predicted moment and shear were higher than the experimental ones was a slight shift in the inflection point upwards, as discussed in the next section. This was expected because steel links provided only partial restraints to the top blocks while the base block was fixed to the floor. In the analysis, it was assumed that moments at both ends of the beam were equal, thus enabling the use of the expression of $V = 2M / L$. However, because of the increase in lever arm, a shift in the inflection point upwards from the beam midspan would lead to a lower shear force associated with the bottom beam section reaching its moment capacity.

4.4.2 Inflection Points

Moment, and hence associated shear force, imposed on the specimens resulted from horizontal displacement applied at the ends of the coupling beams and the restrain against rotation provided by the vertical steel arms. Shears and moments caused by gravity load on coupling beams is generally small compared to those associated with the capacity of the coupling beam. Thus, the effect of gravity load was ignored in the test specimens. Theoretically, moments at both ends of the specimens were equal and in directions such as to induce double curvature, with the inflection point located at beam midpsan.

To evaluate the success of the test setup, in which steel links were used to restrain rotations at the top block and ensure an antisymmetric moment distribution, the location of the inflection point throughout the tests was calculated and compared to the theoretical

midspan location. Using equilibrium, moments at the top and bottom ends of the specimen were calculated from the applied shear force and axial force in each steel link. Then, the location of the inflection point was determined from moments at both ends using similar triangles.

Figure 4.36 shows the experimentally obtained inflection point locations for all specimens, except Specimen CB-6, for which moments at both ends of this specimen could not be calculated due to problems in the acquisition of axial force data from the vertical steel arms. Inflection point locations for the test coupling beams were close to the midspan section of the beam. This indicates that the boundary conditions imposed on the coupling beams led to a nearly perfectly antisymmetric moment distribution along the beam span, as intended. The actual inflection point location was in most cases within 6 in. of the theoretical inflection point location, which was at 33 in. from the face of the walls (midspan section), for all five tests.

As shown in Figure 4.36, the inflection point location shifted up approximately 6 in. in the negative loading direction. Upward shifting of the infection point indicates that moment at the bottom beam end was larger than that at the top end, resulting in more damage at the bottom part of the specimens.

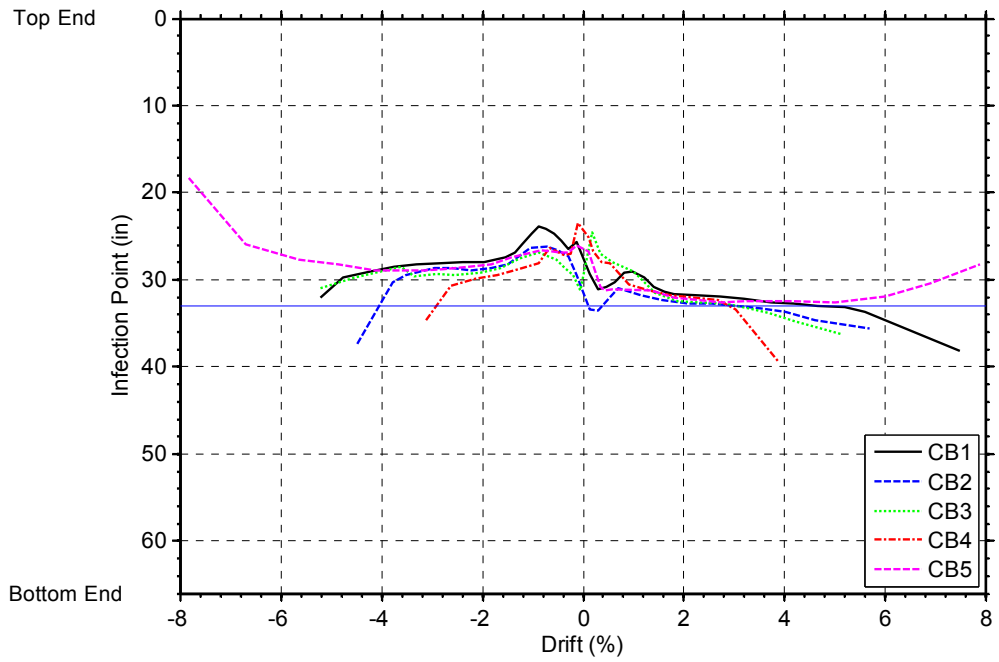

Figure 4.36 Location of inflection points

4.4.3 Longitudinal Strain Distribution

Longitudinal strains varied nearly linearly across the depth of the cross section in all specimens. This validates the use of Bernoulli's assumption that plane sections remains plane after loading. For slender beams, this assumption enables the use of beam theory for the beam analysis. The moment-curvature analyses presented in Section 4.4.5 were based on the assumption of plane sections remaining plane after loading and the results presented in this section substantiates such an assumption.

Figure 4.37 shows the distribution of longitudinal strains at selected drifts for all specimens. In these plots, the average longitudinal strains calculated from coordinates of markers defining a quadrilateral element in each strip (see Section 4.1.1), are shown. Tensile strains are positive in these plots. Longitudinal strains for the end strips were not included in these plots because the first and last rows of markers were placed on the end blocks and not the coupling beams. Additional plots of longitudinal strain distributions for all specimens are shown in Figure C.1 through Figure C.6 of Appendix C.

For Specimen CB-1, the longitudinal strain in Strips 2, 3, and 4 was irregular. Inconsistency of longitudinal strains in middle squares is obvious. It is believed that this irregularity arose from anomaly of data from markers in this region. Elsewhere, longitudinal strains were nearly linearly distributed across the beam depth. Longitudinal strains were larger in Strips 11 and 12, where most flexural cracks at the bottom beam end formed. At large drift levels, longitudinal strains became significant due to inelastic deformations at the beam ends. Throughout the tests, longitudinal strains in the middle strips, especially Strips 6, 7, and 8, were very small because of the low moment in this region of the coupling beam.

A similar trend was observed in the other specimens, where longitudinal strains were largest near the ends of the coupling beams and smallest near the infection point at the midspan of the beam. Longitudinal strains near the midspan were almost zero in all cases. Moreover, longitudinal strains at the bottom strip (Strips 11 and 12 for the beams with the aspect ratio of 3.3 and 2.75, respectively) were larger than those at the top strip (Strip 2) for all test specimens. This is in agreement with the upward shift in the inflection point location discussed in Section 4.4.2.

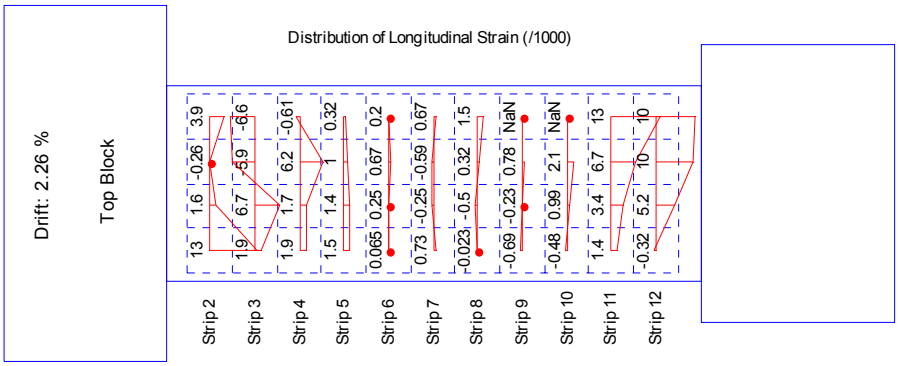

(a) Specimen CB-1

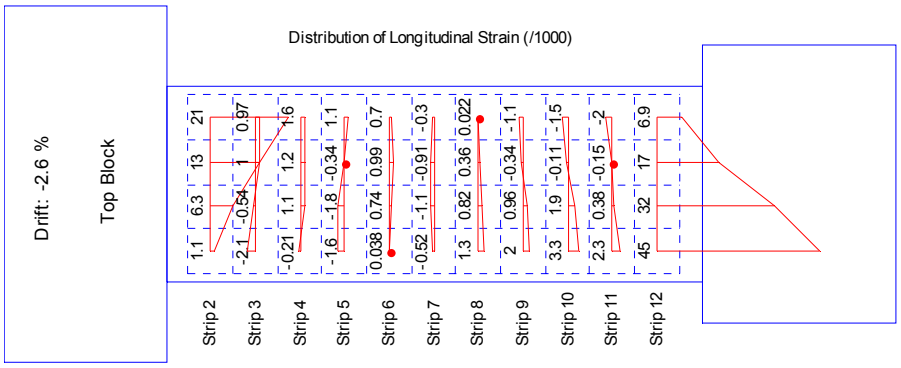

(b) Specimen CB-2

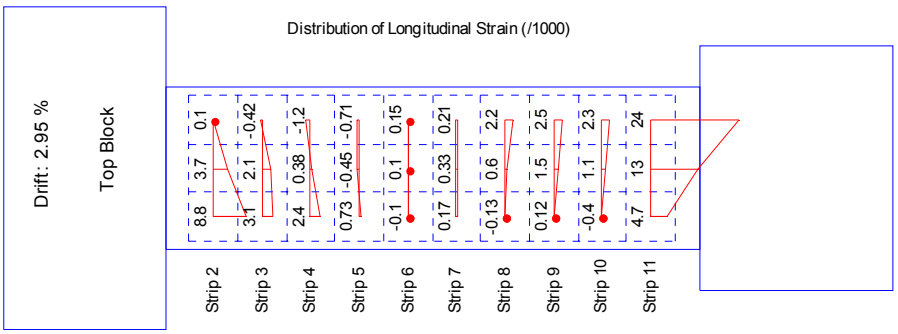

(c) Specimen CB-3

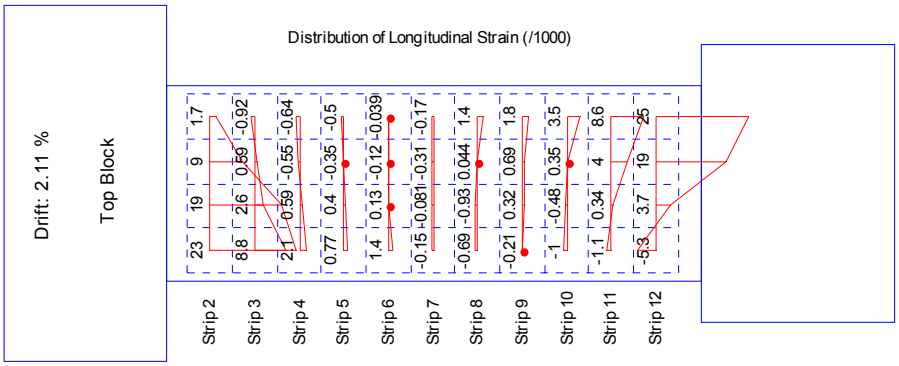

(d) Specimen CB-4

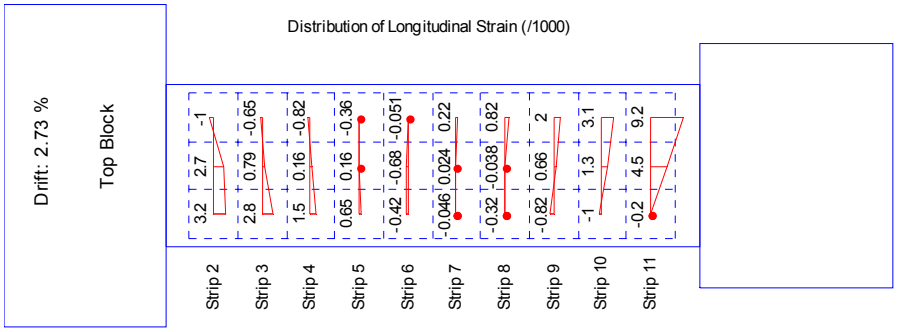

(e) Specimen CB-5

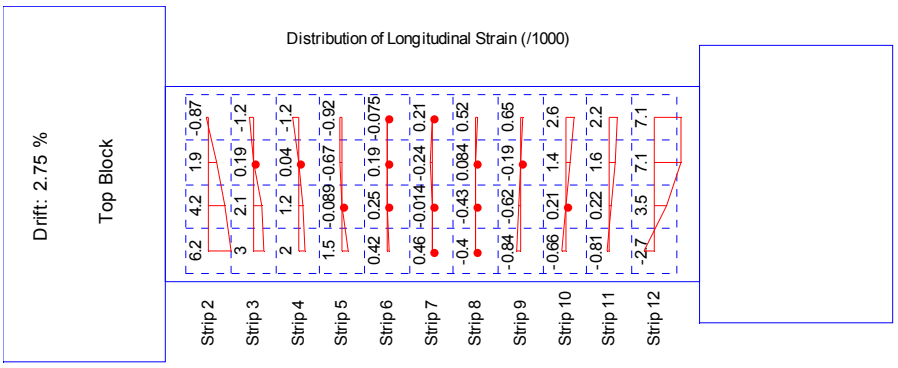

(f) Specimen CB-6

Figure 4.37 Longitudinal strains at selected drifts

4.4.4 Curvature Distribution

Curvature along the beam height was calculated from the strips of Optotrak markers. The relative rotation between adjacent rows of markers was first determined and then, the average curvature for each strip was determined by dividing the differential rotation by the distance between the two adjacent rows of markers, as follows (Figure 4.38),

$$\phi_i = \frac{\left(y_2^i - y_1^i\right) - \left(y_2^{i-1} - y_1^{i-1}\right)}{\Delta x_i \times l} \tag{4-15}$$

where ϕ_i is the average curvature (rad/in) over Strip i of length Δx_i (in), y_2^i and y_1^i, and y_2^{i-1} and y_1^{i-1} are the y-coordinates of the edge markers at the top and bottom corners of Strip i (in), respectively, and l is the horizontal distance between the edge markers.

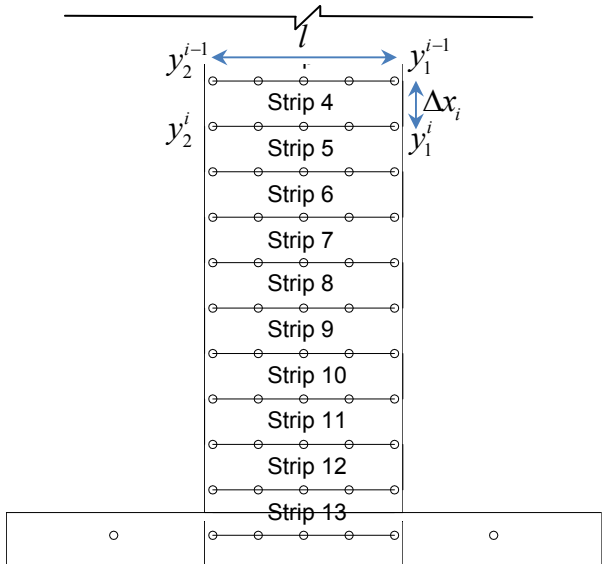

Figure 4.38 Corner markers and notation used to calculate average curvature for a given strip

Curvature distributions at selected cycle peak drifts for all specimens are shown in Figure 4.39. When more than one cycle was applied at a given drift level, the value shown correspond to the first cycle. Curvature distribution at the end strips is not shown in Figure 4.39 due to the effect of concentrated rotations at the beam-wall interfaces caused by bar strain penetration into the walls. Curvature profiles are plotted separately

for the negative and positive loading direction. In some cases, curvature could not be determined near the end of the test due to concrete spalling, resulting in either unavailable or unreliable coordinates obtained from markers. In each plot, the theoretical curvature at first yield, obtained from a moment-curvature analysis, is shown in vertical blue lines. The values of the theoretical yielding curvature, assuming an axial force of 40 kips, are provided in Table 4.9.

Curvature was nearly linearly distributed over the length of the coupling beams. For Strip 7 of the coupling beams with an aspect ratio of 2.75 (CB-1, CB2, CB4, and CB-6), curvature was almost zero at each cycle peak drift. For the coupling beams with 3.3 aspect ratio (CB-3 and CB-6), Strips 6 and 7 also showed very low values of curvature throughout the tests. This further confirms the good agreement between the theoretical and experimental inflection point locations.

For Specimens CB-1 through CB-4, curvatures at both beam ends became significant as plastic hinges formed at these locations Some inconsistencies were observed in the curvature data for Specimen CB-1, however, particularly for Strip 3, for which curvatures were opposite in sign. This was likely the result of unreliable data from markers.

Despite the large drift demand, curvature in the middle strips (Strips 5-10) was below the theoretical yielding curvature for all HPFRC coupling beams. For Specimen CB-4, which was the RC coupling beam, curvature in Strips 2, 3, 10, 11, 12 exceeded the calculated yielding curvature at drifts beyond 1%.

Table 4.9 Theoretical yield curvature based on section modeling

Specimen	Calculated yield curvature ϕ_y (rad/in)
CB-1	2.0×10^{-4}
CB-2	2.6×10^{-4}
CB-3	2.6×10^{-4}
CB-4	1.7×10^{-4}
CB-5	3.0×10^{-4}
CB-6	2.0×10^{-4}

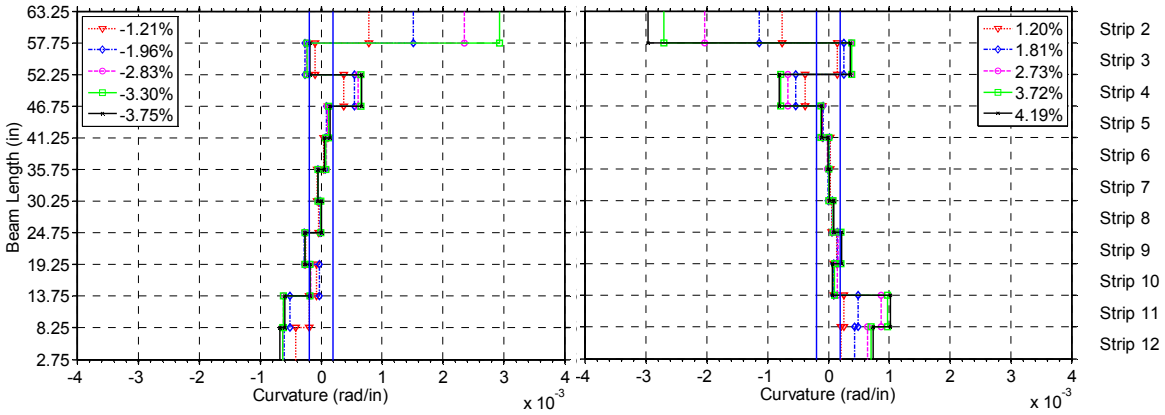

(a) Specimen CB-1

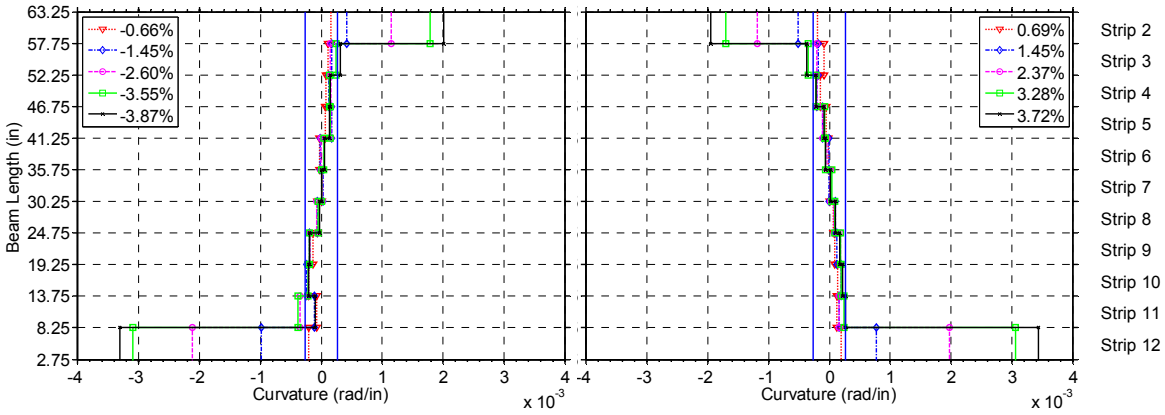

(b) Specimen CB-2

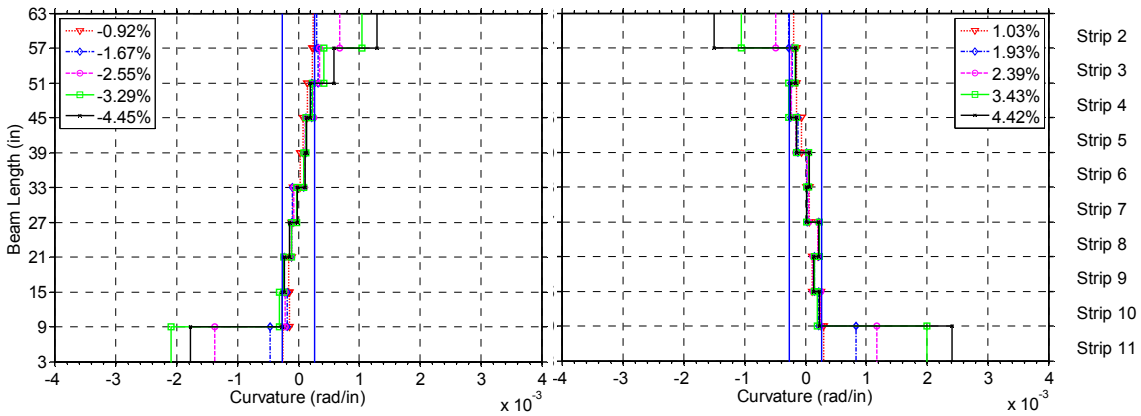

(c) Specimen CB-3

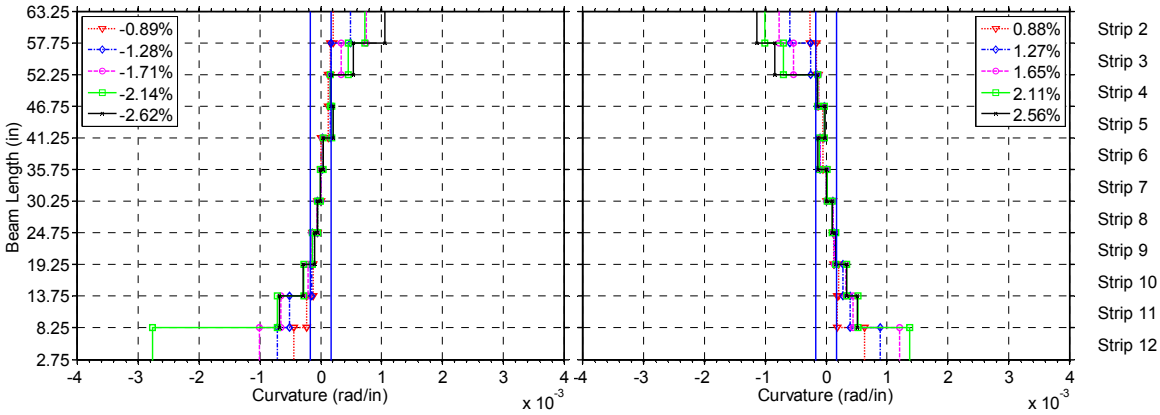

(d) Specimen CB-4

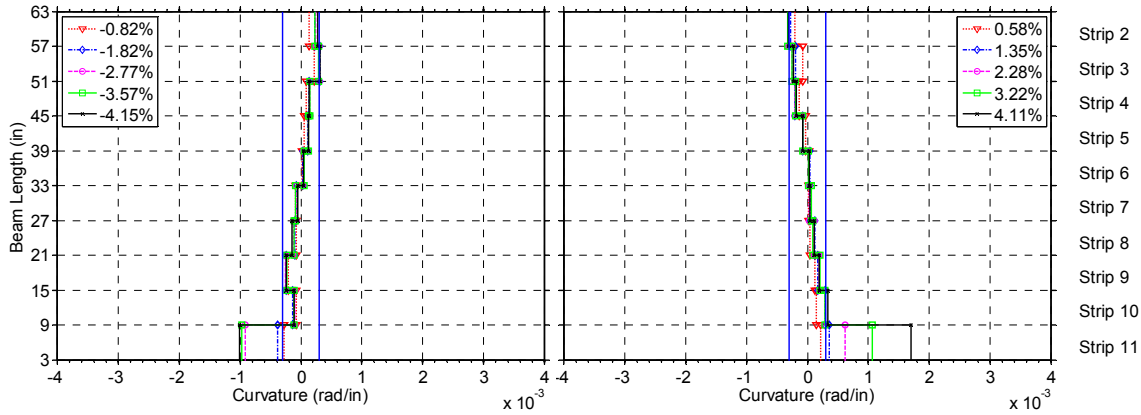

(e) Specimen CB-5

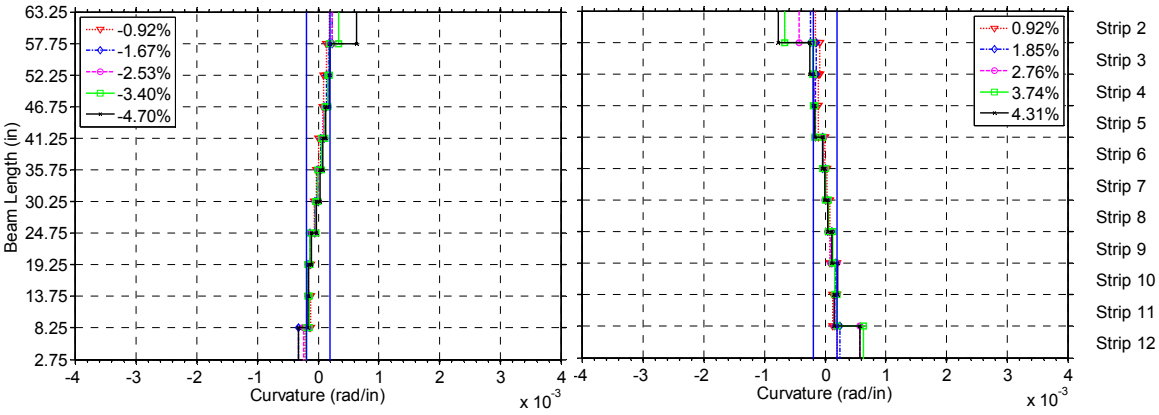

(f) Specimen CB-6

Figure 4.39 Average curvature distribution of all coupling beam specimens

4.4.5 Moment-Curvature Response

To predict the moment-curvature response at the critical sections, a nonlinear section analysis, referred to as moment-curvature analysis, was performed. Prediction of moment-curvature response was then compared to the experimental results. The nonlinear moment-curvature response under monotonic loading is based on the Bernoulli assumption that plane sections remain plain under the action of axial load and moment. The term "nonlinear" indicates that nonlinear stress-strain relationships of materials, i.e. concrete, HPFRC, and steel, is taken into account when calculating the moment-curvature response.

Generally, the moment-curvature analysis requires iteration until equilibrium is reached. First, the compressive strain at the extreme fiber is assumed. Then, the neutral axis depth is assumed and strains at locations of reinforcing bars are calculated using a linear strain distribution according to the Bernoulli assumption of plane sections remaining plane after loading. Stresses in the concrete and reinforcing steel can be subsequently determined from the constitutive relation of each material and equilibrium of forces checked. If the forces normal to the section are not in equilibrium, a new value for the neutral axis depth is assumed, followed by a recalculation of the strains, stresses and resultant forces. This procedure is repeated until equilibrium of forces is reached, after which moment is then calculated. The process is repeated for different compressive strains at the extreme fiber until either the compressive strain capacity of the concrete or the strain capacity of the steel is achieved, or a significant strength drop has occurred

In this study, a computer program written in MATLAB was used to develop the moment-curvature response. The tensile stress-strain relation for the HPFRC material was taken into account. Because bars of different diameter could have different material properties, i.e. different yield and ultimate strengths, the program was written such that different reinforcing bar properties could be specified for a single section.

In this study, a maximum compressive strain of 0.008 was used for the HPFRC. For regular concrete, a strain capacity of 0.006 was assumed. A Hognestad's parabola with a linear descending branch was adopted for the constitutive model of concrete and HPFRC, as discussed in Section 3.8.5. The normalized slopes for the linear descending tail, Z, of 50 and 150 were used for modeling the HPFRC matrix and regular concrete,

respectively. The tensile stress-strain response of HPFRC was modeled using a piece-wise linear relation, as shown in Figure 4.40. The four points in the model were selected to fit the test results reported by Liao et al. (2006), as shown in Section 3.8.5. The tensile stress-strain vales for modeling of concrete and HPFRC are given in Table 4.10.

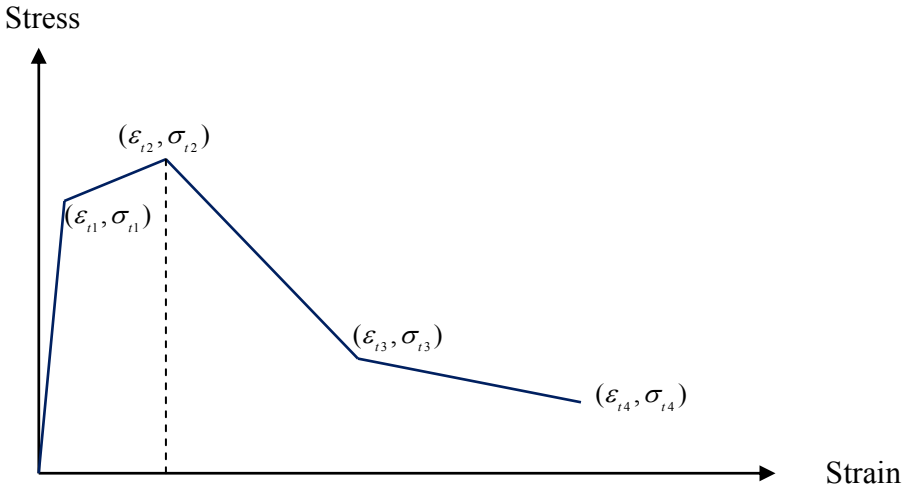

Figure 4.40 Tensile stress-strain model for HPFRC matrix

Table 4.10 Stress-strain values for modeling of regular concrete and HPFRC

Matrix	σ_{t1} (psi)	ε_{t1}	σ_{t2} (psi)	ε_{t2}	σ_{t3} (psi)	ε_{t3}	σ_{t4} (psi)	ε_{t4}
Regular concrete	450	0.00008	0	0.00008	-	-	-	-
HPFRC[1]	400	0.0001	500	0.005	200	0.015	100	0.02
HPFRC[2]	650	0.0001	700	0.005	200	0.015	100	0.02

[1] for Specimen CB-1
[2] for Specimens CB-2, CB-3, CB-5, and CB-6

The stress-strain response of reinforcing steel was modeled as shown in Figure 4.41. This model includes several parameters: yield stress (f_y), modulus of elasticity (E_s), strain at the beginning of the strain-hardening region (ε_{sh}), initial modulus of the strain hardening branch (E_{sh}), ultimate tensile strength (f_{su}), and ultimate tensile strain (ε_{su}). The stress-strain model can be expressed by the following equations.

For $\varepsilon_s \leq \varepsilon_y$

$$f_s = E_s \varepsilon_s \tag{4-16}$$

For $\varepsilon_y < \varepsilon \le \varepsilon_{sh}$

$$f_s = f_y \tag{4-17}$$

For $\varepsilon_{sh} < \varepsilon \le \varepsilon_{sm}$

$$f_s = f_y + (f_{su} - f_y)\left[2\left(\frac{\varepsilon - \varepsilon_{sh}}{\varepsilon_{sm} - \varepsilon_{sh}}\right) - \left(\frac{\varepsilon - \varepsilon_{sh}}{\varepsilon_{sm} - \varepsilon_{sh}}\right)^2\right] \tag{4-18}$$

For $\varepsilon_{sm} < \varepsilon \le \varepsilon_{su}$

$$f_s = f_{su} \tag{4-19}$$

where $\varepsilon_{sm} = \varepsilon_{sh} + \dfrac{2\left(f_{su} - f_y\right)}{E_{sh}}$

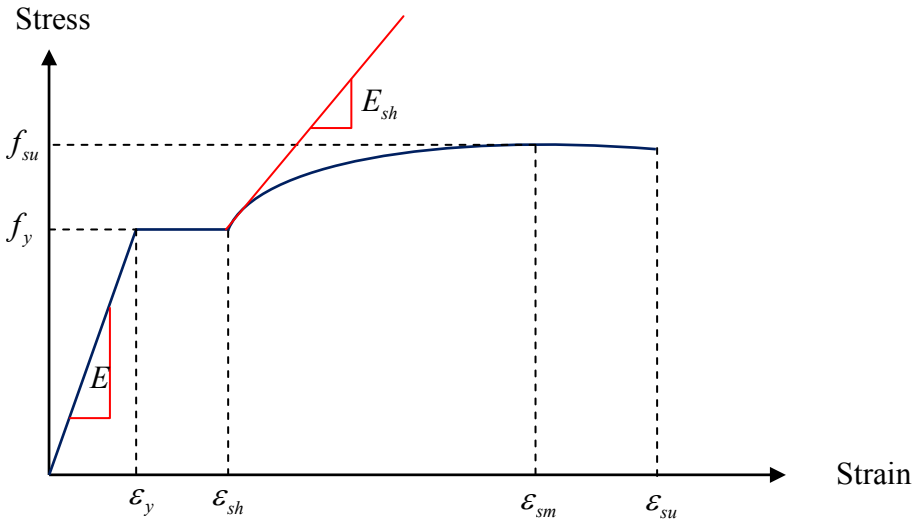

Figure 4.41 Tensile stress-strain model for reinforcing steel

The values of material properties used in this model were approximated from the results of the tension tests performed on bar samples.

When calculating the moment-curvature responses, different analyses were performed for axial forces ranging between 0 and 100 kips. These axial forces corresponded to those observed during the tests, as discussed in section 4.3. Experimental moment-curvature responses of strip 12 for Specimens CB-1 and CB-4, shown in Figure 4.42 and Figure 4.43, respectively, agree well with the predicted responses. For strip 12 which was near the end of the beam and subjected to large moment demand, it can be

seen from the plots that cracked stiffness and yield moment-curvature of the test were in close agreement with the prediction.

Using the moment in the middle of the strip, the measured moment-curvature response of Strip 12 for Specimen CB-2 was slightly softer than the theoretical moment-curvature relationship, as shown in Figure 4.44. This was likely the results of a weak section created by the termination of the U-shape dowel bars within this strip. However, the response for Strip 11 Figure 4.45, which was slightly away from this weak region, was in good agreement with the predicted response, particularly with regard to cracked stiffness and yield moment and curvature.

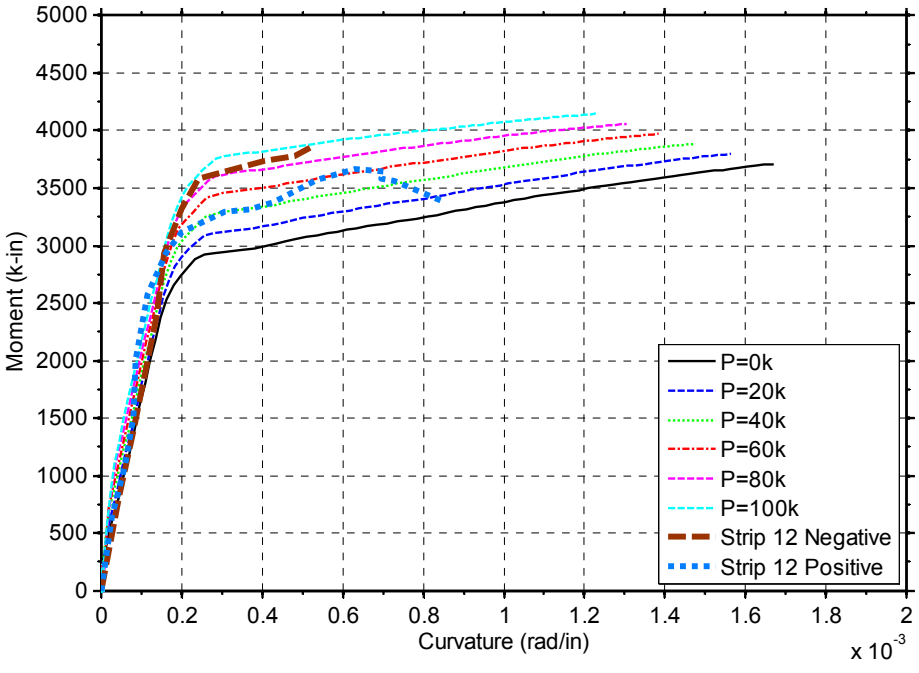

Figure 4.42 Moment versus curvature response for Specimens CB-1

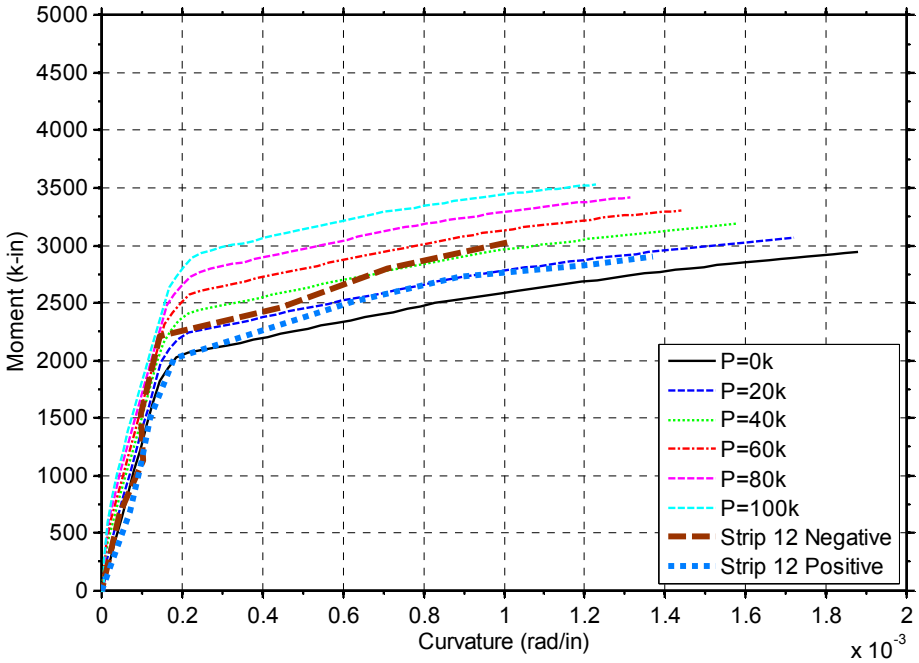

Figure 4.43 Moment versus curvature response for Specimens CB-4

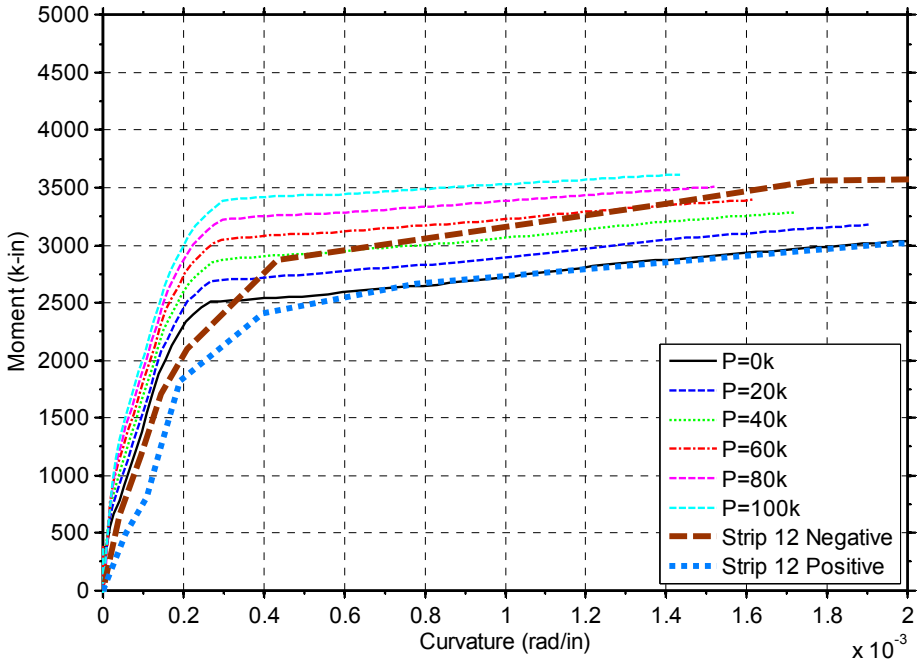

Figure 4.44 Moment versus curvature response for Strip 12 of Specimens CB-2

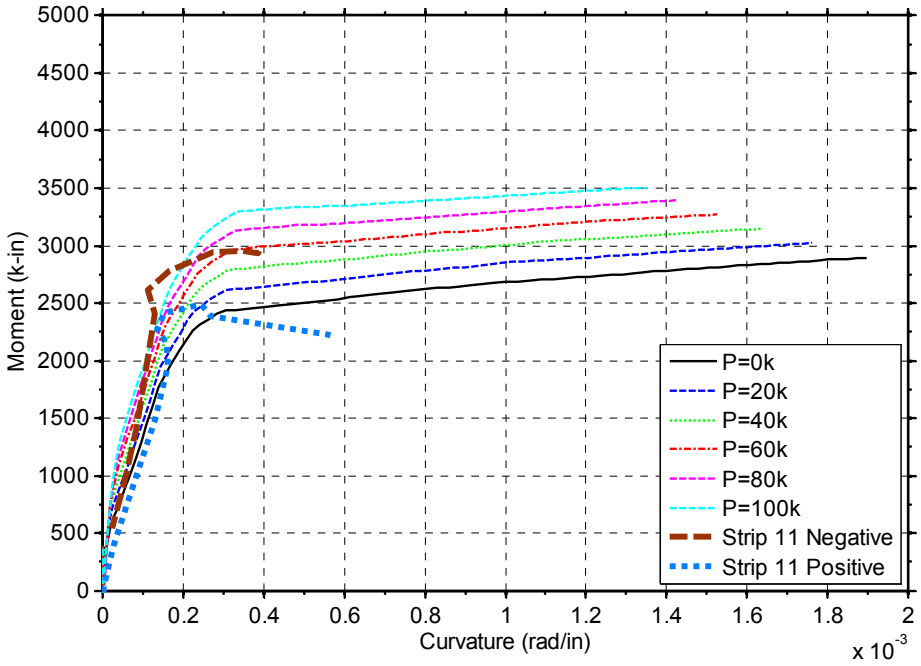

Figure 4.45 Moment versus curvature response for Strip 11 of Specimens CB-2

The moment-curvature responses at the end strips for all specimens were substantially softer than the theoretical responses. Figure 4.46 shows the experimental response for Strip 13 of Specimen CB-1. The softer response can be attributed to axial strain penetration of reinforcing bars into the end blocks, which manifested itself as an opening of the cold joint between the coupling beam and the end blocks with the associated apparent increase in curvature. The same behavior was also observed in the tests of HPFRC coupling beams with aspect ratio of 1.75 (Lequesne 2011).

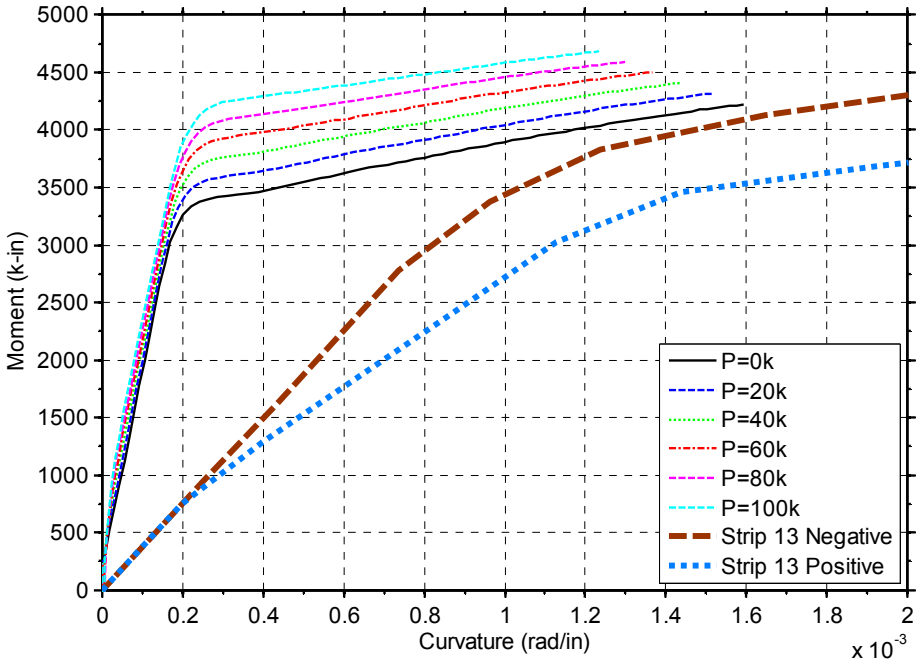

Figure 4.46 Moment versus curvature at the end strip for Specimen CB-1

4.4.6 Plastic Hinge Length

The measured curvature distributions showed that inelastic flexural deformations concentrated on the first two marker strips at the beam ends. The length of the first two strips was 8.25 in. and 9 in. from the beam-wall interfaces for the coupling beams with an aspect ratio of 2.75 and 3.3, respectively. For Specimen CB-1 and CB-4, whose aspect ratio was 2.75, some inelastic behavior was also detected in Strips 3 and 10, which were 13.75 in. away from the beam-wall interfaces. Therefore, a plastic hinge length of half the coupling beam (*h/2*), which corresponds to 12 in. and 10 in. for the coupling beams with an aspect ratio of 2.75 and 3, respectively, seems reasonable. This plastic hinge length of *h/2* was similar to that observed by Lequesne (2011) in the tests of HPFRC coupling beams with 1.75 aspect ratio.

4.5 SHEAR BEHAVIOR

4.5.1 Analysis of Shear Strength

In general, reinforced concrete members resists shear through five basic mechanisms: shear resisted by the member compression zone (V_{cz}), aggregate interlock (V_a), dowel action by the longitudinal reinforcement (V_{dowel}), shear carried by transverse reinforcement through truss action (V_s), and shear resistance from diagonal reinforcement, if any. Because it is difficult to determine V_{cz}, V_a, and V_{dowel} separately, these three components are normally identified as the shear concrete contribution and denoted as V_c. Therefore, shear strength of the test coupling beams can be primarily attributed to contributions from HPFRC, transverse reinforcement (through truss action), and diagonal reinforcement, if any, as follows,

$$V = V_c + V_d + V_s \tag{4-20}$$

where V_d and V_s are the shear resisted by diagonal and transverse reinforcement, respectively. For the test specimens, V_d and V_s were determined from the recorded strains of reinforcement, using the constitutive model developed by Sakai and Mahin (2004), as discussed in Section 3.8.5. For calculation of V_s a diagonal crack projection on the beam longitudinal axis equal to the member effective depth *d*, which is close to that observed in this experimental study was assumed. Shear contribution from concrete, V_c, was then estimated as,

$$V_c = V - V_d - V_s \tag{4-21}$$

where V is applied shear.

4.5.2 Shear Contribution of Shear Resistance Mechanisms

Shear resistance from HPFRC exceeded $3.5\sqrt{f_c'}$ (psi) for all HPFRC specimens (CB-1, CB-2, CB-3, CB-5, and CB-6), and in the particular case of Specimens CB-1, CB-2, and CB-3, this contribution exceeded $5\sqrt{f_c'}$ (psi). For Specimens CB-5 and CB-6, which did not have diagonal reinforcement, shear resisted by HPFRC was lower than for the other HPFRC specimens due to the larger area of transverse reinforcement provided. These test results suggest that it is possible that the use of a lower transverse

reinforcement ratio in Specimens CB-5 and CB-6 would also have resulted in adequate behavior.

From Table 4.11 and Figure 4.47, the largest shear contribution of HPFRC to the coupling beams with diagonal reinforcement was close to 60% for Specimens CB-1, CB-2, and CB-3. On the other hand, shear contribution of HPFRC for the coupling beams without diagonal reinforcement was approximately 40%. These results are a clear indication of the effectiveness of HPFRC to significantly contribute to coupling beam shear strength, even at large drift levels. Confinement provided by HPFRC, in combination with stirrups, was ample to prevent buckling of diagonal reinforcement in the middle region of the beam. Minor shear-related damage observed in the tests also confirms the ability of HPFRC to provide resistance to crack opening by transferring tension across cracks, thereby increasing shear strength of the coupling beams.

Diagonal reinforcement was not very effective in resisting shear in the tested coupling beams, as expected, due to its shallow angle of inclination with respected to the beam axis. As indicated in Table 4.11, shear contribution from diagonal reinforcement was below 15% for Specimens CB-1 through CB-3, and 20% for Specimen CB4. Shear resistance provided by diagonal bars was less than $2\sqrt{f_c'}$ (psi) in all test specimens containing diagonal reinforcement, as shown in Figure 4.48 and Figure 4.49. This low contribution to shear strength led to the elimination of diagonal bars in Specimens CB-5 and CB-6.

It should be reminded that the contribution of HPFRC to shear strength can only be considered an approximation. First, dowel action of reinforcement was not included in the calculation of shear strength. Second, the recorded strains in transverse reinforcement included the influence of confinement that stirrups provided to the whole section, which likely led to an overestimation of the contribution of transverse reinforcement to member shear strength. Third, stresses in reinforcing steel were estimated from strains measured at single locations, likely to be influenced by their distance to cracks, and from an approximate model (see Section 3.8.5). Based on the results from Specimen CB-1, CB-2, and CB-3, a shear stress of $5\sqrt{f_c'}$ (psi) is deemed appropriate for the shear contribution of HPFRC, as recommended by Lequesne (2011).

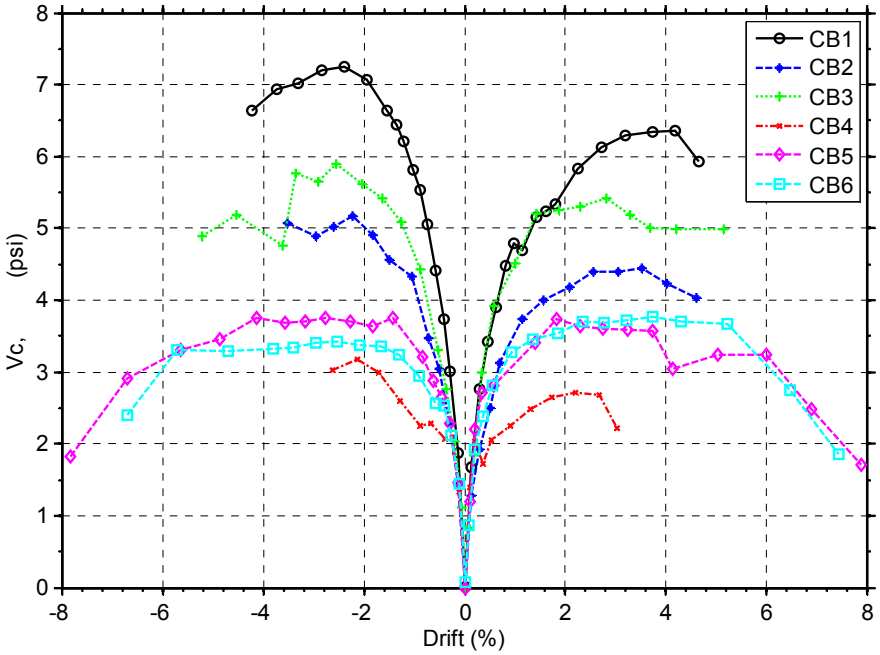

Figure 4.47 Shear contribution from HPFRC and concrete at each cycle peak drift

Table 4.11 Estimated contribution to shear resistance from V_{HPFRC}, V_c, V_d, and V_s at peak shear force of all specimens

CB	Shear mechanism	Positive Drift		Negative Drift	
		$\sqrt{f_c'}A_{cw}$ (psi)	% of total shear	$\sqrt{f_c'}A_{cw}$ (psi)	% of total shear
CB1	V_{HPFRC}	6.2	60%	6.9	65%
	V_d	1.3	12%	1.1	11%
	V_s	2.9	28%	2.7	25%
CB2	V_{HPFRC}	4.4	52%	5.1	59%
	V_d	1.3	15%	1.4	16%
	V_s	2.8	33%	2.2	25%
CB3	V_{HPFRC}	5.4	56%	5.7	56%
	V_d	1.0	11%	1.5	15%
	V_s	3.2	33%	2.9	29%
CB4	V_c	2.7	36%	3.2	42%
	V_d	1.5	20%	1.0	13%
	V_s	3.3	44%	3.3	44%
CB5	V_{HPFRC}	3.6	38%	3.8	39%
	V_s	5.8	62%	5.9	61%
CB6	V_{HPFRC}	3.7	42%	3.4	40%
	V_s	5.2	58%	5.1	60%

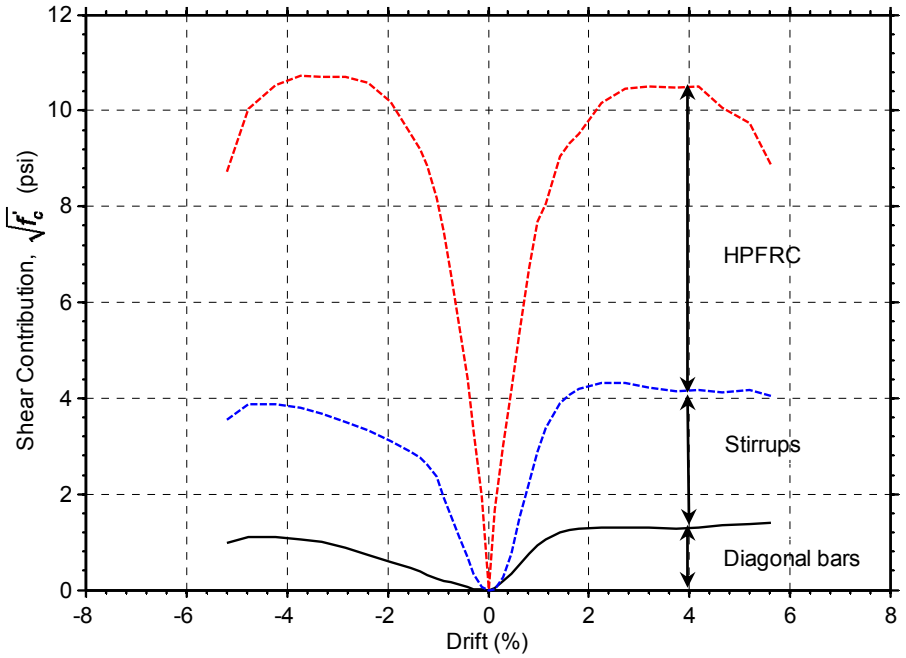

(a) Specimen CB-1

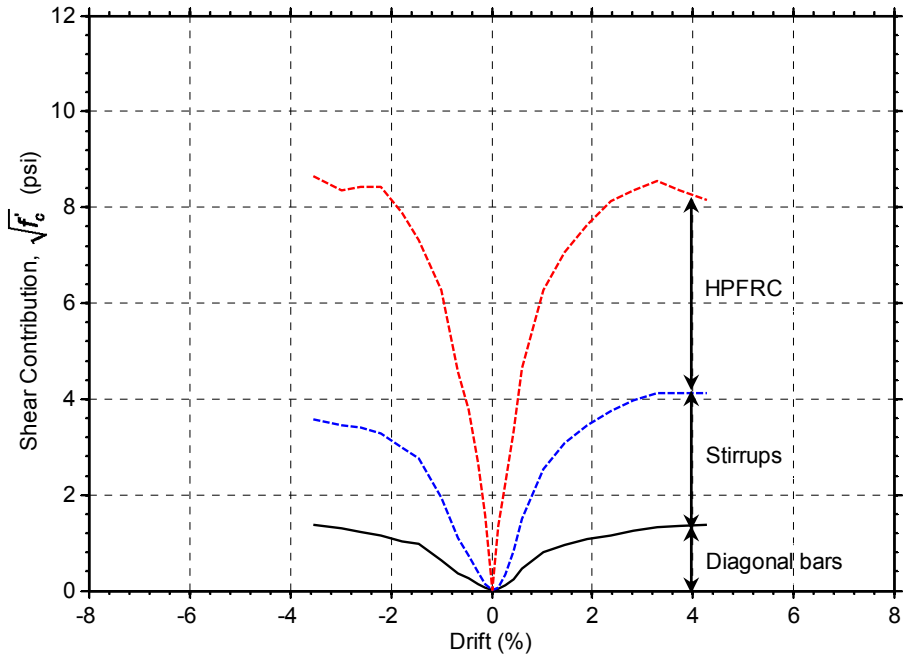

(b) Specimen CB-2

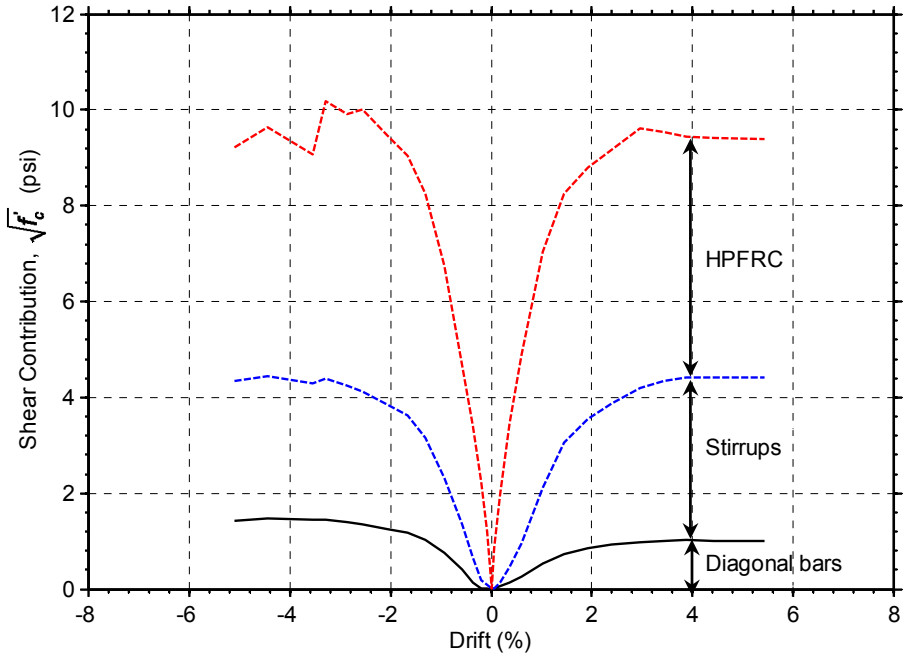

(c) Specimen CB-3

Figure 4.48 Estimated shear contribution from HPFRC, diagonal bars, and stirrups for Specimens CB-1, CB-2, and CB-3

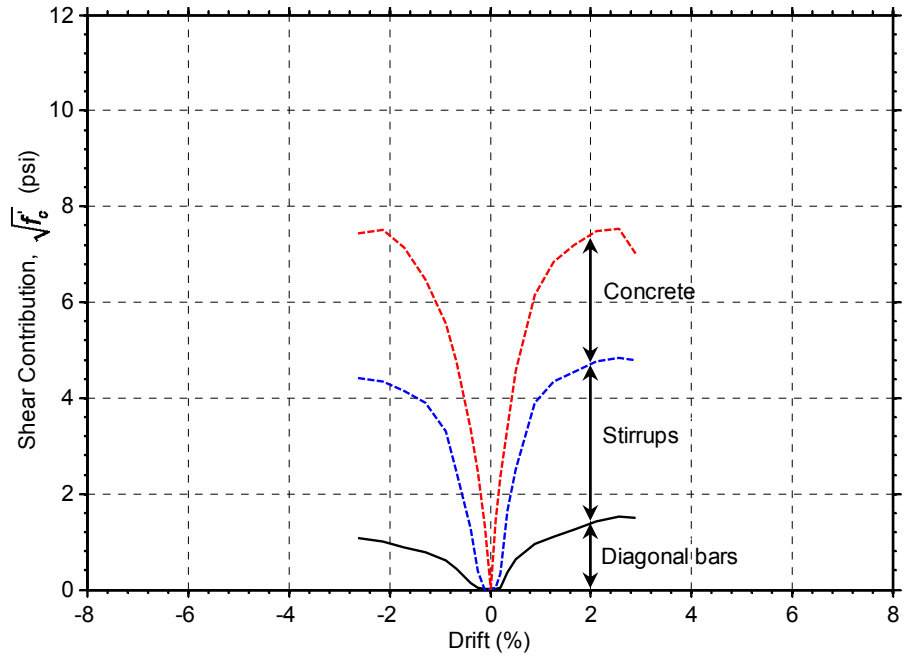

Figure 4.49 Estimated shear contribution from concrete, diagonal bars, and stirrups for Specimen CB-4

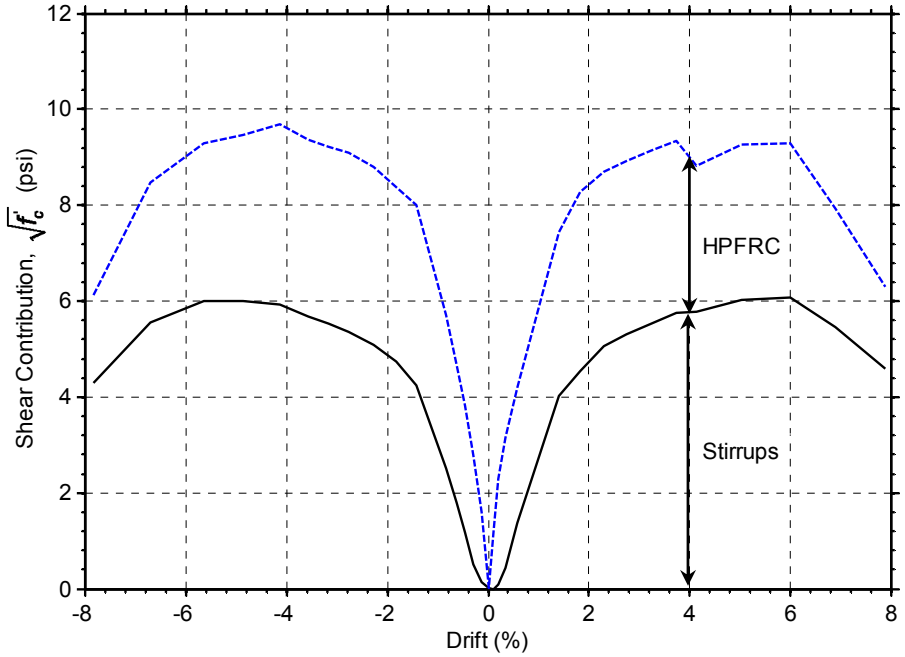

(a) Specimen CB-5

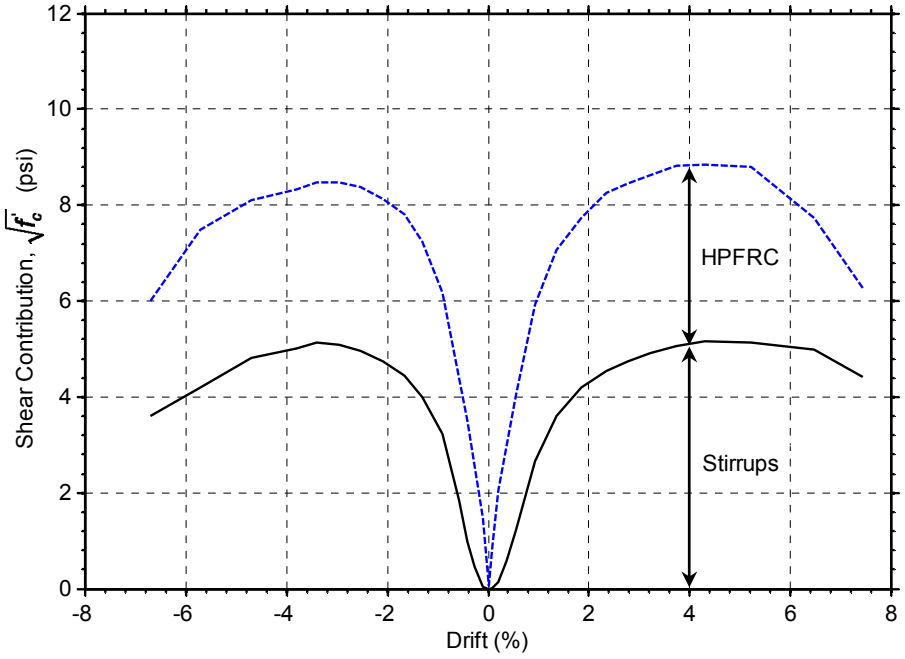

(b) Specimen CB-6

Figure 4.50 Estimated shear contribution from HPFRC and stirrups for Specimens CB-5 and CB-6

4.5.3 Sliding Shear Response

Sliding occurred along through-depth flexural cracks within plastic hinge regions. In these locations, shear strain calculated from Optotrak marker readings would be overestimated due to the effect of sliding shear displacement. It is therefore important to identify when significant sliding first occurred so that an accurate estimation of the actual shear strain can be made. Moreover, estimation of sliding displacements will allow the evaluation of their contribution to total drift in the coupling beam specimens, as will be discussed in Section 4.8.

Shear sliding was identified from the shear versus relative horizontal displacement response obtained from readings of makers in the two rows adjacent to the sliding plane (one row on either side) (see Figure 4.51 for the particular case of Strip 2 in Specimen CB-2). From this response, a secant stiffness from zero force to peak force during the loading portion of each cycle was calculated. The drift at which sliding began was assumed to correspond to the intersection of tangent lines drawn at low and high drifts in the sliding stiffness versus drift plot, as shown in Figure 4.52.

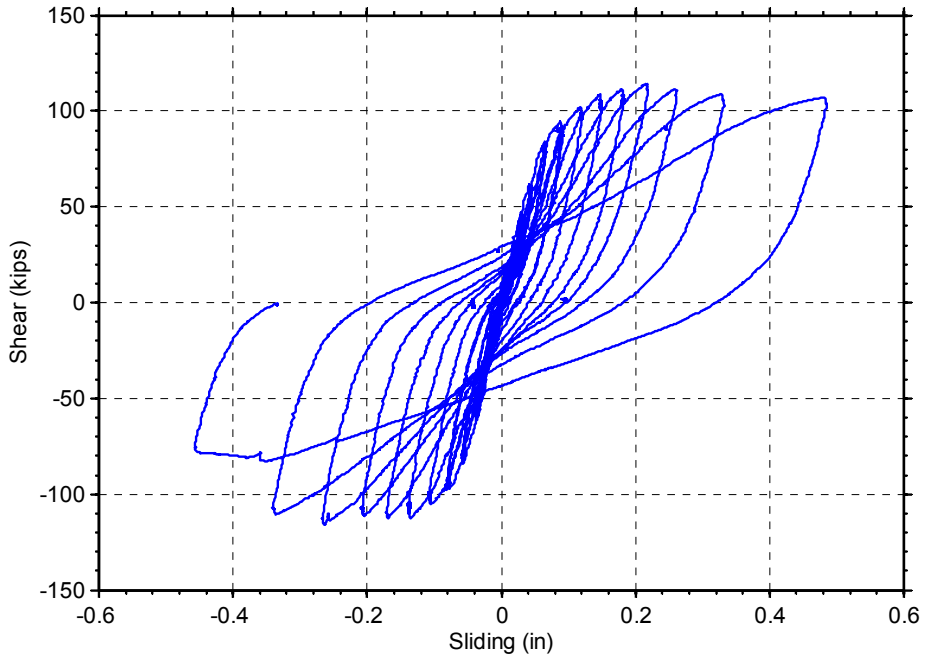

Figure 4.51 Load versus relative horizontal displacement response for Strip 2 of Specimen CB-2

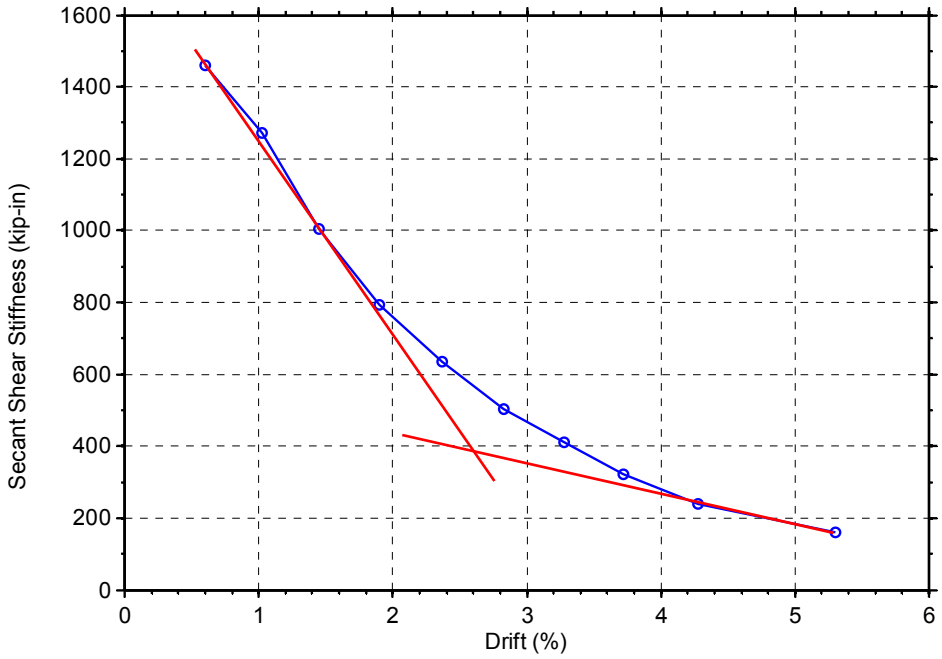

Figure 4.52 Secant shear stiffness (for marker strip involving sliding plane) versus drift response and identification of drift at which sliding displacements were assumed to begin

Sliding occurred within Strips 2 and 12 for specimens with 2.75 aspect ratio (CB-1, CB-2 and CB-4). For the specimens with 3.3 aspect ratio (CB-3 and CB-5), sliding was observed at Strips 2 and 11. For the end strips incorporating the beam-wall interfaces, it was assumed that sliding occurred from the beginning of the tests. Table 4.12 lists the specimen drift and location where sliding was detected using the approach mentioned above.

From Table 4.12, it can be seen that all specimens sustained shear forces greater than 80% of the peak shear at drifts substantially greater than that at which sliding was assumed to begin. Sliding displacement causes pinching of load-drift hysteresis, reducing the energy dissipation capacity. However, hysteresis response for all specimens, except Specimen CB-6, showed little or no pinching, indicating minimal effect of sliding displacement. As seen in Section 4.8, the contribution of sliding displacement to overall drift was less than 15%, which reflected the minimal impact of sliding displacement. After flexural cracks developed at the ends of beams, the strength of beams was

maintained until the end of the test due to increasing strength contribution of diagonal bars as they strain hardened.

Table 4.12 Drift at which sliding was assumed to begin

Specimen	Loading Direction	% Drift at which sliding was first observed		Maximum drift with 80% peak force
		Second strip from top end	Second strip from bottom end	
CB1	Positive	2.7	2.3	5.6
	Negative	2.0	2.0	5.2
CB2	Positive	2.4	2.4	5.7
	Negative	2.2	2.2	3.8
CB3	Positive	3.0	2.4	5.3
	Negative	2.5	2.5	4.6
CB4	Positive	2.1	1.7	3.0
	Negative	1.7	1.7	2.6
CB5	Positive	4.1	3.2	6.8
	Negative	4.9	3.1	6.8
CB6	Positive	None	None	6.4
	Negative	None	None	5.8

Figure 4.53 shows shear sliding displacements at selected drifts in both loading directions for all tested specimens. It can be seen that sliding displacements were pronounced at the beam-wall interfaces and beam ends (plastic hinge region) for all specimens.

HPFRC Specimens CB-1 to CB-3 which contained diagonal bars, showed stable behavior at drifts as large as 5% without significant pinching in their load versus drift hysteresis response (Figure 4.54 (a)-(c)). Despite its lower drift capacity, RC specimen CB4, with diagonal bars, also showed stable behavior after sliding occurred, but with a drift capacity on the order of 3% (Figure 4.54 (d)). This indicates that diagonal bars can effectively minimize the degradation of stiffness associated sliding shear, as suggested by Paulay (1974).

Specimen CB-5, without diagonal bars and with an aspect ratio of 3.3, showed a stable response even after sliding started. Hysteresis response of this specimen did not show excessive pinching due to the minimal effect of sliding displacement discussed earlier.

Specimen CB-6, without diagonal bars and with a 2.75 aspect ratio, on the other hand, showed significant sliding displacements at the bottom beam-wall interface during the later drift cycles, resulting in larger pinching in the hysteresis response compared to the other specimens. Sliding displacements of almost 1 in. were monitored at 4.7% drift in the negative direction. No appreciable sliding was observed within the beam because damage was localized at the bottom beam-wall interface.

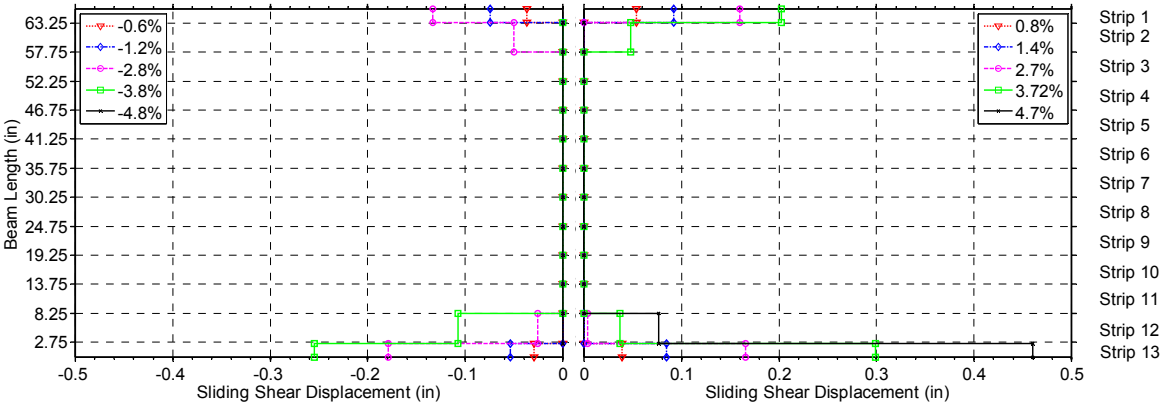

(a) Specimen CB-1

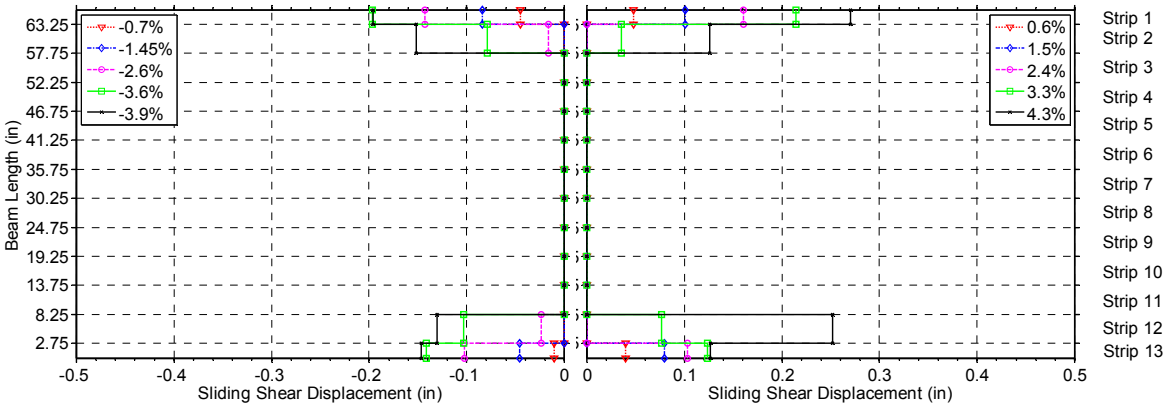

(b) Specimen CB-2

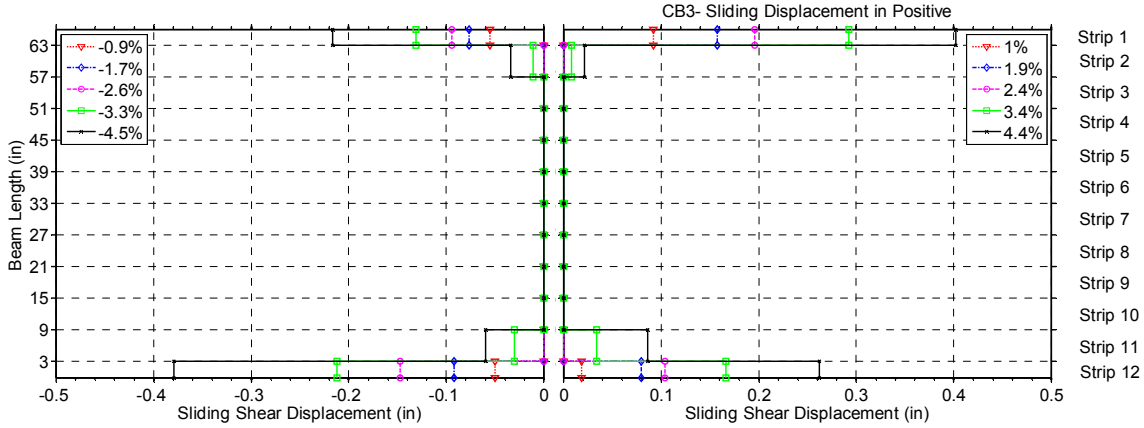

(c) Specimen CB-3

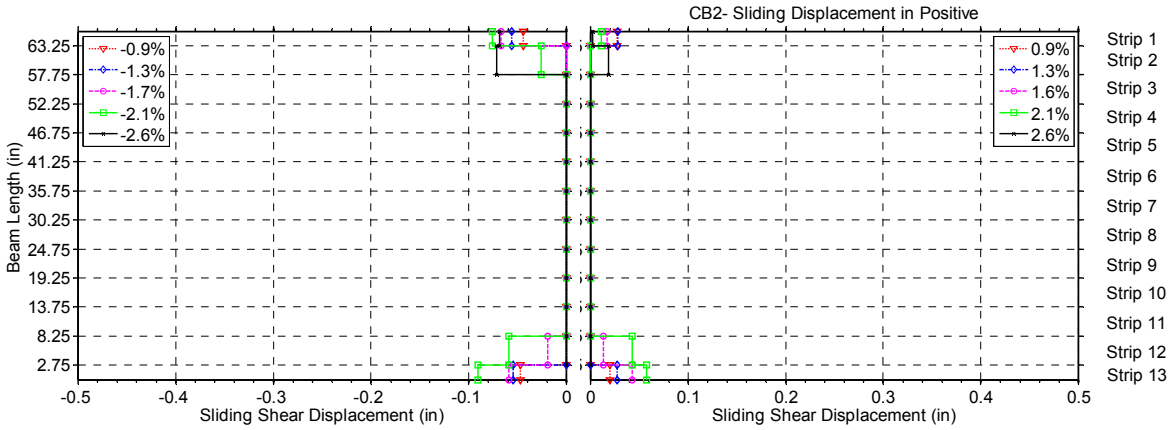

(d) Specimen CB-4

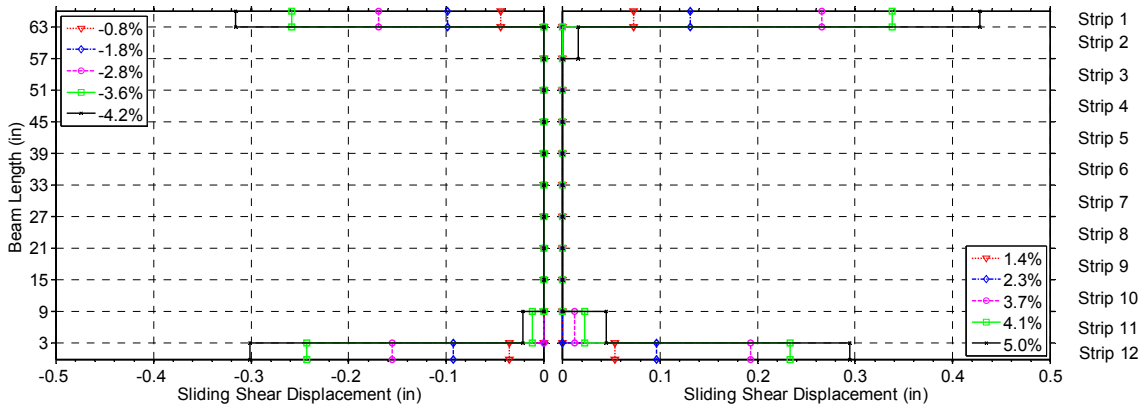

(e) Specimen CB-5

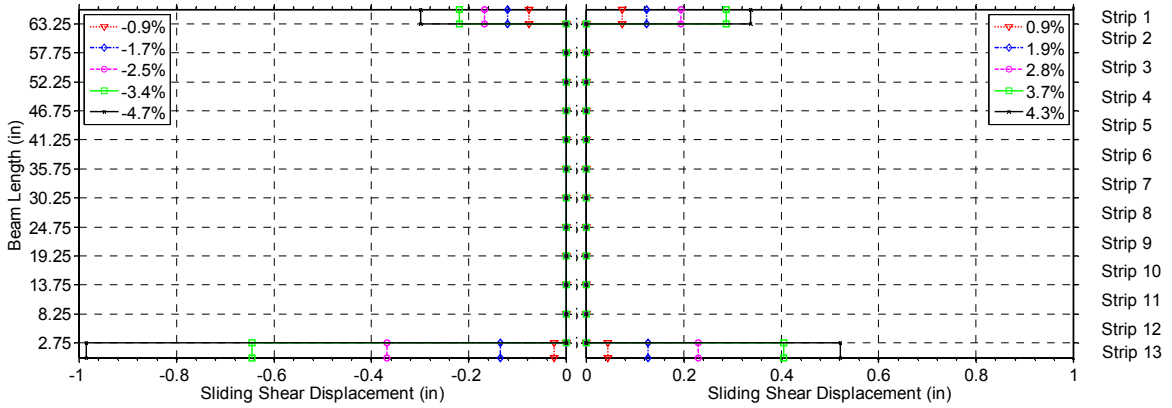

(f) Specimen CB-6

Figure 4.53 Sliding shear displacement at selected cycle peak drifts

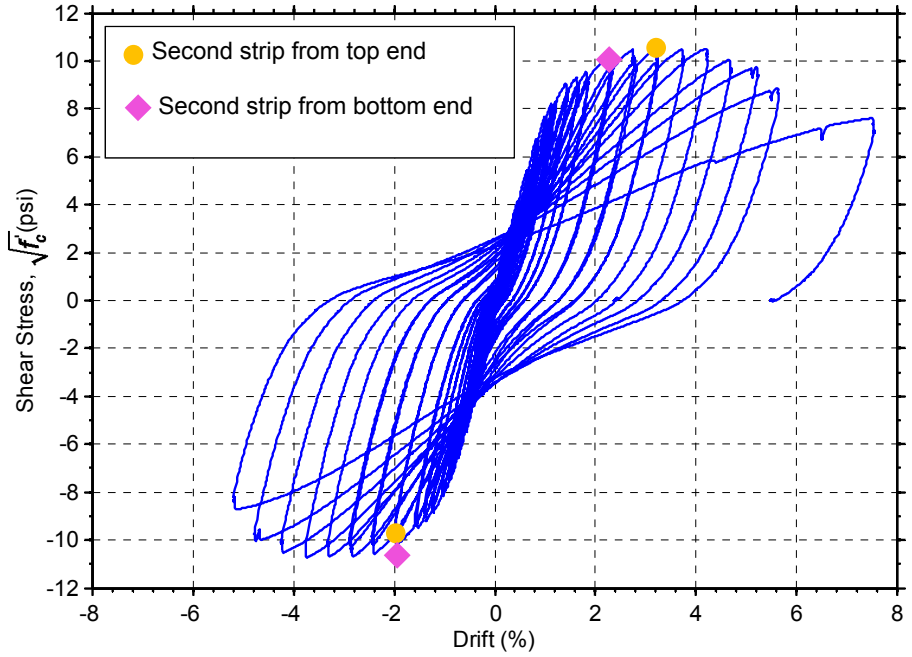

(a) Specimen CB-1

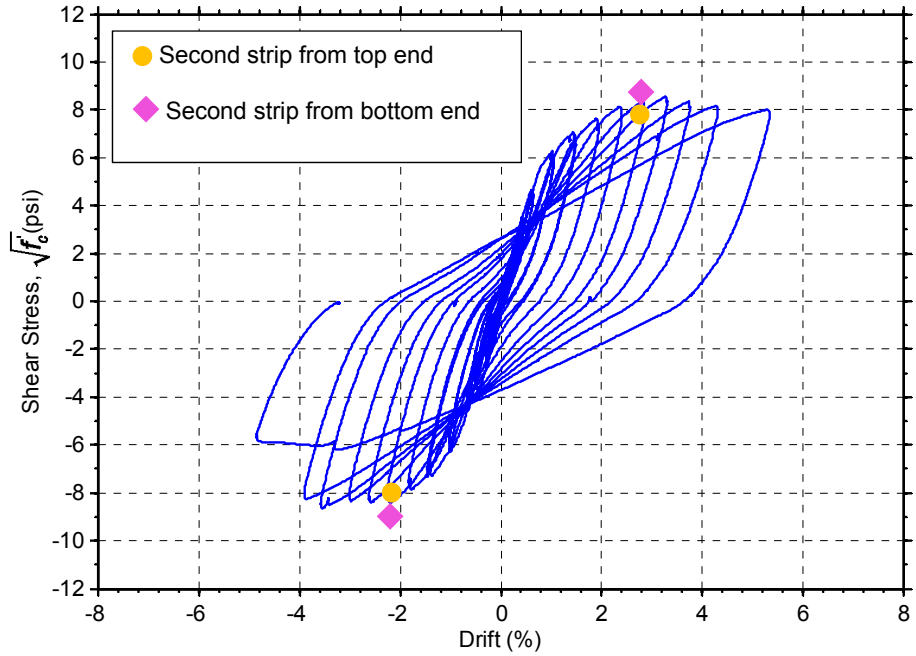

(b) Specimen CB-2

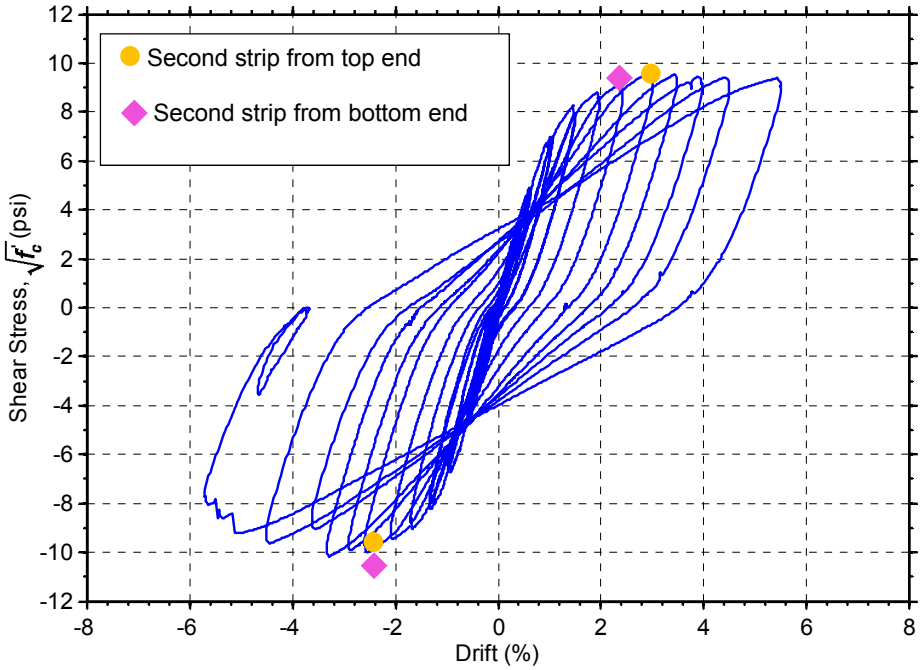

(c) Specimen CB-3

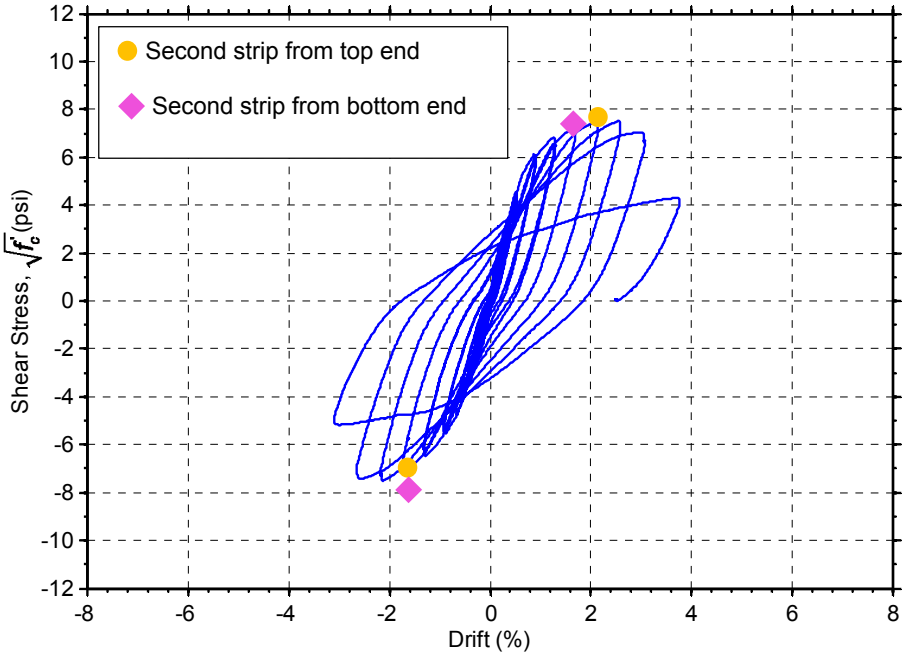

(d) Specimen CB-4

Figure 4.54 Drift at which sliding was assumed to begin

4.5.4 Average Shear Strains

From measurements obtained through the Optotrak system, it was possible to determine the shear strain field over the length of the coupling beams. Shear strains were calculated using Eq. (4.11) in Section 4.1.4. Average shear strain in each strip was then determined by averaging shear strain of all squares in that strip. For strips in which sliding displacement occurred, shear strain was calculated up to the point where sliding was assumed to begin (see Section 4.5.3). Therefore, the calculated shear strain in that strip is only an approximation.

The shear stress versus shear strain hysteresis loops for all specimens exhibited pinching. Figure 4.55(a) – (b) show plots of average shear stress versus shear strain in Strips 2 and 12 for Specimen CB-2. Shear strains in these plots included the effect of sliding displacement. Initiation of sliding displacement is marked with the vertical red lines. An average of shear strain from Strips 3 to 11 of Specimen CB-2 was plotted against average shear strain in Figure 4.55(c).

Figure 4.56 shows the shear strain at selected drifts for all specimens. The data plotted indicate larger shear strains near the ends of the beams for all specimens. This was expected due to the softening caused by flexural cracking. For all HPFRC specimens, shear strain in the middle region especially near the inflection point, was below 0.005 rad throughout the tests. This shear strain level corresponded to minor damage (narrow diagonal cracks of width less than 0.008 in.).

For Specimen CB-1, which was subjected to the largest shear among all test specimens, large shear distortions were measured in Strip 10-12, as shown in Figure 4.56(a). In particular, Strip 11 exhibited the largest shear strain because a large diagonal crack (0.06 in.) was developed in this strip with a shear strain of 1.9% at approximately 4.7% drift. Shear strain in Strips 10 to 12 were greater than 1% at 3.8% drift in the negative direction, while the shear strain in Strip 9 was close to 1% at this drift level. Despite this high shear strain, Specimen CB-1 still showed a stable response up to 5% drift in the negative loading direction.

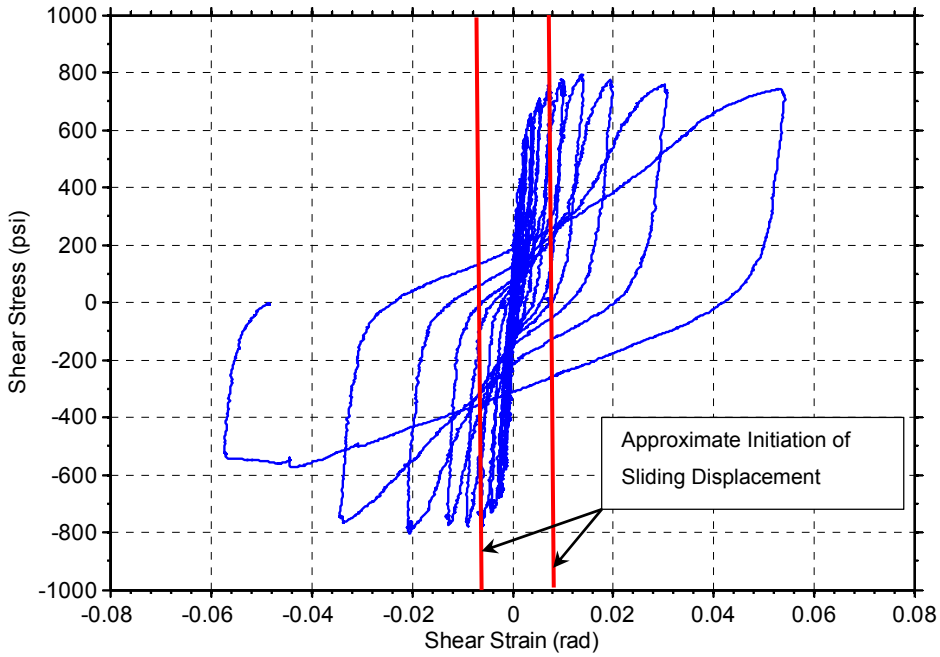

(a) Strip 2

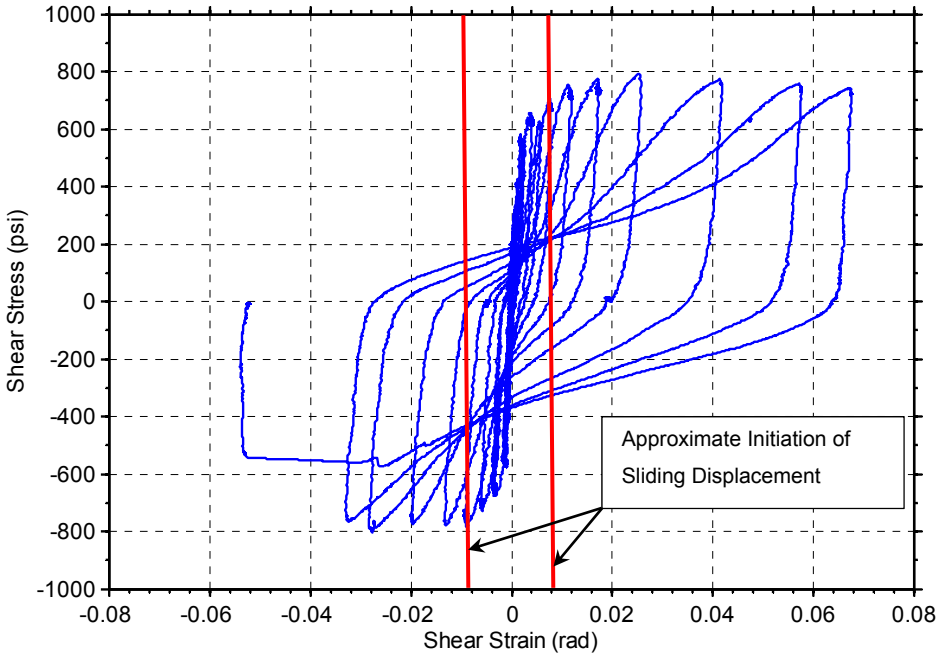

(b) Strip 12

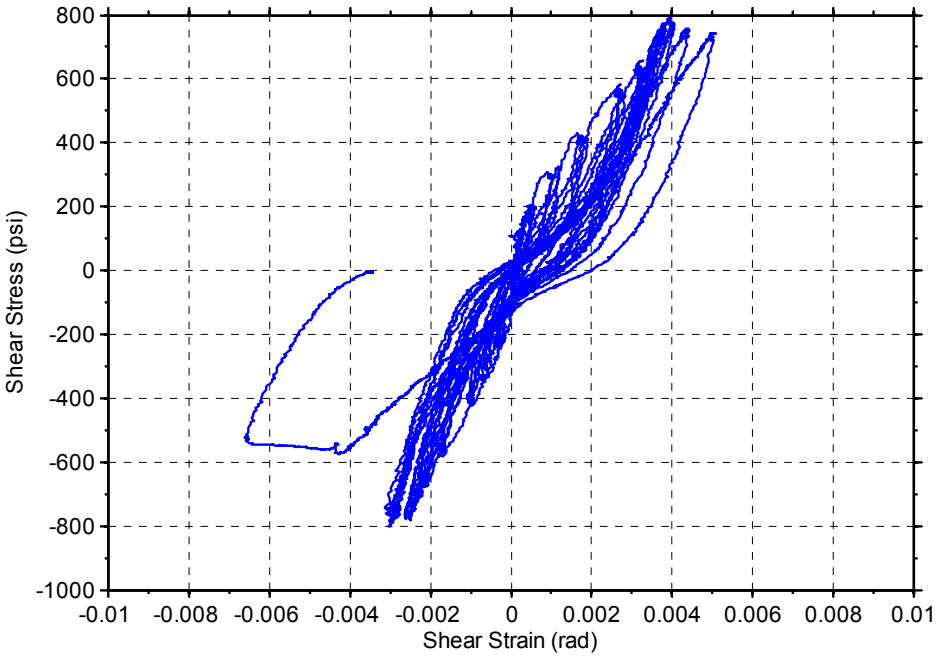

(c) Strip 3 to Strip11

Figure 4.55 Shear stress versus shear strain for Specimen CB-2

Shear distortions in the RC specimen (CB-4) had a similar trend as that in the HPFRC specimens. Shear strains in Strips 4 to 10 were below 0.5% throughout the test. The largest shear strain that could be reliably measured was 1% in Strip 12 for drifts of up to 2%. Spalling of concrete made it impossible to determine shear strains at larger drifts.

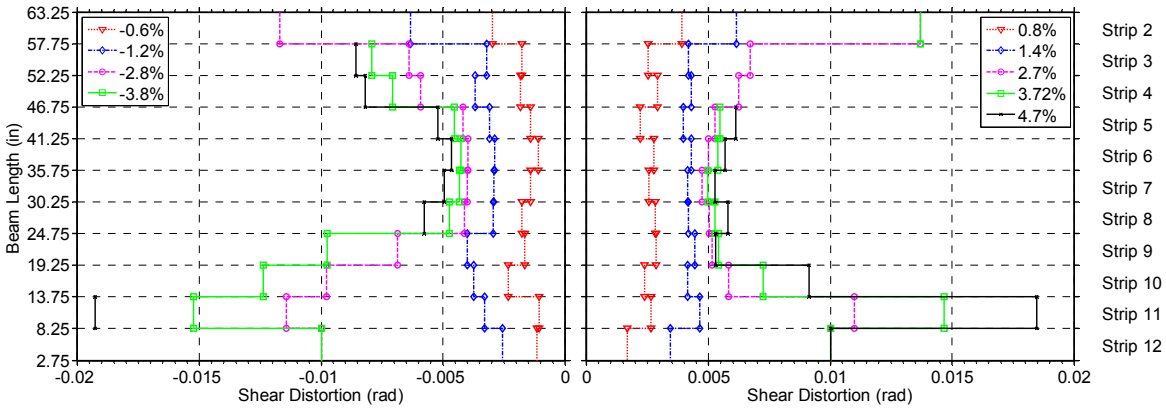

(a) Specimen CB-1

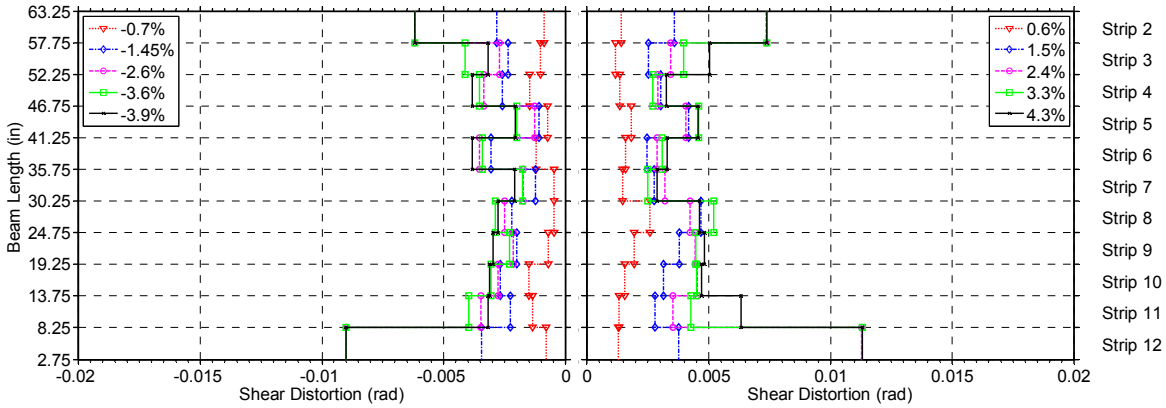

(b) Specimen CB-2

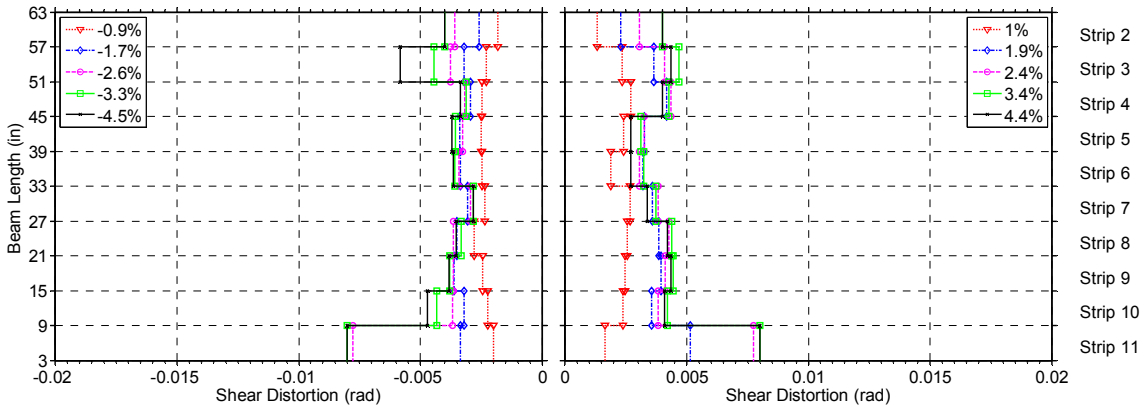

(c) Specimen CB-3

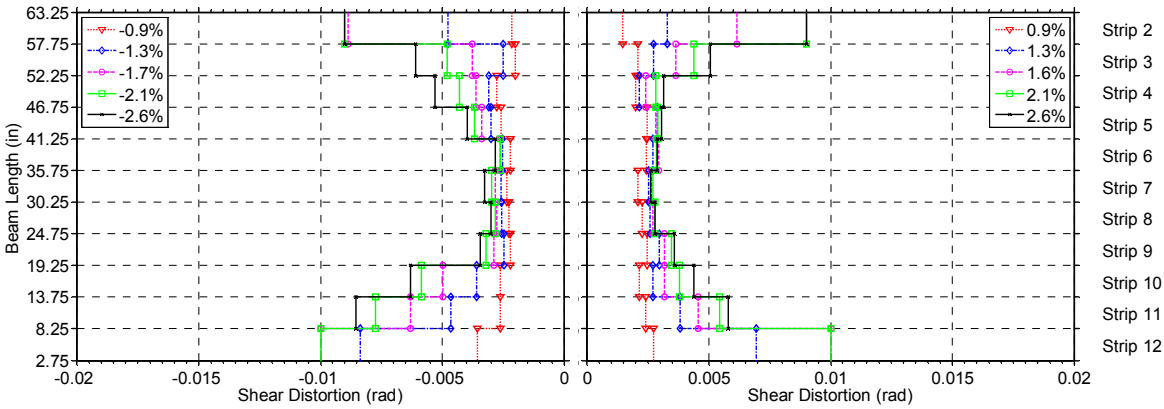

(d) Specimen CB-4

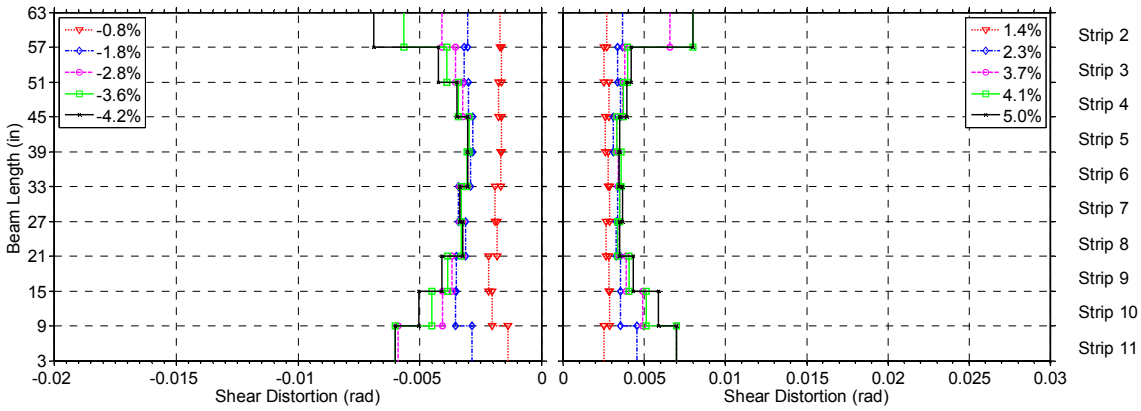

(e) Specimen CB-5

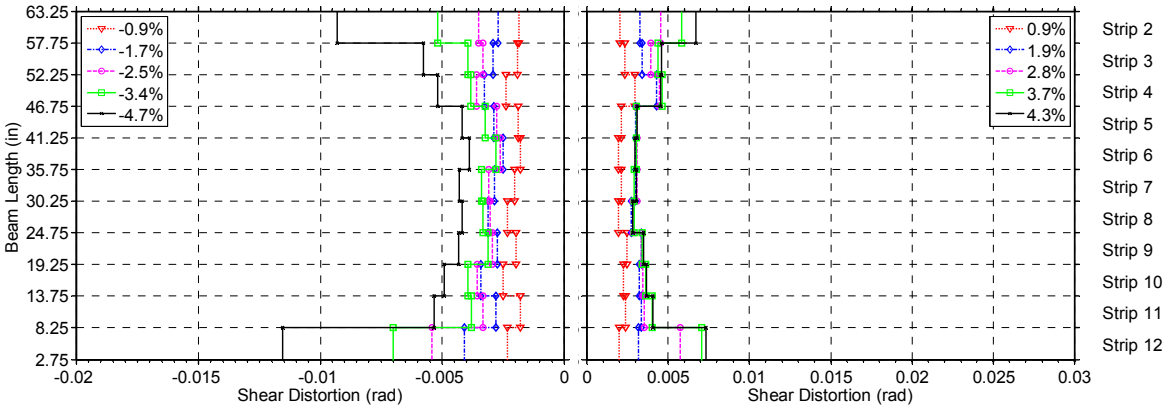

(f) Specimen CB-6

Figure 4.56 Average shear strains for all specimens

4.5.5 Shear Friction

The shear-friction concept (Hofbeck et al. 1969) provides a convenient approach to design members susceptible to shear sliding. Using this concept and assuming a sliding shear mechanism to develop along the critical horizontal crack, the nominal shear strength of the coupling beams can be estimated as:

$$V_n = \mu[(A_{vf} f_y)_L + (A_{vf} f_y)_D \cos\alpha + P] + (A_{vf} f_y)_D \sin\alpha \quad (4\text{-}22)$$

where V_n is the nominal shear strength (kips), μ is the shear friction coefficient, A_{vf} is the area of steel crossing the shear plane (in^2), f_y is the yield stress of the steel crossing the shear plane (ksi), P is the axial force in the coupling beams, and α is the angle of inclination of diagonal reinforcement with respect to the beam longitudinal axis. The subscript L and D refer to longitudinal and diagonal reinforcement, respectively.

The shear strength estimated from the shear-friction analogy includes two components of the tensile force in the diagonal reinforcement $(A_{vf} f_y)_D$. A normal (clamping) component $(A_{vf} f_y)_D \cos\alpha$ is associated with the frictional force $\mu(A_{vf} f_y)_D \cos\alpha$, while the component parallel to the crack, $(A_{vf} f_y)_D \sin\alpha$, directly resists sliding shear. The normal or clamping force further increases with the presence of axial force in the coupling beams. This impact is addressed with the incorporation of the frictional force μP.

Rearranging Eq. (4.22) such that the shear friction coefficient is a common factor to the right hand side of the equation yields,

$$V - (A_{vf} f_y)_D \sin\alpha = \mu[(A_{vf} f_y)_L + (A_{vf} f_y)_D \cos\alpha + P] \quad (4\text{-}23)$$

$V_{sf} = (A_{vf} f_y)_L + (A_{vf} f_y)_D \cos\alpha + P$, Eq. (4.23) can be written as

$$V - (A_{vf} f_y)_D \sin\alpha = \mu V_{sf} \quad (4\text{-}24)$$

For Specimen CB-5 and CB-6, the terms associated with diagonal reinforcement were omitted from the equation because of no diagonal bars were present in these beams.

In estimating the shear friction coefficient from Eq. (4.24), the applied shear V was substituted for the nominal shear strength V_n, and the actual yield stress f_y obtained from reinforcing bar tests was used and multiplied by a factor 1.1 to account for strain

hardening of the reinforcement. Moreover, to account for a flexural crack, only half of the total area of reinforcement (A_{vf}) crossing the shear plane was used in the equation.

Figure 4.57 shows the envelope of the shear force assumed to be resisted through a shear friction mechanism ($V-(A_{vf}f_y)_D \sin\alpha$), normalized by the shear friction strength (V_{sf}), versus the sliding displacement along the horizontal cracks that formed in the region where the dowel bars were terminated. Horizontal sliding was calculated from the differential horizontal movement of Optotrak markers in adjacent rows of the strips where the dowel bars were terminated.

The data plotted in Figure 4.57 shows that the peak calculated shear friction coefficient varied between 0.35 and 0.56. These coefficients are much lower than that of 1.4 for concrete placed monotonically, specified in ACI Building Code (ACI 318-11 Section 11.6.4.3). Thus, using the shear-friction model to predict sliding shear capacity of the coupling beams would not be conservative. This was expected because in the tests of Specimens CB-1 through CB-5, the dominant sliding shear displacements developed within the precast coupling beams along a sliding plane created by flexural cracks. These sliding shear displacements were not created by a direct shear and thus, using the shear-friction model with the shear friction coefficients specified in the ACI Building Code would not be appropriate. The data plotted in Figure 4.57 indicate that a shear friction coefficient of 0.35 might be more suitable for use in a shear-friction model and adequate to control excessive sliding along the critical crack at the end of the dowel reinforcement in HPFRC coupling beams.

Figure 4.58 shows the envelope of the shear force assumed to be resisted through a shear friction mechanism ($V-(A_{vf}f_y)_D \sin\alpha$), normalized by the shear friction strength (V_{sf}), versus the sliding displacement along the cold joints for Specimen CB-5 and CB-6. The data plotted in these figures shows that the peak calculated shear friction coefficient was 0.35 and 0.43 for Specimen CB-5 and CB-6, respectively. These coefficients are slightly lower than that of 0.6 for concrete placed against hardened concrete not intentionally roughened, specified in ACI Building Code (ACI 318-11 Section 11.6.4.3).

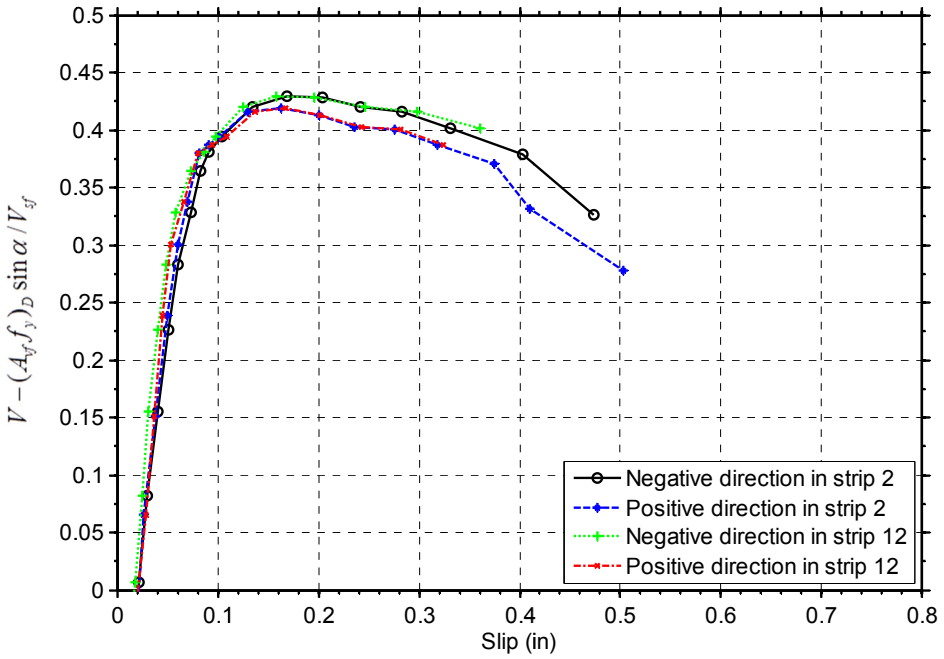

(a) Specimen CB-1

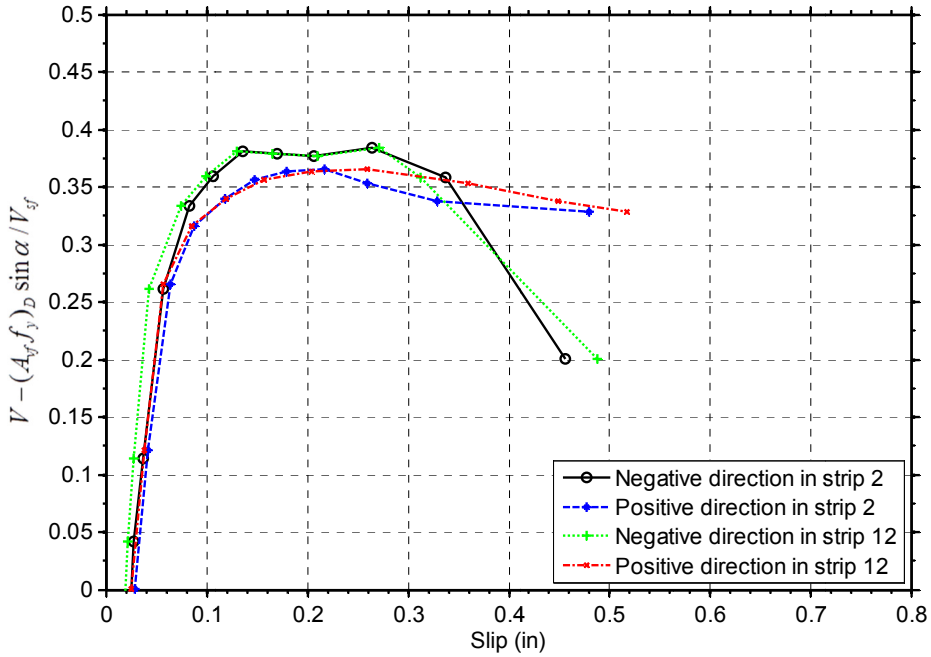

(b) Specimen CB-2

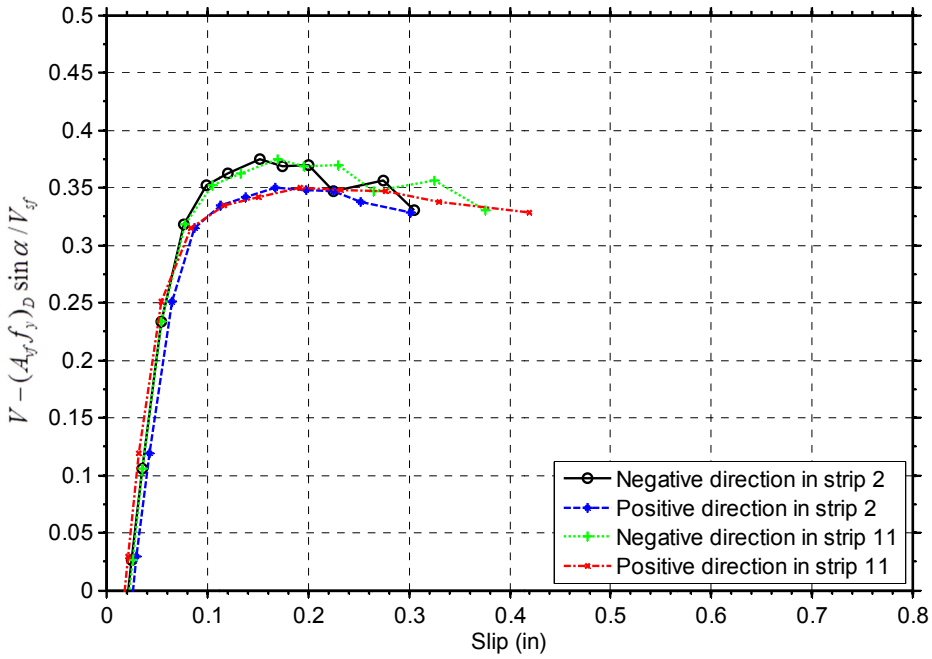

(c) Specimen CB-3

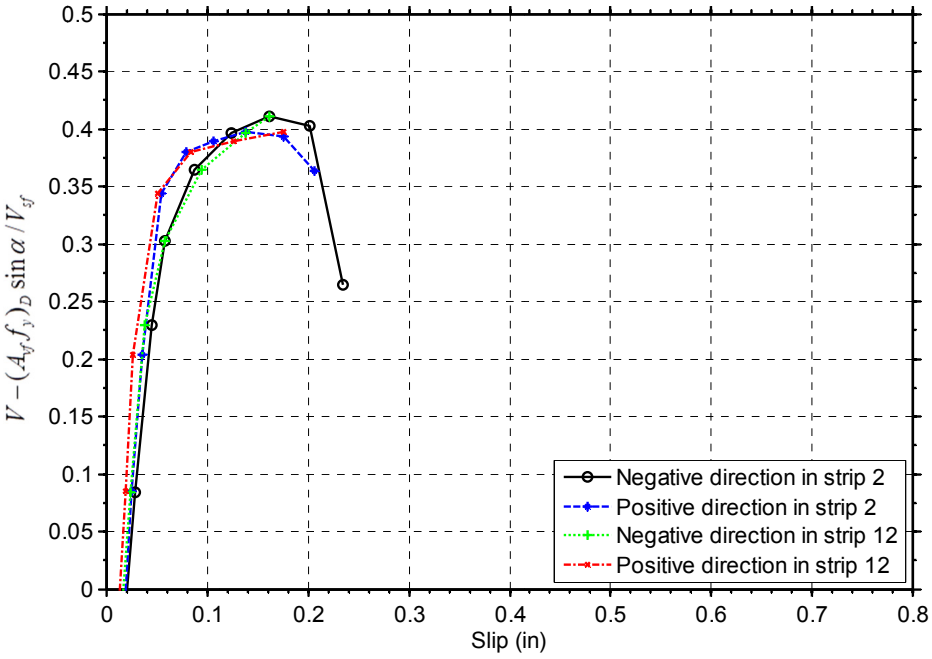

(d) Specimen CB-4

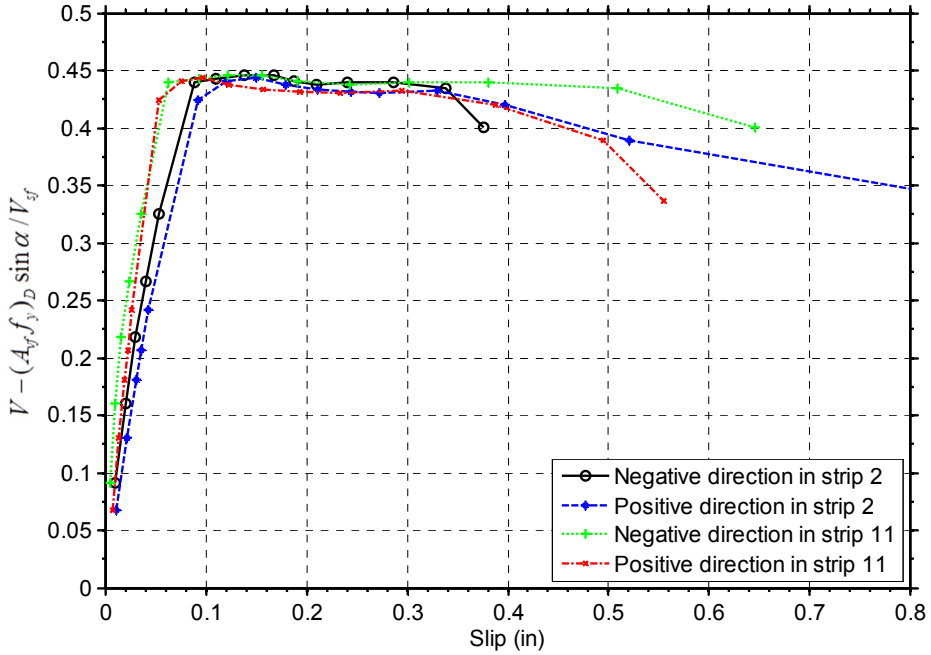

(e) Specimen CB-5

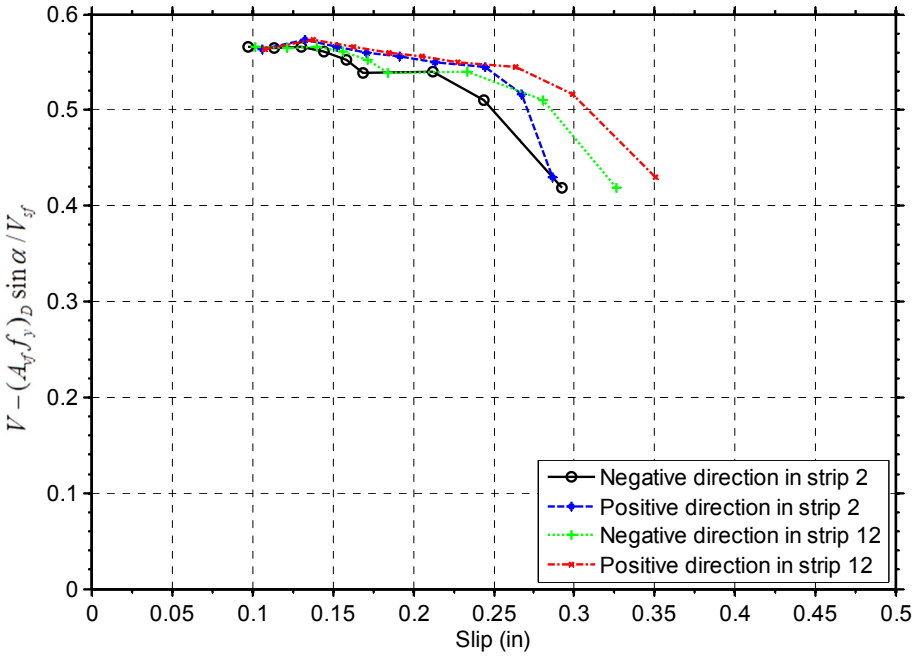

(f) Specimen CB-6

Figure 4.57 Shear force resisted by shear friction normalized by shear friction strength versus slip

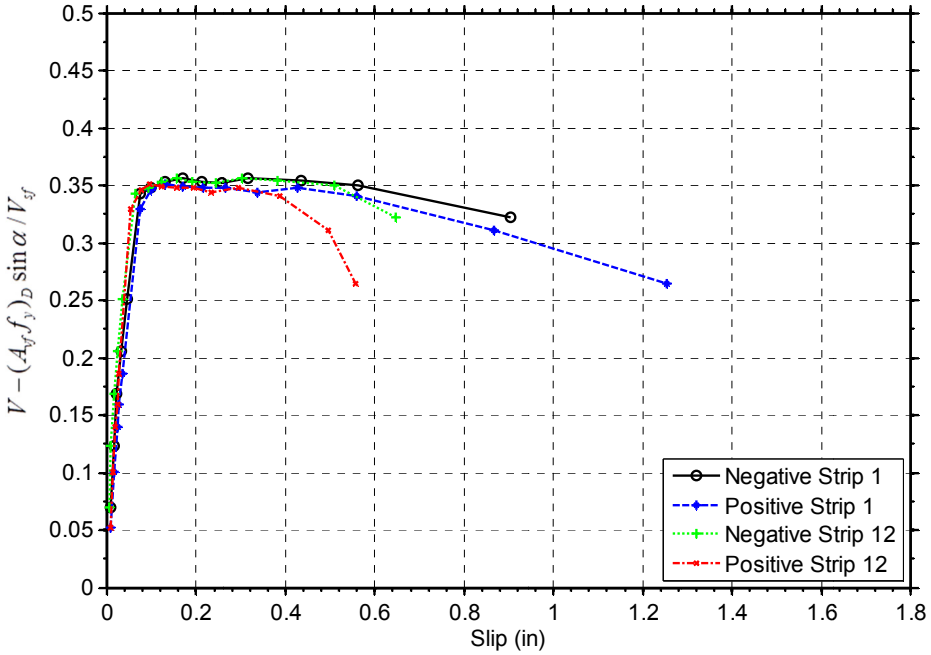

(a) Specimen CB-5

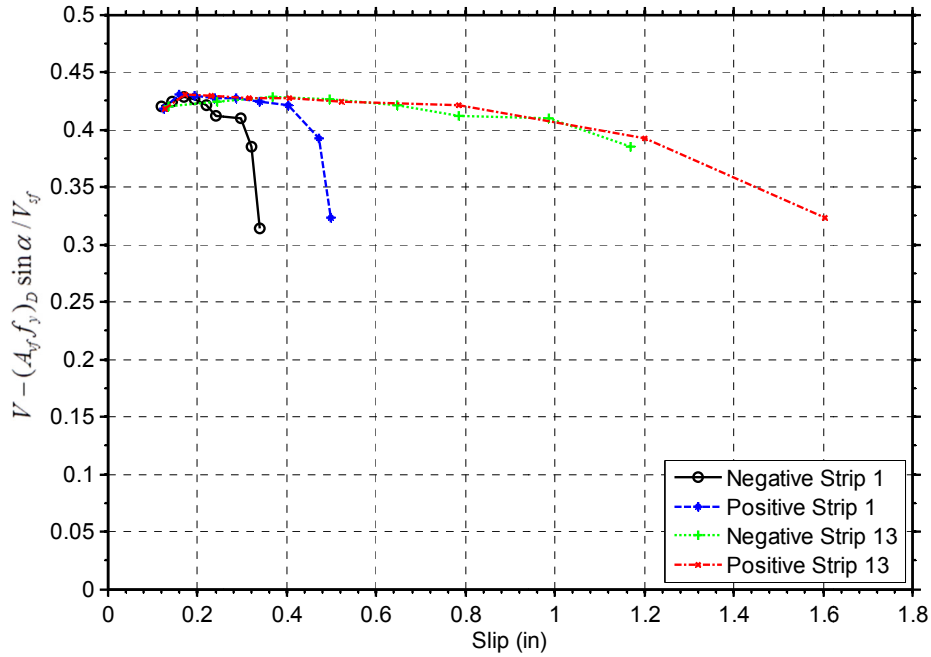

(b) Specimen CB-6

Figure 4.58 Shear force resisted by shear friction normalized by shear friction strength versus slip at cold joints for Specimens CB-5 and CB-6

4.6 REINFORCEMENT STEEL STRAINS

Strains in the reinforcing steel were measured by gauges capable of measuring strains beyond the yield strain. The location and label of the strain gauges attached on longitudinal, diagonal, and transverse reinforcement in each specimen is shown in Figure A.1-A.6 in Appendix A. The progress of yielding for the reinforcement in each specimen is shown in Figure 4.59 with black circles indicating yielding of reinforcement.

In Specimen CB-1, yielding of longitudinal reinforcement was first observed at the bottom beam-wall interface (gauge L2) during the cycle to 0.63% drift. At 0.83% drift, values of strains in longitudinal bars (L2, L7, and L8) at the beam-wall interface were above yielding. Yielding also spread to gauge L11, which was 17.5 in. above the bottom beam-wall interface. As discussed in Section 4.4.2, the inflection point was slightly above the midspan, indicating that moment at the bottom end was larger than that at the top end of the coupling beams. Thus, yielding tended to occur in the lower part before the upper part of the specimen. At 1.43% drift, yielding of longitudinal and diagonal reinforcement was recorded in all locations except at the midspan. Strains on longitudinal bars at the midspan (gauge L5 and L10) indicated that reinforcement did not yield throughout the test because of low moment in this location. Yielding of diagonal reinforcement near the midspan (gauge D2 and D5) was detected during the loading cycle of 2.3% drift. At this drift level, a shear of 120 kips ($9.8\sqrt{f_c'}$ (psi)) was applied to the specimen. At the end of the test, yielding of diagonal reinforcement and stirrups was observed all over the beam.

For Specimen CB-2, yielding of longitudinal and diagonal reinforcement extended over 17.5 in. from the ends into the beam. Yielding was first recorded at the beam wall-interface during the loading cycle to 0.63% drift. At this drift level, yielding was also detected in dowel bars at the bottom end and gauge L2, which was 17.5 in. above the bottom beam-wall interface. Yielding progressed into the beam as higher drifts were applied. At the end of the test, only strain gauges at the midspan longitudinal and diagonal reinforcement did not yield, corresponding to very low moment demand in this region.

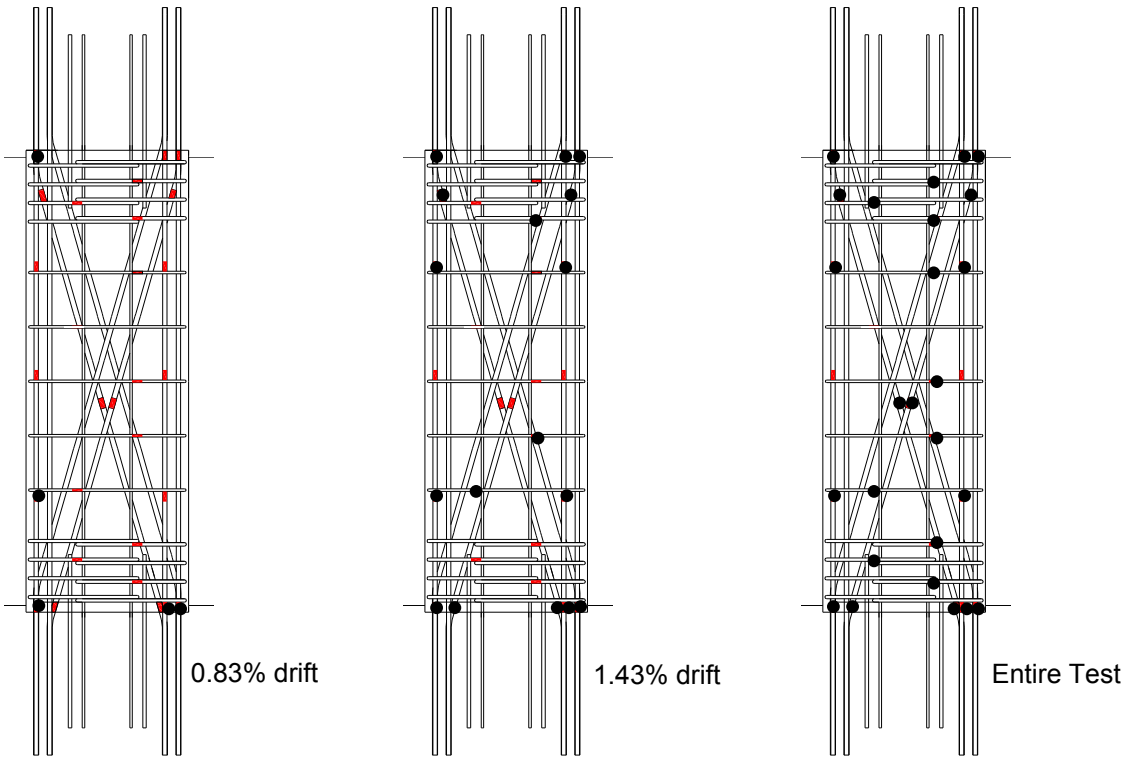

(a) Specimen CB-1

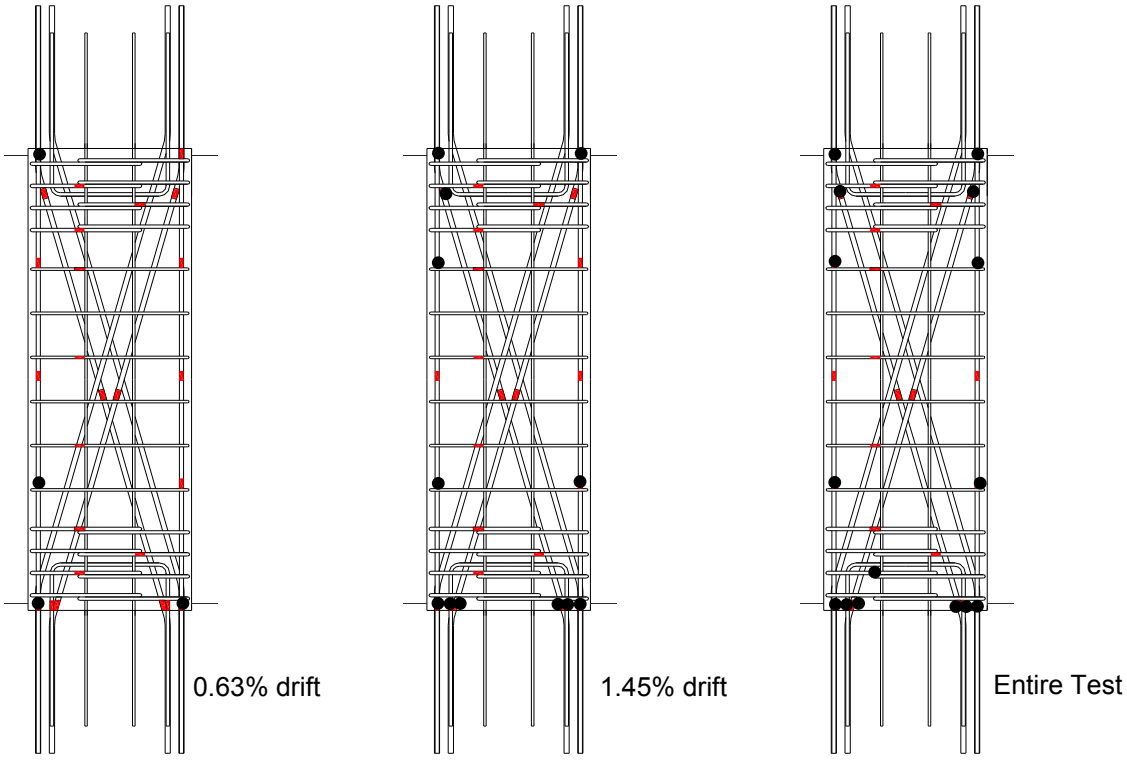

(b) Specimen CB-2

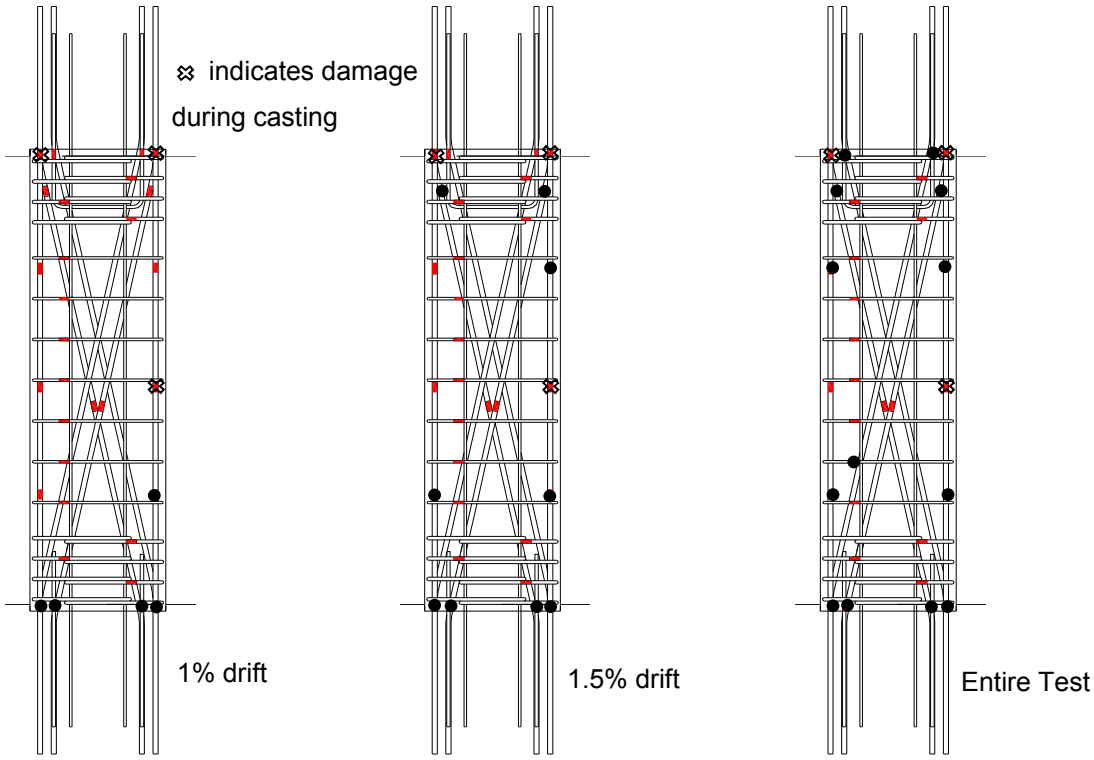

(c) Specimen CB-3

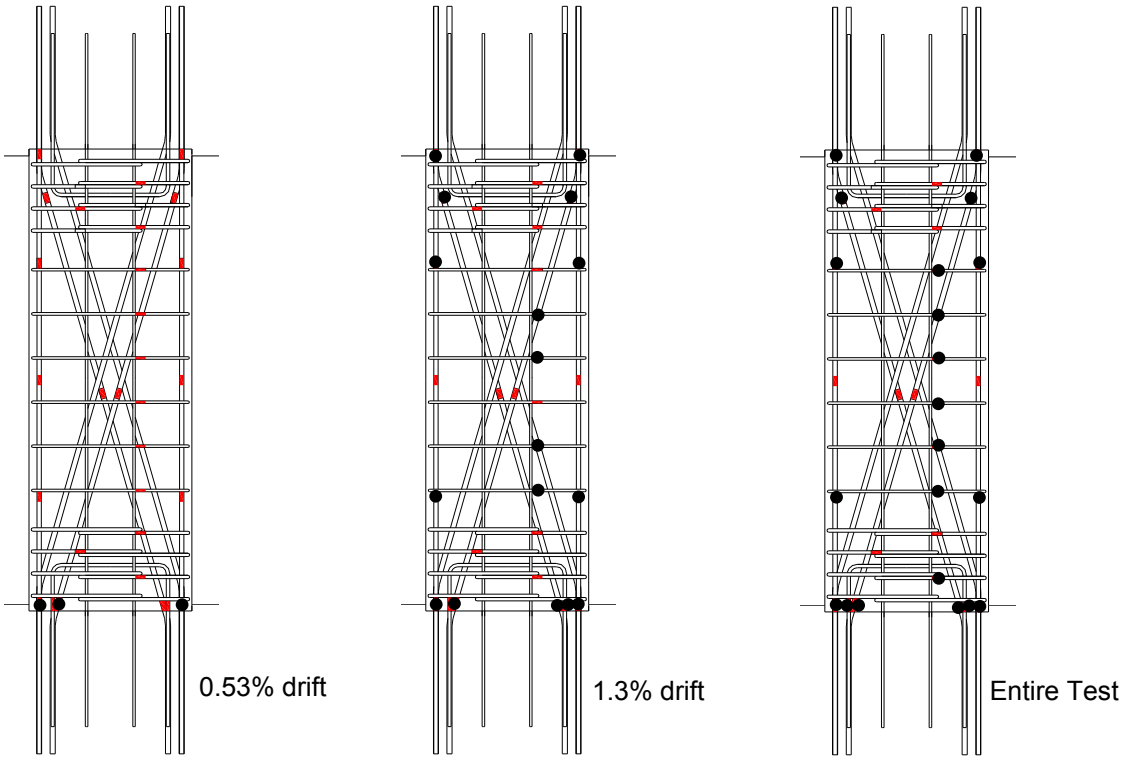

(d) Specimen CB-4

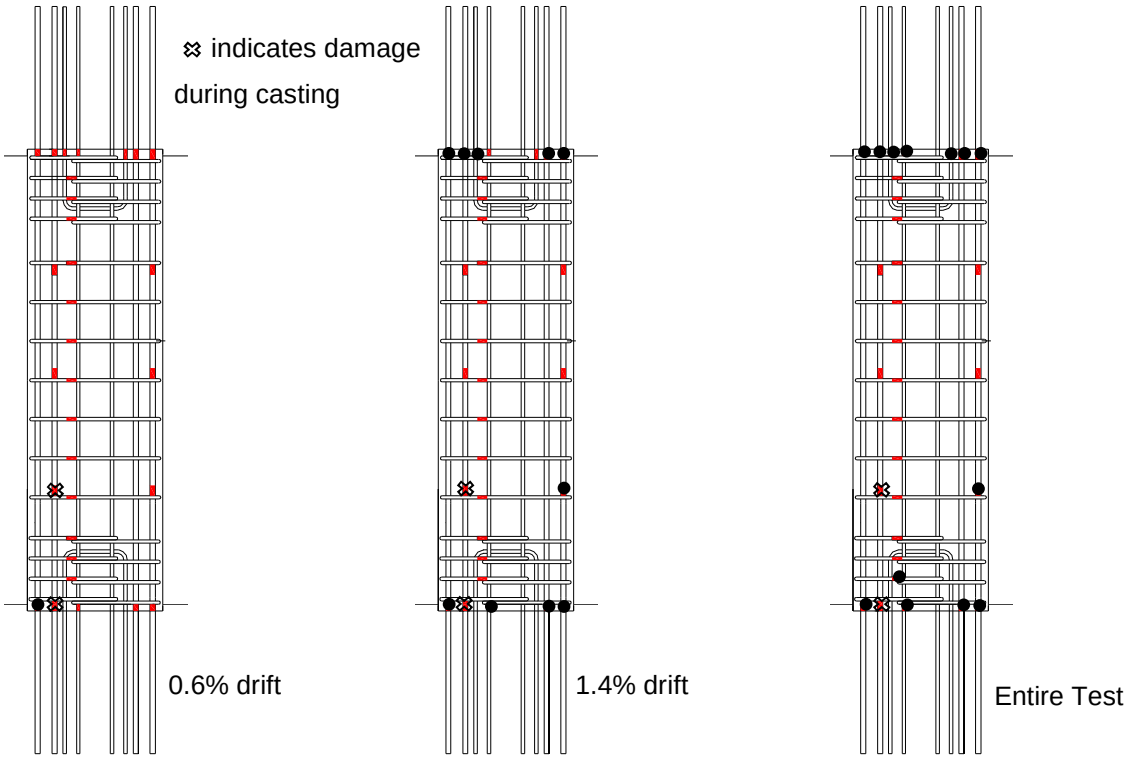

(e) Specimen CB-5

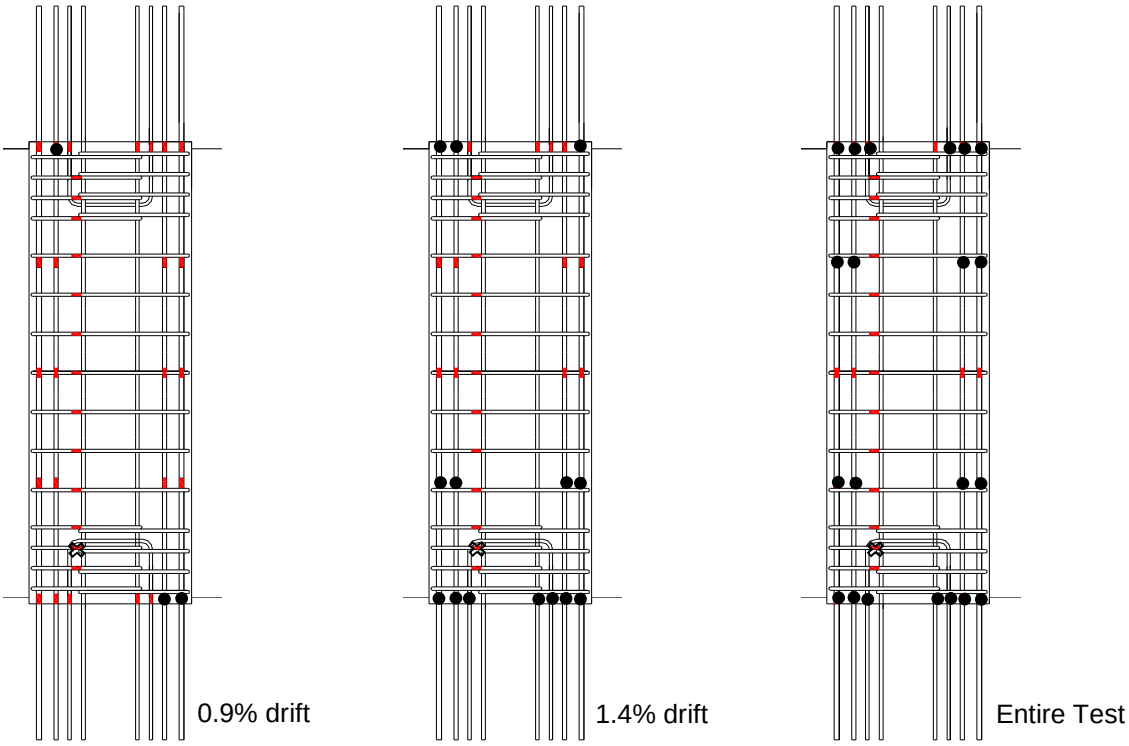

(f) Specimen CB-6

Figure 4.59 Yielding progress of reinforcement

A similar trend to strains in Specimen CB-1 and CB-2 was observed in Specimen CB-3. Yielding of longitudinal and diagonal reinforcement was first detected at the bottom beam-wall interface at approximately 1% drift. The inelastic activity spread into the beam at 1.5% drift. Unfortunately, all strain gauges on the main longitudinal reinforcement at the top beam-wall interface were damaged while casting concrete and strains at this interface could not be recorded. At the termination of the test, most of main reinforcement yielded except longitudinal reinforcement at midspan.

The progress of reinforcement yielding in Specimen CB-4 was similar to the first three specimens. Yielding first occurred at the bottom beam-wall interface due to the larger moment at the bottom than at the top of the specimen. At approximately 1.3% drift, most strain gauges on longitudinal and diagonal reinforcement recorded strains beyond yielding. Only midspan reinforcement did not yield. Readings from strain gauges L2, L4, L7, and L9 revealed significant inelastic response (Figure 4.59(d)) compared to Specimen CB-2, which had a similar reinforcement configuration. The lower amount of inelastic activity in Specimen CB-2 was mainly due to the excellent bond capacity developed between HPFRC and reinforcement.

For Specimen CB-5, yielding was first detected in the strain gauge L1 at the bottom interface at approximately 0.6% drift. As the drift level reached 1.4%, longitudinal and dowel reinforcement at the beam-wall interface had also yielded. Inelastic activity of Specimen CB-5 mostly concentrated at the ends of the coupling beam, corresponding to the large curvature distribution where inelastic behavior was concentrated near both ends of the beam. At the end of the test, yielding in the middle part of the beam was observed only in strain gauge L11, which was 17.5 in. away from the bottom interface.

In Specimen CB-6, yielding was first observed in longitudinal reinforcement at the beam-wall interface at approximately 0.9% drift. Yielding spread 17.5 in. into the beam from the bottom interface at 1.4% drift. At this drift, dowel and intermediate reinforcement at the bottom beam-wall interface had already yielded. As drift increased, more inelastic activity occurred in the upper part of the beam. From Figure 4.59(f), it can be seen that yielding was recorded up to the distance of 17.5 in. from both ends of the beam. This inelastic behavior agrees with the curvature distribution in which inelastic

behavior is shown in the first and last four strips of markers (approximately 20 in. from the ends). Yielding was not detected at the midspan of the beam.

The midspan transverse reinforcement in most HPFRC Specimens, except Specimen CB-1, remained elastic throughout the test. In Specimen CB-1, a transverse reinforcement ratio of 0.46% (and a volumetric ratio of 0.67%) was selected. This reinforcement ratio was smaller than that in other specimens. When subjected to very high shear stress beyond $10\sqrt{f_c'}$ (psi), this transverse reinforcement underwent yielding in most locations. The transverse reinforcement in the middle part (gauge S7 and S8) started to yield during the loading cycle to 1.4% drift. As the drift demand increased, yielding spread to other locations (gauge S4 and S6). Despite yielding of the midspan transverse reinforcement, Specimen CB-1 did not suffer from shear-related damage, indicating that HPFRC effectively provided further shear strength to the beam. As seen in Section 4.5.2, shear contribution from HPFRC in this specimen was beyond $6\sqrt{f_c'}$ (psi).

Transverse reinforcement ratios of 0.56% and 0.61% were selected for Specimen CB-2 and CB-3, respectively. This increase in transverse reinforcement, combined with lower shear demand compared to that of Specimen CB-1, resulted in elastic behavior of transverse reinforcement in these two specimens. Shear-related damage was not observed in these specimens and the contribution from HPFRC to shear was beyond $5\sqrt{f_c'}$ (psi), as shown in Section 4.5.2.

The midspan transverse reinforcement in CB-4, which is similar to that of Specimen CB-2, yielded throughout the beam. At 1.3% drift, four strain gauges in the midspan gave an indication of yielding. As drift increased, yielding spread to other stirrups. At the end of the test, all stirrups yielded, many of which were beyond 0.4%. Compared to Specimen CB-2, it is evident that the contribution of HPFRC to shear is more than that of concrete, resulting in lower strains in transverse reinforcement. It should be noted that the maximum strain recorded in transverse reinforcement of Specimen CB-2 was less than 0.2% throughout the test.

In Specimen CB-5, transverse reinforcement ratio was increased to 1.16% (volumetric ratio of 1.8%). This increase was meant to compensate for the shear contribution from diagonal reinforcement, which was left out of this specimen.

Throughout the test, transverse reinforcement did not show a sign of yielding even though very high drift demand (7%) was imposed in the specimen. The maximum strain, which was observed in strain gauge S5, was 0.0026.A similar transverse reinforcement ratio (and volumetric ratio) was used in Specimen CB-6. Again, no yielding of transverse reinforcement was observed, even at a drift level of 7%. The maximum strain of 0.2% was detected in the strain gauge S9. Major diagonal cracks were not observed in these two specimens, indicating that transverse reinforcement and HPFRC can effectively resist high shear despite the lack of diagonal reinforcement.

The column-type transverse reinforcement was fully used to resist the shear force and provide confinement to plastic hinge regions in Specimen CB-1. At approximately 2.7% drift, yielding strains were recorded by most strain gauges in the plastic hinge regions. At the end of the test, all strain gauges in the plastic hinge regions indicated yielding strains with a maximum strain of 0.3% recorded in strain gauge S9. It should be noted that the column-type transverse reinforcement in Specimen CB-1 consisted of four legs of No. 3 bars at 2.75-in spacing. This was equivalent to the volumetric transverse reinforcement of 2.9%, which was much lower than that used in other specimens. With increase in the volumetric ratio of transverse reinforcement in other specimens, yielding of the column-type confinement was seldom observed.

4.7 ENERGY DISSIPATION CAPACITY

In earthquake-resistant design of a coupled wall system, the coupling beams are expected to possess not only large displacement capacity but also good energy dissipation capacity. The energy dissipated by the specimens during each loading cycle was determined by calculating the area enclosed by each load-displacement hysteresis loop as shown in Figure 4.60. The first and second cycle at each drift of the load-displacement hysteresis loop was separately analyzed to evaluate the effect of reduced stiffness in the repeated cycle on energy dissipation. To account for different drift levels reached for positive and negative loading directions in a given cycle, average drift values were used.

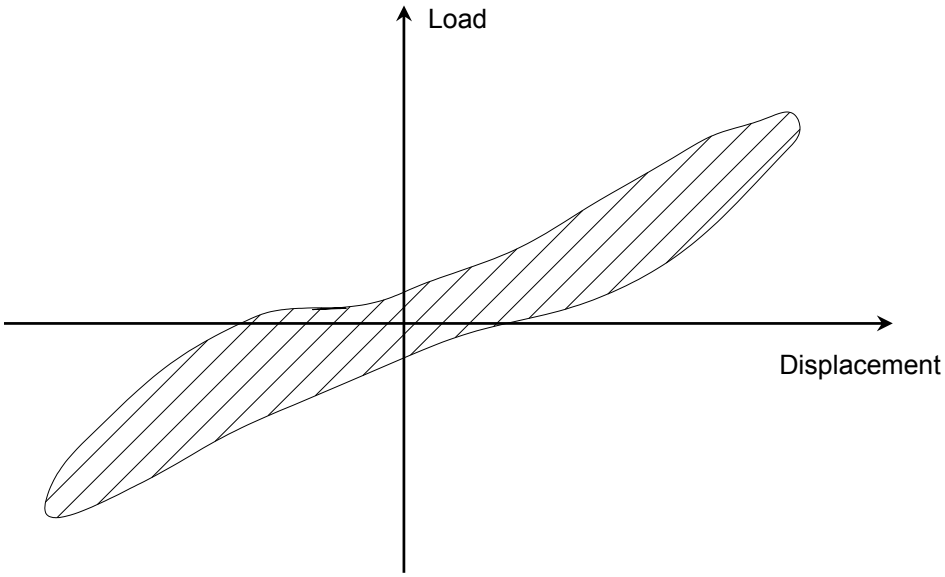

Figure 4.60 Definition of energy dissipation per cycle

All HPFRC specimens show good energy dissipation with wide shear versus drift hysteresis loops, as indicated in Section 4.2. Figure 4.61 shows the accumulation of energy dissipation versus peak first cycle drift for all specimens. Energy dissipated by HPFRC coupling beams linearly increase with the drift up to 5%, indicating the effectiveness of HPFRC to stabilize the coupling beams by providing more strength and confinement. The RC coupling beam (CB4) shows stable behavior and energy dissipation comparable to HPFRC specimen up to 3% drift. However, the lower displacement capacity of the RC specimen compared with that of the HPFRC coupling beams results in lower total energy dissipation. For drifts smaller than 1%, the energy dissipated was quite small for all specimens because the specimens behaved primarily in the elastic range.

The mechanisms of energy dissipation did not appreciably degrade with repeated cycles. Figure 4.62 shows the energy dissipated in the first and repeat cycles to the same drift level for Specimen CB-1. Similar trends were observed in other specimens. In all specimens, the energy dissipated during the first cycle was slightly larger than that in the second cycle at the same drift level, mainly because of the small decay in stiffness that the specimens experienced during the second cycle.

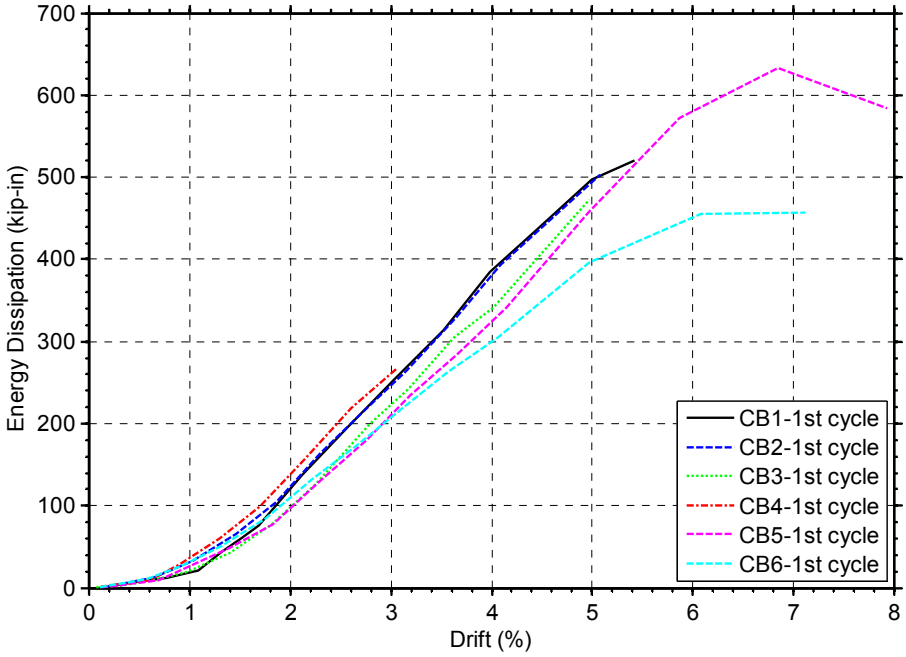

Figure 4.61 Energy dissipate per cycle versus drift

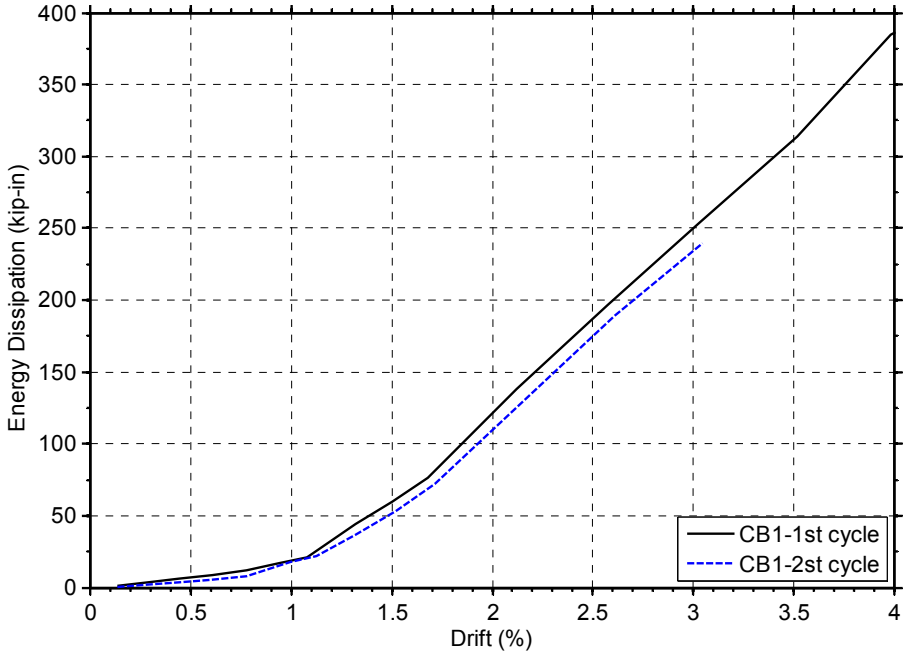

Figure 4.62 Energy dissipated in repeated cycles is similar to that in the first cycles, indicating no degradation of energy dissipation mechanisms

Because all specimens had different load carrying capacities, it is more useful to compare energy dissipation capacity of different specimens using a normalized energy dissipated. The value of the normalized energy dissipation provided information about shape of the load versus displacement hysteresis loop. Pinching in the hysteresis loop is reflected by a smaller value of the normalized dissipated energy. The normalized dissipated energy was defined as the ratio of the energy dissipated during a given loading cycle to the energy dissipated by an equivalent elasto-plastic system (Figure 4.63). The area enclosed by an equivalent elasto-plastic system was dictated by the stiffness of the system. In this study, the loading and unloading stiffness of the elasto-plastic system was set equal to the peak-to-peak stiffness at the first loading cycle to 0.5% drift. Normalized dissipated energy is sensitive to the selected stiffness of an equivalent elasto-plastic system, so readers should be careful in interpreting the results.

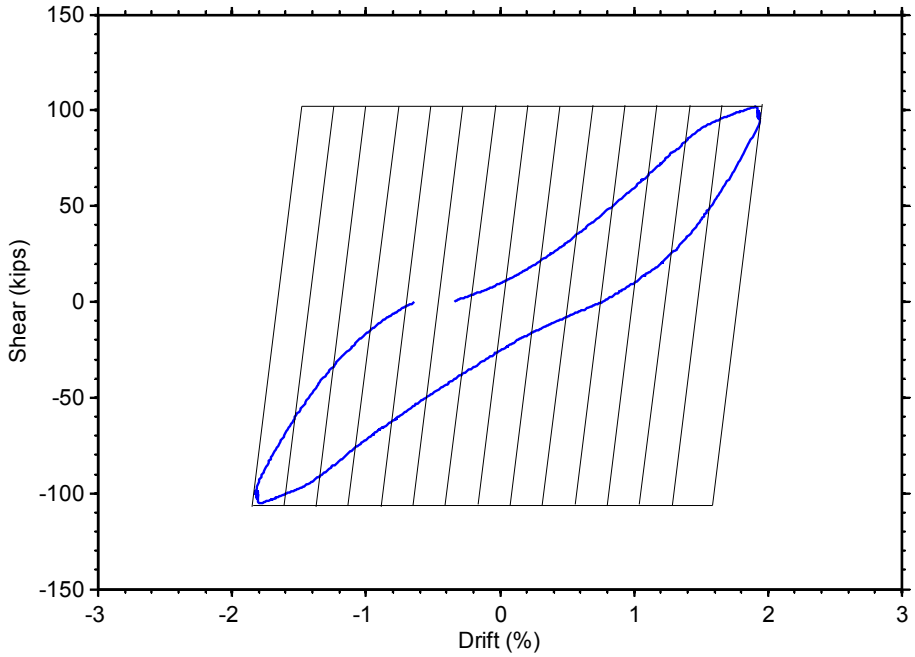

Figure 4.63 An equivalent elasto-plastic system used to normalize the energy dissipated per cycle

A normalized energy dissipation of approximately 0.4 was generally exhibited beyond 1% drift (Figure 4.64) for all specimens, except Specimen 6 (CB-6). Specimen CB-6, the HPFRC coupling beam without diagonal bars, possessed the lowest normalized energy dissipated due to the pinching in the load versus drift hysteresis loop. This beam underwent large sliding shear displacement at the bottom beam-wall interface, causing the pinching in the load-displacement response. The normalized energy dissipated of 0.32 was fairly constant after 4% drift where sliding shear displacement started.

Lequesne (2011) analyzed the normalized energy dissipated from reinforced concrete coupling beams tests and compared it to that of HPFRC coupling beams. Table 4.20 summarizes Lequesne's analysis with the addition of the normalized energy dissipated for HPFRC coupling beam tested in this study. Despite the significant reduction in or elimination of diagonal reinforcement, this series of HPFRC tests exhibited an energy dissipation capacity close to that of comparable diagonally reinforced concrete coupling beams with similar aspect ratios.

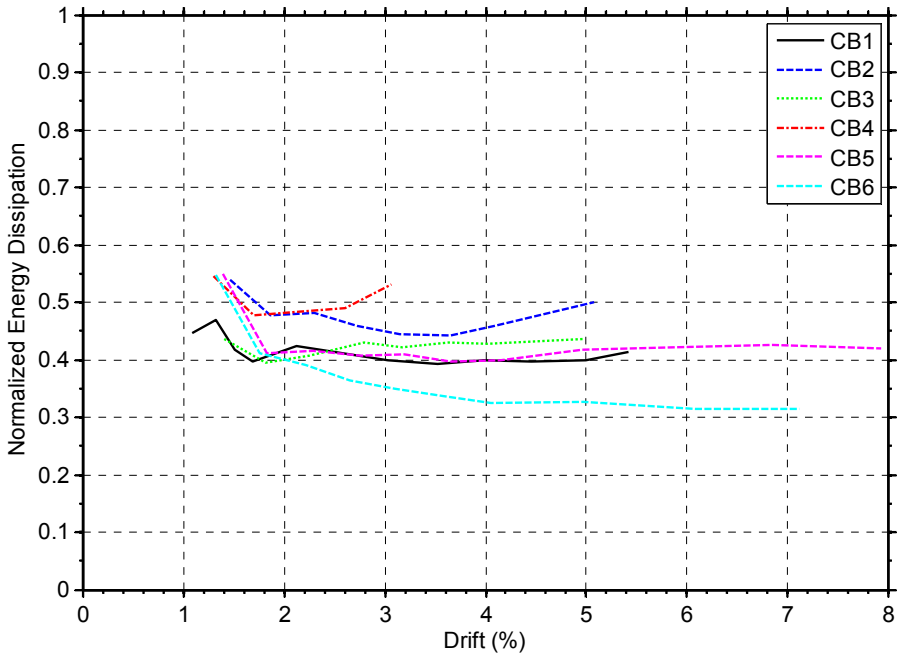

Figure 4.64 The normalized energy dissipation of approximately 0.4 was generally exhibited beyond 1% drift.

Table 4.20 Normalized energy dissipation of HPFRC coupling beams compared to that of coupling beams tested by other researchers (Adopted from Lequesne (2010))

Researchers	Year	Aspect Ratio	Axial Force (Y/N)	HPFRC (Y/N)	Diagonal bars (Y/N)	Normalized Energy Dissipation
Shiu et al.	1978	2.5	N	N	Y	0.50
Naish et al.	2009	2.4	N	N	Y	0.55
Tegos et al.	1988	2	Y	N	Y	0.35
Lequesne et al.	2010	1.75	Y	Y	Y	0.40
Galano et al.	2000	1.5	N	N	Y	0.45
Tassios et al.	1996	1.5	N	N	Y	0.35
Canbolat	2005	1	N	N	Y	0.40
Canbolat	2005	1	N	Y	Y	0.25
Current study	2012	3.3	Y	Y	Y	0.45
Current study	2012	3.3	Y	Y	N	0.40
Current study	2012	2.75	Y	Y	Y	0.43
Current study	2012	2.75	Y	N	Y	0.45
Current study	2012	2.75	Y	Y	Y	0.40
Current study	2012	2.75	Y	Y	N	0.35

4.8 DRIFT COMPONENTS

Several deformation mechanisms contributed to drift applied to the coupling beams. The most significant contributions were attributed to flexural deformation, shear distortion, concentrated flexural rotation at the beam ends and sliding displacements. The relative contribution of each component was determined from the data recorded by Optotrak system.

Flexural rotation was calculated based on the curvature determined from each strip as discussed in Section 4.4.4. Using the moment-area theorem, drift due to flexural rotation can be expressed as

$$\delta_\theta = \frac{\sum_{i=2}^{n-1} \phi_i \cdot \overline{x}_i \cdot \Delta x_i}{a} \tag{4-25}$$

Where n is the total number of strips, ϕ_i is the average curvature of strip i, $\overline{x}_i$ is the distance from the middle of strip i to the top beam-wall interface, Δx_i is the length of each strip (Figure 4.38), and a is the length of coupling beams. It should be noted that the first

and last strip (referring to Figure 4.29) were not included in calculating flexural rotations because markers in the first and last rows were placed on the top and base blocks.

Drift due to concentrated flexural rotation in the first and last strip was separately considered primarily due to the effect of slip-extension at the beam-wall interface. To distinguish this flexural rotation at the end strips from pure bending in the remaining part of the specimens, the term "steel strain penetration" was used. Drift due to steel strain penetration was determined in the same manner as that due flexural rotation (Eq. 4.25).

Drift due to shear distortion was determined from an actual shear strain where the impact of sliding was eliminated from the total shear strain, as discussed in Section 4.5.3. Average shear strain in each strip, as shown in Section 4.5.4, was multiplied by the length of each strip to obtain displacement. Then, displacements were summed up for all strips and divided by the length of the coupling beam to obtain the drift due to shear distortion. This drift can be expressed in the flowing equation.

$$\delta_{\gamma} = \frac{\sum_{i=1}^{n}(\gamma_i \cdot \Delta x_i)}{a} \tag{4-26}$$

where γ_i is average shear strain in strip *i*, Δx_i is the length of each strip (Figure 4.38), and *a* is the length of coupling beams.

Drift due to sliding at the beam-wall interface and critical cracks within the plastic hinge regions was estimated from sliding displacement, as discussed in Section 4.5.3, divided by the beam length.

$$\delta_s = \frac{\overline{x}}{a} \tag{4-27}$$

where $\overline{x}$ is the sliding shear displacement, and *a* is the length of the coupling beams.

Figure 4.65 shows plots of the predicted drift normalized by the applied drift. The relative contribution of the primary mechanisms contributing to the deformation of the coupling beam specimens is separated in five parts. The lower part shows the drift due to elastic and inelastic flexural rotations outside the end strips of markers. The second area corresponds to the drift due to steel strain penetration, which concentrated at the beam-wall interface of the specimens. The third region represents the drift due to shear distortion over the entire length of the specimens. The top two parts indicates the drift due to sliding at the beam-wall interface and critical cracks developed within the plastic

hinge regions. The summation of the calculated drift components ranges from 90% to 110% of the actual drift, showing a good agreement with the applied drift.

The contribution of flexural rotations within the coupling beams was between 20% and 55% of the applied drift. For the specimens with diagonal reinforcement (CB-1 through CB-4), steel strain penetration contributed approximately 20-40% of the overall drift imposed on the specimens. The specimens without diagonal reinforcement (CB-5 and CB-6) experienced a larger contribution of steel strain penetration, from which 50-55% of the applied drift was observed. This large contribution corresponded to the damage concentrated at the ends of both specimens. In particular, damage leading to the failure of Specimen CB-6 was localized at the bottom end of the coupling beam. After 2% drift, the contribution of flexural rotations within this coupling beam was very small. However, considering flexural rotations and steel strain penetration as flexural mechanisms contributing to drift, it can be seen that their contribution to drift was 70-80% of the total applied drift.

Shear deformations contributed only 15-20% of the applied drift, corresponding to minor shear-related damage in all specimens. Sliding at the beam-wall interface was small in the specimens with diagonal reinforcement. However, specimens without diagonal reinforcement showed larger sliding at the interface when large drifts were applied, resulting in a contribution of 10-20% of the applied drift due to sliding. It can be observed from Figure 4.65(f) that after 2% drift in the negative direction, the contribution of sliding at the interface increased significantly while contributions from other mechanisms decreased. This contribution implies the usefulness of diagonal reinforcement in limiting sliding shear displacement.

Sliding at critical flexural cracks was pronounced in Specimen CB-2. Sliding started after 2% drift and its contribution to total drift increased as larger drifts were applied. At 5% drift, the contribution of sliding at critical cracks contributed approximately 15% to the total drift. Drift due to sliding at critical cracks was smaller in other specimens. For specimen CB-1 and CB-3, column-type transverse reinforcement and HPFRC maintained integrity of the plastic hinge regions and preserved aggregate interlock mechanism, resulting in less sliding displacement across flexural cracks.

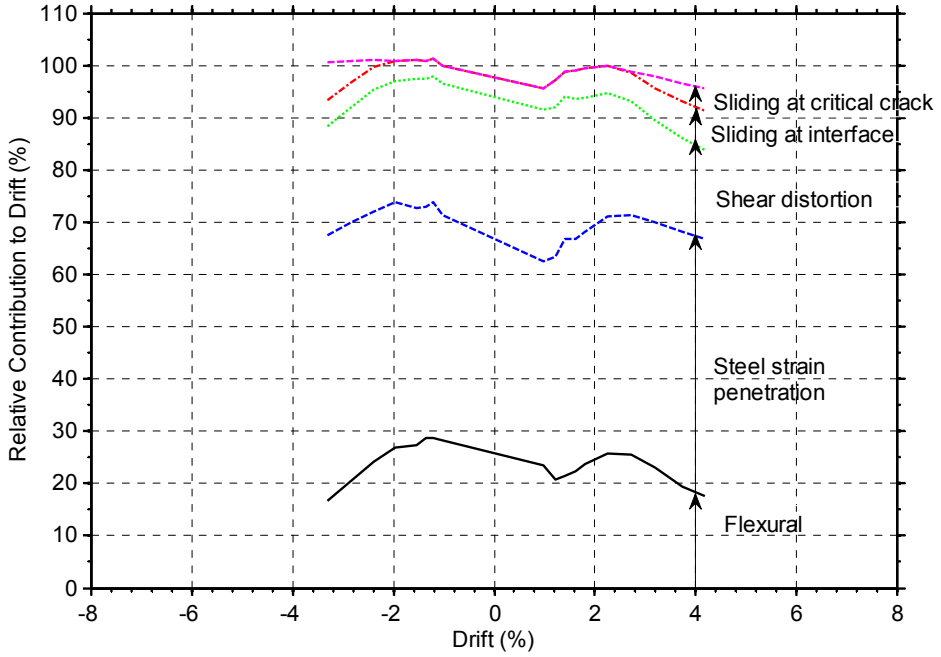

(a) HPFRC Specimen CB-1

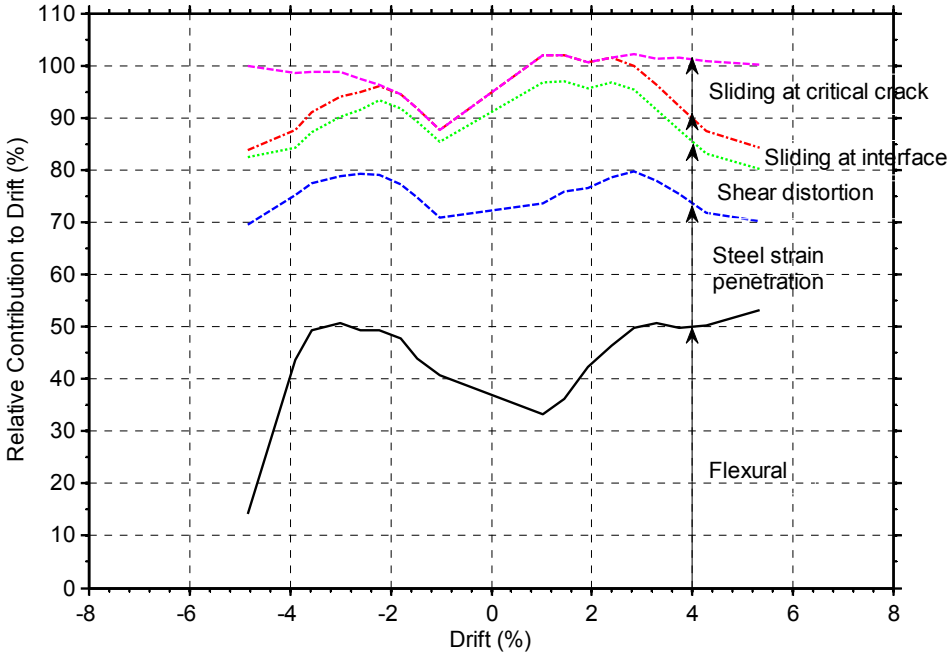

(b) HPFRC Specimen CB-2

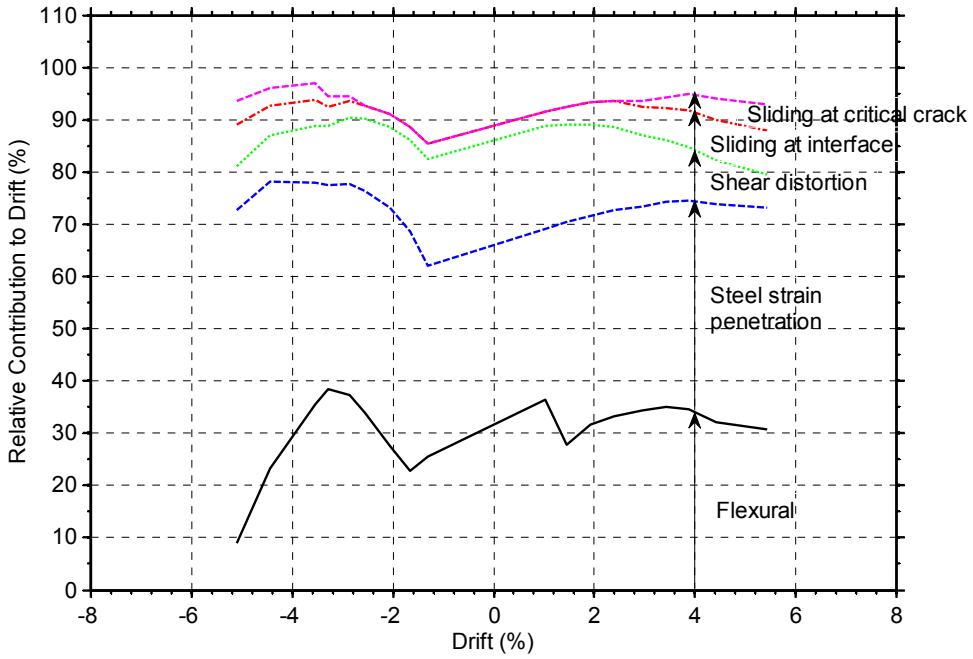

(c) HPFRC Specimen CB-3

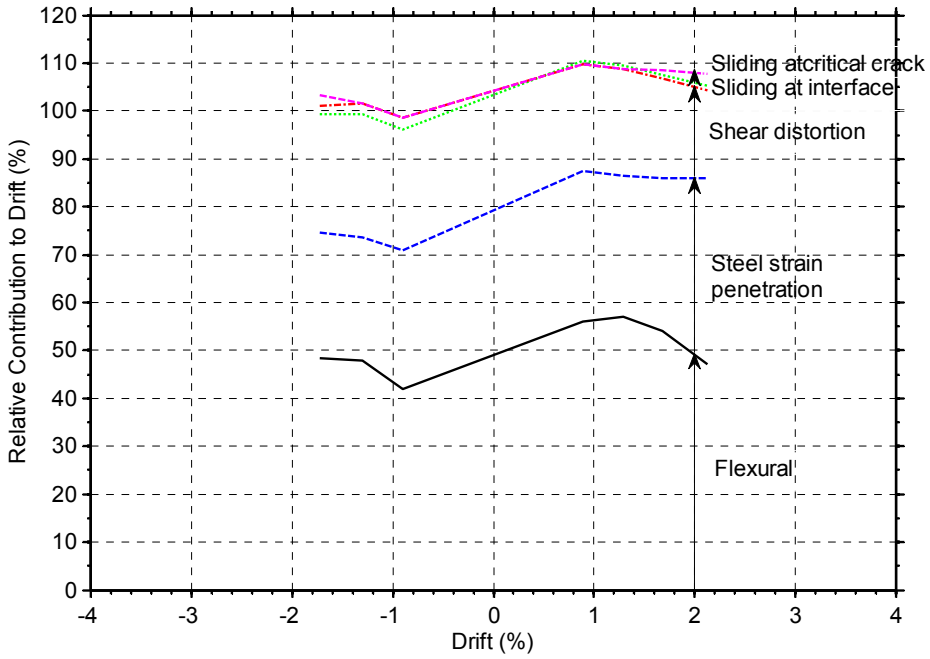

(d) RC Specimen CB-4

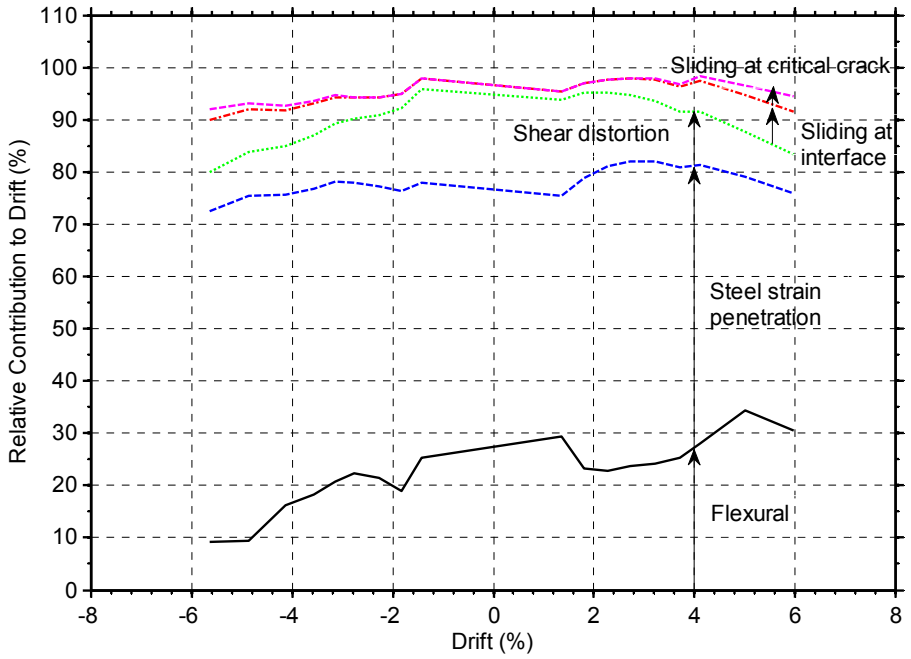

(e) HPFRC Specimen CB-5

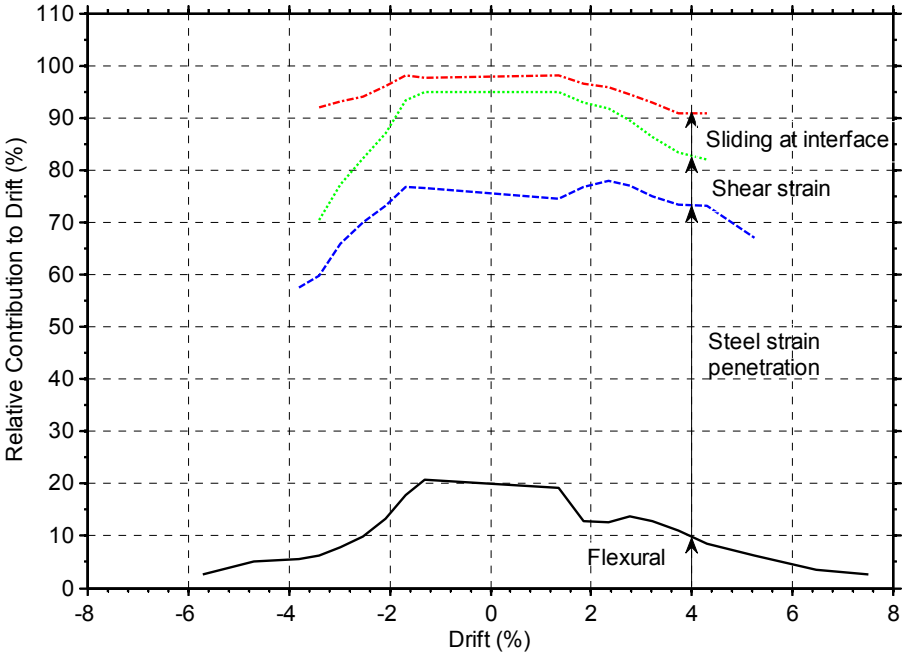

(f) HPFRC Specimen CB-6

Figure 4.65 Relative contributions of deformation components to specimen drift

4.9 STIFFNESS RETENTION CAPACITY

Stiffness degradation of the coupling beam specimens was evaluated in terms of the secant stiffness, determined from peak-to-peak displacement for each load versus displacement hysteresis loop. As can be seen from hysteresis loops in Section 4.2, the secant stiffness decreased as larger drifts were applied. To evaluate the degradation of stiffness during the repeated loading cycle at the same drift level, the secant stiffness versus peak cycle drift for the first and second cycle of each specimen is plotted in Figure 4.66. The secant stiffness in repeated cycles to the same drift level was, although slightly smaller, generally similar to the first loading cycle. This indicates that stiffness does not appreciably degrade with low numbers of repeat cycles.

To account for the variations of specimen parameters, such as the reinforcement ratios and matrix types of concrete, the peak-to-peak secant stiffness values were normalized with respect to the secant stiffness at approximately 0.25% drift for each specimen. Table 4.13 shows the value of the secant stiffness used for the normalization in each specimen.

Table 4.13 Initial secant stiffness values at approximately 0.25% drift

Specimen	Stiffness (kip/in)	Drift[1] (%)
CB-1	200	0.29
CB-2	181	0.27
CB-3	177	0.28
CB-4	219	0.23
CB-5	180	0.25
CB-6	217	0.23

[1] The drift value listed refers to the average drift in the cycle where the secant stiffness was evaluated.

The data plotted in Figure 4.67 shows that all HPFRC specimens had a higher normalized stiffness compared to the RC specimen (CB-4), demonstrating the superior capacity of HPFRC in resisting shear and retaining stiffness of the specimens. The plot also shows that the rate of stiffness degradation decreases as drift increases for all specimens. Among HPFRC specimens, coupling beams with diagonal bars were better able to maintain their normalized stiffness compared to HPFRC specimens without diagonal bars.

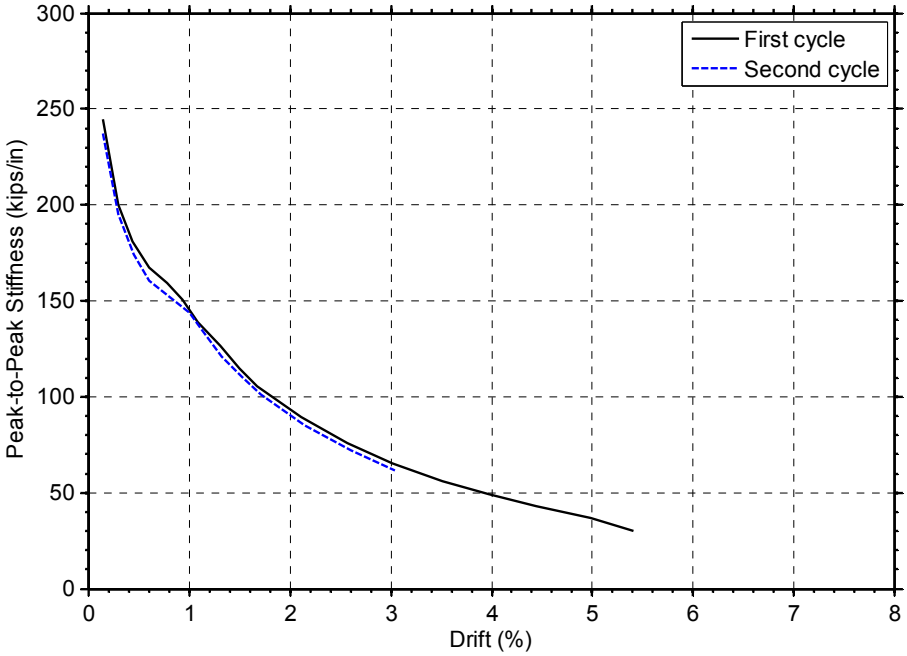

(a) Specimen CB-1

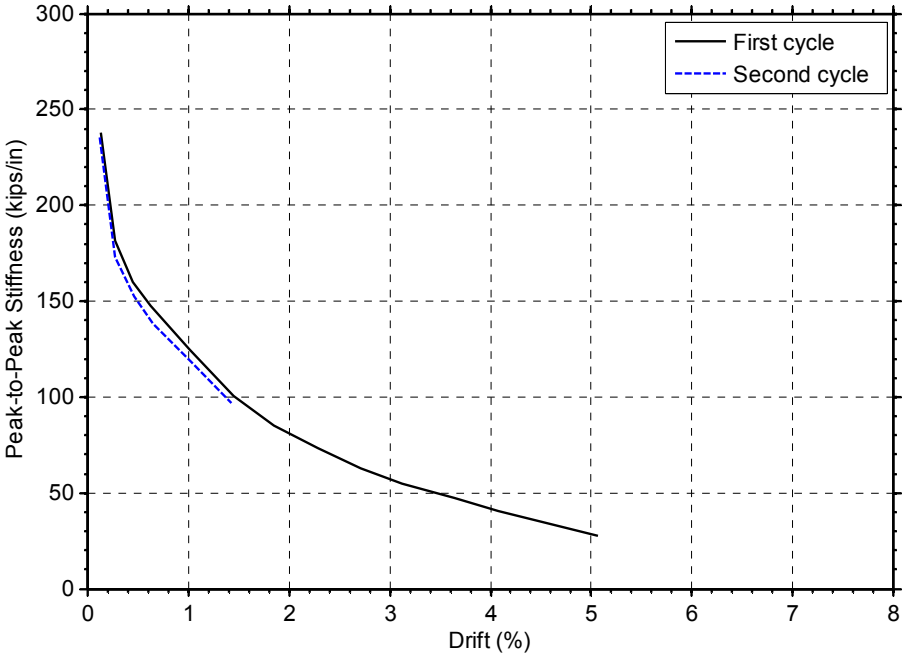

(b) Specimen CB-2

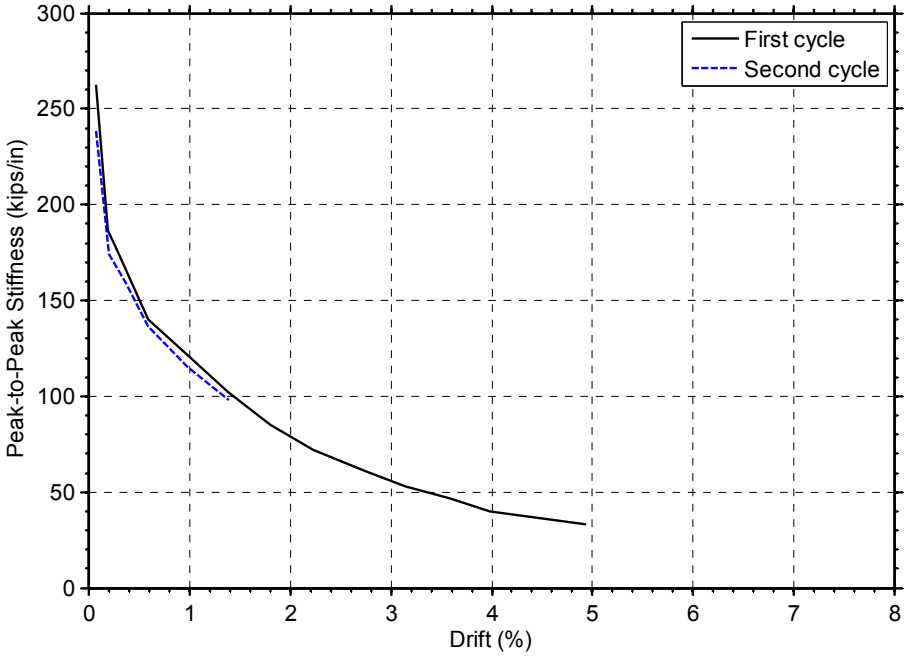

(c) Specimen CB-3

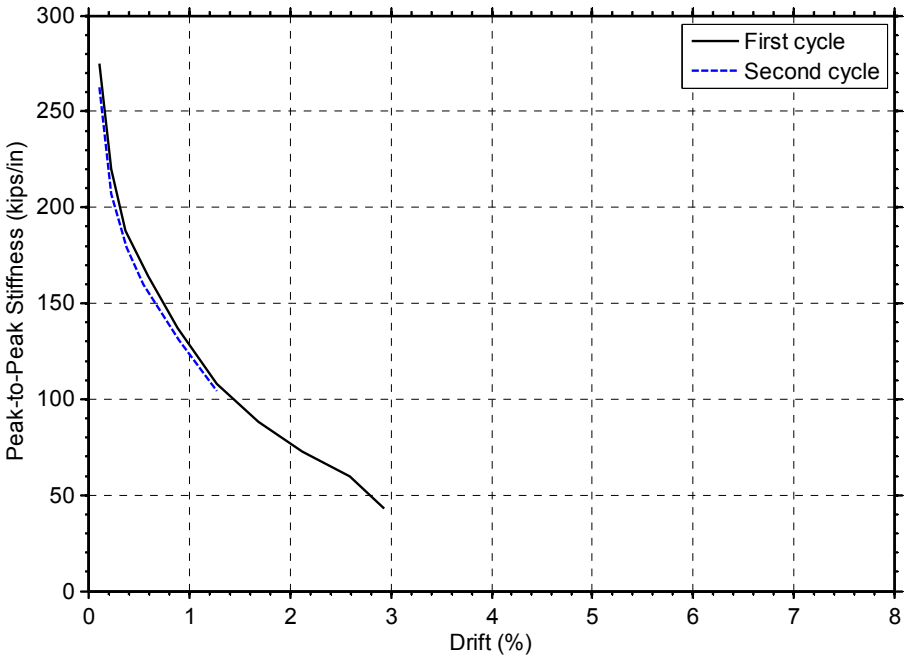

(d) Specimen CB-4

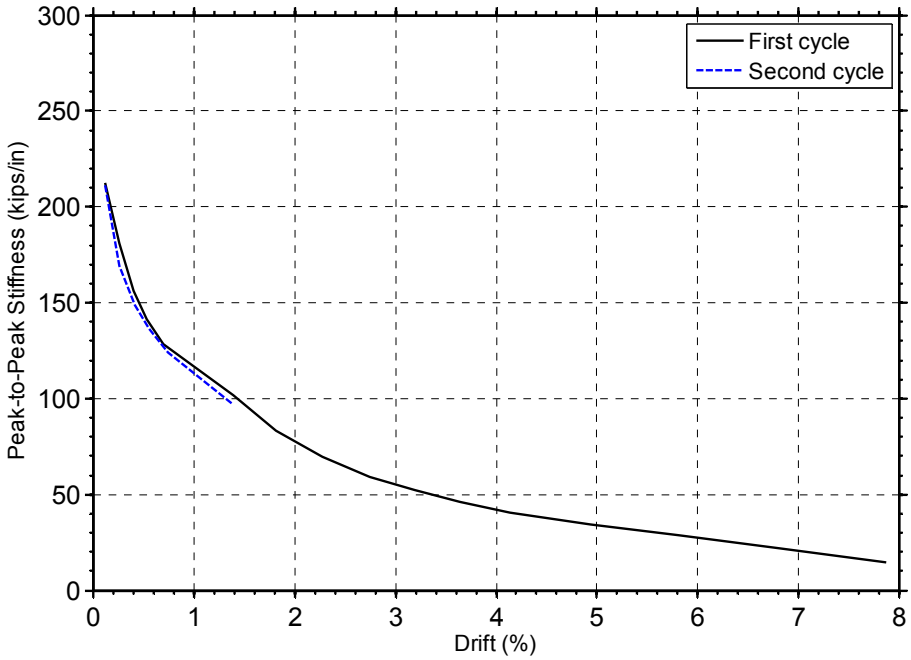

(e) Specimen CB-5

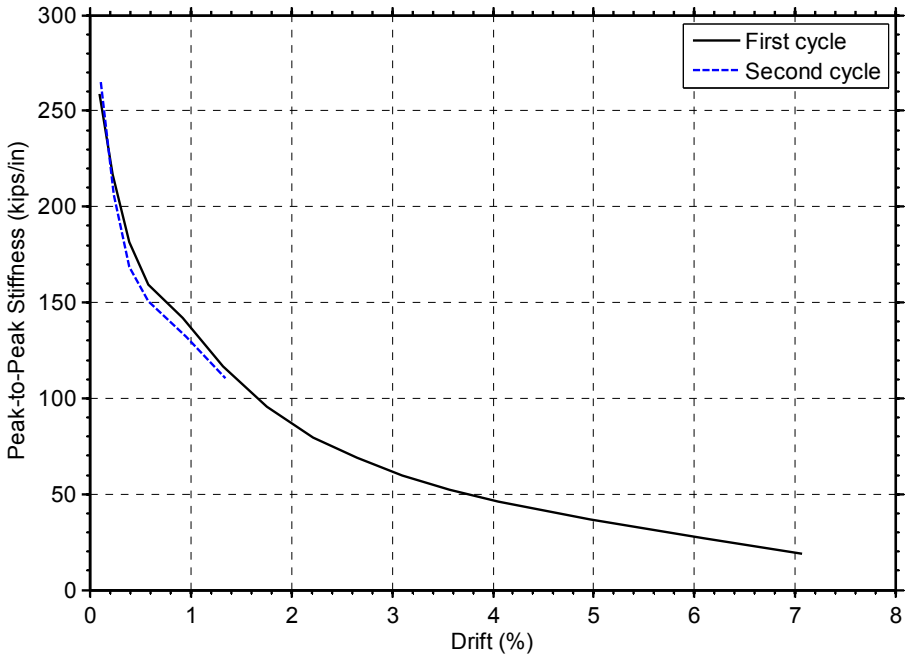

(f) Specimen CB-6

Figure 4.66 Peak-to-peak stiffness versus peak cycle drift in the first and second cycle

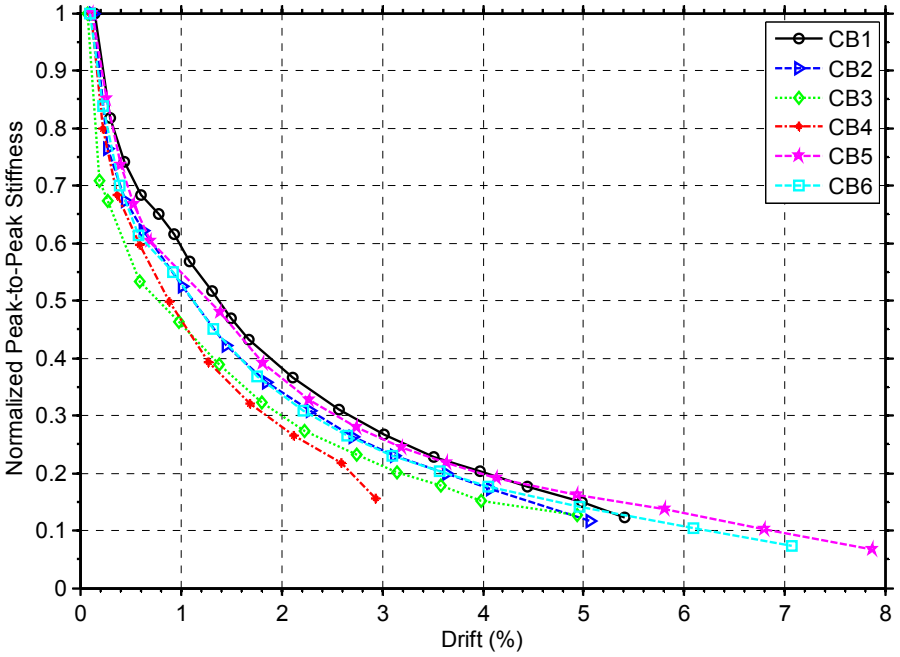

Figure 4.67 Normalized peak-to-peak stiffness versus peak cycle drift

4.10 FLEXURAL STIFFNESS

Under seismic actions, a reinforced concrete coupling beam is subjected to flexural cracking, which reduces the stiffness of a member. In estimating the flexural stiffness, an average value of *EI* for an entire length of a beam should be assumed.

FEMA 356 prestandard for the Seismic Rehabilitation of Buildings recommends a value of $0.5E_cI_g$ for bending rigidity of coupling beams, where I_g is the moment of inertia of the gross section. Supplementary #1 of ASCE/SEI 41-06 incorporates a reduced value for effective stiffness of $0.3E_cI_g$. To evaluate this proposed value of the effective flexural stiffness, the experimental flexural stiffness was estimated from the response of applied shear force versus displacement due to flexural deformation.

Figure 4.68 shows the secant flexural stiffness normalized by the gross section stiffness (E_cI_g) versus peak cycle drift. Assuming fixed supports at both ends of the specimens, secant flexural stiffness was determined from $E_cI_{eff} = (VL_n^2)/(12\Delta)$, where V is the applied shear force (kips), L_n is the length of the coupling beams (in.), and Δ is the displacement due to the flexural deformation.

First yield was detected at approximately 0.75% drift in most specimens. At this drift level, the experimentally effective flexural stiffness ranges from $0.13E_cI_g$ to $0.2E_cI_g$. This value agrees with the effective stiffness of $0.12E_cI_g$ at the yield rotation reported by Nash (2010) and $0.2E_cI_g$ found in the HPFRC coupling beam tests by Lequesne (2011). It should be noted that this effective stiffness includes the effect of slip-extension at the beam-wall interface when estimating flexural displacement. Based on the test results in Figure 4.68, it is recommended to use an effective yield stiffness of $0.13E_cI_g$ to $0.2E_cI_g$ for the precast coupling beams with an aspect ratio between 2.75 and 3.3.

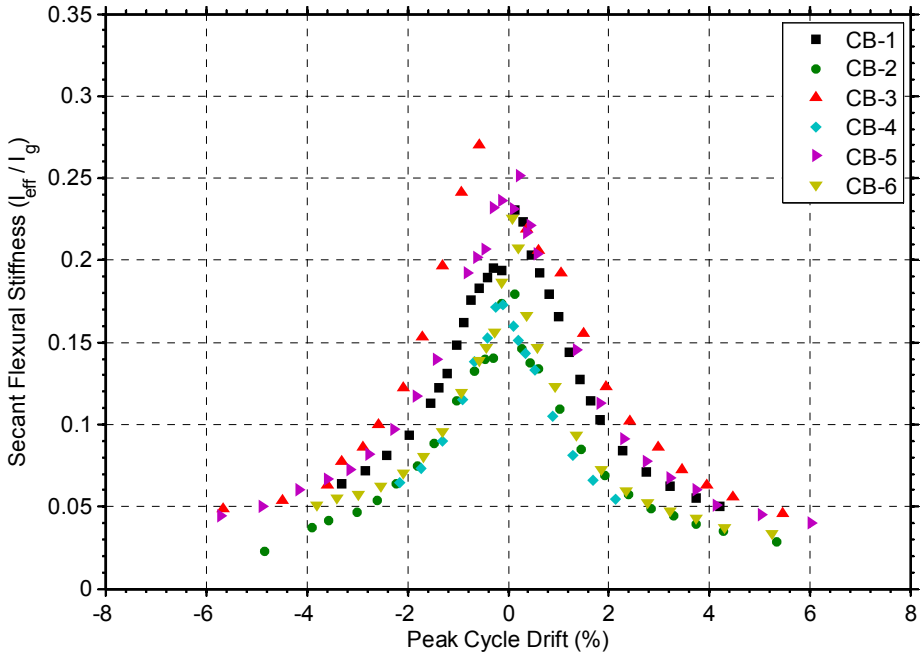

Figure 4.68 Experimental secant flexural stiffness

4.11 SHEAR STIFFNESS

The shear stiffness of the coupling beams was estimated from the average shear stress versus average shear strain response. The effect of sliding shear displacement was removed from the total shear strain, as described in Section 4.5.4. Thus, the shear strains presented here were actual ones. These shear strains were averaged to obtain a single shear strain for the specimen. Then, shear stiffness was calculated from the slope of the secant stiffness drawn from the origin to the peak average shear strain in each peak drift cycle.

Figure 4.69 shows the secant shear stiffness normalized by the shear modulus (G) versus peak cycle drift. Assuming a poison ratio, $\nu = 0.15$, shear modulus can be calculated from $G = E_c / [2 \cdot (1+\nu)]$, where $E_c = 57000\sqrt{f_c'}$ (psi). The data in Figure 4.69 shows that the experimental shear stiffness is much lower than the shear modulus. At drifts beyond 1.5%, the shear stiffness is reduced to approximately 10% of the theoretical shear modulus. Moreover, the shear stiffness of the reinforced concrete coupling beam specimen (CB-4) is lower than those of HPFRC specimens at the same drift level in the negative direction. This lower shear stiffness corresponds to larger diagonal cracks developed in this RC specimen.

The experimental shear stiffness is also compared to the shear rigidity of $0.4E_c A_w$ specified in ASCE/SEI 41-06. Figure 4.70 shows the effective shear stiffness normalized by E_c versus the peak cycle drift. Effective shear stiffness is much lower than the recommended shear rigidity in ASCE/SEI 41-06. This result is similar to the effective shear stiffness reported by Lequesne (2011) for the tests of HPFRC precast coupling beams with an aspect ratio of 1.75.

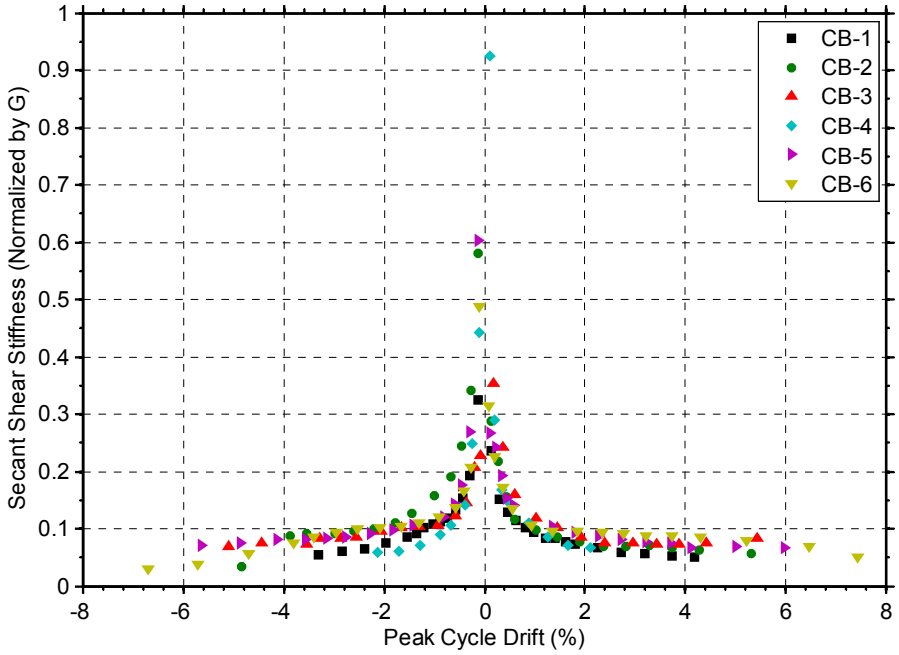

Figure 4.69 Experimental shear stiffness normalized by G

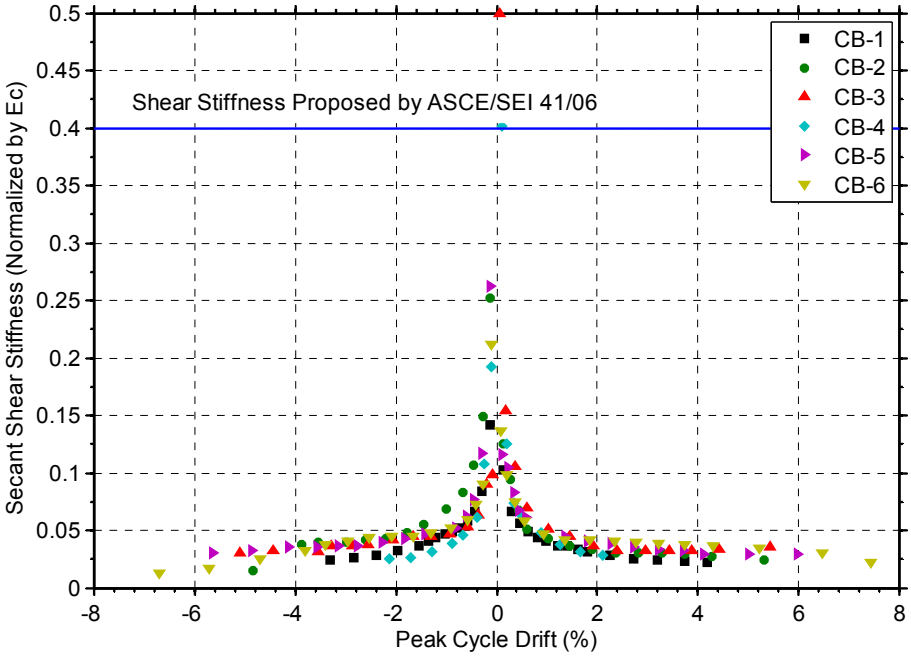

Figure 4.70 Experimental shear stiffness normalized by E_c

CHAPTER 5
NONLINEAR FINITE ELEMENT MODELING OF COUPLING BEAMS

Numerical models using the finite element software VecTor2 (Wong and Vecchio 2002) were conducted in order to determine material models and assumptions needed for simulating the behavior of the HPFRC coupling beam specimens. Such models and assumptions could then be used in parametric analyses of HPFRC coupling beams. However, as this research included a substantial experimental component, these parametric analyses were beyond the scope of this study. Discussion focuses on material models, boundary conditions, and limitations of the models. The numerical results are then compared to the test results to evaluate the ability of the models to reasonably simulate the flexural and shear behavior of the coupling beams.

5.1 VecTor2

VecTor2 employs a smeared, rotating crack approach to represent the behavior of cracked concrete. The behavior of cracked concrete is assumed to be orthotropic and is based on the Modified Compression Field Theory (MCFT) (Vechio and Collins 1986) and the Disturbed Stress Field Model (DSFM) (Vecchio 2000). The MCFT is based on the assumption that the principal angles for stress and strain are equal. However, in cases where no slip along cracks or reorientation of principal angles occur, the constitutive model used in the MCFT has been found to overestimate the degree of concrete compression softening due to transverse tension (Vecchio 2000). Thus, slip along cracks is explicitly considered in the DSFM and the expression to estimate the degree of compression softening in the concrete modified. With explicit calculation of crack shear slip deformations, the DSFM eliminates the crack shear check required by the MCFT (Wong and Vecchio, 2002).

5.2 GUIDELINES FOR MODELING HPFRC COUPLING BEAMS IN VecTor2

5.2.1 Geometry Modeling and Element Types

The finite element models of the test coupling beams were created using the pre-processor program "FormWorks" included in the VecTor2 bundled version 3.5 (Full version). FormWorks provides a user-friendly interface to facilitate the preparation of input files for VecTor2. The post-processor "Augustus", another bundled program with VecTor2, was used to extract and display graphically the results from the analyses.

Each finite element model consisted of three types of concretes with smeared reinforcement, as shown in Figure 5.1. Concrete Type 1 represented concrete in the middle part of the coupling beam, where regular stirrup-type transverse reinforcement was provided. Both end regions of the coupling beam, where column-type confinement was used, were modeled using Concrete Type 2. The two concrete blocks simulating the wall boundary regions were modeled using Concrete Type 3.

In VecTor2, diagonal bars could be modeled using either truss elements or smeared reinforcement. To avoid the difficulty of meshing diagonal truss elements and to obtain uniformly rectangular concrete elements, diagonal bars were smeared in the directions of $\pm 16.1^{o}$ with respect to the beam longitudinal axis (y-axis; see Figure 5.1) for the coupling beams with an aspect ratio of 2.75. For the coupling beams with a 3.3 aspect ratio, smeared diagonal bars had directions of $\pm 12.8^{o}$ with respect to the beam longitudinal axis (y-axis). This smeared diagonal reinforcement was defined together with the concrete properties as in the case of transverse reinforcement.

Coupling beam longitudinal and dowel reinforcement was modeled using truss elements. This reinforcement was embedded in concrete and perfect bond between the bars and surrounding concrete was assumed. On the other hand, both longitudinal and transverse reinforcements were smeared in Concrete Type 3 (top and base blocks).The steel links used to maintain both top and bottom blocks parallel during the test, as well as to provide some axial restraint to the coupling beams, also had to be modeled. These links could be defined either by stand-alone truss elements (Figure 5.1) or by truss elements embedded in concrete whose compressive strength and elastic modulus were set close to zero (Figure 5.2). The advantage of modeling the steel links with truss elements embedded in concrete was the ease with which axial forces developed in each steel link

could be examined using the post-processor "Augustus". The analyses in this study were performed in both fashions with generally similar results.

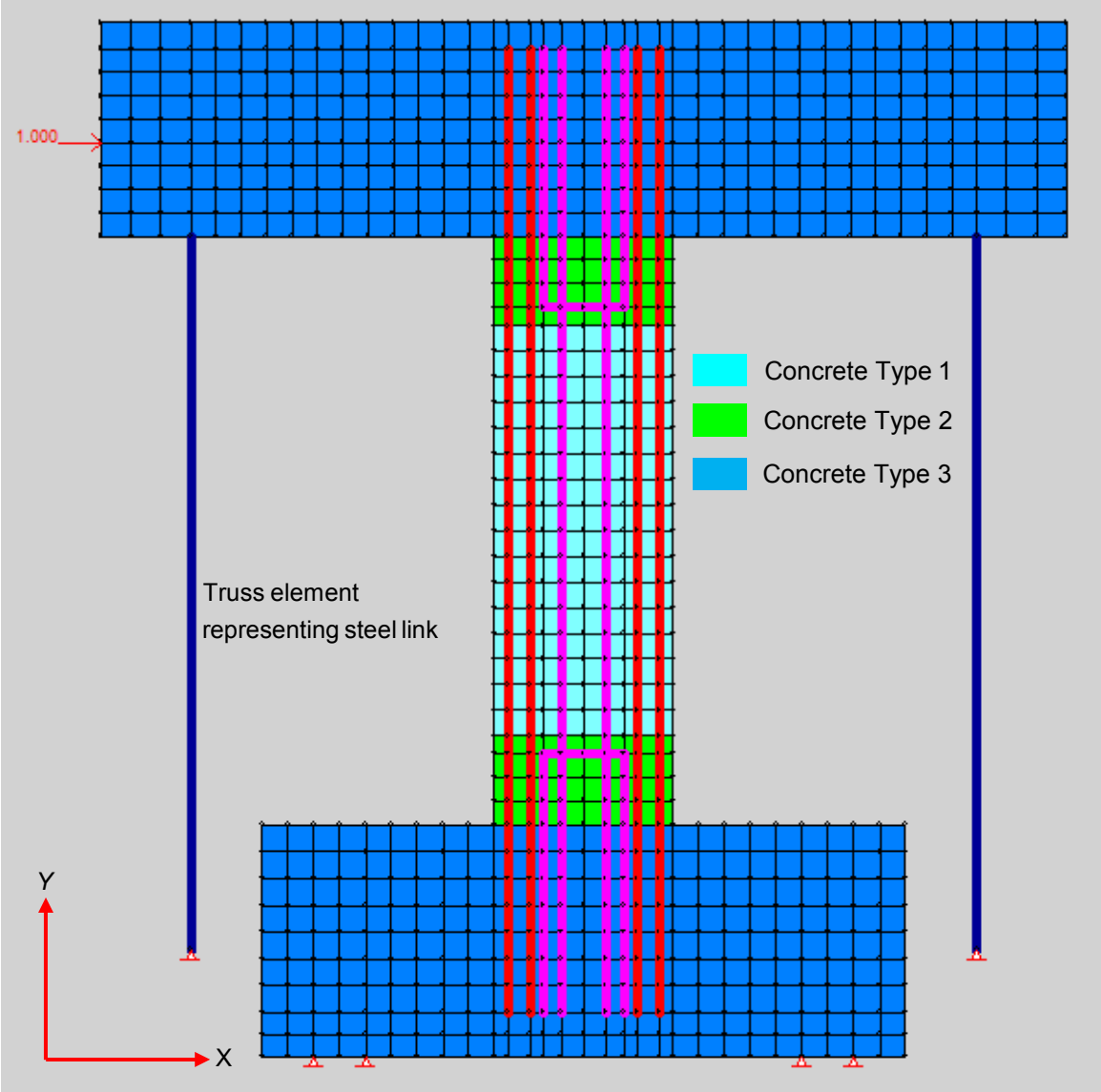

Figure 5.1 Concrete materials for modeling coupling beams

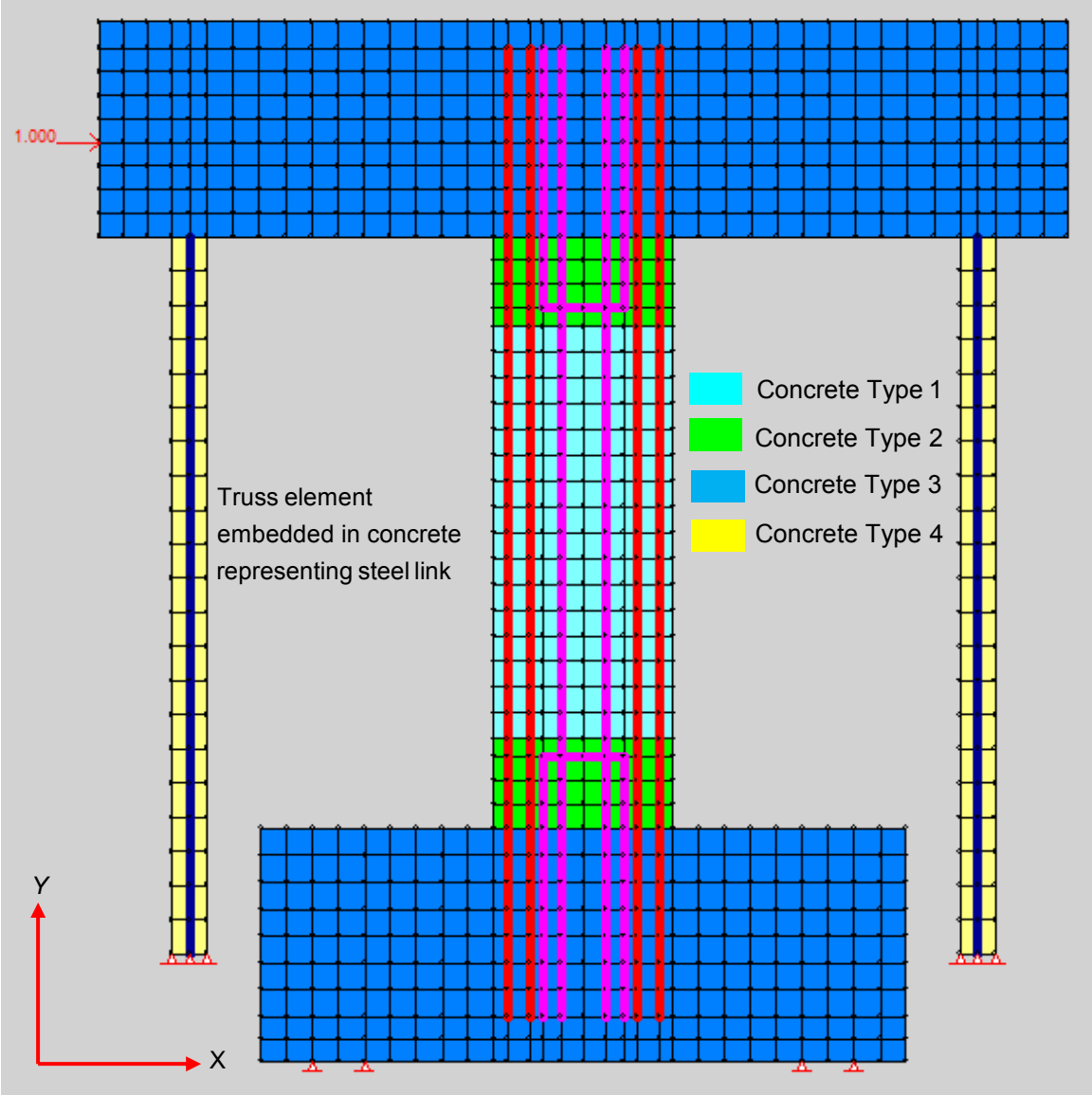

Figure 5.2 Concrete Type 4 and truss elements used to model steel links

The area of steel links specified in the models was adjusted such that they led to axial forces in the coupling beams within the range of those measured during the tests, as discussed in Section 5.3.3. Areas of 1500 mm^2 and 1200 mm^2 were found appropriate for modeling the steel links used in the HPFRC and reinforced concrete specimens, respectively. The strengths of 250 MPa and 690 MPa were assigned to yield and ultimate strengths of these steel links. In the models, these steel links remained elastic and stable.

The coupling beam specimen models were meshed automatically using the meshing functionality in FormWorks. The element size was approximately 75 mm x 75

mm for the coupling beams and both base and top blocks. Rectangular elements were used for all concrete elements.

The details and properties of the various concrete type models used for Specimens CB-1 through CB-6 are listed in Tables 5.1-5.6. The mechanical properties of the reinforcement used in the models were obtained from direct tension tests. Results from such tests are shown in Table 3.4. It should be noted that only SI units are allowed in VecTor2. Properties of concrete and steel used in the models were converted from U.S. customary units.

Table 5.1 Concrete element types used for modeling Specimen CB-1

Concrete Type	Location	f_c' (MPa)	Thickness (mm)	Reinforcement				
				Size	Direction* (degree)	Ratio (%)	f_y (MPa)	f_u (MPa)
1	Coupling beam	49.7	152.4	#3 #6 #6	0^o 73.9^o 106.1^o	0.46 0.61 0.61	414 510 510	634 655 655
2	Coupling beam	49.7	152.4	#3 #6 #6	0^o 73.9^o 106.1^o	1.33 0.61 0.61	414 510 510	634 655 655
3	Blocks	34	457	#6 #4	0^o 90^o	3.00 3.00	530 530	660 660
4	Steel links	0.5	457	-	-	-	-	-

* Angle with respect to horizontal or "x" axis.

Table 5.2 Concrete element types used for modeling Specimen CB-2

Concrete Type	Location	f_c' (MPa)	Thickness (mm)	Reinforcement				
				Size	Direction* (degree)	Ratio (%)	f_y (MPa)	f_u (Mpa)
1	Coupling beam	59	152.4	#3 #6 #6	0^o 73.9^o 106.1^o	0.56 0.61 0.61	414 572 572	634 703 703
2	Coupling beam	59	152.4	#4 #6 #6	0^o 73.9^o 106.1^o	2.10 0.61 0.61	414 572 572	682 703 703
3	Blocks	34	457	#6 #4	0^o 90^o	3.00 3.00	530 530	660 660
4	Steel links	0.5	457	-	-	-	-	-

* Angle with respect to horizontal or "x" axis.

Table 5.3 Concrete element types used for modeling Specimen CB-3

Concrete Type	Location	f_c' (MPa)	Thickness (mm)	Reinforcement				
				Size	Direction* (degree)	Ratio (%)	f_y (MPa)	f_u (MPa)
1	Coupling beam	61.4	152.4	#3	0^o	0.61	448	745
				#6	77.2	0.73	545	690
				#6	102.8	0.73	545	690
2	Coupling beam	61.4	152.4	#4	0^o	2.22	531	662
				#6	77.2	0.73	545	690
				#6	102.8	0.73	545	690
3	Blocks	34	457	#6	0^o	3.00	530	660
				#4	90^o	3.00	530	660
4	Steel links	0.5	457	-	-	-	-	-

* Angle with respect to horizontal or "x" axis.

Table 5.4 Concrete element types used for modeling Specimen CB-4

Concrete Type	Location	f_c' (MPa)	Thickness (mm)	Reinforcement				
				Size	Direction* (degree)	Ratio (%)	f_y (MPa)	f_u (MPa)
1	Coupling beam	62	152.4	#3	0^o	0.56	428	676
				#6	73.9^o	0.61	448	690
				#6	106.1^o	0.61	448	690
2	Coupling beam	62	152.4	#4	0^o	2.10	441	690
				#6	73.9^o	0.61	448	690
				#6	106.1^o	0.61	448	690
3	Blocks	34	457	#6	0^o	3.00	530	660
				#4	90^o	3.00	530	660
4	Steel links	0.5	457	-	-	-	-	-

* Angle with respect to horizontal or "x" axis.

Table 5.5 Concrete element types used for modeling Specimen CB-5

Concrete Type	Location	f_c' (MPa)	Thickness (mm)	Reinforcement				
				Size	Direction* (degree)	Ratio (%)	f_y (MPa)	f_u (MPa)
1	Coupling beam	68	152.4	#4	0^o	1.16	530	660
2	Coupling beam	68	152.4	#4	0^o	2.22	530	660
3	Blocks	34	457	#6 #4	0^o 90^o	3.00 3.00	530 530	660 660
4	Steel links	0.5	457	-	-	-	-	-

* Angle with respect to horizontal or "x" axis.

Table 5.6 Concrete element types used for modeling Specimen CB-6

Concrete Type	Location	f_c' (MPa)	Thickness (mm)	Reinforcement				
				Size	Direction* (degree)	Ratio (%)	f_y (MPa)	f_u (MPa)
1	Coupling beam	68	152.4	#4	0^o	1.16	586	697
2	Coupling beam	68	152.4	#4	0^o	2.22	586	697
3	Blocks	34	457	#6 #4	0^o 90^o	3.00 3.00	530 530	660 660
4	Steel links	0.5	457	-	-	-	-	-

* Angle with respect to horizontal or "x" axis.

5.2.2 Material Models

VecTor2 included various models to represent the behavior of concrete and reinforcement. The models that best suited the specimens examined in this study are shown in Table 5.7. In the following, a brief description of the models used in this study, as provided in the VecTor2 Manual (Wong and Vecchio 2002), is given. Details of these models can be found in the VecTor2 Manual.

Table 5.7 Material and analysis models used for modeling the test coupling beams

Convergence Criteria	Displacements – Weighted
Concrete Models	
Compression Pre-Peak	Hognestad (Parabola)
Compression Post-Peak	Modified Park-Kent
Compression Softening	Vecchio 1992 – A
Tension Stiffening	Modified Bentz 2003
Tension Softening	Custom Input (Strain Based) / Linear
FRC Tension	Not Considered
Confinement Strength	Kupfer / Richart
Dilation	Variable - Kupfer
Cracking Criterion	Mohr-Coulomb (Stress)
Crack Stress Calculation	Basic (DSFM/MCFT)
Crack Width Check	Omitted or Agg/5 max crack width
Crack Slip Calculation	Walraven (Monotonic)
Creep and Relaxation	Not Available
Hysteretic Response	Nonlinear w/ Plastic Offsets
Concrete Bond	Eligehausen
Reinforcement Models	
Hysteretic Response	Bauschinger Effect (Seckin)
Dowel Action	Tassios (Crack Slip)
Buckling	Refined Dhakal-Maekawa

VecTor2 does not allow a user-defined compressive stress-strain response of concrete, but provides several models for compression pre-peak and post-peak concrete response. The default concrete pre-peak response "*Hognestad (Parabola)*" was used for all models in this study. The concrete post-peak response was modeled using the *Modified Park-Kent* model (Park, Priestley et al. 1982). This model was modified from a stress-strain curve proposed by Kent and Park to account for the improved concrete compressive strength and ductility due to confinement.

The *Vecchio 1992-A* model was used to simulate the compression softening behavior of concrete. The concrete compression softening is the reduction of uniaxial compressive strength in the presence of transverse cracking and tensile straining. As shown in Figure 5.3, both the stress and strain at peak stress are reduced by the softening parameter β_d. This parameter β_d is a function of the ratio between the principal tensile strain and the principal compressive strain ($\varepsilon_{c1}/\ \varepsilon_{c2}$). In the *Vecchio 1992-A* model, the ratio of the principal tensile strain to the principal compressive strain is limited to 400.

The peak reduced compressive strength (f_p) and corresponding strain (ε_p) are calculated as follows,

$$\beta_d = \frac{1}{1 + C_s \cdot C_d} \leq 1 \tag{5-1}$$

$$C_d = \begin{cases} 0 & if \quad r < 0.28 \\ 0.35(r - 0.28)^{0.8} & if \quad r \geq 0.28 \end{cases} \tag{5-2}$$

$$r = \frac{-\varepsilon_{c1}}{\varepsilon_{c2}} \leq 400 \tag{5-3}$$

$$C_s = \begin{cases} 1 & \text{if shear slip not considered} \\ 0.55 & \text{if shear slip considered} \end{cases} \tag{5-4}$$

$$f_p = \beta_d f_c^{'} \tag{5-5}$$

$$\varepsilon_p = \beta_d \varepsilon_o \tag{5-6}$$

For $e_c \geq e_p$ and $e_c \leq e_o$, the softened response is determined by multiplying the base response by β_d . For $e_o < e_c < e_p$, the compressive stress is computed as $f_c = \beta_d f_c^{'}$.

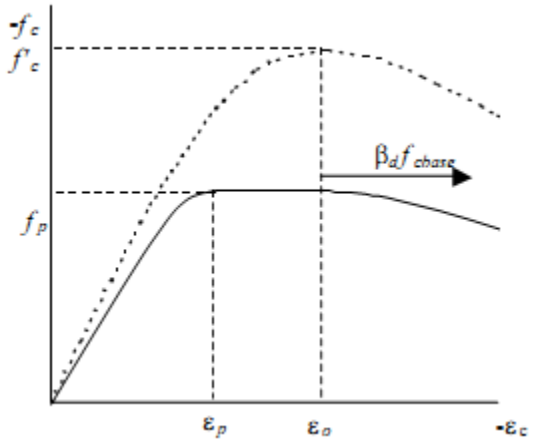

Figure 5.3 Softened stress-strain concrete compression model (Wong and Vecchio 2002)

Tensile behavior of concrete in VecTor2 is represented by tension stiffening and tension softening. Concrete tension stiffening, which is due to the tension resisted by the concrete in between cracks due to bond between concrete and reinforcement was simulated through the *Modified Bentz 2003* model. Tension softening was used to account for the post-cracking behavior of concrete. This is crucial, especially for

modeling fiber-reinforced concrete, and is discussed in Section 5.2.3. In VecTor2, the post-cracking tensile behavior of concrete elements is determined from the larger of the two tensile stresses calculated from the tension-stiffening and tension-softening models.

$$f_{c1} = \max(f_{c1}^{a}, f_{c1}^{b}) \tag{5-7}$$

where f_{c1} is the post-cracking tensile stress, f_{c1}^{a} is the stress due to tension stiffening, and f_{c1}^{b} is the stress due to tension-softening.

In the *Modified Bentz 2003* model, the average concrete tensile stress-strain response is determined as,

$$f_{c1}^{a} = \frac{f_{cr}}{1+\sqrt{3.6m \cdot \varepsilon_{c1}}} \; for \; \varepsilon_{c1} > \varepsilon_{cr} \tag{5-8}$$

where f_{cr} is the concrete cracking stress, ε_{c1} is the principal tensile strain, ε_{cr} is the cracking strain, and *m* is a bond parameter that reflects the ratio of concrete volume to the bonded surface area determined as,

$$m = \frac{A_c}{\sum d_b \pi} \tag{5-9}$$

where A_c is the area of concrete in tension and $\Sigma \pi d_b$ is the summation of the perimeters of the reinforcing bars within that area. This relationship clearly indicates that elements with poorer bond, and thus larger *m*, exhibit lower tension stiffening.

Apart from tension softening models, the *fib Model Code 2010* model, available in *FRC tension models*, can be used to explicitly include the tensile behavior of a fiber-reinforced concrete. In this model, fibers are defined in the reinforcement component properties together with concrete properties, as in the case of smeared reinforcement. The writer's attempt to use this model in the current version of VecTor2, however, did not yield good results. Therefore, FRC tension models were not further considered in this study.

Concrete confinement increases compressive strength and ductility. Confined strength models in VecTor2 use the strength enhancement factor, β_l, to increase the uniaxial compressive strength ($f_c^{'}$) and corresponding strain (ε_o). The modified peak

compressive strength (f_p) and strain (ε_p) in the presence of both confinement and softening are determined as,

$$f_p = \beta_d \beta_l f_c^{'} \tag{5-10}$$

$$\varepsilon_p = \beta_d \beta_l \varepsilon_o \tag{5-11}$$

where β_d is the parameter accounting for compression softening, as discussed earlier.

The *Kuper / Richart* model was used to simulate the enhanced compressive strength and ductility of concrete due to confinement. For triaxial compression, where $f_{c3} < f_{c2} < f_{c1} < 0$, β_l is determined in the *Kuper/Richart* model as,

$$\beta_l = \left[1 + 0.92 \left(\frac{f_{cn}}{f_c^{'}} \right) - 0.76 \left(\frac{f_{cn}}{f_c^{'}} \right)^2 \right] + 4.1 \left(\frac{f_{cl}}{f_c^{'}} \right) \qquad for\ f_{c2} < f_{c1} < 0 \tag{5-12}$$

where $f_c^{'}$ is the compressive concrete cylinder strength, f_{c1} and f_{c2} are lateral compressive stresses acting on the concrete, and f_{cl} is the lateral confining stress, taken as the least principal compressive stress:

$$f_{cl} = -f_{c1} > 0 \tag{5-13}$$

and

$$f_{cn} = -(f_{c2} - f_{c1}) > 0 \tag{5-14}$$

In Eq. (5-12), the first term is a modification of the model proposed by Kupfer et al. (1969) and the second term is the confinement effect in columns with spiral reinforcement suggested by Richart et al. (1928).

For other compressive stress directions, β_l can be calculated by interchanging f_{c3}, f_{c2}, and f_{c1} as necessary.

Concrete lateral expansion may significantly contribute to the total strains in the principal maximum strain direction. “If these strains are incorrectly attributed to tensile straining due to stress, the compression softening effect may be overestimated (Wong and Vecchio, 2002).” To address this issue, Vecchio (1992) modified the formulation of the concrete stiffness matrix by adding the Poisson ratios, ν_{12} and ν_{21} that relate stresses and strains in the principal directions.

When confined by reinforcement, the lateral expansion causes passive confining pressure, which may increase strength and ductility of concrete in compression. In this study, the effect of lateral concrete expansion under compression on strength and ductility of the member was modeled using the *Variable – Kupfer* model (Kupfer et al., 1969). In this model, the Poisson's ratio (ν_{ij}), which relates the concrete expansion in the *i*-direction due to compressive strain, ε_{cj}, in the principal *j*-direction, is determined as,

$$\nu_{ij} = \begin{cases} 0 & for -0.5\varepsilon_p < \varepsilon_{cj} < 0 \\ \nu_o \left[1 + 1.5 \left(\dfrac{-2\varepsilon_{cj}}{\varepsilon_p} - 1 \right)^2 \right] \le 0.5 & for\ \varepsilon_{cj} < -0.5\varepsilon_p \end{cases} \tag{5-15}$$

where ε_p is the strain at the peak compressive stress. This dilation model nonlinearly increases the Poisson's ratio as compressive strain increases.

The Concrete Cracking Criterion was modeled using the *Mohr-Coulomb (Stress)* model. The cracking strength, f_{cr}, is calculated as,

$$f_{cr} = f_{cru}\left(1 + \frac{f_{c3}}{f_c^{'}}\right), \qquad 0.20 f_t^{'} \le f_{cr} \le f_t^{'} \tag{5-16}$$

where $f_t^{'}$ is concrete tensile strength, and f_{cru} is determined as,

$$f_{cru} = f_c^{'} \frac{2c \cdot \cos\phi}{2\cos\phi} \tag{5-17}$$

$$c = f_c^{'} \frac{1 - \sin\phi}{2\cos\phi} \tag{5-18}$$

ϕ is assumed to be 37 degrees in VecTor2.

Provided $\varepsilon_{c3} < \varepsilon_{c2} < \varepsilon_{c1}$, the principal compressive stress, f_{c3}, is calculated as,

$$f_{c3} = \begin{cases} -f_c^{'}\left[2\left(\dfrac{\varepsilon_{c3}}{\varepsilon_o}\right) - \left(\dfrac{\varepsilon_{c3}}{\varepsilon_o}\right)^2 \right] & for \quad \varepsilon_o < \varepsilon_{c3} < 0 \\ -f_c^{'} & for \quad \varepsilon_{c3} < \varepsilon_o < 0 \\ 0 & for \quad 0 < \varepsilon_{c3} \end{cases} \tag{5-19}$$

The Crack Stress Calculation was performed using the *Basic DSFM* model. The crack slip calculation models allow VecTor2 to explicitly account for average strains due to shear slip along cracks. The *Walraven (Monotonic)* model was utilized to calculate the slip along the crack in this study.

"The crack width check serves to reduce average compressive stresses when crack widths exceed a specified limit. This check was implemented for the analysis of shear-critical reinforced concrete members having little or no shear reinforcement (Wong and Vecchio, 2002)." The crack width check reduces the average compressive stress, f_{c2}^{*}, by a crack coefficient β_{cr} as

$$f_{c2} = \beta_{cr} f_{c2}^{*} \tag{5-20}$$

$$\beta_{cr} = \begin{cases} 1 & for \quad w < w_l \\ 1-(w-w_l)/3 \quad \geq 0 & for \quad w > w_l \end{cases} \tag{5-21}$$

where w is the crack width and w_l is the limiting crack width. If crack width check is omitted, β_{cr}=1.0.

This check was omitted for the analyses of the HPFRC coupling beams in this study because the models failed prematurely when the crack width check was selected. For RC Specimen CB-4, a crack width check of 5 mm was selected.

Due to internal damage of concrete, stress-strain curve under loading, unloading, and reloading does not follow the same paths. The default "*Nonlinear with Plastic Offsets*" model was found to be adequate for the modeling of the hysteresis behavior of concrete in the coupling beams of this study. This model uses nonlinear Ramsberg-Osgood formulations to define the unloading path in the compression and tension domains.

Concrete stress, f_c, for unloading in compression to strain ε_c is determined as,

$$f_c = \begin{cases} f_{cm} + E_c(\varepsilon_c - \varepsilon_{cm}) + \dfrac{E_c(\varepsilon_c - \varepsilon_{cm})^{N_c}}{N_c(\varepsilon_c^p - \varepsilon_{cm})^{N_c - 1}} & for \quad 1 \leq N_c \leq 20 \\ E_c(\varepsilon_c - \varepsilon_c^p) & for \quad N_c \leq 1 \quad or \quad N_c \geq 20 \end{cases} \tag{5-22}$$

where ε_{cm} is the maximum previously attained compressive strain, f_{cm} is the corresponding stress, ε_c^p is the current plastic offset strain, E_c is the elastic modulus of concrete, and N_c is the Ramsberg-Osgood coefficient calculated as,

$$N_c = \frac{E_c \cdot (\varepsilon_c^p - \varepsilon_{cm})}{f_{cm} + E_c(\varepsilon_c^p - \varepsilon_{cm})} \tag{5-23}$$

Concrete stress, f_c, for unloading in tension to strain ε_c is determined as,

$$f_c = \begin{cases} f_{cm} - E_c(\varepsilon_{tm} - \varepsilon_c) + \dfrac{E_c(\varepsilon_{tm} - \varepsilon_c)^{N_t}}{N_t(\varepsilon_{tm} - \varepsilon_c^p)^{N_t - 1}} & for \quad 1 \le N_t \le 20 \\ E_c(\varepsilon_c - \varepsilon_c^p) & for \quad N_t \le 1 \quad or \quad N_t \ge 20 \end{cases} \tag{5-24}$$

where ε_{tm} is the maximum previously attained tensile strain, f_{tm} is the corresponding stress, and N_t is the Ramsberg-Osgood coefficient calculated as,

$$N_t = \frac{E_c \cdot (\varepsilon_{tm} - \varepsilon_c^p)}{E_c(\varepsilon_{tm} - \varepsilon_c^p) - f_{tm}} \tag{5-25}$$

Concrete stress, f_c, for reloading in compression to strain ε_c is determined as,

$$f_c = \begin{cases} 0 & for \quad \varepsilon_c^p < \varepsilon_c < 0 \quad or \quad \varepsilon_c > 0 \\ \dfrac{\varepsilon_c - \varepsilon_c^p}{\varepsilon_{cm} - \varepsilon_c^p} \cdot f_{cm} & for \quad \varepsilon_{cm} < \varepsilon_c < \varepsilon_c^p < 0 \\ f_{bc}(\varepsilon_c) & for \quad \varepsilon_c < \varepsilon_{cm} < 0 \end{cases} \tag{5-26}$$

where $f_{bc}(\varepsilon_c)$ is the defined function of the monotonic stress-strain curve.

At a given compressive strain, ε_c, when the instantaneous plastic strain, $\varepsilon_c^{p'}$, exceeds the current plastic offset strain, ε_c^p, the current plastic strain is updated to $\varepsilon_c^{p'}$.

Concrete stress, f_c, for reloading in tension to strain ε_c is calculated as,

$$f_c = \begin{cases} \dfrac{\varepsilon_c - \varepsilon_c^p}{\varepsilon_{tm} - \varepsilon_c^p} \cdot f_{tm} & for \ \varepsilon_c^p < \varepsilon_c < \varepsilon_{tm} \\ f_{bt}(\varepsilon_c) & for \quad \varepsilon_c > \varepsilon_{cm} \end{cases} \tag{5-27}$$

where $f_{bt}(\varepsilon_c)$ is the function defining the monotonic tensile stress-strain base curve.

The *Bauschinger Effect (Seckin)* model was used to represent the hysteresis behavior of reinforcement. This model accounts for strain hardening and Bauschinger

effect, which is important when simulating the behavior of steel under reversed cyclic stresses.

Dowel action of the reinforcement at the location of cracks was simulated using the default "*Tassios (Crack Slip)*" model. The dowel force, V_d, due to the shear slip, δ_s, along the crack is computed as,

$$V_d = E_s I_z \lambda^3 \delta_s \le V_{du} \tag{5-28}$$

$$I_z = \frac{\pi d_b^4}{64} \tag{5-29}$$

$$\lambda = \sqrt[4]{\frac{k_c d_b}{4 E_s I_z}} \tag{5-30}$$

$$k_c = \frac{127 \cdot c\sqrt{f_c'}}{d_b^{2/3}} \tag{5-31}$$

$$c = 0.8 \tag{5-32}$$

$$V_{du} = 1.27 d_b^2 \sqrt{f_c' f_y} \tag{5-33}$$

where d_b is the diameter of reinforcement, E_s is the elastic modulus of reinforcement, f_y is yield strength, I_z is the moment of inertia of reinforcement, f_c' is the concrete compressive strength, and V_{du} is the ultimate dowel force.

5.2.3 HPFRC Models in VecTor2

HPFRC coupling beams pose unique challenges in finite element modeling because of the incorporation of tensile strain-hardening behavior of HPFRC in the models. In VecTor2, the tensile stress-strain response of HPFRC materials can be included using the "Custom Input (Strain Based)" option in the "Tension Softening" concrete models. When "Custom Input (Strain Based)" was selected, the defined tensile stress-strain response of concrete was activated and modeled using a four-point piecewise linear relation, as indicated under "Tension Softening" in "Auxiliary" tab (Figure 5.4). It should be noted that the "Tension Softening" model not only refers to strain-softening behavior, but also allows the modeling of a strain-hardening response, depending on the input values of the tensile stress-strain model. Stress-strain values used to model the tensile response of HPFRC in this study are shown in Figure 5.5 and Table 5.8, which correspond to the values in Table 4.10 expressed in SI units.

The inclusion of strain-hardening response of HPFRC, however, had an impact on the concrete models used for the top and base blocks of the modeled specimens. The "Tension Softening" model, when activated, applies to all types of concrete used and not to one in particular. This means that the concrete for the top and base blocks would have to be modeled also as HPFRC. Even though the response of the top and base blocks was of little interest in this study, proper simulation of load transfer at the cold joints between the beam ends and the end blocks was critical. At the cold joint sections, the lack of fibers bridging the HPFRC beam and concrete wall interface led to a weaker section compared to adjacent sections. Because of this limitation, phenomena such as sliding at the beam-wall interface could not be well captured. Therefore, comparison of numerical and experimental results focused on the flexural and shear behavior within the coupling beam, as well as concentrated rotations due to bar slip (even though blocks were made of HPFRC in the model), thus excluding the effect of sliding at the beam-wall interfaces.

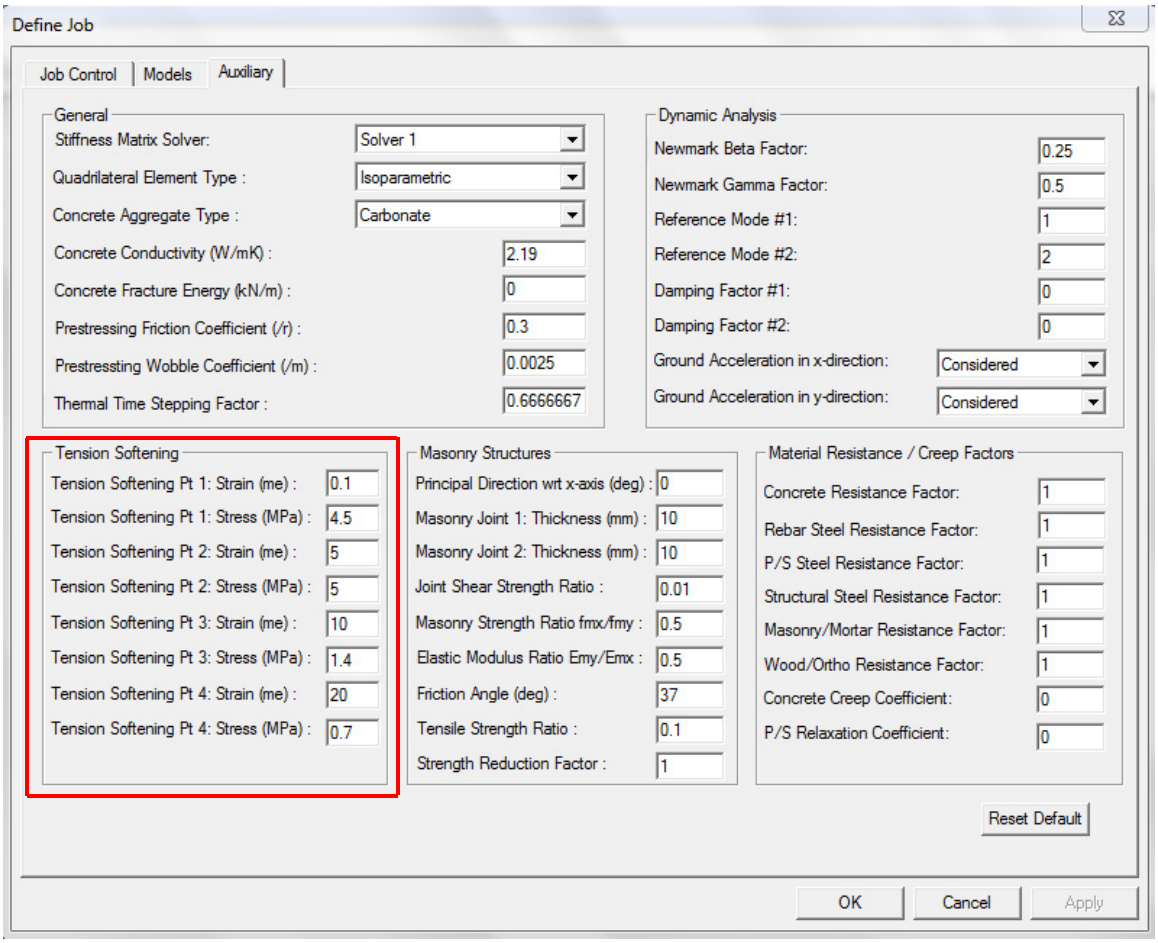

Figure 5.4 Incorporation of HPFRC tensile stress-strain properties in VecTor2

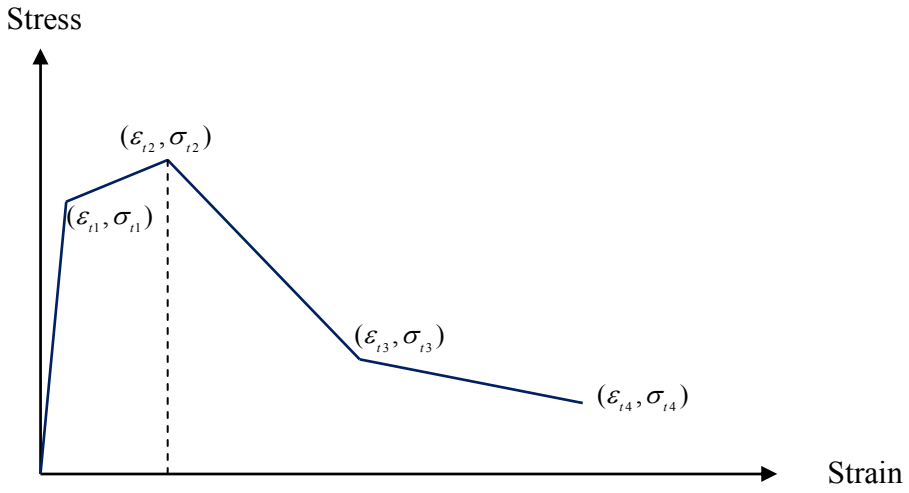

Figure 5.5 Tensile stress-strain model for HPFRC matrix

Table 5.8 Tensile stress-strain values for modeling HPFRC

Matrix	σ_{t1} (MPa)	ε_{t1} (me)[3]	σ_{t2} (MPa)	ε_{t2} (me)	σ_{t3} (MPa)	ε_{t3} (me)	σ_{t4} (MPa)	ε_{t4} (me)
HPFRC[1]	2.8	0.1	3.5	5	1.4	10	0.7	20
HPFRC[2]	4.5	0.1	5	5	1.4	10	0.7	20

[1] for Specimen CB-1
[2] for Specimens CB-2, CB-3 and CB-5
[3] me stands for millistrain

5.2.4 Boundary Conditions and Imposed Displacements

In the FE models, hinge supports were applied to the bottom end of the steel links. Four nodes at the bottom of the concrete base block were constrained in their translational degrees of freedom, corresponding to the location of thread rods used to anchor the base block to the strong floor in the experimental setup. In the experiments, restraint against vertical translation on the base block side trying to uplift was provided by steel plates bearing on top of the base block and connected to steel rods anchored in the laboratory strong floor. This support condition, however, was not included because models with additional nodes on top of the base block restrained yielded similar results.

The coupling beam models were subjected to reversed cyclic displacements at the top concrete block. The analysis consisted of displacement cycles as indicated in Tables D.1 to D.6 in Appendix D. These displacement cycles were slightly different from the actual cycles imposed on the test coupling beams. As discussed in Section 4.1.3, predefined drifts were adjusted to account for rotations of the base and top blocks and slip of the base block, resulting in irregular patterns of adjusted or "actual" drifts. Applying non uniform actual drifts to the models would add substantial unjustified complications. Therefore, imposed displacements applied to the models were slightly adjusted to obtain idealized regular patterns of cyclic displacements.

5.3 ANALYSIS RESULTS

5.3.1 Load-Drift Responses

The load versus drift response for each test specimen, obtained from the FE analyses, is compared with the experimental response in Figures 5.6(a) through Figure 5.6(f). The numerical models of Specimens CB-1 through CB-4 adequately captured the overall response of the test specimens. The models for Specimens CB-2 and CB-3, however, slightly over-predicted the peak load.

The model for Specimen CB-5, on the other hand, did not adequately simulate the entire load-drift response of the test specimen. The model failed at approximately 4.8% drift, compared to 6.8% drift in the actual coupling beam specimen. The reason for the underestimation of drift was the fact that concentrated deformations due to bond slip and shear slip at the interface between the beam ends and the end blocks could not be properly modeled. While these deformations at the beam-wall interfaces were small for Specimens CB-1 through CB-4 (damage ultimately localized at the end of the dowel reinforcement), these deformations were significant in Specimens CB5 and CB6 (see Section 4.8).

When comparing the response obtained from the FE models with the experimental drift excluding sliding along beam-wall interfaces (i.e., drift contributed by flexural and shear deformations within the coupling beam, as well as rotations due to steel strain penetration), as shown in Figures 5.7(a) through 5.7(e), it can be seen that the two responses agreed reasonably well. It should be mentioned that for Specimens CB-1 and CB-4, drifts contributed by shear and flexural deformations, and steel strain penetration, could not be obtained for the whole test due to the loss of some Optotrak markers during testing.

The model for Specimen CB-6 did not adequately capture the behavior of the test specimen. The model failed at approximately 4.1% drift, compared to 6.5% drift in the actual coupling beam specimen, as shown in Figure 5.6(f). Moreover, the load-drift response of the model did not exhibit pinching, as opposed to that of the test specimen. The pinching of hysteresis for the test specimen resulted from sliding shear displacement at the bottom beam-wall interface, which VecTor2 could not properly model.

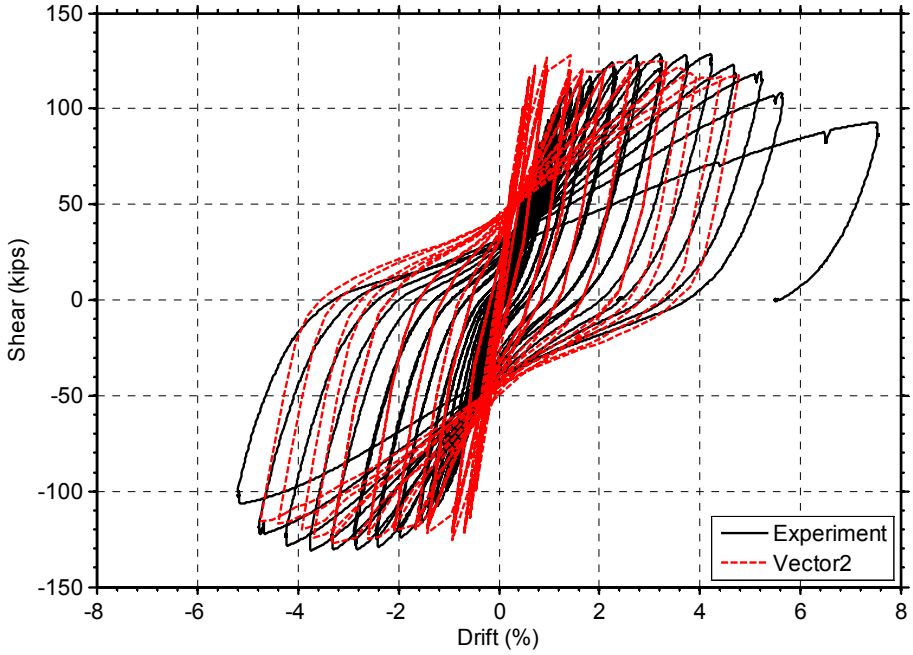

(a) Specimen CB-1

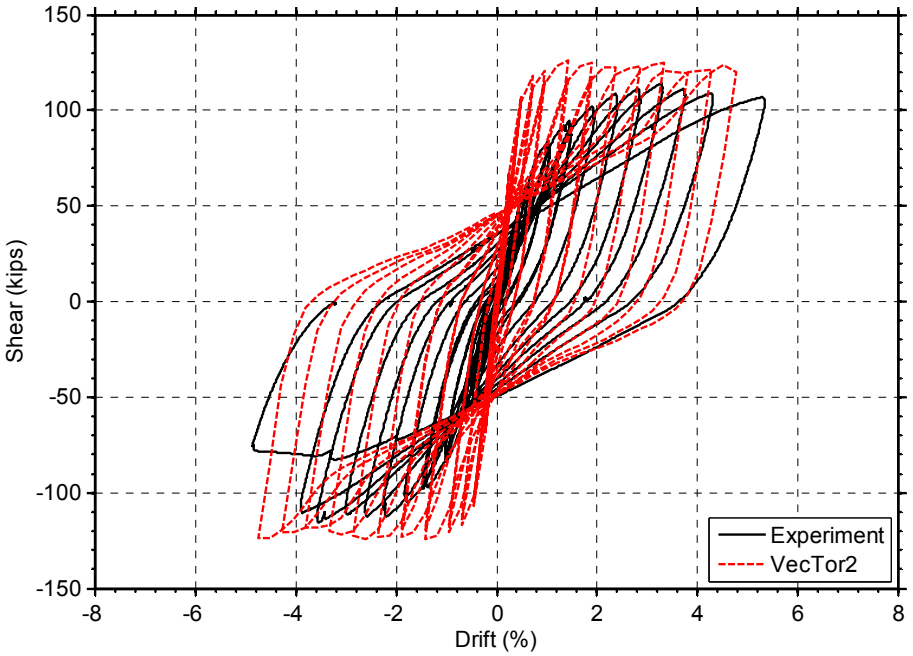

(b) Specimen CB-2

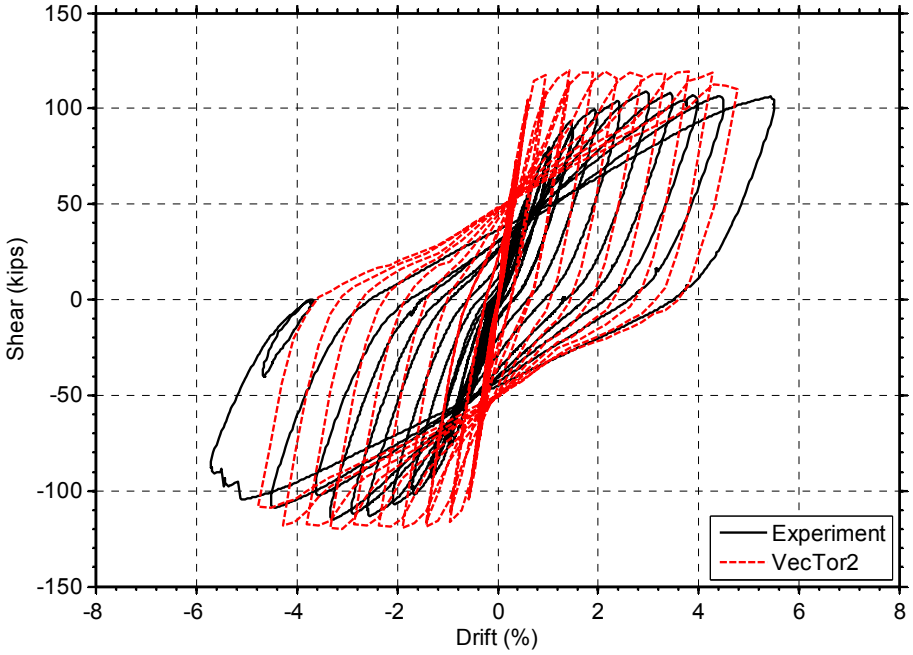

(c) Specimen CB-3

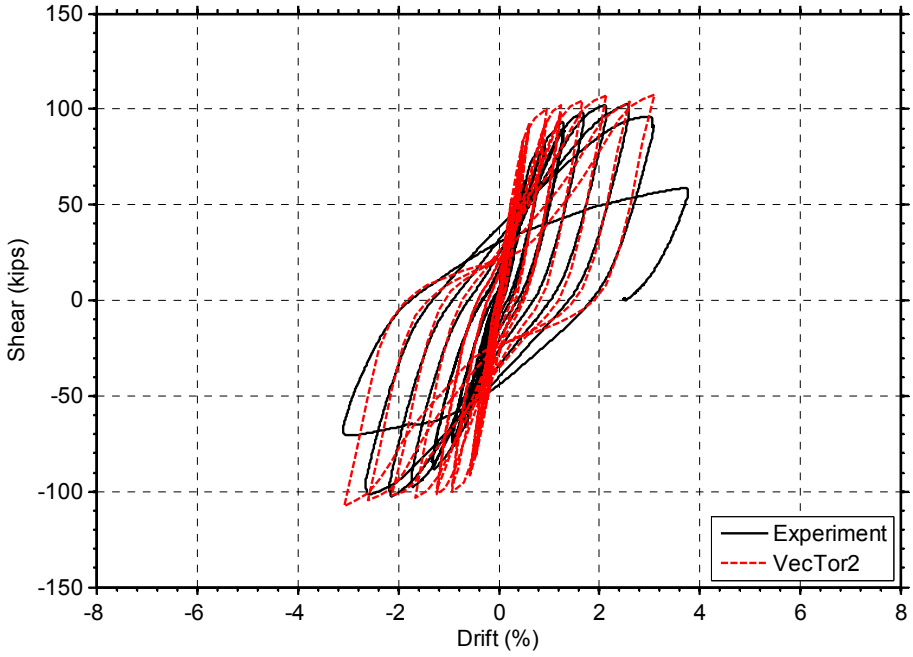

(d) Specimen CB-4

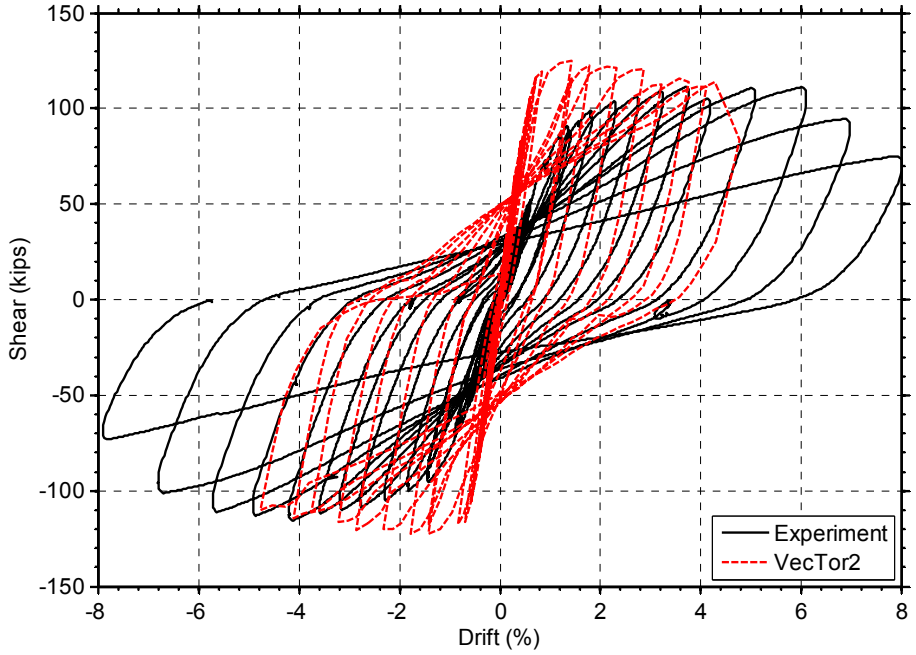

(e) Specimen CB-5

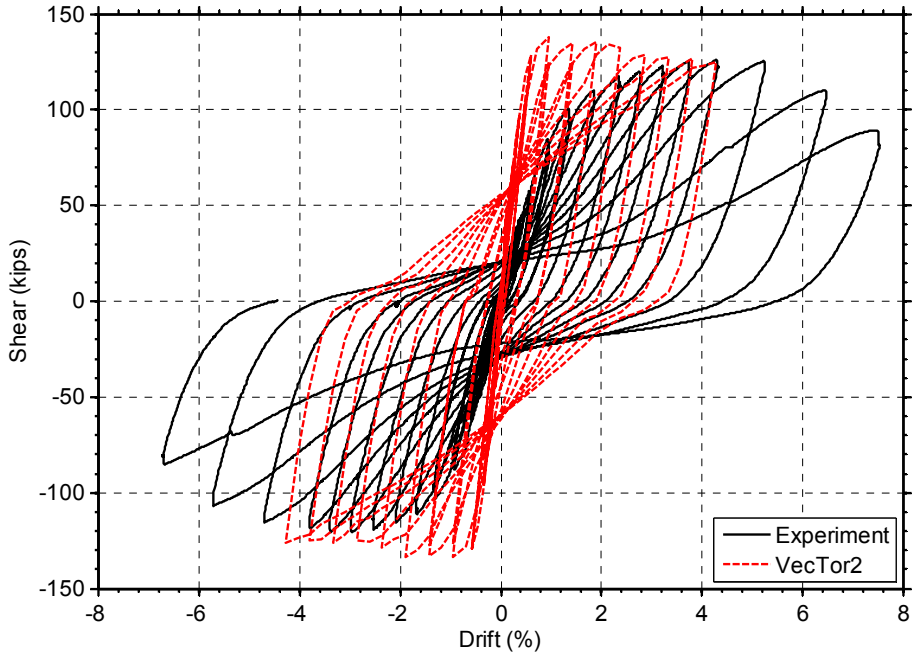

(f) Specimen CB-6

Figure 5.6 Experimental and simulated VecTor2 shear force versus drift responses

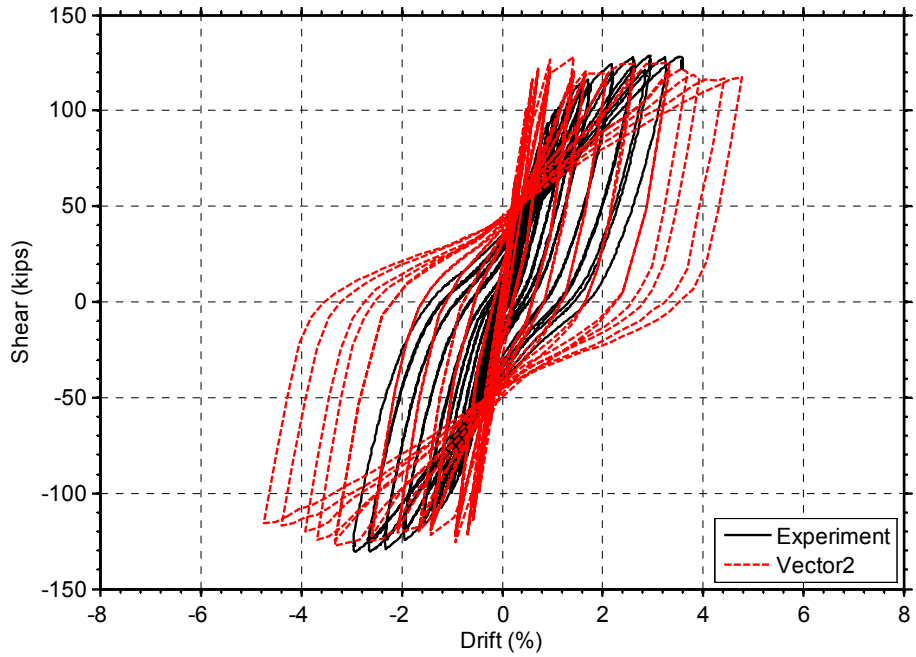

(a) Specimen CB-1

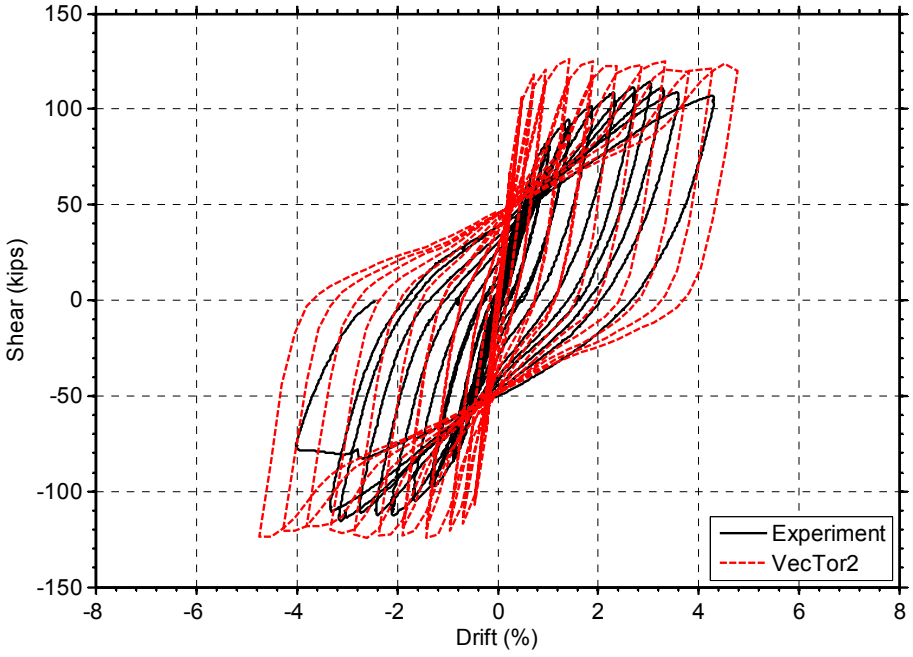

(b) Specimen CB-2

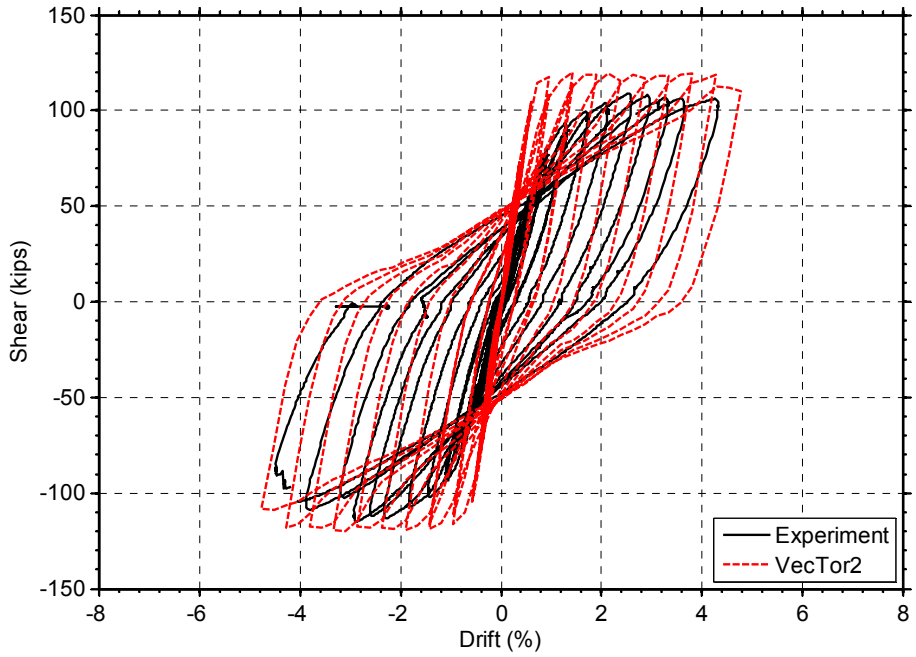

(c) Specimen CB-3

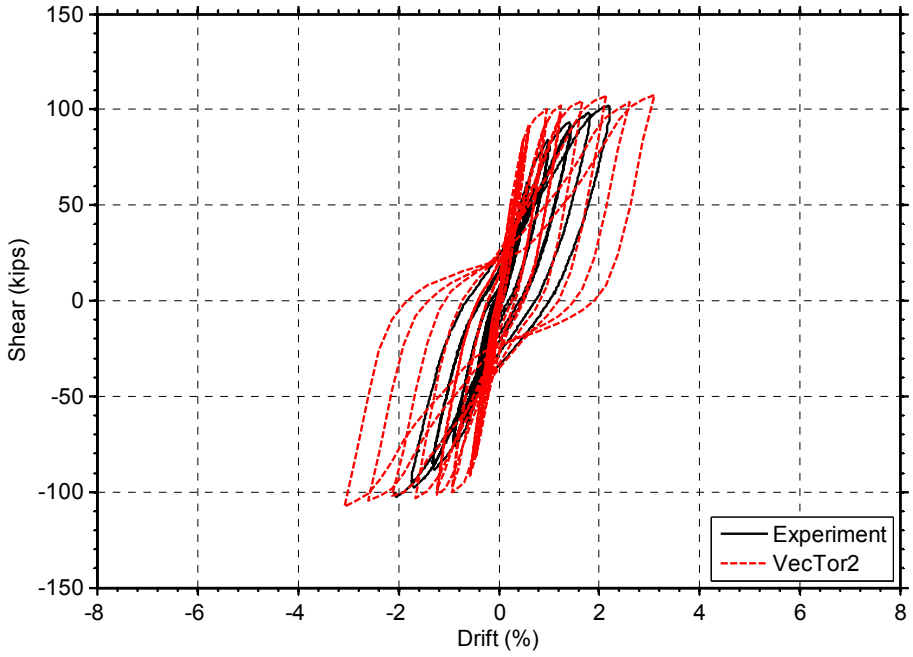

(d) Specimen CB-4

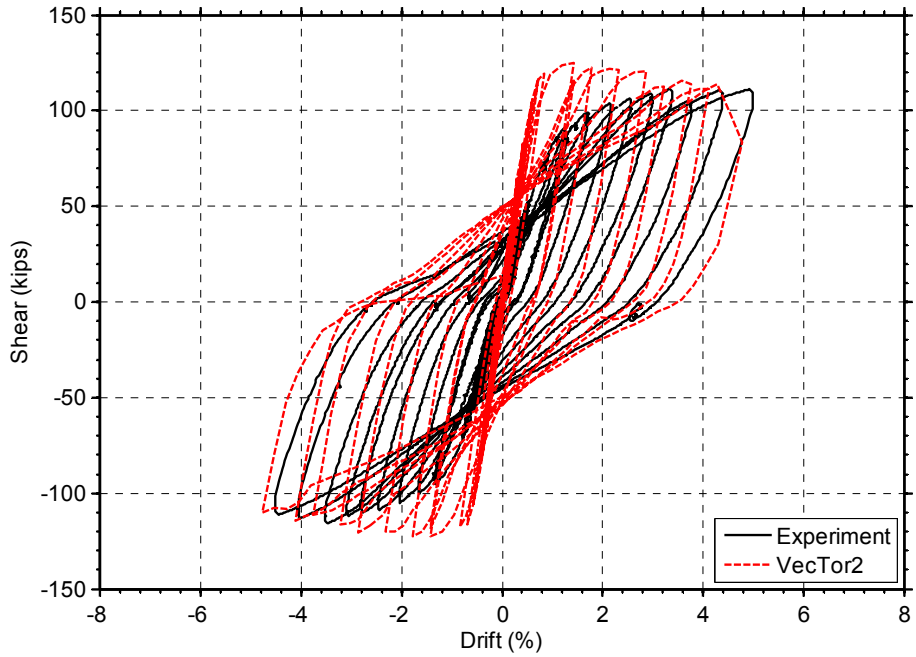

(e) Specimen CB-5

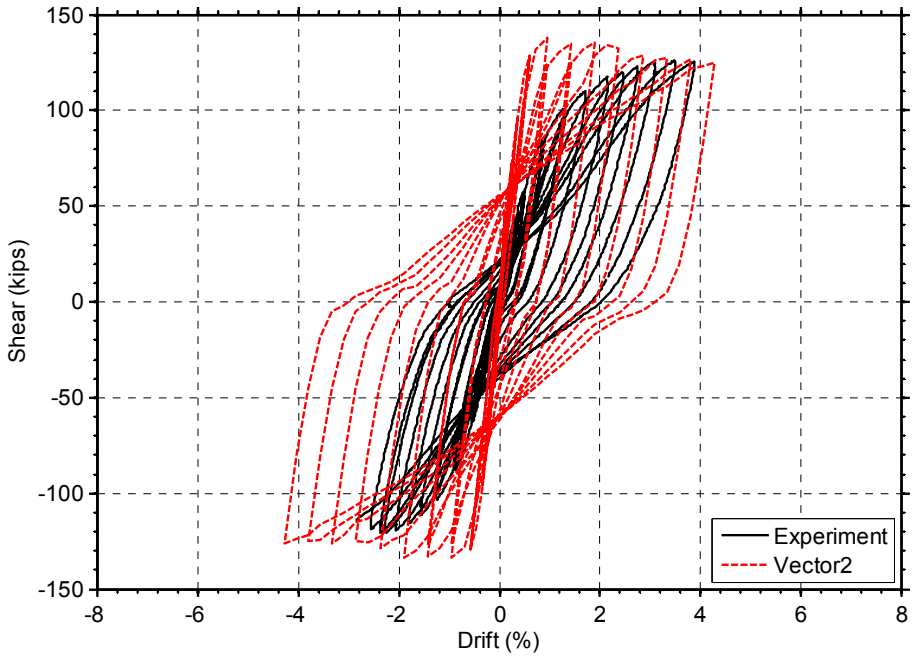

(f) Specimen CB-6

Figure 5.7 Comparison of shear-drift response from VecTor2 and experimental shear versus drift response (excluding shear sliding along beam-wall interfaces)

All of the models over-predicted the specimen stiffness in the early loading cycles. This over-prediction was believed to be primarily caused by the flexibility of the steel links, which was not constant during testing, while truss elements with constant properties were used in the FE models. In the early loading cycles, the flexibility of the steel links was found to be much higher than that in the later cycles. The effect of steel link flexibility on specimen stiffness can be seen in Figures 5.8(a) through (e). In these plots, the envelopes of the simulated hysteresis response using very flexible and stiff links are compared with the experimental hysteresis responses. Stiff links refer to links with steel area of 1500 mm^2, as discussed in Section 5.2.1, to ensure reasonable axial forces could be generated. On the other hand, very flexible links led to negligible axial forces developed in the steel links. Very flexible links were modeled using a steel area of 500 mm^2 with the same yield and ultimate strength as those used in stiff links, as defined in Section 5.2.1. From Figures 5.8(a) through (e), it can be seen from these plots that increasing flexibility of the steel links decreased the stiffness of the coupling beams in the early cycles. This stiffness was close to that of the test specimens for the early cycles, particularly for Specimens CB-3 and CB-4, while being slightly higher than that of the experimental stiffness for Specimens CB1, CB-2 and CB-5.

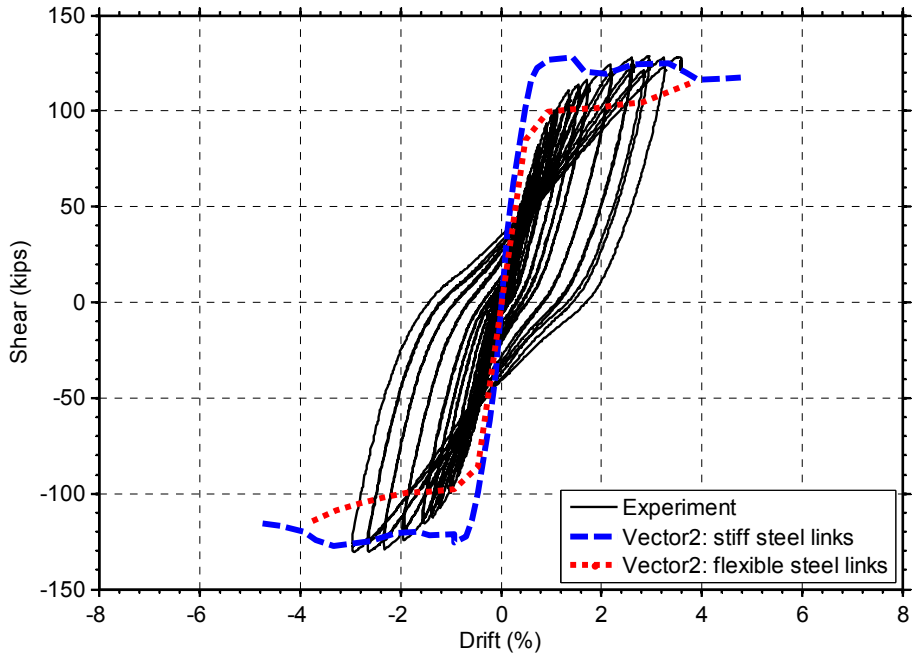

(a) Specimen CB-1

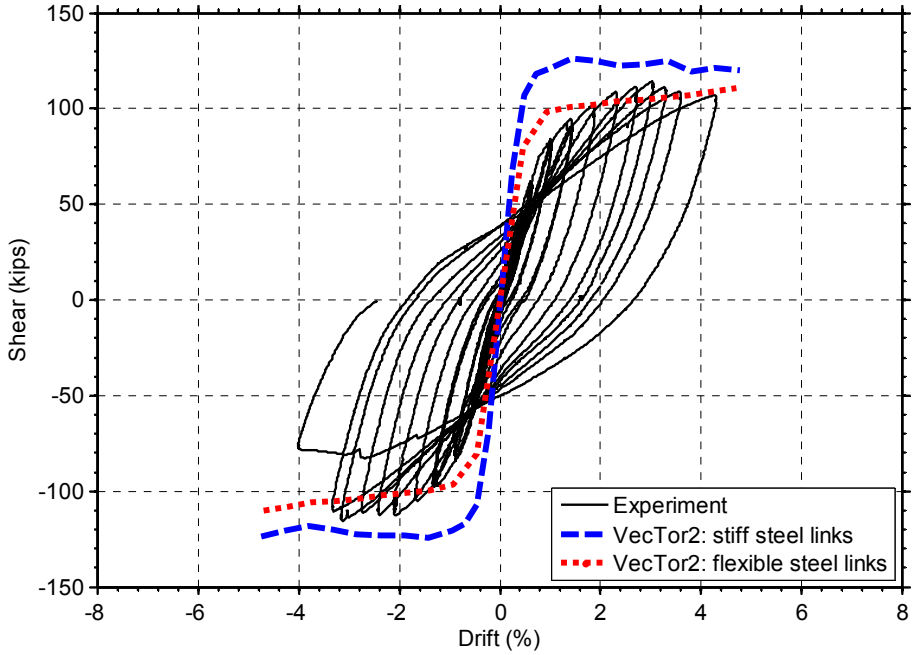

(b) Specimen CB-2

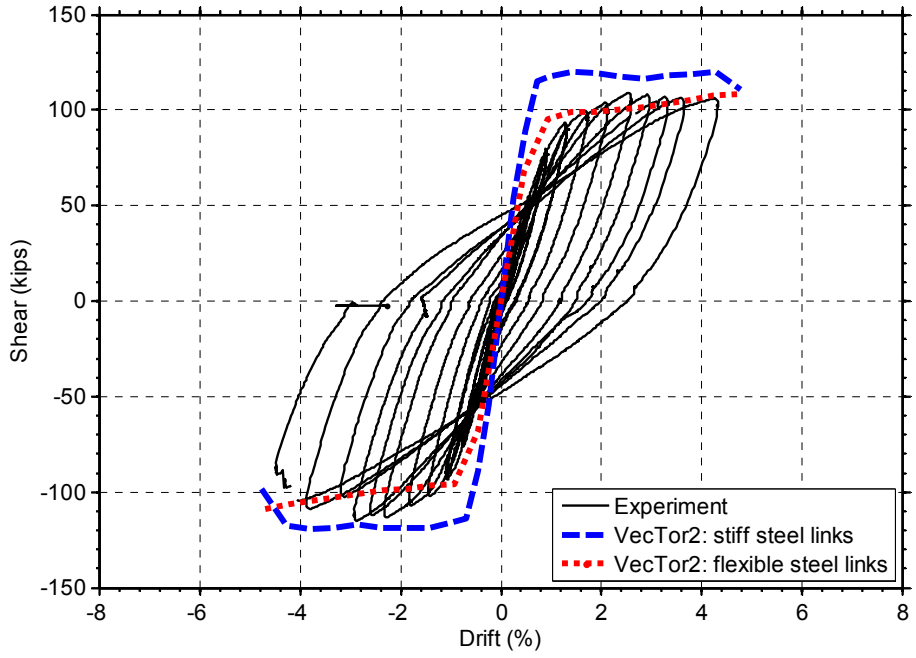

(c) Specimen CB-3

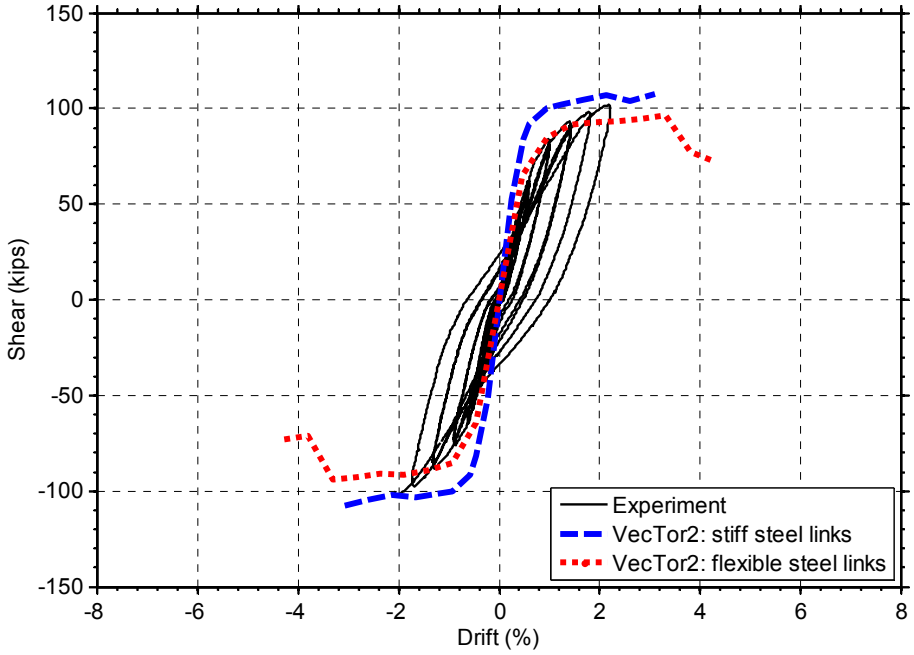

(d) Specimen CB-4

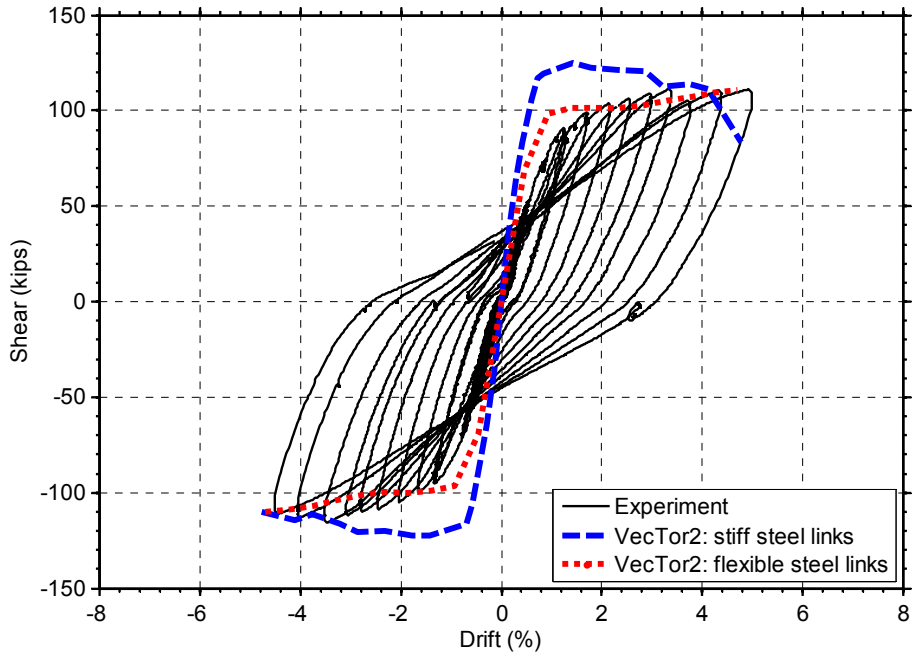

(e) Specimen CB-5

Figure 5.8 Experimental hysteresis response and envelopes of analytical shear force versus drift responses with stiff and flexible steel links

5.3.2 Failure Modes and Crack Patterns

Figures 5.9(a) through (d) show crack patterns of the HPFRC models for Specimens CB-1, CB-2, CB-3, and CB-5. Substantial flexural cracking at the beam ends, indicating flexural deformations played a significant role on specimen behavior. Shear-related damage from diagonal cracks was minor (with crack widths less than 0.3 mm at 4.8% drift for all HPFRC models), as indicated in the figures, and consistent with the experimental observations. The analytical models failed by large flexural cracks (greater than 20 mm) at the ends of the coupling beams. Even though the failure planes occurred near the termination of dowel bars in the test specimens, overall damage of the HPFRC specimens was well captured in the VecTor2 models.

For RC Specimen C-4, flexural cracks developed in the model near the termination of dowel bars at approximately 1% drift. As drift increased, additional flexural cracks formed within the plastic hinges, as illustrated in Figure 5.10. Diagonal cracks at 1.2% drift had a maximum width of approximately 0.5 mm. At approximately 2% drift, diagonal cracks wider than 3 mm developed in the middle area of the beam. Diagonal cracks became even wider (4 mm) and spread throughout the beam as drift reached 3%, as shown in Figure 5.11. These diagonal cracks caused pinching of the analytical hysteresis loops (Figure 5.6(d)). Diagonal cracks developed in the test specimen, however, were less than 1 mm in width prior to failure. It is likely that diagonal bars modeled with smeared reinforcement were not as efficient as concentrate diagonal reinforcement, resulting in wider diagonal cracks.

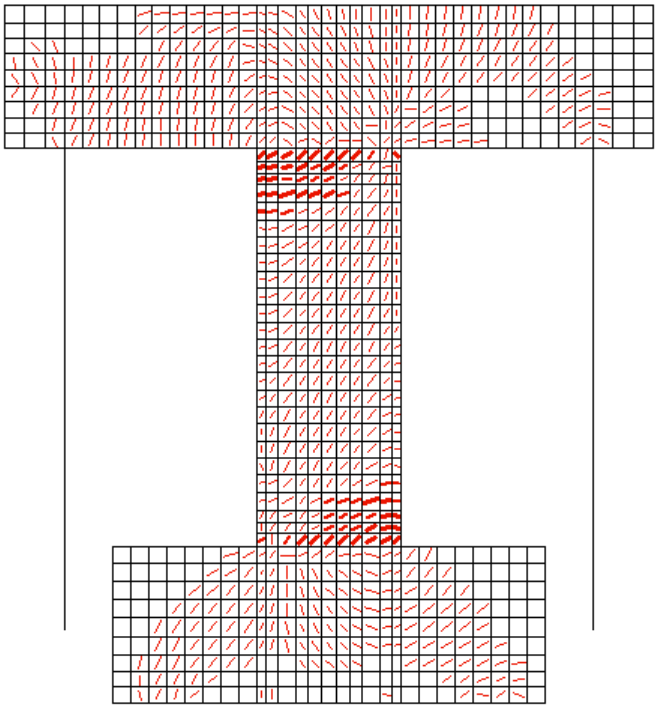

(a) Specimen CB-1

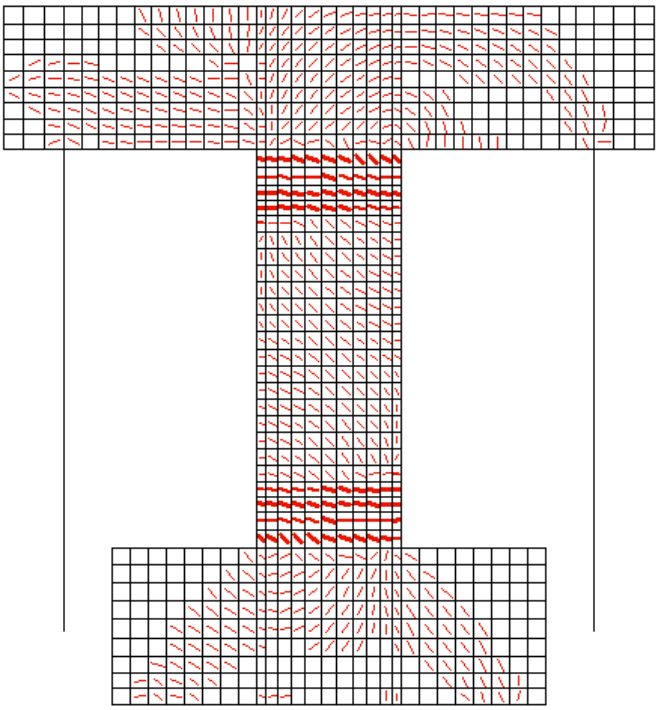

(b) Specimen CB-2

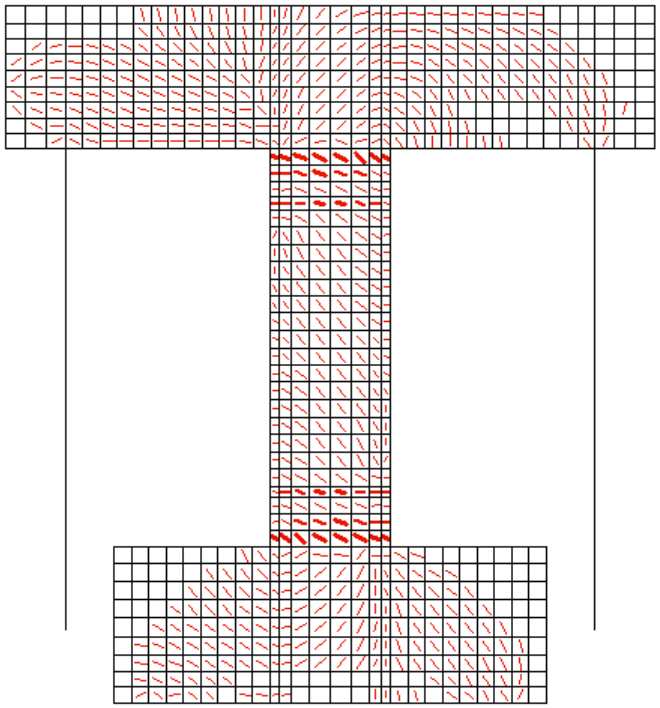

(c) Specimen CB-3

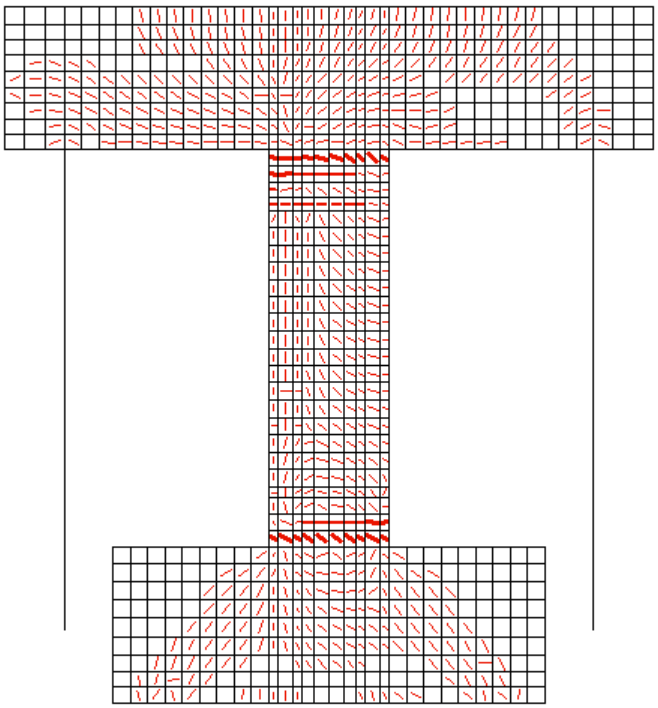

(d) Specimen CB-5

Figure 5.9 Crack patterns for the HPFRC coupling beam numerical models at approximately 4.8% drift

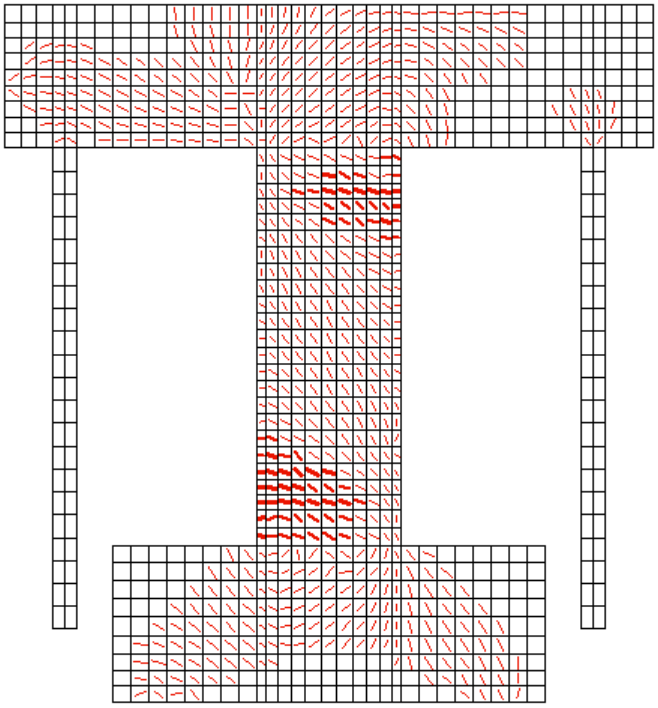

Figure 5.10 Crack patterns of the RC coupling beams numerical model at approximately 2% drift

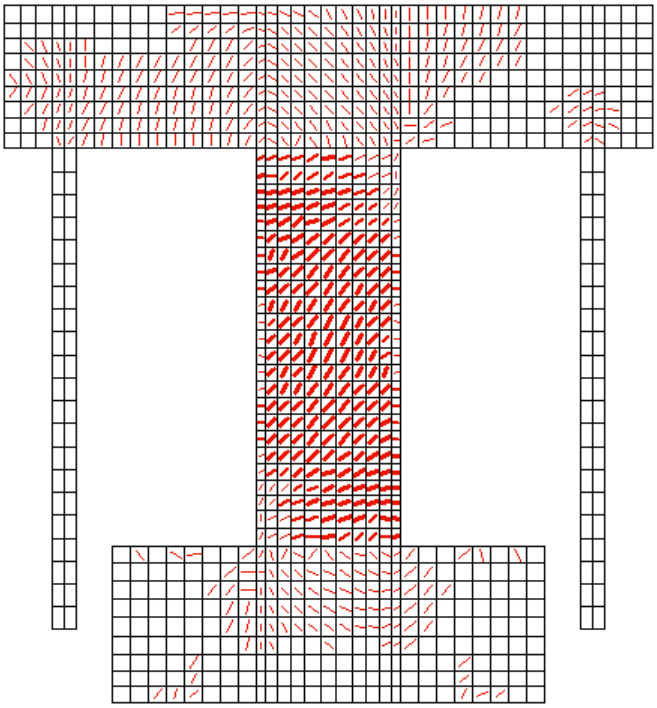

Figure 5.11 Crack patterns of the RC coupling beams numerical model at approximately 3% drift

Axial forces and end moments developed in selected coupling beam models were examined to ensure that they were in reasonable agreement with those in the test specimens. Tables 5.9 and 5.10 show axial forces and end moments for the models of Specimens CB2 and CB-5, respectively, at various drift levels in the positive loading direction. The axial forces obtained from the numerical models were reasonable when compared to the ranges of axial forces developed in the test specimens (40-90 kips). It is believed that major discrepancies in maximum axial forces likely resulted from concentrated deformations at the beam-wall interfaces, which could not be properly captured in the numerical models. Even though differences in maximum axial forces were large in some cases, they represented only 3% of the axial force capacity of both specimens. Peak end moments obtained from the numerical models were in reasonable agreement with those of the test specimen, which ranged between 3000 and 3800 kip-in. in the positive direction for drifts beyond 1.5%. However, differences between end moments obtained from the numerical models and from the experiments were expected due to the discrepancy in axial forces that developed in the numerical models and those measured during the experiments.

Table 5.9 Axial force and end moments obtained from the numerical model of Specimen CB-2

Drift (%)	Axial force		Moment at top end		Moment at bottom end	
	kN	kips	kNm	kip-in	kNm	kip-in
1.4	5	45	400	3500	430	3800
1.9	205	45	390	3470	420	3700
2.4	210	45	390	3460	400	3580
2.9	215	50	390	3440	400	3510
3.3	220	50	380	3350	420	3740
3.8	220	50	370	3270	400	3520
4.3	215	50	370	3290	400	3570
4.8	215	50	390	3420	400	3530

Table 5.10 Axial force and end moments obtained from the numerical model of Specimen CB-5

Drift (%)	Axial force		Moment at top end		Moment at bottom end	
	kN	kips	kNm	kip-in	kNm	kip-in
1.4	205	45	430	3770	430	3830
1.9	215	50	420	3720	410	3650
2.4	220	50	410	3660	410	3660
2.9	220	50	410	3650	410	3660
3.3	220	50	400	3580	410	3650
3.8	230	50	350	3090	410	3580
4.3	270	60	370	3310	420	3720
4.8	275	60	360	3190	410	3590

5.4 A SUMMARY OF RECOMMENDATIONS FOR FINITE ELEMENT MODELING OF HPFRC COUPLING BEAMS

- Diagonal bars can be modeled as smeared reinforcement together with concrete properties. In RC Specimen CB-4, however, this approach seems to have led to larger crack widths than those measured during the experiments.
- Steel links can be modeled as stand-alone truss elements or truss elements embedded in concrete whose elastic modulus and compressive strength are set close to zero. For the particular case of the coupling beams tested in this investigation, an area of 1500 mm^2 and a yield strength high enough to ensure elastic behavior of the links (250 MPa in this case were found to be appropriate to ensure stability of the steel links and axial forces within the range of those measured during the tests.
- The tensile stress-strain response of HPFRC materials can be included in VecTor2 using the "Custom Input (Strain Based)" option in the "Tension Softening" concrete models.
- Except tension softening models and crack width check, default concrete and reinforcement models recommended by VecTor2 were appropriate for modeling the HPFRC coupling beam specimens. Omission of the crack width check is recommended to prevent premature failure of the numerical model.

CHAPTER 6
SUMMARY AND CONCLUSIONS

6.1 SUMMARY

Structural walls are frequently used as the primary components of the lateral-load resisting system in medium- and high-rise buildings. Due to architectural requirements, structural walls often contain window and door openings, which divide a single wall into more slender walls interconnected by short members called "coupling beams". Well-designed coupled walls are more efficient than the same walls uncoupled because the shear transfer between the walls and coupling beams leads to higher lateral stiffness and strength, as well as energy dissipation. However, coupling beams must possess sufficient deformation capacity in order to ensure adequate system behavior during strong ground motions. This is typically achieved through the use of heavily confined diagonal reinforcement which, unfortunately, has proven to be a daunting construction task.

Due to limitations in story height, coupling beams used in modern office and residential buildings are relatively slender, with aspect ratios on the order of 3.0. In these beams, the effectiveness of diagonal reinforcement is questionable because of the shallow angle of diagonal reinforcement, which is less than 20 degrees with respect to the beam longitudinal axis. Further, the small transverse (shear) component of the diagonal reinforcement force requires the use of larger amounts of steel reinforcement compared to deeper beams designed for the same shear force, leading to additional reinforcement congestion and construction difficulties. However, experimental research (Naish et al. 2009) has shown that diagonal reinforcement, combined with column-type confinement, is still needed in relatively slender RC coupling beams to prevent sliding shear failure and ensure stable behavior under earthquake-type loading.

The construction difficulties posed by the use of heavily confined diagonal reinforcement cages in coupling beams has led researchers to investigate other design alternatives with various degrees of success. One such alternative includes the use of

tensile strain-hardening, high-performance fiber-reinforced concrete (HPFRC). Due to its enhanced ductility, HPFRC materials have proven to be a viable alternative to regular concrete in shear-critical members. Particularly, experimental results from previous research showed that HPFRC can be successfully used as a means to reduce diagonal and confinement reinforcement in coupling beams with aspect ratios of 1.0 and 1.75. These results paved the way to the application of HPFRC in more slender coupling beams with aspect ratios on the order of 3.0.

In this study, the use of HPFRC in slender coupling beams was experimentally evaluated as a means to reduce the need for diagonal and confinement reinforcement. To further simplify reinforcement detailing, the possibility of eliminating diagonal reinforcement in slender HPFRC coupling beams was also investigated. Six precast coupling beams with aspect ratios of 2.75 and 3.3 and peak shear stress demands ranging from $8\sqrt{f_c'}$ to $10\sqrt{f_c'}$ (psi) were test under large displacement reversals. Five specimens were constructed with HPFRC, three of them containing diagonal bars. The remaining two HPFRC specimens were constructed without diagonal bars, while one specimen was constructed with regular concrete

Numerical modeling of the test coupling beams was conducted to determine suitable material models and assumptions required to simulate with reasonable accuracy the behavior of HPFRC coupling beams under large shear reversals. For this purpose, the finite element software VecTor2, a two-dimensional nonlinear finite element program developed at the University of Toronto, was used. The hysteresis response and crack patterns were examined and compared to the experimental results. Guidelines for modeling slender precast coupling beams are proposed based on comparison between numerical and experimental results.

6.2 CONCLUSIONS

The following conclusions can be drawn from the experimental and analytical results of the research program:

(1) Slender HPFRC coupling beams reinforced with a 1.5% volume fraction of high-strength (330 ksi tensile strength), 1.2 in. long and 0.015 in. diameter hooked steel

fibers and subjected to large shear reversals with peak shear stresses in the range of $8.7\sqrt{f_c'}$ to $10.7\sqrt{f_c'}$ (psi) showed a stable behavior despite the elimination of diagonal reinforcement. Drift capacities of approximately 7.0% and 6.5% were achieved in the HPFRC coupling beams without diagonal bars and with aspect ratios of 3.3 and 2.75, respectively.

(2) When diagonal reinforcement was used in the HPFRC coupling beams, the shear resistance provided by that reinforcement was estimated to be below 15% of the total shear. This low shear contribution justified the elimination of diagonal bars for slender HPFRC coupling beams with an aspect ratio on the order of 3.0.

(3) The use of an HPFRC material with a 1.5% volume fraction of high-strength strength (330 ksi tensile strength), 1.2 in. long and 0.015 in. diameter hooked steel fibers allowed a significant relaxation in coupling beam confinement reinforcement. Special column-type confinement reinforcement was used only over a length of half the beam depth from the wall face at both beam ends, where inelastic deformations occurred. In the remaining portions of the coupling beam, the HPFRC material provided sufficient confinement to the diagonal reinforcement, allowing the use of regular stirrup-type transverse reinforcement.

(4) Precasting the HPFRC coupling beams and embedding them approximately 1-inch into the wall was found to be a simple and efficient construction method. The coupling beam moment capacity and associated shear were successfully transferred to the walls by embedding the longitudinal, dowel and diagonal (if any) reinforcement into the wall at least one development length. No shear keys were found necessary to successfully transfer shear between the coupling beam and walls.

(5) For design purposes, shear strength contribution from the HPFRC material can be conservatively estimated to be $5\sqrt{f_c'}$ (psi) times the beam cross sectional area.

(6) The substantially larger drift capacity and damage tolerance exhibited by the HPFRC specimens with an aspect ratio of 2.75 compared to those of an equally reinforced regular concrete coupling beam specimen confirmed the effectiveness of HPFRC in providing confinement and increasing shear strength, which led to higher coupling beam ductility.

(7) Energy dissipated in the HPFRC coupling beams per loading cycle, normalized by the energy dissipated by an equivalent elasto-plastic system, was approximately 0.35-0.45 for drifts larger than 1.5%. Despite the significant reduction in or elimination of diagonal reinforcement area, the HPFRC coupling beam specimens still exhibited normalized energy dissipation values close to those of well-detailed diagonally reinforced concrete specimens with similar aspect ratios.

(8) An effective flexural stiffness of $E_c I_g / 8$ to $E_c I_g / 5$ at 0.75% drift (first yield) is recommended for precast coupling beams with an aspect ratio between 2.75 and 3.3. This stiffness is consistent with that of other tests of diagonally reinforced concrete coupling beams, indicating that the precast embedment does not considerably reduce the flexural stiffness of the coupling beams.

(9) The effective shear stiffness of slender coupling beams was below $0.05E_c A_g$ at drifts beyond 1%. This low shear stiffness is similar to that of precast HPFRC coupling beams with an aspect ratio of 1.75 and suggests that the effective shear stiffness of $0.4E_c A_g$ recommended by ASCE/SEI 41-06 is not appropriate for modeling of coupling beams.

(10) The flexural and shear behavior of the test coupling beams was simulated with reasonable accuracy through the use of the finite element software VecTor2, which

is based on the Modified Compression Field Theory and Disturbed Stress Field Theory. Modeling diagonal bars as smeared reinforcement was found to be adequate for the HPFRC coupling beams. However, shear sliding at the beam-wall interfaces could not be properly captured, which resulted in an underestimation of drift capacity.

6.3 RECOMMENDATIONS FOR FUTURE RESEARCH

In this research study, the use of high-performance fiber-reinforced concrete (HPFRC) in slender coupling beams with aspect ratios on the order of 3.0 was experimentally and analytically investigated. Further experimental work and finite element modeling are recommended in the following areas.

(1) Influence of axial force on behavior of coupling beams, as well as analytical models that can accurately simulate beam expansion and magnitude of axial forces developed during earthquakes.

(2) Possibility of eliminating diagonal reinforcement in precast HPFRC coupling beams with aspect ratios on the order of 2.0. The large drift capacity exhibited by conventionally reinforced HPFRC coupling beams with aspect ratios of 2.75 and 3.3 suggests that a complete elimination of diagonal reinforcement may be possible in coupling beams with lower aspect ratios, which would lead to a much simpler coupling beam design and construction.

(3) Finite element modeling of HPFRC coupling beam-RC wall interfaces in order to accurately capture concentrated rotations and sliding at these critical sections.

APPENDIX A

STRAIN GUAGE LOCATIONS

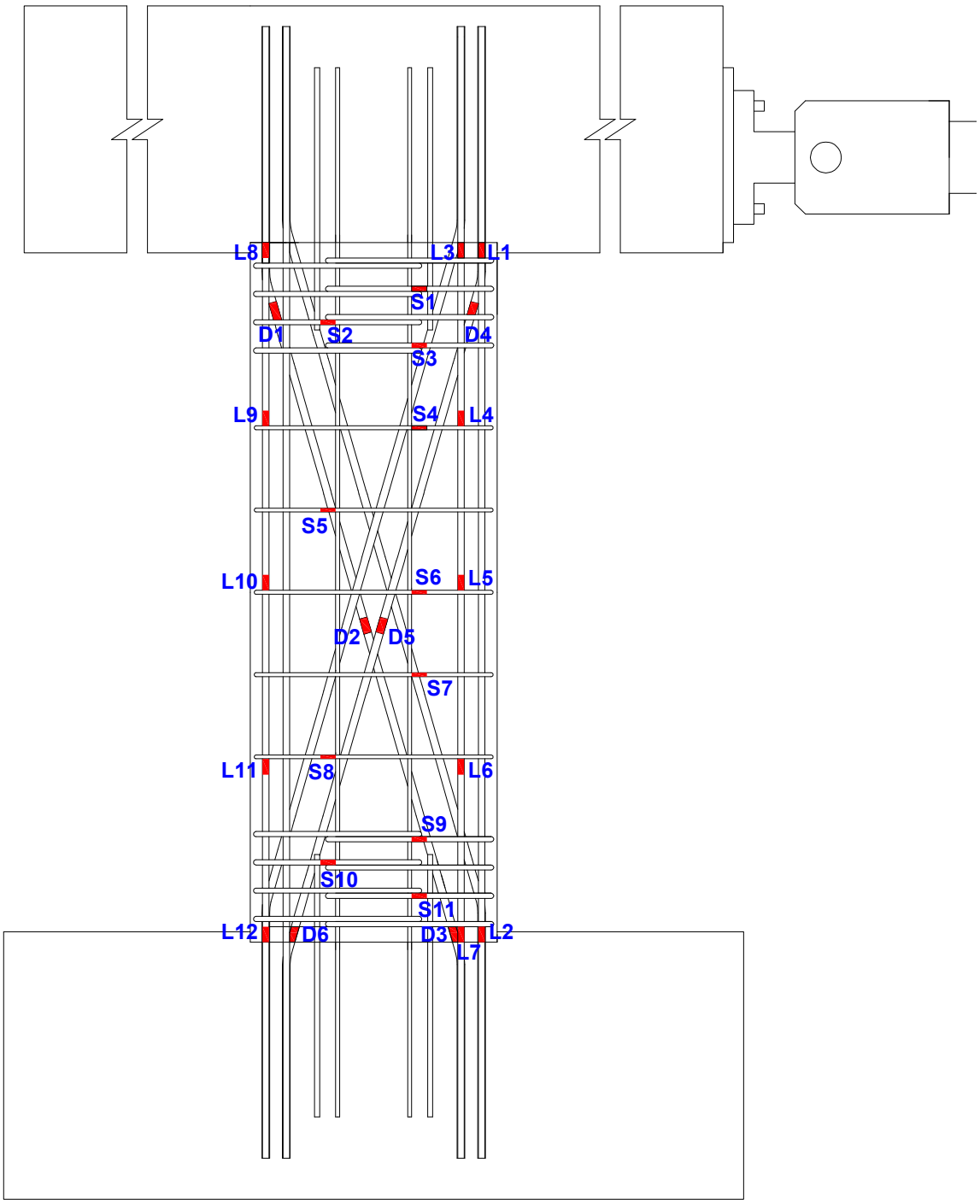

Figure A.1 Specimen CB-1 strain gauge layout

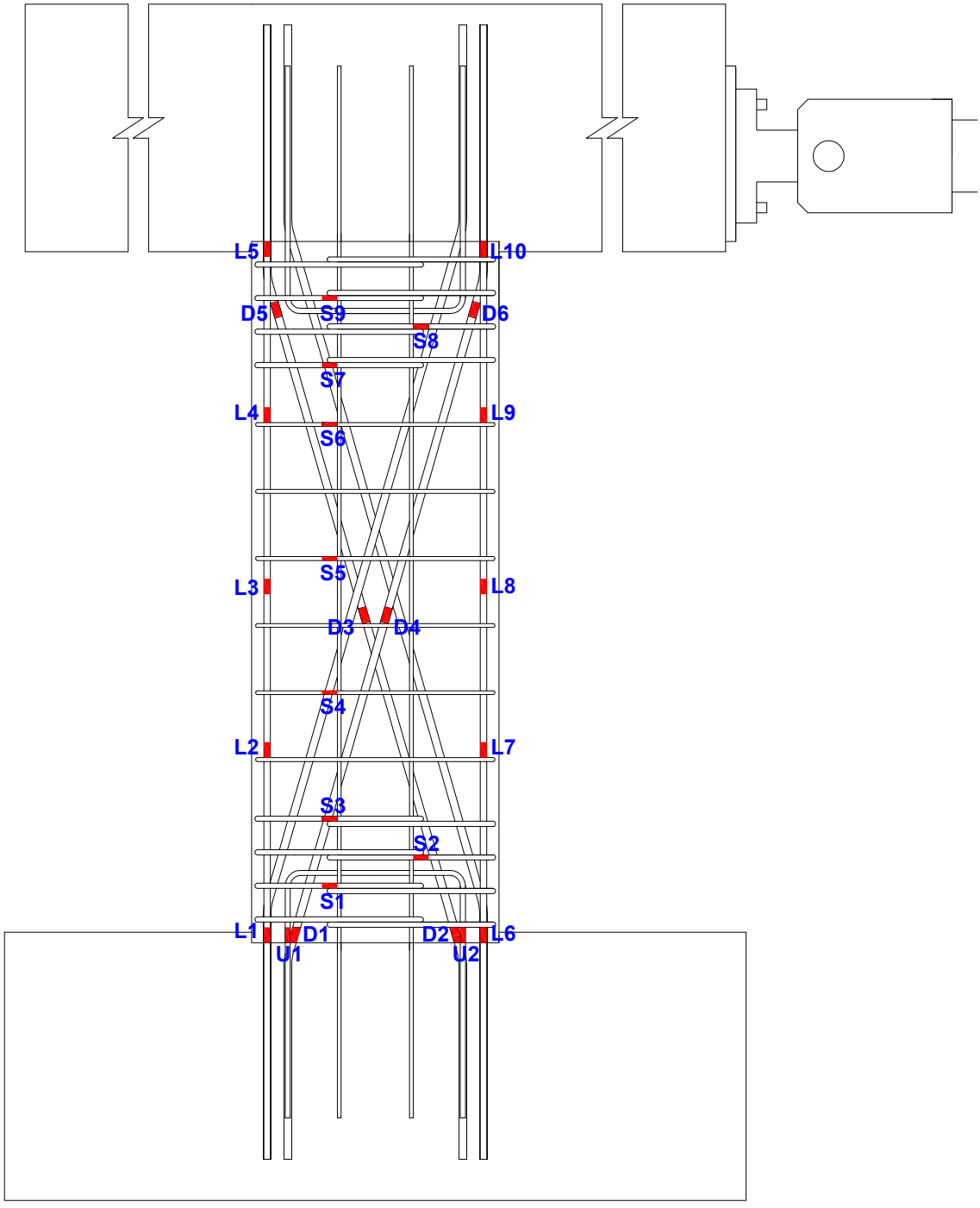

Figure A.2 Specimen CB-2 strain gauge layout

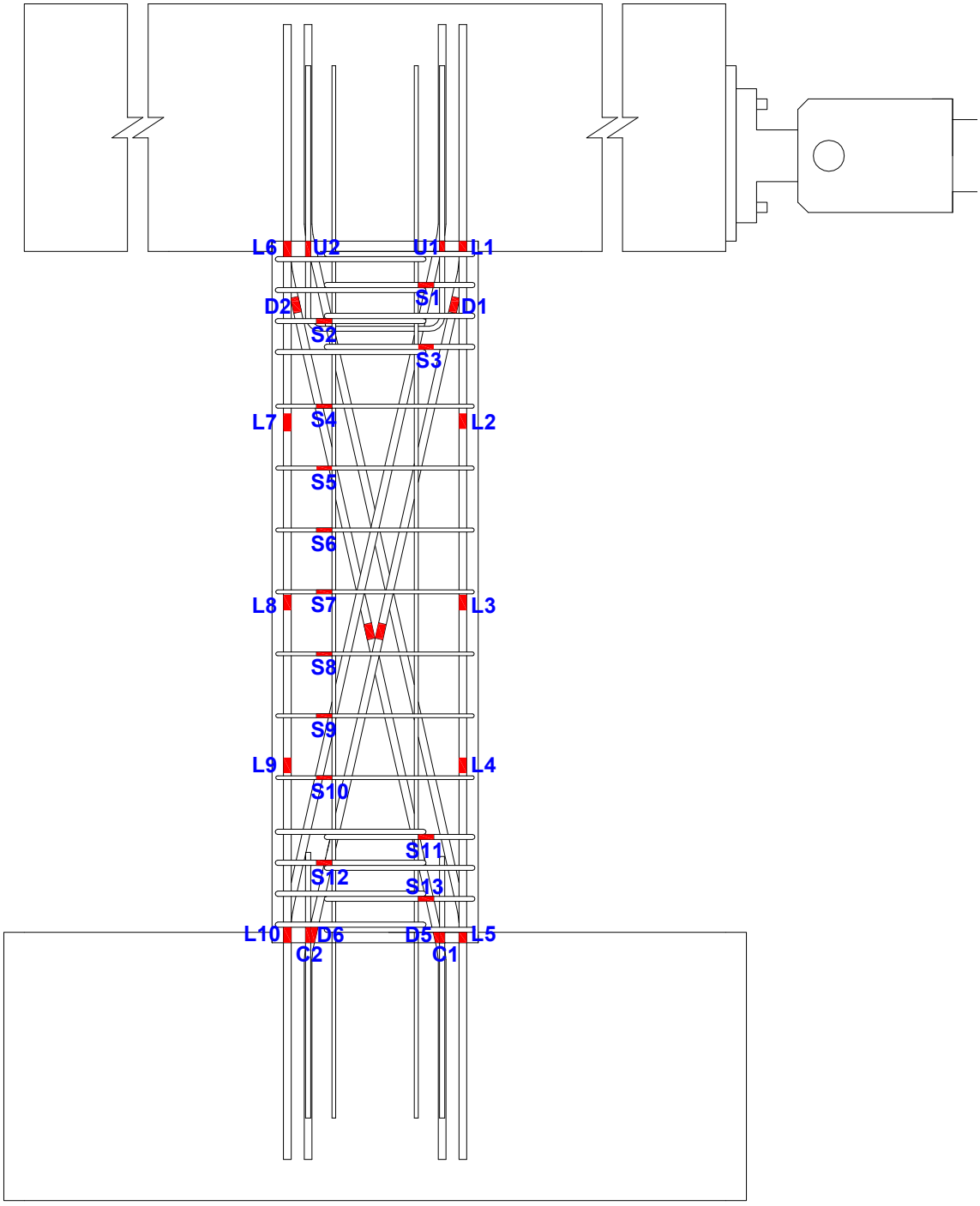

Figure A.3 Specimen CB-3 strain gauge layout

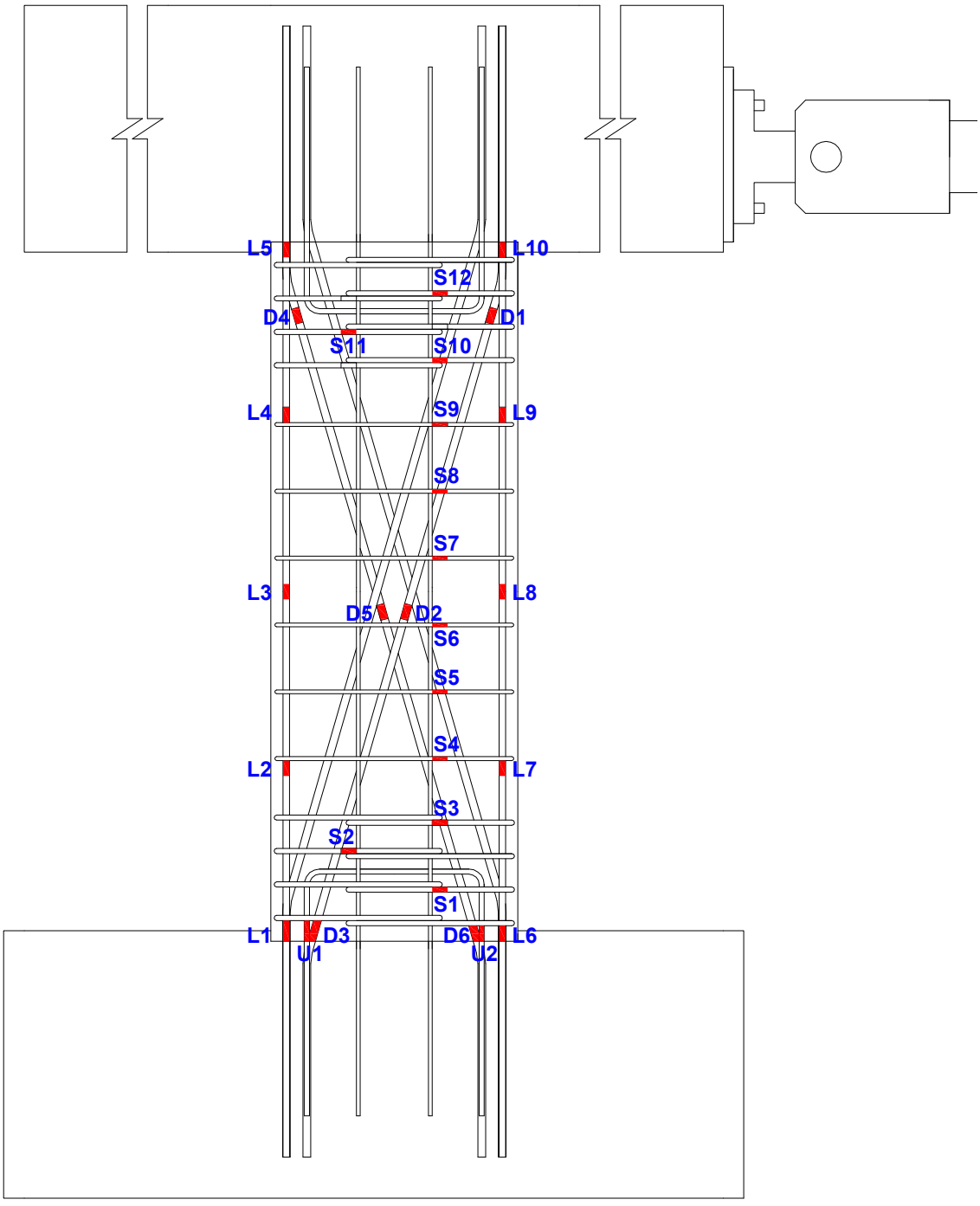

Figure A.4 Specimen CB-4 strain gauge layout

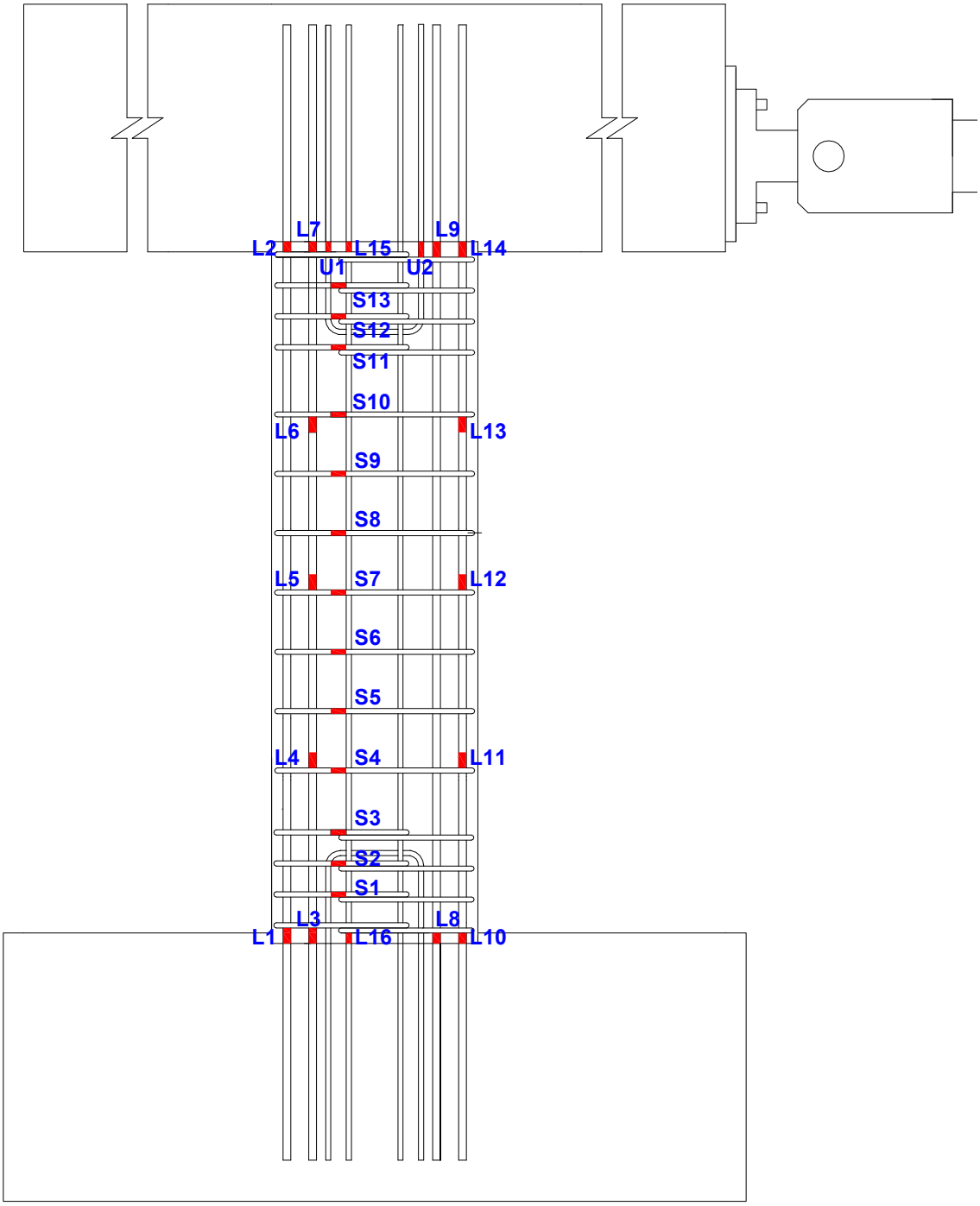

Figure A.5 Specimen CB-5 strain gauge layout

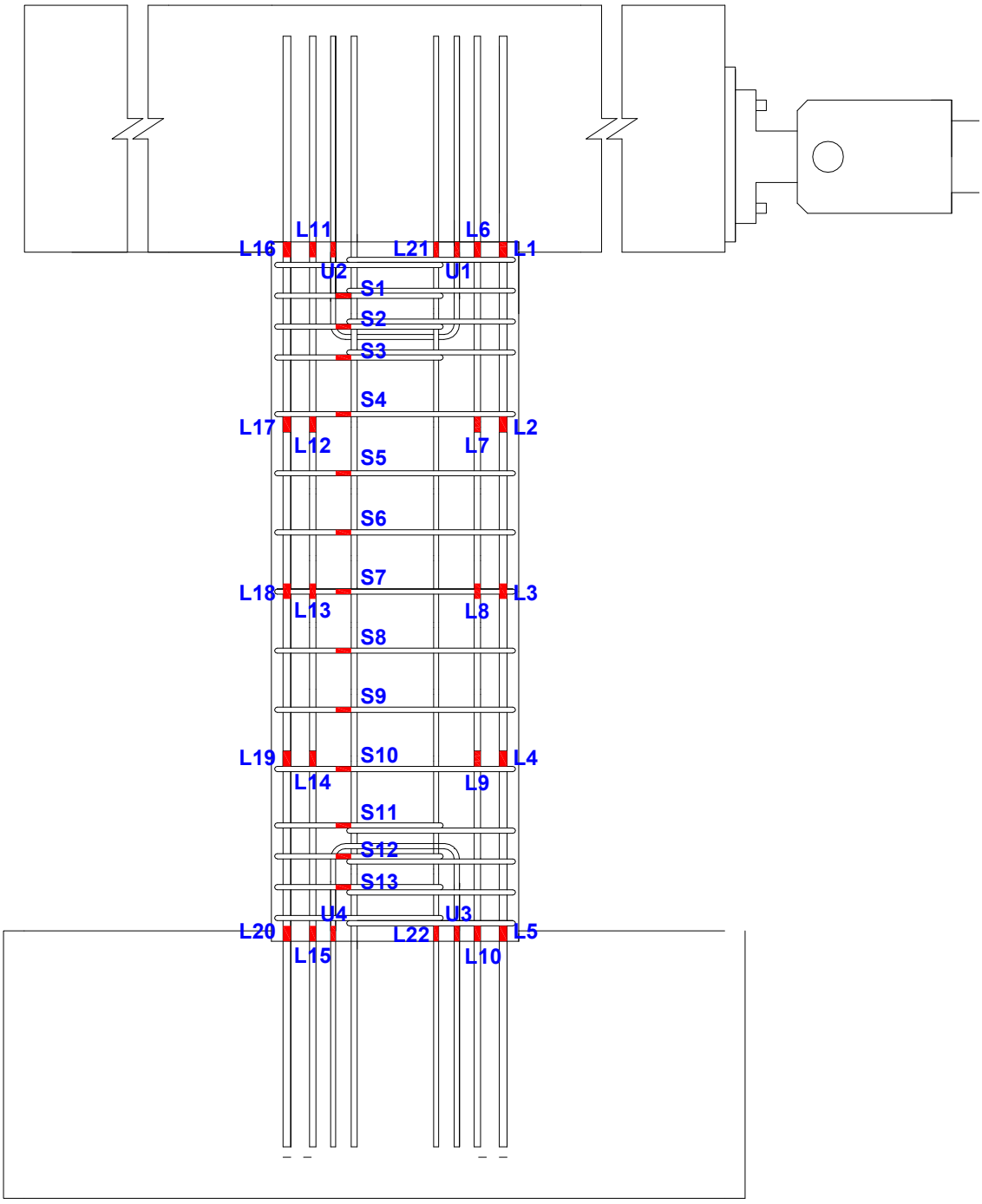

Figure A.6 Specimen CB-6 strain gauge layout

APPENDIX B

LOAD-DISPLACEMENT HISTORY

Table B.1 Load-displacement history for Specimen CB-1

Cycle	Load (kips)	Target Drift (%)	Adjusted Drift (%)
1	20.5 -23.7	0.27 -0.26	0.14 -0.13
2	20.0 -22.7	0.25 -0.27	0.13 -0.14
3	36.5 -40.6	0.51 -0.52	0.30 -0.29
4	35.8 -38.6	0.51 -0.51	0.30 -0.28
5	51.0 -53.9	0.75 -0.75	0.45 -0.42
6	49.7 -51.9	0.76 -0.75	0.46 -0.42
7	66.4 -67.3	1.00 -1.00	0.63 -0.58
8	61.4 -65.3	1.00 -1.01	0.64 -0.56
9	82.2 -80.4	1.27 -1.27	0.82 -0.73
10	79.3 -77.6	1.28 -1.26	0.83 -0.73
11	93.6 -91.1	1.51 -1.51	0.98 -0.88
12	100.1 -88.4	1.69 -1.50	1.13 -0.87
13	98.2 -99.9	1.69 -1.74	1.14 -1.02
14	101.5 -98.6	1.78 -1.77	1.21 -1.04
15	110.1 -107.6	2.05 -2.03	1.41 -1.21
16	105.4 -104.1	2.04 -2.01	1.43 -1.20
17	113.1 -111.8	2.30 -2.27	1.62 -1.37
18	110.4 -109.9	2.30 -2.29	1.65 -1.38
19	116.1 -115.7	2.51 -2.51	1.81 -1.54
20	113.3 -114.5	2.52 -2.55	1.84 -1.58
21	123.8 -124.2	3.02 -3.04	2.26 -1.96

Cycle	Load (kips)	Target Drift (%)	Adjusted Drift (%)
22	120.1 -119.9	3.05 -3.04	2.31 -1.98
23	126.7 -128.6	3.54 -3.54	2.73 -2.40
24	122.3 -124.2	3.55 -3.55	2.77 -2.43
25	127.8 -130.3	4.04 -4.03	3.20 -2.84
26	121.0 -125.2	3.99 -4.04	3.21 -2.87
27	127.4 -130.0	4.55 -4.54	3.72 -3.30
28	127.8 -130.4	5.03 -5.03	4.19 -3.75
29	121.9 -127.9	5.54 -5.56	4.65 -4.23
30	118.4 -122.4	6.06 -6.14	5.19 -4.78
31	107.4 -105.8	6.40 -6.55	5.60 -5.21
32	92.0 -0.2	8.23 5.49	7.49 5.53

Table B.2 Load-displacement history for Specimen CB-2

Cycle	Load (kips)	Target Drift (%)	Adjusted Drift (%)
1	18.1 -21.0	0.25 -0.26	0.13 -0.13
2	18.5 -19.5	0.26 -0.25	0.13 -0.13
3	29.9 -35.4	0.52 -0.51	0.27 -0.29
4	28.3 -33.4	0.51 -0.50	0.30 -0.28
5	44.4 -50.4	0.78 -0.78	0.44 -0.47
6	47.0 -45.2	0.79 -0.79	0.43 -0.49
7	61.8 -61.0	1.02 -1.03	0.61 -0.67
8	60.7 -57.3	1.04 -1.04	0.63 -0.67
9	83.9 -83.9	1.55 -1.54	1.03 -1.02
10	80.2 -79.4	1.54 -1.53	1.03 -1.01
11	94.5 -97.7	2.04 -2.12	1.45 -1.47
12	90.4 -92.6	2.02 -2.04	1.47 -1.40
13	102.0 -105.2	2.53 -2.53	1.92 -1.80
14	108.6 -112.6	3.04 -3.03	2.38 -2.22
15	111.5 -112.4	3.54 -3.54	2.83 -2.60
16	114.3 -111.4	4.01 -4.03	3.29 -3.00
17	111.5 -115.6	4.50 -4.68	3.74 -3.57
18	109.0 -110.4	5.02 -5.05	4.28 -3.89
19	107.1 -82.6	6.03 -4.34	5.33 -4.84

Table B.3 Load-displacement history for Specimen CB-3

Cycle	Load (kips)	Target Drift (%)	Adjusted Drift (%)
1	-13.5 9.6	-0.22 0.24	-0.08 0.06
2	-13.6 10.3	-0.22 0.24	-0.1 0.06
3	-25.2 22.3	-0.43 0.44	-0.21 0.18
4	-24.6 21.7	-0.45 0.46	-0.21 0.19
5	-33.9 30.5	-0.61 0.56	-0.30 0.26
6	-38.6 39.0	-0.72 0.71	-0.37 0.37
7	-52.7 55.2	-1.01 1.01	-0.58 0.60
8	-53.0 53.5	-1.02 1.01	-0.59 0.60
9	-76.4 79.7	-1.50 1.53	-0.92 1.04
10	-74.2 75.2	-1.52 1.51	-0.96 1.02
11	-93.4 93.4	-2.03 2.03	-1.32 1.49
12	-90.0 89.7	-2.03 2.03	-1.30 1.49
13	-102.4 99.7	-2.53 2.52	-1.70 1.94
14	-107.1 103.9	-3.01 2.98	-2.09 2.42
15	-113.4 108.8	-3.63 3.55	-2.58 2.99
16	-112.2 108.0	-4.06 4.08	-2.88 3.45
17	-115.1 106.8	-4.57 4.59	-3.31 3.95
18	-102.6 106.6	-5.07 5.12	-3.59 4.46
19	-109.0 106.3	-6.08 6.09	-4.48 5.46
20	-104.5	-6.79	-5.67

Table B.4 Load-displacement history for Specimen CB-4

Cycle	Load (kips)	Target Drift (%)	Adjusted Drift (%)
1	19.3 -18.0	0.29 -0.28	0.10 -0.11
2	18.8 -18.5	0.28 -0.30	0.10 -0.12
3	32.1 -33.8	0.52 -0.55	0.20 -0.26
4	30.7 -32.0	0.53 -0.54	0.21 -0.26
5	46.0 -45.7	0.77 -0.80	0.34 -0.41
6	44.2 -44.0	0.77 -0.80	0.34 -0.41
7	62.3 -64.9	1.03 -1.20	0.52 -0.67
8	61.1 -53.4	1.03 -1.04	0.52 -0.57
9	83.8 -75.9	1.53 -1.53	0.89 -0.90
10	80.7 -74.8	1.54 -1.55	0.88 -0.92
11	93.3 -88.5	2.03 -2.03	1.29 -1.30
12	89.4 -86.5	2.02 -2.05	1.26 -1.31
13	98.2 -97.5	2.51 -2.55	1.68 -1.73
14	102.1 -102.7	3.03 -3.02	2.13 -2.15
15	102.8 -101.7	3.53 -3.54	2.57 -2.63
16	95.8 -70.7	3.87 -3.98	3.05 -3.09
17	59.1 1.1	4.53 2.85	3.75 2.51

Table B.5 Load-displacement history for Specimen CB-5

Cycle	Load (kips)	Target Drift (%)	Adjusted Drift (%)
1	14.2 -18.9	0.26 -0.27	0.10 -0.14
2	13.9 -18.2	0.26 -0.26	0.10 -0.13
3	27.2 -33.3	0.47 -0.48	0.22 -0.30
4	25.4 -31.6	0.48 -0.48	0.22 -0.29
5	37.5 -45.5	0.68 -0.74	0.35 -0.46
6	37.3 -43.8	0.70 -0.74	0.37 -0.46
7	42.8 -55.7	0.82 -0.97	0.45 -0.61
8	45.4 -55.0	0.88 -0.99	0.49 -0.63
9	50.1 -68.2	1.00 -1.28	0.57 -0.83
10	51.3 -71.3	1.05 -1.37	0.60 -0.90
11	91.1 -95.5	1.97 -2.07	1.35 -1.43
12	88.6 -87.7	2.00 -2.00	1.38 -1.40
13	98.9 -100.0	2.49 -2.52	1.81 -1.83
14	103.8 -105.0	3.01 -3.04	2.29 -2.28
15	106.4 -108.6	3.49 -3.59	2.74 -2.77
16	109.1 -110.1	4.00 -4.03	3.23 -3.16
17	111.5 -111.8	4.53 -4.48	3.74 -3.57
18	105.2 -115.8	5.09 -5.13	4.13 -4.15
19	110.7 -113.0	6.00 -6.04	5.02 -4.86
20	111.0 -111.1	6.99 -7.00	6.00 -5.63
21	94.7 -101.1	8.01 -8.09	6.89 -6.70
22	75.1 -73.0	8.87 -9.13	7.89 -7.84

Table B.6 Load-displacement history for Specimen CB-6

Cycle	Load (kips)	Target Drift (%)	Adjusted Drift (%)
1	12.5 -21.0	0.24 -0.28	0.08 -0.12
2	15.8 -20.7	0.28 -0.29	0.09 -0.12
3	29.2 -36.6	0.52 -0.53	0.20 -0.26
4	30.6 -34.6	0.54 -0.53	0.22 -0.26
5	42.5 -50.0	0.76 -0.79	0.36 -0.42
6	40.9 -46.5	0.76 -0.78	0.37 -0.42
7	57.5 -62.7	1.03 -1.04	0.57 -0.58
8	55.6 -59.9	1.03 -1.04	0.57 -0.59
9	84.5 -88.1	1.51 -1.52	0.92 -0.92
10	80.7 -86.7	1.54 -1.55	0.96 -0.96
11	100.6 -103.1	2.03 -2.03	1.34 -1.30
12	96.0 -98.9	2.04 -2.05	1.37 -1.31
13	110.1 -111.2	2.56 -2.53	1.85 -1.67
14	117.6 -115.7	3.11 -3.03	2.35 -2.08
15	120.3 -119.6	3.54 -3.56	2.76 -2.53
16	123.1 -120.9	4.02 -4.06	3.22 -2.97
17	125.7 -120.9	4.52 -4.55	3.74 -3.40
18	126.3 -118.7	5.08 -4.99	4.31 -3.79
19	125.3 -115.6	6.02 -6.12	5.23 -4.70
20	110.2 -106.8	7.14 -7.03	6.46 -5.71
21	89.3 -85.6	8.04 -8.02	7.51 -6.70

APPENDIX C

LONGITUDINAL STRAIN DISTRIBUTION

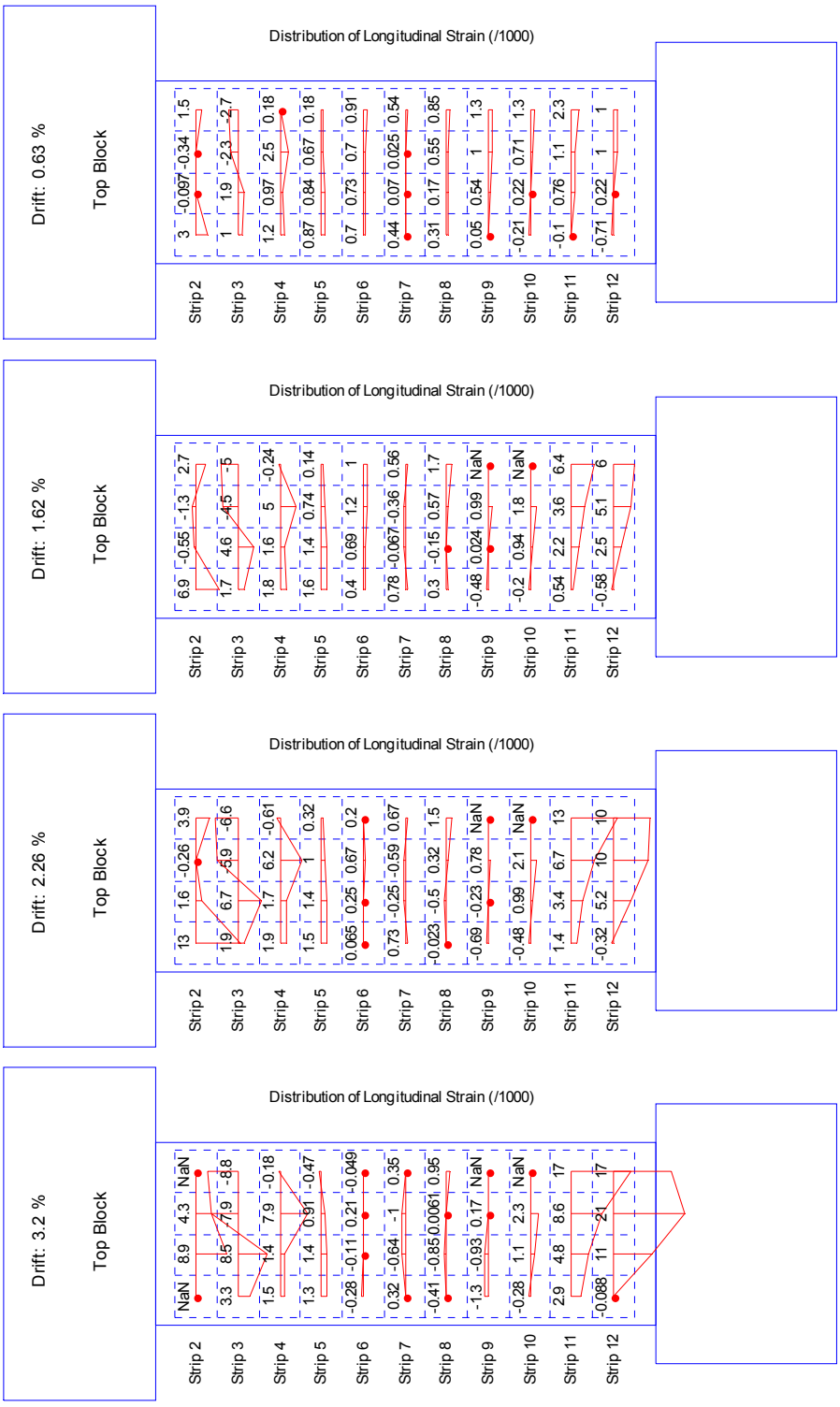

Figure C.1 Longitudinal strains at various drifts in negative loading direction for Specimen CB-1

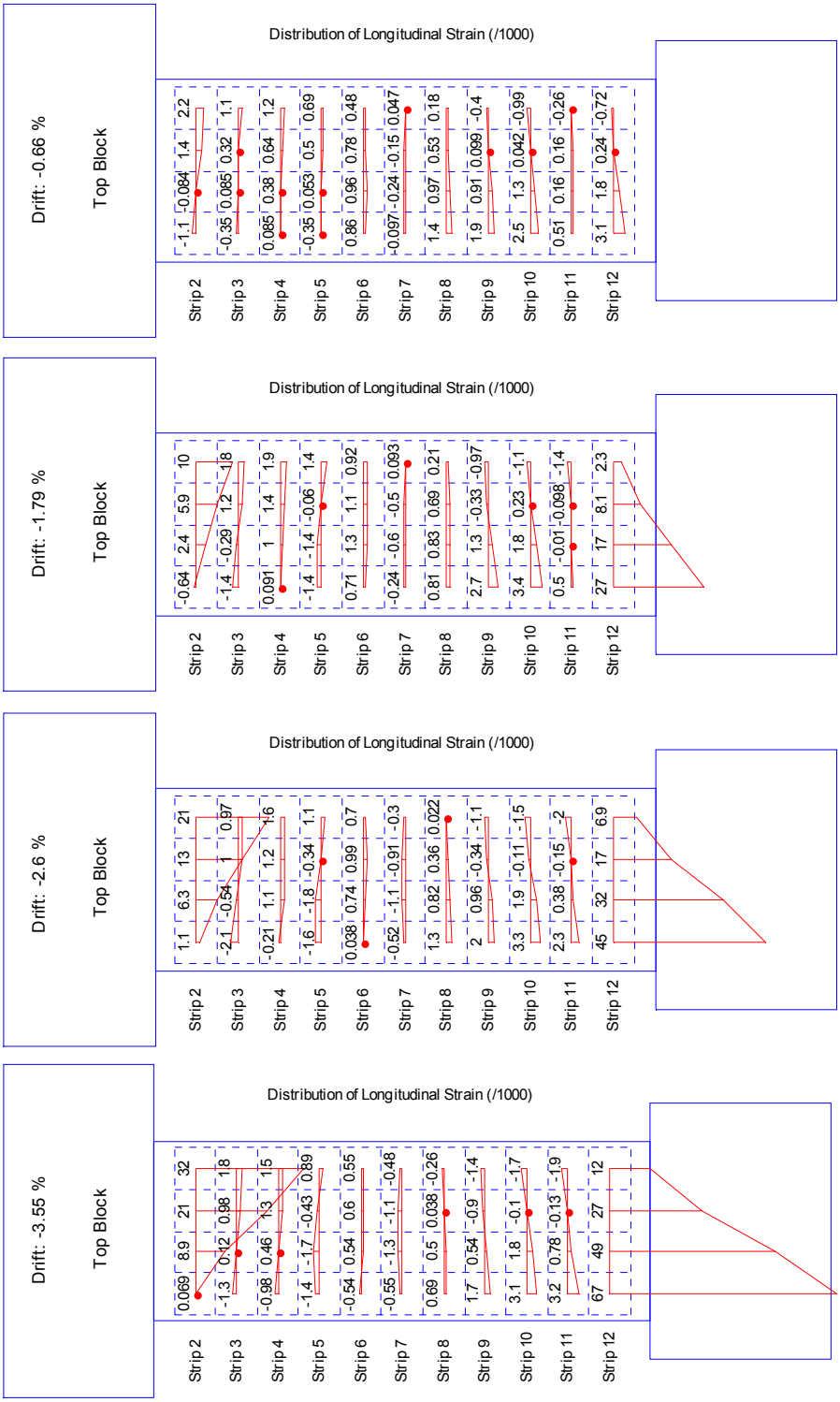

Figure C.2 Longitudinal strains at various drifts in negative loading direction for Specimen CB-2

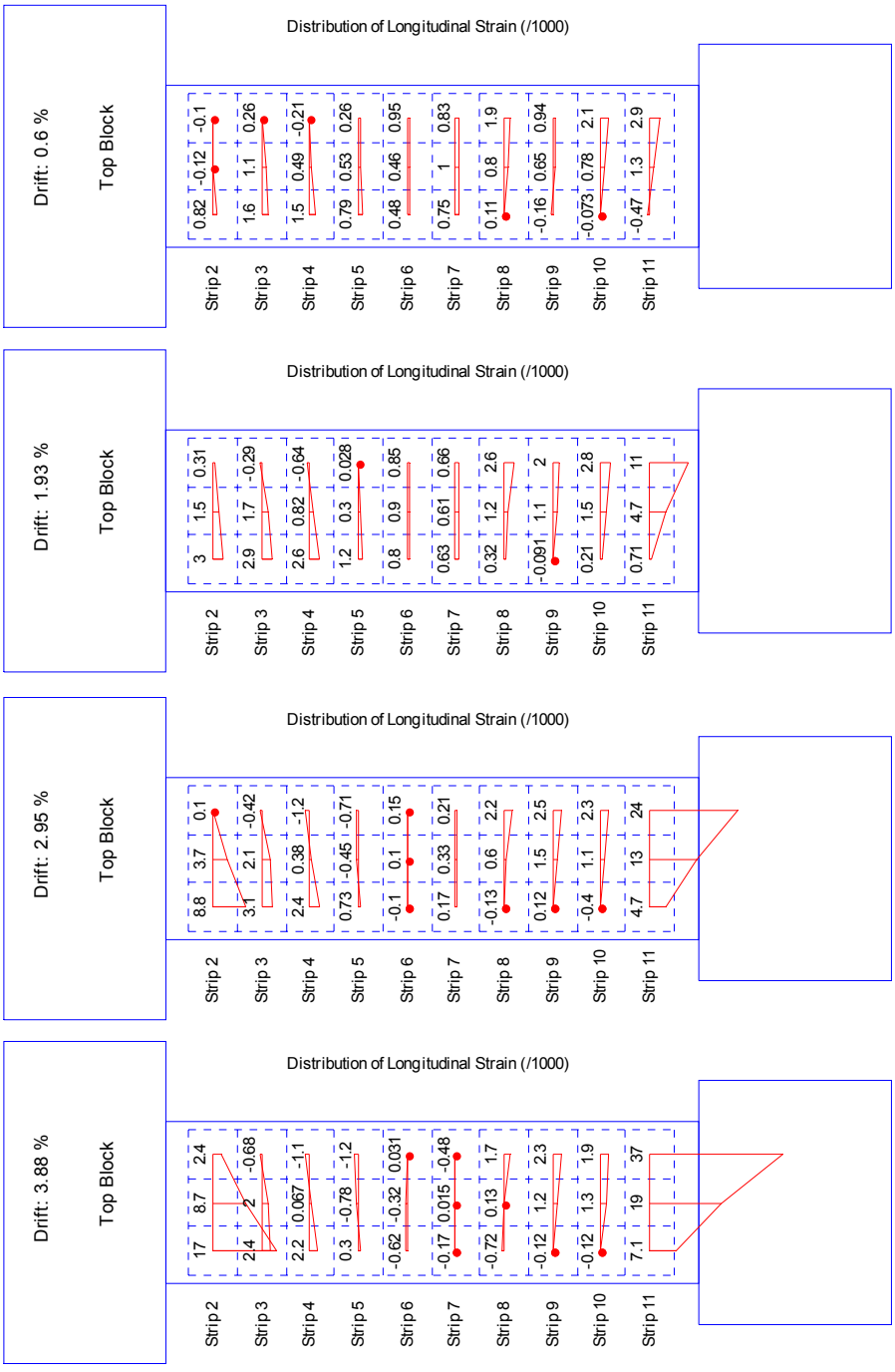

Figure C.3 Longitudinal strains at various drifts in negative loading direction for Specimen CB-3

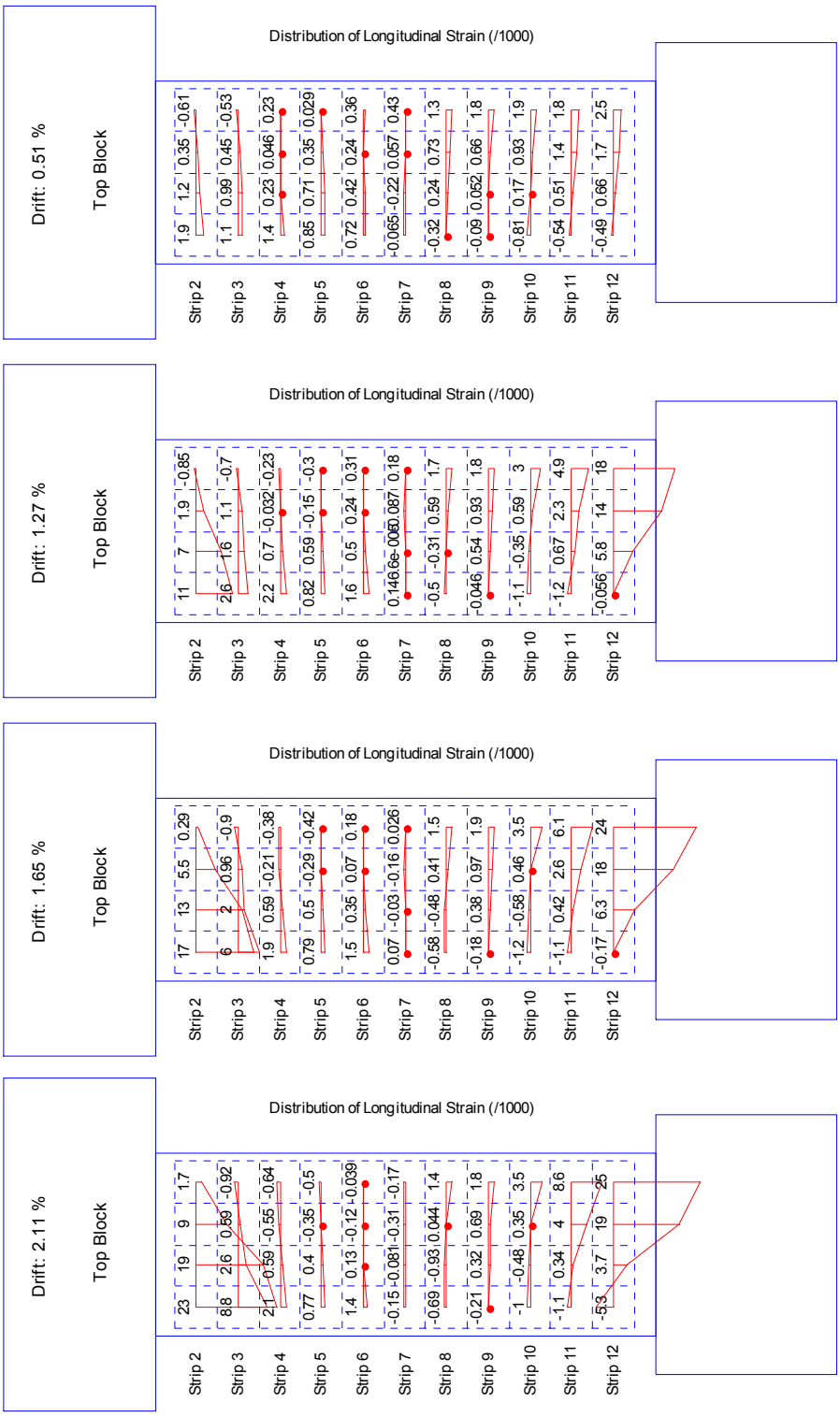

Figure C.4 Longitudinal strains at various drifts in the negative direction of Specimen CB-4

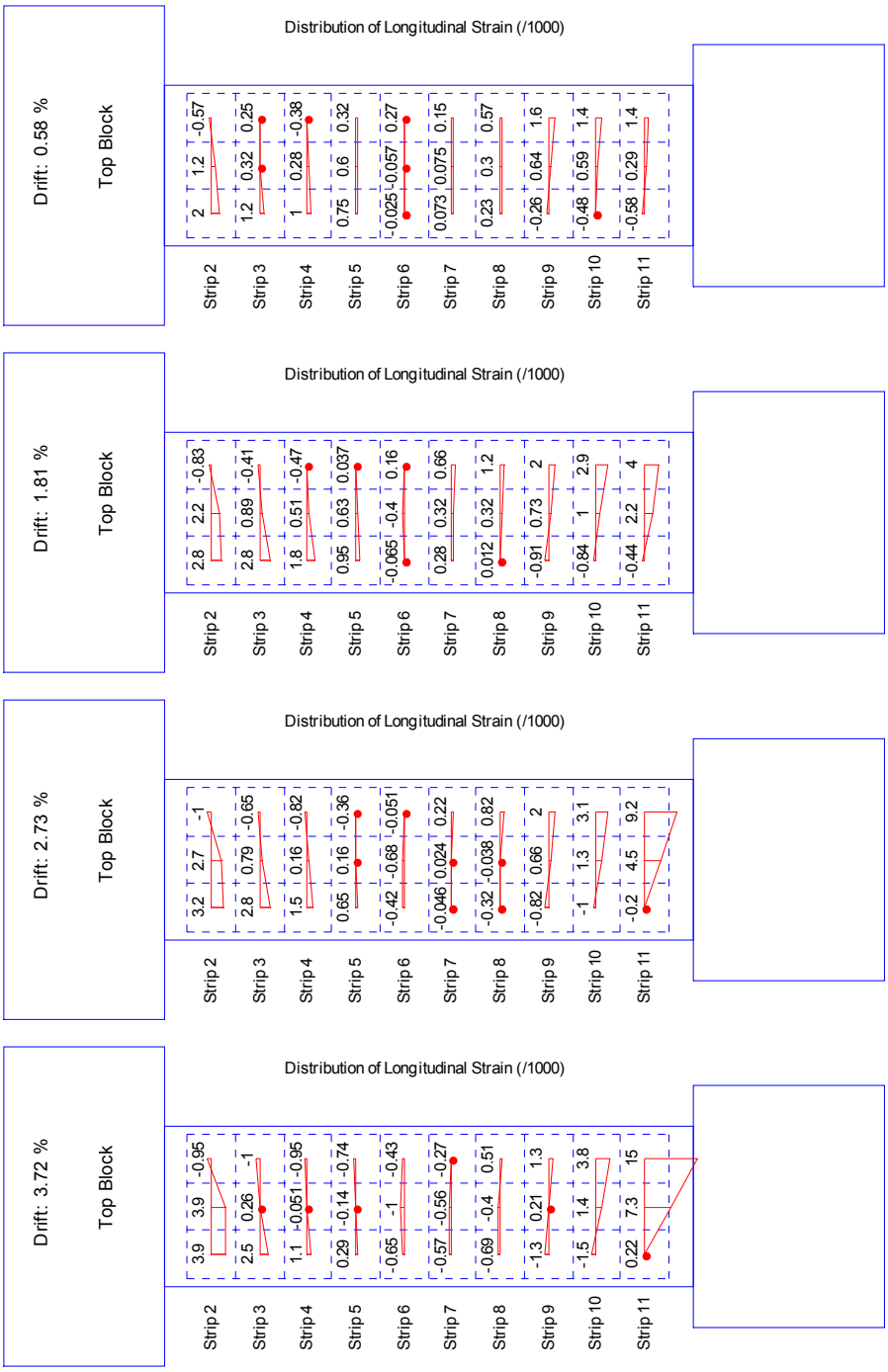

Figure C.5 Longitudinal strains at various drifts in negative loading direction for Specimen CB-5

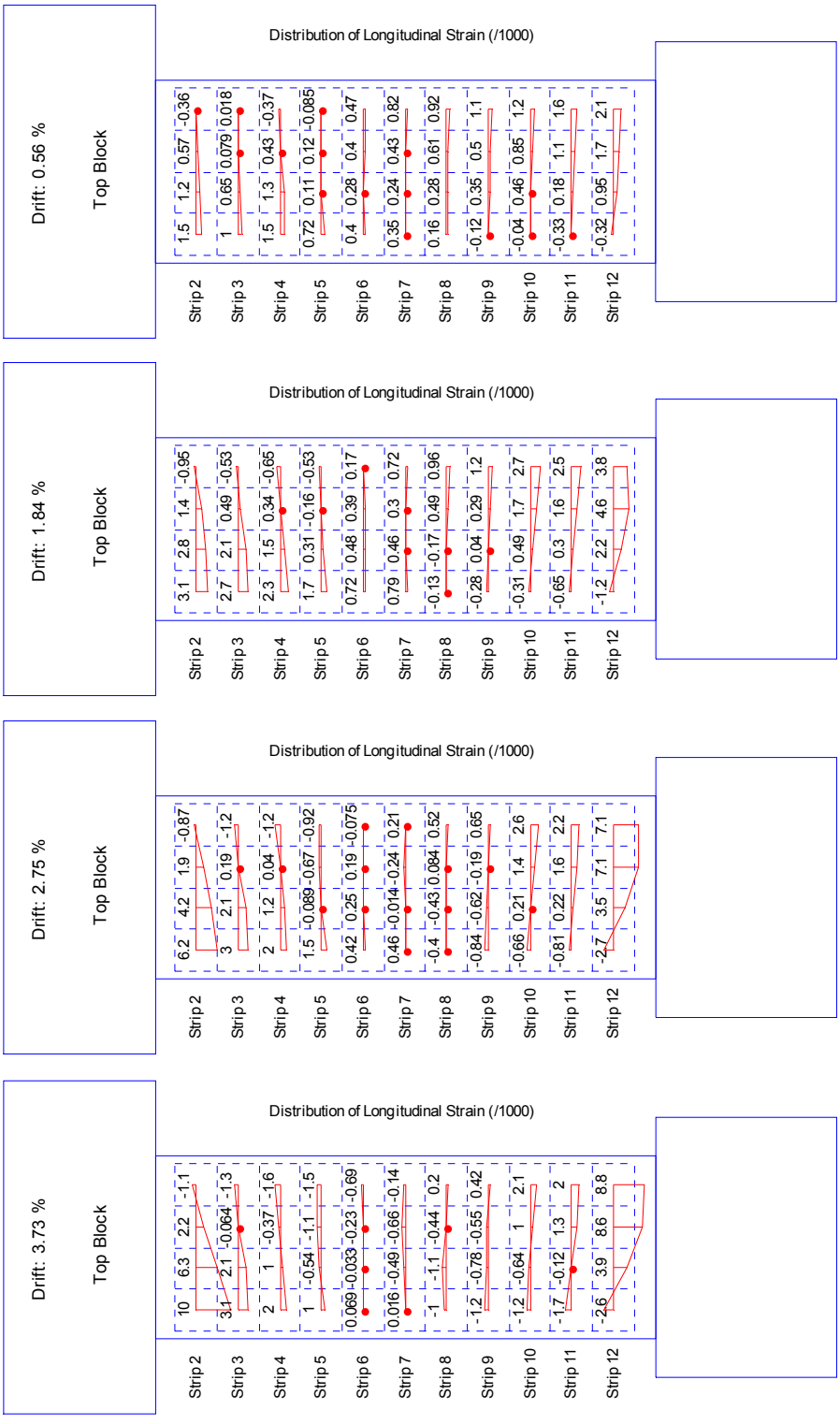

Figure C.6 Longitudinal strains at various drifts in negative loading direction for Specimen CB-6

APPENDIX D
IDEALIZED DISPLACEMENT PATTERNS IMPOSED ON THE VECTOR2 MODELS

Table D.1 Lateral displacement pattern for the model of Specimen CB-1

Cycle	Drift (%)	Applied Displacement (mm)
1	0.12	2
	-0.12	-2
2	0.12	2
	-0.12	-2
3	0.24	4
	-0.24	-4
4	0.24	4
	-0.24	-4
5	0.48	8
	-0.48	-8
6	0.48	8
	-0.48	-8
7	0.60	10
	-0.60	-10
8	0.60	10
	-0.60	-10
9	0.72	12
	-0.72	-12
10	0.72	12
	-0.72	-12
11	0.95	16
	-0.95	-16
12	0.95	16
	-0.95	-16
13	0.95	16
	-0.95	-16
14	0.95	16
	-0.95	-16
15	1.43	24
	-1.43	-24
16	1.43	24
	-1.43	-24
17	1.43	24
	-1.43	-24
18	1.43	24
	-1.43	-24

Cycle	Drift (%)	Applied Displacement (mm)
19	1.67	28
	-1.67	-28
20	1.67	28
	-1.67	-28
21	2.09	35
	-2.09	-35
22	2.09	35
	-2.09	-35
23	2.62	44
	-2.62	-44
24	2.62	44
	-2.62	-44
25	3.34	56
	-3.34	-56
26	3.34	56
	-3.34	-56
27	3.70	62
	-3.70	-62
28	3.94	66
	-3.94	-66
29	4.41	74
	-4.41	-74
30	4.77	80
	-4.77	-80

Table D.2 Lateral displacement pattern for the model of Specimen CB-2

Cycle	Drift (%)	Applied Displacement (mm)
1	0.12	2
	-0.12	-2
2	0.12	2
	-0.12	-2
3	0.24	4
	-0.24	-4
4	0.24	4
	-0.24	-4
5	0.48	8
	-0.48	-8
6	0.48	8
	-0.48	-8
7	0.60	10
	-0.60	-10
8	0.60	10
	-0.60	-10
9	1.07	18
	-1.07	-18
10	1.07	18
	-1.07	-18
11	1.43	24
	-1.43	-24
12	1.43	24
	-1.43	-24
13	1.91	32
	-1.91	-32
14	2.39	40
	-2.39	-40
15	2.86	48
	-2.86	-48
16	3.34	56
	-3.34	-56
17	3.82	64
	-3.82	-64
18	4.29	72
	-4.29	-72
19	4.77	80
	-4.77	-80

Table D.3 Lateral displacement pattern for the model of Specimen CB-3

Cycle	Drift (%)	Applied Displacement (mm)
1	0.12	2
	-0.12	-2
2	0.12	2
	-0.12	-2
3	0.24	4
	-0.24	-4
4	0.24	4
	-0.24	-4
5	0.36	6
	-0.36	-6
6	0.36	6
	-0.36	-6
7	0.60	10
	-0.60	-10
8	0.60	10
	-0.60	-10
9	0.95	16
	-0.95	-16
10	0.95	16
	-0.95	-16
11	1.43	24
	-1.43	-24
12	1.43	24
	-1.43	-24
13	1.91	32
	-1.91	-32
14	2.39	40
	-2.39	-40
15	2.86	48
	-2.86	-48
16	3.34	56
	-3.34	-56
17	3.82	64
	-3.82	-64
18	4.29	72
	-4.29	-72
19	4.77	80
	-4.77	-80

Table D.4 Lateral displacement pattern for the model of Specimen CB-4

Cycle	Drift (%)	Applied Displacement (mm)
1	0.12	2
	-0.12	-2
2	0.12	2
	-0.12	-2
3	0.24	4
	-0.24	-4
4	0.24	4
	-0.24	-4
5	0.48	8
	-0.48	-8
6	0.48	8
	-0.48	-8
7	0.60	10
	-0.60	-10
8	0.60	10
	-0.60	-10
9	0.95	16
	-0.95	-16
10	0.95	16
	-0.95	-16
11	1.25	21
	-1.25	-21
12	1.25	21
	-1.25	-21
13	1.67	28
	-1.67	-28
14	2.15	36
	-2.15	-36
15	2.62	44
	-2.62	-44
16	3.10	52
	-3.10	-52
17	3.76	63
	-3.70	-62

Table D.5 Lateral displacement pattern for the model of Specimen CB-5

Cycle	Drift (%)	Applied Displacement (mm)
1	0.24	4
	-0.24	-4
2	0.24	4
	-0.24	-4
3	0.48	8
	-0.48	-8
4	0.48	8
	-0.48	-8
5	0.72	12
	-0.72	-12
6	0.72	12
	-0.72	-12
7	0.95	16
	-0.95	-16
8	0.95	16
	-0.95	-16
9	1.43	24
	-1.43	-24
10	1.43	24
	-1.43	-24
11	1.91	32
	-1.91	-32
12	1.91	32
	-1.91	-32
13	2.39	40
	-2.39	-40
14	2.86	48
	-2.86	-48
15	3.34	56
	-3.34	-56
16	3.82	64
	-3.82	-64
17	4.29	72
	-4.29	-72
18	4.77	80
	-4.77	-80

Table D.6 Lateral displacement pattern for the model of Specimen CB-6

Cycle	Drift (%)	Applied Displacement (mm)
1	0.24	4
	-0.24	-4
2	0.24	4
	-0.24	-4
3	0.48	8
	-0.48	-8
4	0.48	8
	-0.48	-8
5	0.72	12
	-0.72	-12
6	0.72	12
	-0.72	-12
7	0.95	16
	-0.95	-16
8	0.95	16
	-0.95	-16
9	1.43	24
	-1.43	-24
10	1.43	24
	-1.43	-24
11	1.91	32
	-1.91	-32
12	1.91	32
	-1.91	-32
13	2.39	40
	-2.39	-40
14	2.86	48
	-2.86	-48
15	3.34	56
	-3.34	-56
16	3.82	64
	-3.82	-64
17	4.29	72
	-4.29	-72
18	4.77	80
	-4.77	-80

REFERENCES

ACI Committee 318, A. C. (2011). *Building Code Requirements for Structural Concrete (ACI318-11)*, American Concrete Institute, Farmington Hills, MI.

ACI Committee 544.1R-96 (2009). *State of the Art Report of Fiber Reinforced Concrete (Reapproved in 2009)*, American Concrete Institute, Farmington Hills, MI.

Adebar, P., Hindi, R., and Gonzalez, E. (2001). "Seismic Behavior of Full-Scale Diagonally Reinforced Slender Coupling Beam."Technical report, University of British Columbia, Vancouver, British Columbia, Canada.

Adebar, P., Mindess, S., Pierre, D. S., and Olund, B. (1997). "Shear Tests of Fiber Concrete Beams without Stirrups." *ACI Structural Journal*, 94(1), 68-76.

Adepegba, D., and Regan, P. E. (1981). "Performance of Steel Fibre Reinforced Concrete in Axially Loaded Short Columns." *International Journal of Cement Composites and Lightweight Concrete*, 3(4), 255-259.

Aktan, A. E., and Bertero, V. V. (1981). "The Seismic Resistant Design of RC Coupled Structural Walls." *EERC*, Earthquake Engineering Research Center, University of California, Berkeley, 166 pp.

Aristizabal-Ochoa, J. D. (1982). "Dynamic Response of Coupled Wall Systems." *Journal of the Structural Division*, 108(ST8), 1846-1857.

Aristizabal-Ochoa, J. D. (1983). "Seismic Analysis of Slender Coupled Walls." *Journal of Structural Engineering*, 109(7), 1538-1552.

Aristizabal-Ochoa, J. D. (1987). "Seismic Behavior of Slender Coupled Wall Systems." *Journal of Structural Engineering*, 113(10), 2221-2234.

Balaguru, P. N., and Shah, S. P. (1992). *Fiber Reinforced Cement Composites*, McGraw Hill, Inc, 530 pp.

Barney, G. B., Shiu, K. N., Rabbat, B. G., Fiorato, A. E., Russell, H. G., and Corley, W. G. (1978). "Earthquake Resistant Structural Walls - Tests of Coupling Beams " Portland Cement Association, Stokie, Illinois, 151 pp.

Batson, G., Jenkins, E., and Spatney, R. (1972). "Steel Fibers as Shear Reinforcement in Beams." *Am Concrete Inst Journal & Proceedings*, 69(10).

Bentur, A., and Mindess, S. (2006). *Fibre Reinforced Cementitious Composites*, Talor & Francis, London, 601 pp.

Binney, J. R. (1972). "Diagonally Reinforced Coupling Beam." Master thesis, University of Canterbury, Christchurch, New Zealand.

Canbolat, A., Parra-Montesinos, G., and Wight, J. K. (2004). "Behavior of Precast High-Performance Fiber Reinforced Cement Composite Coupling Beams under Large Displacement Reversals." *The 13 th World Conference on Earthquake Engineering*Vancouver, BC, Canada, 15 pp.

Canbolat, A., Parra-Montesinos, G. J., and Wight, J. K. (2005). "Experimental Study on Seismic Behavior of High-Performance Fiber-Reinforced Cement Composite Coupling Beams." *ACI Structural Journal*, 102(1), 159-166.

Canbolat, B. A. (2004). "Seismic Behavior of High-Performance Fiber Reinforced Cementitious Composite Coupling Beams." PhD dissertation, The University of Michigan, Ann Arbor, MI, 193 pp.

Chao, S.-H., Naaman, A. E., and Parra-Montesinos, G. J. (2009). "Bond Behavior of Reinforcing Bars in Tensile Strain-Hardening Fiber Reinforced Cement Composites." *ACI Structural Journal*, 106(6), 897-906.

Chompreda, P. (2005). "Deformation Capacity and Shear Strength of Fiber Reinforced Cement Composite Flexural Members Subjected to Displacement Reversals." PhD dissertation, The University of Michigan, Ann Arbor, MI, 186 pp.

Dinh, H., Parra-Montesinos, G., and Wight, J. (2011). "Shear Strength Model for Steel Fiber Reinforced Concrete Beams without Stirrup Reinforcement." *Journal of Structural Engineering*, 137(10), 1039-1051.

Fanella, D. A., and Naaman, A. E. (1985). "Stress-Strain Properties of Fiber Reinforced Mortar in Compression." *ACI Journal Proceeding,* 82(4), 475-483.

Galano, L., and Vignoli, A. (2000). "Seismic Behavior of Short Coupling Beams with Different Reinforcement Layouts." *ACI Structural Journal*, 97(6), 876-885.

Gong, B., Shahrooz, B. M., and Gillum, A. J. (1998). "Cyclic Response of Composite Coupling Beams." *ACI Special Publication*, 174, 89-112.

Harries, K. A., Mitchell, D., Cook, W. D., and Redwood, R. G. (1993). "Seismic Response of Steel Beams Coupling Concrete Walls." *Journal of Structural Engineering*, 119(12), 3611-3629.

Hofbeck, J., Ibrahim, I., and Mattock, A. H. (1969). "Shear Transfer in Reinforced Concrete." *ACI Journal Proceeding*, 66(2), 119-128.

Hota, S., and Naaman, A. E. (1997). "Bond Stress-Slip Response of Reinforcing Bars Embedded in FRC Matrices under Monotonic and Cyclic Loading." *ACI Structural Journal*, 94(5), 525-537.

Imam, M., Vandewalle, L., and Mortelmans, F. (1995). "Shear-Moment Analysis of Reinforced High Strength Concrete Beams Containing Steel Fibres." *Canadian Journal of Civil Engineering*, 22(3), 462-470.

Khuntia, M., Stojadinovic, B., and Goel, S. C. (1999). "Shear Strength of Normal and High-Strength Fiber Reinforced Concrete Beams without Stirrups." *ACI Structural Journal*, 96(2), 282-290.

Kim, K., and Parra-Montesinos, G. J. (2003). "Behavior of HPFRCC Low-Rise Walls Subjected to Displacemnet Reversals." *High Performance Fiber Reinforced Cement Composite 4 (HPFRCC 4), Proceeding of the Fourth International RILEM Workshop*, RILEM, Ann Arbor, MI, 505-515.

Kupfer, H., Hilsdorf, H. K., and Rusch, H. (1969). "Behavior of Concrete under Biaxial Stresses." *ACI Journal Proceedings*, 66(8), 656-666.

Kwak, Y. K., Eberhard, M. O., Kim, W. S., and Kim, J. (2002). "Shear Strength of Steel Fiber-Reinforced Concrete Beams without Stirrups." *ACI Structural Journal*, 99(4), 530-538.

Kwan, A. K. H., and Xhao, Z. Z. (2002). "Testing of Coupling Beams with Equal End Rotations Maintained and Local Joint Deformaton Allowed." *Structures & Buildings* 152(1), 67-78.

Lequesne, R. (2011). "Behavior and Design of High-Performance Fiber Reinforced-Concrete Coupling Beams and Coupled-Wall Systems." PhD dissertation, The University of Michigan, Ann Arbor, MI, 277 pp.

Lequesne, R., Parra-Montesinos, G. J., and Wight, J. K. (2009). "Test of a Coupled Wall with High-Performance Fiber-Reinforced Concrete Coupling Beams." *ACI Special Publication* (SP265-01), 1-18.

Lequesne, R., Setkit, M., Parra-Montesinos, G., and Wight, J. K. (2010). "Seismic Detailing and Behavior of Coupling Beams With High-Performance Fiber Reinforced Concrete." *ACI Special Publication* (SP272-11), 189-204.

Liao, W.-C., Chao, S. H., Park, S. Y., and Naaman, A. E. (2006). "Self-Consolidating High Performance Fiber Reinforced Concrete - Preliminary Investigation." Civil Engineering Report, The University of Michigan, Ann Arbor, MI, 68 pp.

Lim, D., and Oh, B. (1999). "Experimental and Theoretical Investigation on the Shear of Steel Fibre Reinforced Concrete Beams." *Engineering Structures*, 21(10), 937-944.

Lim, T. Y., and Paramasivam, P. (1987). "Behavior of Reinforced Steel-Fiber-Concrete Beams in Flexure." *Journal of Structural Engineering*, 113(12), 2439-2458.

Luison, C. J., Somenson, H. M., and Ungaro, M. A. (1970). "Experimental Verification of the Elastic and Plastic Calculus of a Shear Wall." *14th Jornadas Sudamericanas de Ingenieria Estructural*, 5, 230-286.

Mangat, P., and Motamedi Azari, M. (1985). "Influence of Steel Fibre and Stirrup Reinforcement on the Properties of Concrete in Compression Members." *International Journal of Cement Composites and Lightweight Concrete*, 7(3), 183-192.

Mansur, M. A., Ong, K. C. G., and Paramasivam, P. (1986). "Shear Strength of Fibrous Concrete Beams without Stirrups." *Journal of Structural Engineering*, 112(9), 2066-2079.

Minelli, F. (2005). "Plain and Fiber Reinforced Concrete Beams under Shear Loading: Structural Behavior and Design Aspects." PhD dissertation, University of Brescia, Italy.

Naaman, A. E. (1996). "Strain hardening and deflection hardening fiber reinforced cement composites." *High Performance Fiber Reinforced Cement Composite 4 (HPFRCC 4), Proceeding of the Fourth International RILEM Workshop*, 95-113.

Naaman, A. E. (2008). "High-Performance Fiber Reinforced Cement Composites." *High-performance construction materials: Science and applications*, C. Shi, and Y. L. Mo, eds., World Scientific, Singapore, 91-153.

Naaman, A. E. (1998). "New Fiber Technology." *Concrete International*, 20(7), 57-62.

Naaman, A. E., and Reinhardt, H. W. (1996). "Characterization of High Performance Fiber Reinforced Cement Composites - HPFRCC." *High Performance Fiber Reinforced Cement Composite 2 (HPFRCC 2), Proceeding of the Second International RILEM Workshop,* 1-24.

Naish, D., Wallace, J. W., Fry, A., and Klemencic, R. (2009). "Reinforced Concrete Link Beams: Alternative Details for Improved Construction." Department of Civil and Environmental Engineering, University of California, Los Angeles, 116 pp.

Narayanan, R., and Darwish, I. Y. S. (1987). "Use of Steel Fibers as Shear Reinforcement." *ACI Structural Journal*, 84(3), 216-227.

Paparoni, M. (1972). "Model Studies of Coupling Beams." *Proceeding of the International Conference on Tall Concrete and Masonry Buildings*, 671-681.

Park, R., and Paulay, T. (1975). *Reinforced Concrete Structures*, Wiley, New York, 769 pp.

Park, R., Priestley, M. J. N., and Gill, W. D. (1982). "Ductility of Square-Confined Concrete Columns." *Journal of the Structural Division*, 108(4), 929-950.

Parra-Montesinos, G. J. (2000). "Seismic Behavior, Strength and Retrofit of Exterior RC Column-to-Steel Beam Connections." PhD dissertation, The University of Michigan, Ann Arbor, MI., 296 pp.

Parra-Montesinos, G. J. (2005). "High-Performance Fiber-Reinforced Cement Composites: An Alternative for Seismic Design of Structures." *ACI Structural Journal*, 102(5), 668-675.

Parra-Montesinos, G. J., Peterfreund, S. W., and Chao, S. H. (2005). "Highly Damage-Tolerant Beam-Column Joints through Use of High-Performance Fiber-Reinforced Cement Composites." *ACI Structural Journal*, 102(3), 487-495.

Parra-Montesinos, G. J., Canbolat, B. A., and Jeyaraman, G. (2006) "Relaxation of Confinement Reinforcement Requirements in Structural Walls Through the Use of Fiber Reinforced Cement Composites." *8th U.S. National Conference on Earthquake Engineering*, San Francisco.

Parra-Montesinos, G. J. (2006). "Shear Strength of Beams with Deformed Steel Fibers." *Concrete International*, 28(11), 57-66.

Parra-Montesinos, G. J., and Wight, J. K. (2000). "Seismic Response of Exterior RC Column-to-Steel Beam Connections." *Journal of Structural Engineering*, 126(10), 1113-1121

Paulay, T. (1969). "The Coupling of Reinforced Concrete Shear Walls." *The 4th World Conference on Earthquake Engineering,* Chile, 75-90.

Paulay, T. (1971). "Coupling Beams of Reinforced Concrete Shear Walls." *Journal of the Structural Division*, 97(3), 843-862.

Paulay, T., and Binney, J. R. (1974). "Diagonally Reinforced Coupling Beams of Shear Walls." *ACI Special Publication*, 42, 579-598.

Paulay, T., and Santhakumar, A. R. (1976). "Ductile Behavior of Coupled Shear Walls." *Journal of the Structural Division*, 102(1), 93-108.

Ramakrishnan, V., Brandshaug, T., Coyle, W., and Schrader, E. K. (1980). "A comparative Evaluation of Concrete Reinforced with Straight Steel Fibers and Fibers with Deformed Ends Glued Together into Bundles." *ACI Journal Proceeding*, 77(3), 135-143.

Richart, F. E., Brantzaeng, A., and Brown, R. L. (1928). "A Study of the Failure of Concrete under Combined Compressive Stresses." University of Illinois Engineering Experimental Station, 104 pp.

Romualdi, J. P., and Batson, G. B. (1963). "Mechanics of Crack Arrest in Concrete." *Journal of the Engineering Mechanics Division,* 89(3), 147-168.

Romualdi, J. P., and Mandel, J. A. (1964). "Tensile Strength of Concrete Affected by Uniformly Distributed and Closely Spaced Short Lengths of wire Reinforcement." *ACI Journal Proceedings*, 61(6), 657-670.

Sakai, J., and Mahin, S. A. (2004). "Analytical Investigations of New Methods for Reducing Residula Displacements of Reinforced Concrete Bridge Columns." *PEER-2004/02,* Pacific Earthquake Research Center, University of California at Berkley, California.

Shah, S. P., and Rangan, B. V. (1971). "Fiber Reinforced Concrete Properties." *ACI Journal Proceedings,* 68(2), 126-135.

Shahrooz, B. M., Remmetter, M. E., and Qin, F. (1992). "Seismic Response of Composite Coupled Walls." *Composite Construction in Steel and Concrete II, ASCE*, 429-441.

Shahrooz, B. M., Remmetter, M. E., and Qin, F. (1993). "Seismic Design and Performance of Composite Coupled Walls." *Journal of Structural Engineering*, 119(11), 3291-3309.

Sharma, A. K. (1986). "Shear Strength of Steel Fiber Reinforced Concrete Beams." *ACI Structural Journal*, 83(4), 624-628.

Shui, N. K., Barney, G. B., Fiorato, A. E., and Corley, W. G. (1981). "Earthquake Resistant Walls: Coupled Wall Test "Report to NSF, Portland Cement Association, Skokie, IL.

Swamy, R., and Bahia, H. (1985). "The Effectiveness of Steel Fibers as Shear Reinforcement." *Concrete International*, 7(3), 35-40.

Swamy, R. N., Jones, R., and Chiam, A. T. P. (1993). "Influence of Steel Fibers on the Shear Resistance of Lightweight Concrete I-Beams." *ACI Structural Journal*, 90(1), 103-114.

Taranath, B. (2010). *Reinforced Concrete Design of Tall Building*, CRC Press, Florida.

Tassios, T. P., Moretti, M., and Bezas, A. (1996). "On the Behavior and Ductility of Reinforced Concrete Coupling Beams of Shear Walls." *ACI Structural Journal*, 93(6), 711-720.

Tegos, I. A., and Penelis, G. G. (1988). "Seismic Resistance of Short Columns and Coupling Beams Reinforced with Inclined Bars." *ACI Structural Journal*, 95(1), 82-88.

Vecchio, F. J. (1992). "Finite Element Modeling of Concrete Expansion and Confinement." *Journal of Structural Engineering*, 118(9), 2390-2406.

Vecchio, F. J. (2000). "Disturbed Stress Field Model for Reinforced Concrete: Formulation." *Journal of Structural Engineering*, 126(9), 1070-1077.

Vecchio, F. J., and Collins, M. P. (1986). "The Modified Compression-Field Theory for Reinforced Concrete Elements Subjected to Shear." *ACI Journal Proceedings*, 83(2), 219-231.

Wafa, F. F., and Ashour, S. A. (1992). "Mechanical Properties of High-Strength Fiber Reinforced Concrete." *ACI Materials Journal*, 89(5), 449-455.

Wight, J. K., and MacGregor, J. G. (2009). *Reinforced Concrete: Mechanics and Design*, Pearson Prentice Hall, Upper Saddle River, N.J.

Wong, P. S., and Vecchio, F. J. (2002). "Vector2 & FormWorks User's Manual." The University of Toronto, Toronto, Canada.

Xiao, Y., Esmaeily-Ghasemabadi, A., and Wu, H. (1999). "High-Strength Concrete Short Beams Subjected to Cyclic Shear." *ACI Structural Journal*, 96(3), 392-399.

Zollo, R. F. (1997). "Fiber-Reinforced Concrete: An Overview after 30 Years of Development." *Cement and Concrete Composites*, 19(2), 107-122.